Delft University of Technology

Mesoscale Organization of Precipitating Trade-Cumulus Fields

Alinaghi, P.

DOI
10.4233/uuid:07bbcb17-2c6d-46e3-b50e-4b0d7bd28c41

Publication date
2025

Document Version
Final published version

Citation (APA)
Alinaghi, P. (2025). *Mesoscale Organization of Precipitating Trade-Cumulus Fields*. [Dissertation (TU Delft), Delft University of Technology]. https://doi.org/10.4233/uuid:07bbcb17-2c6d-46e3-b50e-4b0d7bd28c41

Important note
To cite this publication, please use the final published version (if applicable).
Please check the document version above.

Copyright
Other than for strictly personal use, it is not permitted to download, forward or distribute the text or part of it, without the consent of the author(s) and/or copyright holder(s), unless the work is under an open content license such as Creative Commons.

Takedown policy
Please contact us and provide details if you believe this document breaches copyrights.
We will remove access to the work immediately and investigate your claim.

This work is downloaded from Delft University of Technology.
For technical reasons the number of authors shown on this cover page is limited to a maximum of 10.

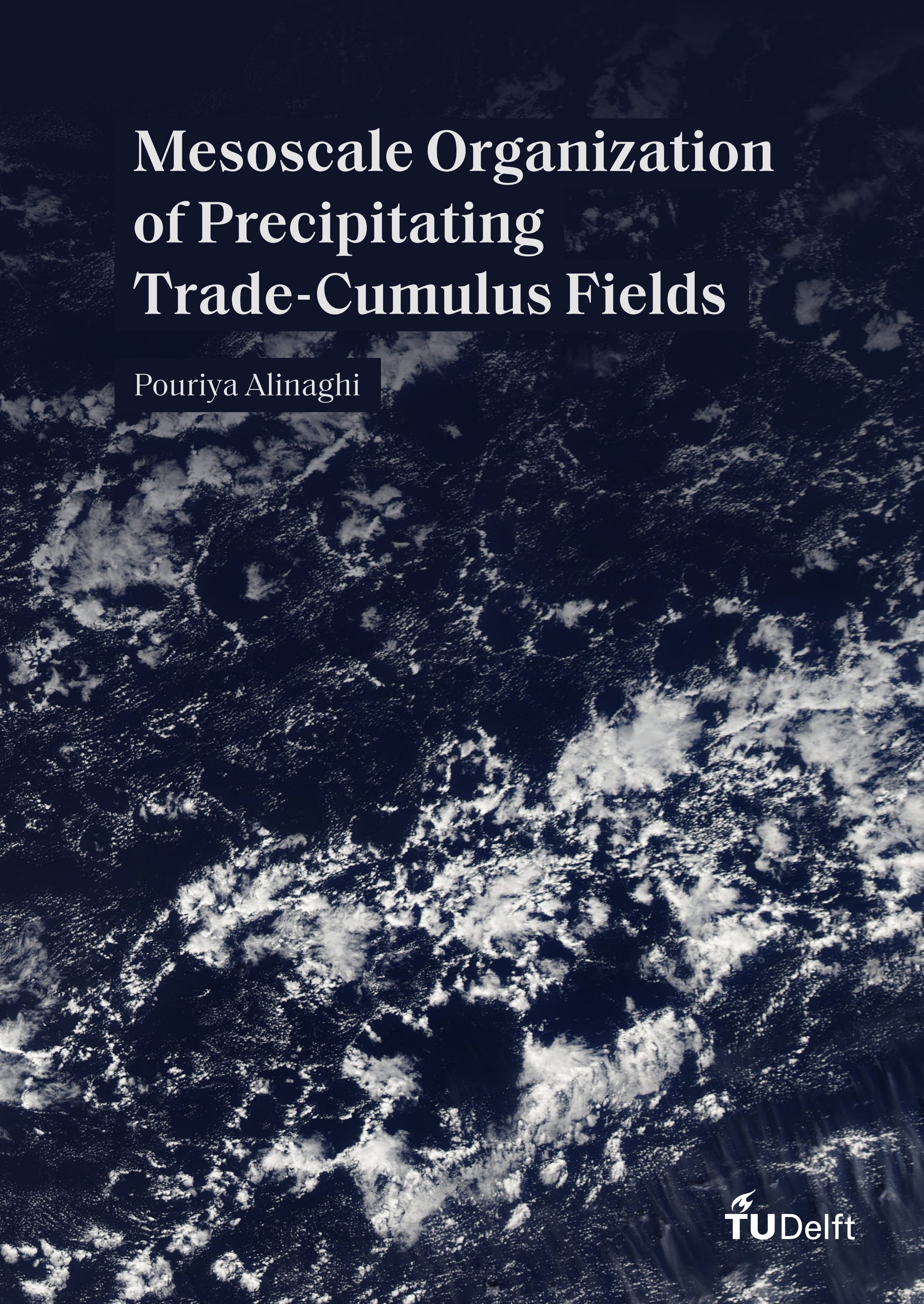

Mesoscale Organization of Precipitating Trade-Cumulus Fields

Pouriya Alinaghi

TU Delft

MESOSCALE ORGANIZATION OF PRECIPITATING TRADE-CUMULUS FIELDS

MESOSCALE ORGANIZATION OF PRECIPITATING TRADE-CUMULUS FIELDS

Doctoral Dissertation

for the purpose of obtaining the degree of doctor
at Delft University of Technology
by the authority of the Rector Magnificus, prof. dr. ir. T.H.J.J. van der Hagen,
chair of the Board for Doctorates
to be defended publicly on
Friday 21 November 2025 at 10:00 o'clock

by

Pouriya ALINAGHI

Master of Science in Applied Earth Sciences,
Delft University of Technology, The Netherlands,
Born in Tehran, Iran.

This dissertation has been approved by the promoters.

Composition of the doctoral committee:

Rector Magnificus,	Chairperson
Prof. dr. A. P. Siebesma,	Delft University of Technology, *promoter*
Dr. F. Glassmeier	Delft University of Technology, *copromoter*
Independent members:	
Dr. S. Bony	CNRS/Sorbonne University, Paris, France
Prof. dr. J. O. Haerter	University of Potsdam, Potsdam, Germany
Prof. dr. ir. F. Lopez Dekker	Delft University of Technology
Dr. S. R. de Roode	Delft University of Technology
Additional member:	
Dr. M. Janssens	Wageningen University & Research
Reserve member:	
Prof. dr. ir. H. W. J. Russchenberg	Delft University of Technology

This project is financially supported by the *Branco Weiss Fellowship—Society in Science, administered by ETH Zurich.*

Keywords: Mesoscale organization, Mesoscale patterns, Trade-wind cumuli, Cold pools, Cloud-radiative effects, Cloud feedbacks, Large-eddy simulations

Printed by: ProefschriftMaken

Cover: Designed by Amin Sohani; based on a NASA Worldview image captured by the MODIS/Aqua satellite on 13 Feb 2020.

The author set this thesis in LaTeX using the Libertinus and Inconsolata fonts.

ISBN/EAN: 978-94-6518-142-4

An electronic version of this dissertation is available at http://repository.tudelft.nl/.

Ever tried. Ever failed. No matter. Try again. Fail again. Fail better.

Samuel Beckett, Nobel Prize Winner in Literature, 1969.

CONTENTS

Summary **xxvii**

Samenvatting **xxix**

Persian Summary **xxxiii**

Preface **xxxvii**

1 Introduction **1**

1.1 Clouds: A beautiful source of inspiration that matters for climate 2

1.2 Trade-cumulus clouds over four spatiotemporal scales 7

1.2.1 Synoptic scales: Tropical large-scale circulations determine where trade cumulus can form 8

1.2.2 Individual cloud scales: A cumulus cloud results from moist convection 8

1.2.3 Microscales: Without aerosols trade cumulus cannot form 10

1.2.4 Mesoscales: Trade cumulus fields organize into mesoscale patterns 10

1.3 Aims of this thesis 13

1.3.1 Mesoscale self-organization of precipitating trade cumuli and its dependence on large- and micro-scales 13

1.3.2 The relevance of mesoscale organization for the radiative effect of trade-wind cumulus cloud fields 15

2 External Drivers and Mesoscale Self-Organization of Shallow Cold Pools in the Trade-Wind Regime **17**

2.1 Introduction 19

2.2 Methodology & Data 21

2.2.1 *Cloud Botany* Ensemble 21

2.2.2 Cold pools diagnosed by the mixed-layer height 23

2.3 Results and Discussion 25

2.3.1 The dependence of cold pools on cloud-controlling factors 25

2.3.2 The dependence of cold-pool evolution on the diurnal cycle 28

2.3.3 The dependence of cold pools on self-organizing mechanisms . . . 28

2.3.4 Implications for mesoscale cloud organization and radiative effect . 35

2.4 Summary. 39

2.5 Supplementary Information 41

3 Cold Pools Mediate Mesoscale Adjustments of Trade-Cumulus Fields to Changes in Cloud-Droplet Number Concentration **47**

3.1 Introduction 49

3.2 Data and Methods 51

3.3 Results and Discussion 54
3.3.1 Cloud-droplet number concentration affects the spatial and temporal properties of trade-cumulus cold pools 54
3.3.2 Cold-pool evolution shows two distinct mesoscale behaviours for low and high cloud-droplet number concentrations 55
3.3.3 Diurnal cycle synchronizes the phases of cold-pool evolution across simulations with perturbed N_c 59
3.3.4 Twomey effect primarily controls the dependence of cloud-radiative effect on N_c 61
3.3.5 N_c induces comparable variations in cloud-radiative effect to the large-scale cloud-controlling factors 63
3.4 Conclusions & Outlook. 64
3.5 Supplementary Information 66

4 Shallow Cumulus Cloud Fields Are Optically Thicker When They Are More Clustered 69
4.1 Introduction 71
4.2 Methodology and Data 71
4.3 Results & Discussions 74
4.3.1 Cloud clustering impacts CRE independently of f_c variability . . . 74
4.3.2 Clustering and cloud optical thickness are positively correlated . . 76
4.3.3 Mean cloud geometric thickness increases with clustering 79
4.4 Conclusions & Outlook. 81
4.5 Supplementary Information 84

5 Cold Pools Warm the Trades in Large-Eddy Simulations 91
5.1 Introduction 93
5.2 Inhibiting cold-pool formation by homogenizing rain evaporation 94
5.3 Results and Discussion 97
5.3.1 Cold pools warm the trades by reducing the outgoing longwave, clear-sky radiation at the top of the atmosphere 97
5.3.2 Cold-pool simulations remain moister because they precipitate less 98
5.3.3 Cold pools arrest runaway mesoscale self-aggregation of moisture . 101
5.3.4 Cold pools lead to slightly deeper clouds with smaller coverage . . 106
5.3.5 Impact of cold pools in comparison with large-scale CCFs 106
5.4 Conclusion 108
5.5 Supplementary Information 110

6 Conclusions and Outlook 115
6.1 Summary of thesis findings 116
6.1.1 Cold pools are coupled to clouds in the form of shallow squall lines in the trades 116
6.1.2 Mesoscale organization of precipitating cumuli is strongly controlled by the large-scale conditions 117
6.1.3 Cold-pool evolution is controlled by the micro-scale variability . . 117
6.1.4 Mesoscale organization affects cloud-radiative effect by modulating both cloud fraction and optical thickness. 118

6.1.5 Cold pools affect radiative budgets in the trades by affecting fields of moisture and not clouds . . . 118
6.2 A conceptual framework for the trade-wind cumulus system . . . 119
6.2.1 Trade-cumulus self-organization tends to exhibit a cyclic behavior . 119
6.2.2 What controls the center, size, and the frequency of the cyclic behavior? . . . 121
6.2.3 How does the system evolve if it is initialized from an already organized state outside the cycle? . . . 123
6.2.4 What does the cyclic behaviour imply for trade-cumulus radiative budgets? . . . 124
6.2.5 Open questions and outlook . . . 125
6.3 Supplementary information . . . 128

Bibliography **131**

Curriculum Vitæ **145**

List of Publications **147**

Acknowledgments **151**

List of Figures

1.1 **Clouds in art and poems.** a) *Wheat Fields* by Jacob van Ruisdael, a renowned Dutch painter whose works are notably inspired by clouds. Clouds he painted appear especially realistic compared with many other artists. b) A typical example of Persian calligraphy in the Shekasteh Nastaligh style by Shahram Roohi, illustrating a poem consisting of clouds by Khayyam, a celebrated Persian poet who lived approximately 900 years ago. The poem starts with: "*The cloud arrived and wept anew upon the grass, Without rose-hued wine, life one must not pass.*" 2

1.2 **Cloudy Earth.** This image is from Meteosat Third Generation – Imager 1 (MTG-I1) taken at 11:50 UTC on 18 March 2023 by the Flexible Combined Imager on MTG-I1. The figure emphasizes that Earth appears predominantly white rather than blue, primarily due to clouds, which cover 67-68% of our planet. 3

1.3 **Cloud-climate feedback throughout years 1989 to 2021.** a) The sensitivity of climate sensitivity parameter λ to cloud-radiative forcing (CRF) (Cess et al., 1989, their Fig. 1). b) The sensitivity of shortwave (SW) and longwave (LW) cloud feedback to different cloud regimes quantified by large-scale subsidence ω in low-sensitivity (blue) and high-sensitivity models (Bony and Dufresne, 2005, their Fig. 2), where the dotted lines show the minimum and maximum of these sensitivities among models. c) The scatter in the projected climate sensitivity among climate models and its dependence on low-cloud climate feedback (Schneider et al., 2017, their Fig. 1). d) The assessed values of cloud feedbacks for each individual component, adapted from Sherwood et al. (2020). e) The last climate feedback estimate from the sixth assessment report (AR6) of the IPCC report (IPCC AR6, 2023, their Chapter 7). 6

1.4 **Cloud types across Hadley cell.** The figure, adapted from George (2021), shows different cloud types and the coupling of clouds to the large-scale circulations across the Hadley cell. 9

1.5 **Mesoscale cloud patterns in the downstream trades.** The subjectively identified cloud patterns by Stevens et al. (2020). Photos are from the NASA Worldview platform and are taken by either Aqua or Terra satellites on 2024/01/31 (Sugar), 2016/12/26 (Gravel), 2017/02/09 (Flowers), and 2024/01/14 (Fish), close to the east coast of Barbados over the North Atlantic Ocean. 12

1.6 **Sketch of the dependence of mesoscale cloud (self-)organization on large- and micro-scale processes.** The horizontal and vertical axes represent spatial and temporal scales. The diagram summarizes the main foci of the thesis, where the response of mesoscale self-organization to variations in micro- and large-scale processes is explored. The large-scale figure is adapted from the book by Mathez and Smerdon (2018). 14

2.1 **A conceptual picture of the trade-cumulus cloud system.** The dashed rectangle box shows the trade cumulus system which is forced by (1) the large-scale CCFs and (2) the diurnal cycle. Having time-invariant and conducive CCFs, this system shows (3) self-organization via interaction between its components, i.e. clouds and cold pools. As a result of these interactions, this system might show (i) a time-invariant, (ii) an unstable, or (iii) an intermittent behaviour. The resulting (4) cloud-radiative effect is expected to depend on the details of links (1) to (3). 20

2.2 **Evolution of cumulus clouds in *Botany*.** (a) Time series of domain-mean liquid-water path ($\mathcal{L}$) and rain-water path ($\mathcal{R}$), averaged over the entire *Botany* ensemble. Grey-shaded areas correspond to nighttime. (b,c,d,e) Contour plots of cloud albedo for the central reference simulation (run 1) that has the mean CCFs of the entire ensemble. 24

2.3 **Cold-pool mask definition.** (a) Contour plot of h_{mix} for hour 29 of the central reference simulation, which its cloud field is shown in Fig. 2.2. The cold-pool mask is shown by the green dashed contour line. (b) The probability density distribution of the h_{mix} shown in (a). 25

2.4 **Multivariate regression of CCFs to predict cold-pool statistics.** (a,c,e) The scatter plot of the results of multivariate regression analysis for $\overline{f}_{cp}$, $\overline{n}_{cp}$, and $\overline{s}_{cp}$ over the last two days of the *Botany* ensemble, where each purple circle stands for one simulation and the black line represents $y = x$. (b,d,f) The standardized beta coefficients (β) of the multiple regression analysis for predicting $\overline{f}_{cp}$, $\overline{n}_{cp}$, and $\overline{s}_{cp}$ as a function of *Botany*'s CCFs. Black error bars indicate the 95% confidence interval of each CCF. The greater the distance of the error bar from zero, the more significant the associated CCF in the regression model (smaller p-values). The p-values of the F-statistic test for all regression models are smaller than 10^{-17}. 27

2.5 **Effect of the diurnal cycle on cold pools.** (a) The time series of the median f_{cp} (continuous line) accompanied by the interquartile range between the 25th and 75th percentiles of f_{cp} (purple shade) for the entire *Botany* ensemble. The f_{cp} time series of the central reference simulation is shown by the dashed line. (b) Time series of f_{cp} for the central reference simulation in the *Botany* dataset with (black) and without (blue) the diurnal cycle. Grey-shaded areas correspond to nighttime. 29

2.6 **Cloud-rain-cold-pool correlations.** (a) Time series of f_c, $\mathcal{L}$, and $\mathcal{P}$. (b) Lag-correlations of f_{cp} with f_c (continuous line), the in-cloud $\mathcal{L}$ (dashed line), and the in-rain $\mathcal{P}$. The highest correlations are marked by the red circle. The correlations are based on the last five days of the simulation without the diurnal cycle, during which the domain-mean total-water path has stabilized (Fig. S3.5). 30

2.7 **Typical stages of the cold-pool system's life cycle.** The left column shows four contour plots of cloud albedo along with the cold-pool mask shown by the dashed, magenta contour lines for hours 164-167 of the simulation without the diurnal cycle. The right column shows y-z-cross-section contour plots of the total specific humidity anomalies associated with the dashed red line in snapshots shown in the left column. Cloud and rain boundaries are shown by the blue and grey contour lines. Circulations are made from the meridional (v) and vertical (w) velocity anomalies and are shown by black streamlines. To reduce the noise from the circulations, v, w are made from the medians of a 5-km window along the x dimension. The h_{mix} is shown by the dashed, magenta contour lines. The South (S), North (N), West (W), and East (E) directions are shown by orange labels. . 31

2.8 **Composite analysis of the evolution of the cold-pool system.** Composite time series of the evolution of the domain-mean precipitation intensity $\mathcal{P}$ with (a) the domain-mean liquid-water path $\mathcal{L}$ and cloud geometric thickness h, (b) maximum near-surface horizontal velocity at cold-pool areas $u_{cp,max}$ and the 99.99th percentile of vertical velocity $w_{P_{99.99}}$ at 200-m level, (c) domain-mean size of cloud objects L_c and precipitation cells L_p within the simulation domain for all life cycles of the cold-pool systems of the last five days of the simulation without the diurnal cycle. The stages of the cold-pool system *Developing, Mature, and Decaying* are marked by colors green, purple, and yellow, respectively. Composited time series were slightly smoothed using a Gaussian low-pass filter. 33

2.9 **Cold-pool-mesoscale organization relationships.** (a) Time series of L_c and L_o. (b) Lag-correlations of f_{cp} with L_c and L_o, with red circles showing the best correlations. (c) Similar composite analysis to Fig. 2.8 for $\mathcal{P}, f_{cp}, L_c$, and L_o of the simulation without the diurnal cycle. (d) The evolution of the standardized L_c and L_o (concerning their mean and standard deviations) through one cold pool's life cycle (hours 70-82). (e) The same relationship as (d) but with lags with respect to f_{cp} time series. The size of each circle in both plots is scaled by the value of f_{cp} at the corresponding time step. The correlations are based on the last five days of the simulation without the diurnal cycle. 37

2.10 **Dependence of cloud-radiative effect on cold pools.** (a) Similar composite analysis to Fig. 2.8 for $\mathcal{P}, f_c, \mathcal{L}$, and net CRE (shortwave SW + longwave LW) of the simulation without the diurnal cycle. (b) The 2D scatter plot of the daily mean cold-pool fraction $\overline{f}_{cp}$ and the fraction of daytime contribution to this mean $r_{cp,day}$ quantified by Eq. 2.5 for the entire *Botany* ensemble. 38

2.11 **Conceptual schematic of the cold-pool system.** Schematic of the cold-pool system evolution during the *Developing*, *Mature*, and *Decaying* stages as shown in sect. 2.3.3 under Figs. 2.7, 2.8. 40

S2.1 **Multivariate regression of CCFs to predict cold-pool statistics.** This plots is as same as the first figure of the results of section 3.1, but for cold pools being defined where $h_{mix} < 400$ m. Comparing two figures with each other, the number of cold pools and their response to CCFs are exactly the same. This analysis further shows that the definition ($h_{mix} < 400$ m) seems a bit stricter compared to our definition, which leads to cold pools being approximately 20% smaller. However, this does not affect the response of cold-pool sizes and fractions to CCFs; i.e., the relative significance of CCFs for cold-pool properties remains the same. 42

S2.2 **Multivariate regression results of cloud-top height $\overline{z}_t$.** (a) The scatter plot of the results of multivariate regression analysis. (b) The standardized beta coefficients of the multiple regression analysis for predicting the domain-mean cloud-top height (z_t) as a function of large-scale CCFs of *Botany* simulations. 43

S2.3 **Multivariate regression results of the liquid-water path $\overline{\mathcal{L}}$.** (a) The scatter plot of the results of multivariate regression analysis. (b) The standardized beta coefficients of the multiple regression analysis for predicting the domain-mean $\mathcal{L}$ as a function of large-scale CCFs of *Botany* simulations. 43

S2.4 **Time series of cold-pool statistics including number and size.** Time series of (a) the number of cold-pool objects, and (b) the average size of cold-pool objects for the center run in the *Botany* dataset. These two metrics are only calculated for cold-pool objects featuring an area larger than 25 km^2. Due to this threshold, the time series of these two metrics are a bit noisy. To better see the signal, the noise in the scatter plot is filtered out in the line plot. The black (blue) line stands for the run with (without) the diurnal cycle. Grey-shaded areas correspond to nighttime. 44

S2.5 **Time series of domain-averaged total water path.** 44

S2.6 **Effect of cold pools on the sub-cloud layer in space and time. Contour plots** of: horizontal velocity (U) anomaly near the surface, and vertical velocity (w) at the 200-m level at hour 165 of the center simulation without the diurnal cycle. The cold-pool mask is shown by the green dashed contour line. **Cross-correlations** during the last five days: f_{cp} with mean and maximum horizontal velocity anomalies at cold pools, and f_{cp} with $w_{P_{99.99}}$ (99.99 th percentile of w). The red circles in the lag-correlations show where the correlation reaches its maximum absolute value. **Message of the figure:** This figure highlights that the dynamic properties of cold pools such as diverging outflows (as measures by the horizontal velocity anomalies) and the resulting convergence at their gust fronts (as measured by $w_{P_{99.99}}$) already reach their maximum values before cold pools reaching their maximum size as measured by f_{cp}. 45

S2.7 **Examples showing the importance of the timing of cold pools for their effect on CRE.** (a) Time series of f_{cp} for simulations 1, 92, and 102 of the *Botany* ensemble with the diurnal cycle. (b) Time series of the net CRE for the same simulations as in (a), with more negative values implying more cooling. Note that the magnitude of LW CRE is much smaller compared to that of SW CRE in our simulations as our focus is on shallow clouds. . . . 46

S2.8 **Dependence of the cold-pools' daytime contribution to the daily mean cold-pool fraction $r_{cp,day}$ on cloud-controlling factors CCFs.** This plot shows the multivariate regression analysis for quantifying the extent to which $r_{cp,day}$ is controlled by CCFs. The results of this figure show that this metric is not fully controlled by CCFs, consistent with the scatter plot shown in Fig. 10b. 46

3.1 **Conceptual picture of the study.** The diagram summarizes how (link 1) cloud fields respond to changes in N_c, and how (link 2) cold pools feed back to clouds (self-organization). The diagram further shows that the trade-cumulus system is forced by (link 3) the large-scale cloud-controlling factors (CCFs) whose relative importance for (link 4) the cloud-radiative effect will be quantified compared to N_c. 51

3.2 **Large-scale and initial conditions of the simulation** for potential temperature θ_l, total moisture q_t, horizontal wind u, and updraft w following the assumptions of the *Cloud Botany* ensemble (Jansson et al., 2023) with parameter values of sea-surface (potential) temperature $\theta_{l0} = 299$ K, near-surface wind speed $u_0 = -10.6$ m/s, moisture scale-height $h_{q_t} = 1810$ m, temperature lapse-rate $\Gamma = 5$ K/km, large-scale vertical velocity variability $w_1 = 0.0393$ cm/s, and the horizontal wind shear $u_z = 0.0022$ (m/s)/m. . . . 52

3.3 **Cloud-field albedo examples.** The figures show how cloud fields develop in our LES simulations featuring the diurnal cycle of insolation with N_c of 20 (1st row), 50 (2nd row), 70 (3rd row), 100 (4th row), 200 (5th row), and 1000 /cm^3 (6th row), at hours 15 (1st column), 30 (2nd column), 40 (3rd column), and 50 (4th column) after the start of simulations. 53

3.4 **Time series of clouds, rain, and spatial properties of cold pools in simulations without the diurnal cycle.** Panels (a-d) show time series of $\mathcal{L}$, $\mathcal{R}$, n_{cp}, and s_{cp} for simulations without the diurnal cycle of solar incoming radiation, where solid lines shown for cold-pool number and size provide a guide to the eye obtained through Gaussian filtering of the original data points. Note that there is significant precipitation in the $N_c = 20$ /cm^3 case before cold pools with diameters larger than the 5-km threshold appear. Panels (e-h) show the response of $\mathcal{L}$, $\mathcal{R}$, n_{cp}, and s_{cp} to N_c. The results from Yamaguchi et al. (2019) averaged over the last 20 hours of their simulations are shown in orange. The results from Seifert et al. (2015) for their near-equilibrium state are shown in blue. Dashed lines are added as a visual guide where the mean values show a trend. 54

3.5 **Effects of cold pools on the organization of the (sub-)cloud layer properties for the simulations without diurnal cycle and with $\mathbf{N_c}$ = 20/$\mathbf{cm^3}$ and $\mathbf{N_c}$ = 1000/$\mathbf{cm^3}$.** For each condition, columns 1-4 indicate the 2D top-views of cloud albedo, total moisture anomalies (q_t') at the 200-m level, the horizontal wind speed anomalies (U') at the first level of the model, and the vertical velocity (w) at the 200-m height. The green dashed contour line marks the cold-pool boundaries quantified from the mixed-layer height fields. In the U' fields, red indicates that cold pools accelerate the wind, while blue indicates they decelerate it. 56

3.6 **Dependence of mesoscale organization of cloud fields on $\mathbf{N_c}$.** The panels (a,c) show the time series of the spatial standard deviation of the liquid-water path σL and the difference between the 5^{th} and 95^{th} percentiles of the mesoscale total moisture anomaly fields ΔQ for the simulations without the diurnal cycle of insolation. Panels (b,d) show their responses to $\mathrm{N_c}$ for hours 24-48 in purple and hours 48-72 in green. Dashed lines are added as a visual guide where the mean values have a trend. 59

3.7 **Effects of the diurnal cycle of insolation on the evolution and $\mathbf{N_c}$-response of rain and cold pools.** Panels (a-c) show time series of rain-water path $\mathcal{R}$, cold-pool number n_{cp}, and cold-pool size s_{cp} for simulations with the diurnal cycle of solar incoming radiation. Nighttime is shown by the grey color. Solid lines shown for cold-pool number and size provide a guide to the eye obtained through Gaussian filtering of the original data points. Note that there is significant precipitation in the $\mathrm{N_c}$ = 20 /cm^3 case before cold pools with diameters larger than the 5-km threshold appear. Panels (d-e) show the response of $\mathcal{R}$, n_{cp}, and s_{cp} to $\mathrm{N_c}$ during the transient (purple), and near-equilibrium (green) phases, which are marked in the time series plots (a-c). Dashed lines are added as a visual guide where there is a trend. 60

3.8 **Sensitivity of relative cloud-radiative effect to cloud-droplet number.** Panels (a-d) show the response of cloud fraction f_c, domain-mean liquid-water path $\mathcal{L}$, cloud albedo $\mathcal{A}_c$, and relative cloud-radiative effect rCRE to $\mathrm{N_c}$ during the non-precipitating (dark grey), transient (purple), and near-equilibrium (green) phases. The results from Yamaguchi et al. (2019) averaged over the last 20 hours of their simulations are shown in orange. The results from Seifert et al. (2015) for their near-equilibrium state are shown in blue. Note that Seifert et al. (2015); Yamaguchi et al. (2019) do not report on the cloud albedo and rCRE in their studies. Dashed lines are added as a visual guide where there is a trend. 62

3.9 **Cloud-field response to large-scale cloud-controlling factors and cloud-droplet number concentration.** The standardized β coefficients of the multiple regression analysis for (a) cloud albedo $\mathcal{A}_c$ and (b) relative cloud-radiative effect rCRE, all averaged over the last two days of the LESs of the *Botany* ensemble. The error bars show the 95% confidence interval for each regressor. The p-values of the F-statistic test of all models are smaller than 10^{-22}. 64

S3.1 **Dependence of several mesoscale cloud organization metrics on $\mathbf{N_c}$.** The panels (a,c,e,g) show the time series of the domain-mean size of cloud objects L_c, the mean fraction of the open-sky areas L_o, the domain-mean of cloud-top height z_t, and the degree of organization I_{org} for the simulations without the diurnal cycle of insolation. Panels (b,d,f,h) show their mean responses to $\mathrm{N_c}$ for hours 24-48 in purple and 48-72 in green. The dashed line is shown as a visual guide where there is a trend. 66

S3.2 **Total-water path time series for several $\mathbf{N_c}$.** The figure shows the development of the domain-mean total-water path, which is the sum of both cloud-water and water-vapor paths. The transient and near-equilibrium phases are marked by purple and green. 67

S3.3 **Cloud-field response to large-scale cloud-controlling factors and cloud-droplet number perturbations.** The standardized β coefficients of the multiple regression analysis for (a) rain-water path $\overline{\mathcal{R}}$, (b) cold-pool fraction $\overline{f}_{cp}$, (c) cold-pool number $\overline{n}_{cp}$, (d) cold-pool size $\overline{s}_{cp}$ (e) liquid-water path $\overline{\mathcal{L}}$, and (f) cloud fraction $\overline{f}_c$, all averaged over the last two days of the LESs of the *Botany* ensemble. The error bars show the 95% confidence interval for each regressor. The larger the distance of the confidence interval with zero, the more significant the corresponding regressor. The p-values of the F-statistic test of all models are smaller than 10^{-15}. 67

4.1 **Distribution of cloud field properties from Aqua MODIS and CERES satellite data.** (a) cloud fraction f_c, (b) degree of organization I_{org}, (c) domain-mean net cloud radiative effect (CRE), (d) domain-mean SWCRE, (e) domain-mean LWCRE, (f) domain-mean cloud-top height z_t, (g) domain-mean cloud optical depth τ_c, (h) domain-mean cloud effective radius r_e, (i) domain-mean cloud field albedo, and (j) domain-mean liquid-water path $\mathcal{L}$. 73

4.2 **Dependence of domain-mean CRE on clustering.** In the first row (a-c), the relationships between I_{org} and SWCRE (a), LWCRE (b), and net CRE (c) are illustrated. The second row (d-f) presents the same relationships, but the data is grouped into four classes based on the 0^{th} (P0), 25^{th} (P25), 50^{th} (P50), 75^{th} (P75), and 100^{th} (P100) percentiles of f_c, indicated by colors ranging from purple to yellow, representing low to high f_c, respectively. The third row (g-i) shows the same relationships but with removing the f_c variability through partial correlation analysis (Eq. 4.6). The mean values of I_{org} (for the 3^{rd} row, $I_{org}|f_c$) in each bin are denoted by red (purple, blue, green and yellow for the 3^{rd} row) circles, with their size proportional to the number of points in the bin. The dots are fitted with a dashed line. Values below the 5^{th} and above the 95^{th} percentile of I_{org} (for the 3^{rd} row, $I_{org}|f_c$) are excluded from the fit. 75

4.3 **Dependence of domain-mean cloud optical depth on clustering.** The scatter plot of MODIS cloud features (a) and the 2-dimensional histogram (b) depict the $I_{org}|f_c$–$\tau_c|f_c$ relationship. Specifically, for the scatter plot in (a), instead of displaying individual points, the entire cloud field is visualized to enhance pattern visualization. Clouds are represented in white, while the blue background represents the ocean color (MODIS true-color images). For plot (b), the mean values of $I_{org}|f_c$ in each bin are denoted by red circles, with their size proportional to the number of points in the bin. The red dots are fitted with a dashed black line. Values below the 5^{th} and above the 95^{th} percentile of $I_{org}|f_c$ are excluded from the fit. 77

4.4 **Dependence of domain-mean liquid water path and effective radius on clustering.** The figure shows the 2D histograms of the relationships between $I_{org}|f_c$ and $\mathcal{L}|f_c$ (a), and between $I_{org}|f_c$ and $r_e|f_c$ (b). The mean values of $I_{org}|f_c$ in each bin are denoted by red circles, with their size proportional to the number of points in the bin. The red dots are fitted with a dashed black line. Values below the 5^{th} and above the 95^{th} percentile of $I_{org}|f_c$ are excluded from the fit. 77

4.5 **Relationship between domain-mean liquid-water path and effective radius**. This figure shows that $\mathcal{L}|f_c$ is positively correlated to $r_e|f_c$. The figure further shows that with increased clustering $I_{org}|f_c$, i.e., going from lower right corner to upper left corner, r_e decreases, while $\mathcal{L}$ increases. The mean values of $r_e|f_c$ in each bin are denoted by red circles, with their size proportional to the number of points in the bin. The red dots are fitted with a dashed black line. Values below the 5^{th} and above the 95^{th} percentile of $r_e|f_c$ are excluded from the fit. 78

4.6 **Dependence of domain-mean geometric thickness, average size of cloud objects, and domain-mean cloud-base height on clustering.** (a) The figure shows the 2D histogram of the relationship between $I_{org}|f_c$ and $h|f_c$. (b) The plot shows the relationship between $I_{org}|f_c$ and the mean-field cloud object size (L_c) with contour colors representing the values of domain-averaged cloud-base height (z_b). The gray shade indicates the inter-quartile range variability of L_c in each bin of $I_{org}|f_c$. For both plots, the mean values of $I_{org}|f_c$ in each bin are denoted by red circles, with their size proportional to the number of points in the bin. The red dots are fitted with a dashed black line. For both plots, values below the 5^{th} and above the 95^{th} percentile of $I_{org}|f_c$ are excluded from the fit. 81

4.7 **Summary of results.** Comparing two cloud fields with identical cloud cover, the highly-clustered cloud field features a larger domain-averaged geometric thickness, a higher liquid water path, more frequent anvils with smaller cloud droplets, and consequently, brighter clouds and therefore larger SW reflection in comparison to the unclustered cloud field. Blue arrows and corresponding equations are supported by theory and thus imply causality. Purple arrows are main results of our study, which only indicate correlations. The gray arrows illustrate apparent paradoxes which are discussed in section 4.3.2. 82

S4.1 The distribution of lifting-condensation level (LCL), domain-mean cloud-base height (z_b), domain-mean cloud-top height (z_t), and domain-mean cloud geometric thickness (h) along the entire *Botany* ensemble. 84

S4.2 The 2D histograms of the relationships between f_c and (a) I_{org}, (b) SWCRE, and (c) LWCRE with the reported Pearson's correlation (R). 84

S4.3 The figure illustrates Eq. 4.6 and emphasizes that we do not fix but control for f_c. Here, we show the example for X =SWCRE. The term $X|f_c$ quantifies variability in SWCRE that cannot be explained by f_c. 85

S4.4 The result of the bi-linear regression analysis in which the target value is SWCRE and the regressors are f_c and Ac|f_c (Ac: cloud albedo observed by CERES). The reported coefficients are for the standardized f_c and Ac|f_c. This plots ensures that the derived f_c from MODIS cloud masks in addition to the observed albedo by CERES can significantly capture the variability in SWCRE. 85

S4.5 The relationship between I_{org} and cloud albedo (A_c), having the effect of f_c eliminated. 86

S4.6 The result of the bi-linear regression analysis in which the target value is ln τ_c and the regressors are ln $\mathcal{L}$ and ln r_e. The reported coefficients are for the standardized ln $\mathcal{L}$ and ln r_e. This plots ensures that ln $\mathcal{L}$ and ln r_e can significantly capture the variability in ln τ_c, in line with theory. 86

S4.7 **Satellite snapshots of cloud-droplet effective radius.** A highly-clustered (a) and an unclustered cloud field snapshots (from NASA Worldview) taken by NOAA-20 satellite on 03/Feb/2021 (10°-16°N, 51°-57°W) and 19/Dec/2021 (14°-18°N, 48°-53°W), respectively. The cloud fields are colored by the value of standard effective radius r_e product, which goes from 4 (yellow) to 30 (red) μm. Note that in the standard satellite product of the field shown in (b), smaller clouds (pixels with low cloud fractions) are already removed from the scene due to high uncertainty in their retrievals. Therefore, to some extents, it assures that our analysis of effective radius is not considerably affected by retrieval issues of these small clouds. 87

S4.8 The figure shows the relationships between a) f_c and I_{org} and b) I_{org} and (net) CRE in Botany simulations. This figure shows that as the domain size decreases from ≈1100 km (in satellites) to ≈150 km (in *Botany*), the correlation between f_c and I_{org} drastically decreases, meaning that f_c and I_{org} do not share information in smaller domains. As a result, the correlation between I_{org} and net CRE does not change after removing the f_c variability (see the difference between plot (b) and Fig. S4.10, a). Nevertheless, in section 3.3, we removed the f_c variability from both CRE and I_{org}, as still CRE variability is primarily controlled by f_c. 87

S4.9 This figure shows how the $f_c - I_{org}$ correlation changes with reducing the domain size from $10^\circ \times 10^\circ$ to $5^\circ \times 5^\circ$. For the latter, we use the dataset which is publicly shared by Janssens et al. (2021). 88

S4.10 All results derived from the hourly analysis of the Cloud Botany dataset during the second day between the 37^{th} and 43^{rd} hours. Values below the 5^{th} and above the 95^{th} percentile of $I_{org}|f_c$ are excluded from the fitting. . . 88

S4.11 Similar to Fig. 4.3(a) but for the Botany dataset during hours 37-43. 89

S4.12 The result of the bi-linear regression analysis in which the target value is the in-cloud $\mathcal{L}$ and the regressors are h and f_{ad}. The reported coefficients are for the standardized h and f_{ad}. 89

5.1 **Temporal evolution of cloud fields in both the CP and NoCP ensembles.** a) Time series of cloud- and rain-water paths averaged over the entire CP (continuous) and NoCP (dashed) ensembles. Grey shades show nighttime. b) and c) are the top-view fields of cloud albedo (first row) and mixed-layer height (second row) for the central reference simulation of the CP and NoCP ensembles, respectively. 96

5.2 **Effects of cold pools on the daily mean net radiative budget at the top of the atmosphere.** a) Decomposition of the net radiative flux at the TOA into shortwave C_s and longwave C_l cloud radiative effects, and the shortwave $F^{\uparrow}_{s,c}$ and longwave $F^{\uparrow}_{l,c}$ outgoing clear-sky fluxes at the TOA. For each component, the y-axis shows the associated TOA radiation of CP ensemble minus that of NoCP ensemble. b) Decomposition of C_s to effects from cloud fraction $F^{\downarrow}_{s}\alpha_c\Delta f$ and albedo $F^{\downarrow}_{s} f\Delta\alpha_c$. c) Dependence of $\Delta F^{\uparrow}_{l,c}$ on the difference between the mean total-water path ΔI between the CP and NoCP ensembles. 98

5.3 **Effects of cold pools on the total-water budget.** a) Difference in moisture budget components (Eq. 5.3) between CP and NoCP cases, with CP minus NoCP tendencies on the y-axis. b) Decomposition of precipitation-induced moistening into rain-evaporation, auto-conversion, and accretion rates for the central reference simulation. c,d) Same decomposition as a,b for the full ensemble. Components are averaged over hours 12-36, when simulations start diverging in total moisture. Each simulation's mean is marked by a cross (×), the ensemble mean by squares, interquartile range edges by horizontal bars, and the central reference simulation mean by a red circle. 100

5.4 **Effects of cold pools on rain and surface precipitation flux.** Moisture space of the total-water content anomaly q_t' (a,b) cloud- and rain-water contents q_l and q_r (c,d) for the CP and NoCP ensembles. q_l is shown by the dashed, white-to-red contour lines. Plots d) and f) show the 2D histogram of 10-km total-water anomalies I' vs. 10-km rain-water path $\mathcal{R}$ and surface precipitation flux $\mathcal{P}$, with c) and e) showing the cumulative contribution of I' bins to the mean $\mathcal{R}$ and $\mathcal{P}$ of each ensemble. 102

5.5 **Impact of cold pools on mesoscale self-aggregation of moisture.** (a) Differences between terms in Eq. 5.9 for the CP and NoCP ensembles. At each time step, components are averaged over 10-km blocks where I' exceeds the 90th percentile. Time averages are taken over hours 12–36, when the simulations begin to diverge in total moisture. Crosses (×) indicate individual simulation means, squares show the ensemble mean, and horizontal bars mark the interquartile range. (b) Ensemble-averaged time series of mesoscale 10-km vertical motion (w'_m) in the lowest 5 km for NoCP (orange) and CP (black), with CP contributions from cold-pool edges (green), inside (blue), and outside (magenta). (c-g) Vertical profiles of (b) for hours 16-37. (i-k) Same as (e-g), but without weighting by (h), which shows the distribution of the fractions of cold-pool regions within highly moist (rainy) 10-km blocks. 105

5.6 **Effects of cold pools on the response of the TOA radiative fluxes to CCFs.** a,b) Results of multiple regression analysis for the TOA shortwave cloud radiative effect C_s with the beta coefficients shown in b). c,d) Results of multiple regression analysis for the TOA longwave clear-sky radiative effect $-F^{\uparrow}_{l,c}$ with the beta coefficients shown in d). The p-values of the F-statistic of both models are smaller than 10^{-12}. 108

S5.1 **Multivariate regression results of the gradient production term $-w'_m \frac{\partial q_{t,m}}{\partial z}$.** (Left) The scatter plot of the results of multivariate regression analysis with around 130 k points from the mesoscale blocks of the entire ensemble in 3D. (Right) The standardized beta coefficients of the multiple regression analysis for predicting the gradient production term ($-w'_m \frac{\partial q_{t,m}}{\partial z}$) as a function of mesoscale vertical ascent w'_m and gradient of mesoscale moisture $\frac{\partial q_{t,m}}{\partial z}$. The error bars show the confidence intervals at the 99.99^{th} level of confidence. **Message** is that the gradient production term is strongly controlled by the mesoscale vertical motion and the effect of w'_m is around five times larger than that of moisture gradient in height. 110

S5.2 **Cloud-circulation coupling in CP vs. NoCP ensembles.** The left column shows four contour plots of cloud albedo along with the cold-pool mask shown by the dashed, magenta contour lines for two time steps of CP (upper part) and NoCP (lower part) ensemble. The right column shows y-z-cross-section contour plots of the total specific humidity anomalies associated with the dashed red line in snapshots shown in the left column. Cloud and rain boundaries are shown by the blue and grey contour lines. Circulations are made from the meridional (v) and vertical (w) velocity anomalies and are shown by black streamlines. To reduce the noise from the circulations, v, w are made from the medians of a 5-km window along the x dimension. The h_{mix} is shown by the dashed, magenta contour lines. The South (S), North (N), West (W), and East (E) directions are shown by orange labels. 111

S5.3 **Impact of cold pools on cloud fraction.** 2D histograms of (b) 10-km total-water anomalies (I) vs. cloud fraction (f_c) and (d) 10-km vertical velocity (w) vs. cloud fraction. Cumulative contributions to the mean f_c are shown in (a) and (c), respectively. 113

S5.4 **Impact of cold pools on liquid-water path.** 2D histograms of 10-km total-water anomalies (I') vs. 10-km (b) cloud-base mass flux ($\mathcal{M}$), (d) cloud-top height (z_t), and (f) cloud-liquid-water path ($\mathcal{L}$). Cumulative contributions of I bins to the mean values are shown in (a), (c), and (e), respectively. 114

6.1 **Conceptual diagram of the evolution of the trade-cumulus system.** Plots show diagram sketches of the temporal evolution of the a) process space spanned by the mesoscale moisture (self-)aggregation ΔQ and cold-pool dynamics $\mathcal{D}_{cp}$ and b) mesoscale organization space spanned by the geometry-based organization metrics. The mean of (near-)steady state is shown by the black dot in both process space ($\overline{\Delta Q}$,$\overline{\mathcal{D}}_{cp}$) and organization space ($\overline{\mathcal{L}}$,$\overline{f}_c$). 120

6.2 **Conceptual diagram of the trade-cumulus system and its dependence on large-scale conditions.** The figures illustrate changes in the cyclic behavior of trade-cumulus self-organization in response to increased large-scale wind speed, instability, and subsidence. Low-transparency diagrams indicate the reference evolution (Fig. 6.1), while high-transparency curves show the new evolution. 122

6.3 **Conceptual diagram of the trade-cumulus system and its dependence on cloud-droplet number concentration.** The figures illustrate changes in the behavior of trade-cumulus self-organization in response to variations in cloud-droplet number concentration $\mathrm{N_c}$. Low-transparency diagrams indicate the reference evolution with $\mathrm{N_c} > 50$ /cm^3 (Fig. 6.1), while high-transparency curves show the new evolution with decreased $\mathrm{N_c}$ to concentrations of 20/cm^3. The purple arrow here means that both cold pools (blue) and mesoscale aggregation (red) are growing together. . . 123

S6.1 **Temporal evolution of mesoscale processes shaping organization of trade-cumulus fields.** The left plot shows the temporal evolution of the mesoscale moisture self-aggregation metrics ΔQ and cold-pool fraction f_{cp} as processes shaping the mesoscale self-organization of trade-cumulus fields. The right plot shows how the domain-mean size of cloud objects within the simulation domain L_c and cloud fraction f_c, as proxies for mesoscale self-organization of trade-cumulus fields, evolve temporally. The time series are from the central reference simulation of the *Cloud Botany* ensemble with the cloud-droplet number concentration of 1000 /cm^3. . . . 128

S6.2 **Dependence of the mesoscale moisture aggregation metric on CCFs.** Multivariate regression results of the mesoscale moisture aggregation metric ΔQ with CCFs as regressors. The results are based on the simulations of the *Cloud Botany* Ensemble. 128

S6.3 **Dependence of liquid-water path standard deviation in time $\sigma_{\mathcal{L}}$ on CCFs.** Multivariate regression results of the liquid-water path $\mathcal{L}$ standard deviation in time $\sigma_{\mathcal{L}}$ with CCFs as regressors. The results are based on the simulations of the *Cloud Botany* Ensemble. 129
S6.4 **Dependence of cloud-cover standard deviation in time σ_{f_c} on CCFs.** Multivariate regression results of the cloud-cove standard deviation in time σ_{f_c} with CCFs as regressors. The results are based on the simulations of the *Cloud Botany* Ensemble. 129
S6.5 **Initializing the central reference simulation of the *Cloud Botany* ensemble from a non-homogeneous cloudy state.** The figure presents two experiments designed to investigate how the central reference simulation, without a diurnal cycle (explored in Chapter 2), evolves when initialized from an organized, precipitating cloud state with existing cold pools. White circles represent points from the central reference simulation when started from a homogeneous, non-cloudy state. The left and right plots illustrate the evolution of the simulation when initialized from a point outside the cycle. In both cases, the system tends to return to the cycle, whose center and size appear to be dictated by large-scale factors. The x- and y-axes show the cloud fraction f_c and liquid-water path $\mathcal{L}$. 130
S6.6 **Evolution of cloud-and rain-water path on 300 by 300 km^2 domains.** Domain-size sensitivity of the response of cloud- and rain-water path evolution to cloud-droplet number concentrations $\mathrm{N_c}$ in comparison with results of **Chapter 3**. 130

LIST OF TABLES

2.1 **Parameters of the *Botany* ensemble.** Overall statistics of the ensemble's parameters determining CCFs. 22

5.1 **Parameters of the LES ensemble.** Overall information about the ensemble's parameters determining CCFs. Note that in addition to simulations above, the ensemble has a central reference simulation with the mean of CCFs above. This means our ensemble features 19 simulations in total. . . 95

SUMMARY

Shallow cumulus clouds in the trade-wind regions are the most abundant cloud type on Earth and play a crucial role in regulating the planet's energy balance by reflecting incoming solar radiation back to space. Despite their importance, trade cumuli remain a major source of uncertainty in climate projections. This is largely because climate models struggle to represent the processes shaping these clouds—processes that span a wide range of spatial and temporal scales. One key gap lies in the mesoscale organization of trade cumuli (hundreds of kilometers), where clouds spontaneously form striking, coherent patterns—features that are typically unresolved in climate models. The relevance of this mesoscale structure to low-cloud radiative feedbacks remains essentially unknown. This thesis aims to improve our understanding of the mesoscale organization of trade-wind cumulus cloud fields, with a focus on self-organization—the spontaneous emergence of structures not driven by large-scale or microphysical cloud-controlling factors (CCFs), but by interactions within the system itself (e.g., between clouds).

After introducing trade-wind cumulus clouds and the range of scales contributing to their formation in Chapter 1, Chapter 2 investigates the role of rain-evaporation-driven downdrafts, known as cold pools, in driving the self-organization of trade-cumulus fields. We show that cold pools are intricately coupled and interact with clouds in the form of structures resembling shallow squall lines. Using a 103-member ensemble of large-domain, large-eddy simulations, we provide a comprehensive analysis of how cold-pool spatial properties respond to large-scale CCFs. Among these, horizontal large-scale wind speed, subsidence, and tropospheric stability emerge as the dominant controls. In addition, the diurnal cycle of insolation, as a time-varying CCF, strongly controls the evolution of trade-cumulus cold pools, with cold-pool activity peaking at nighttime due to enhanced net radiative cooling, which destabilizes the atmosphere. Finally, Chapter 2 demonstrates that cold pools modulate cloud-radiative effect through their influence on both the horizontal and vertical cloud extent.

Chapter 3 addresses the influence of microscale variations on the mesoscale self-organization of trade-cumulus fields. Using large-eddy simulations, we vary cloud-droplet number concentrations and find that trade-cumulus self-organization exhibits two distinct behaviors in response to microscale changes. In low droplet concentration cases, rain efficiency is high, resulting in widespread cold pools across the simulation domain. These cold pools evolve from an initial randomly distributed stage within the simulation domain into large, long-lived squall lines that persist due to the collision of cold pools at their fronts. This regime is characterized by stable time series with oscillations around a stable state. In contrast, high droplet concentration cases exhibit strong intermittency: cold pools form, develop, decay, and dissipate. In such cases, cold-pool interactions are rare, and they interact with clouds in the form of small, short-lived, squall-line structures. This chapter also compares the impact of microscale variations to that of large-scale CCFs on trade-cumulus cloud fields. We find that cloud-droplet number concentration is as influential as large-scale horizontal wind and subsidence in shaping the trade-cumulus albedo.

Chapter 4 investigates whether mesoscale organization affects the radiative effects of trade-cumulus fields independently of variations in cloud cover. Using the concept of partial correlation, and combining twenty years of satellite data with a large ensemble of large-eddy simulations, we control for cloud-cover variations and find that, as trade-cumulus fields become more clustered, they also become geometrically thicker, contain more cloud water, and exhibit smaller cloud radii. This implies that shallow cumulus cloud fields are optically thicker when they are more clustered. As a result, more clustered cloud fields reflect up to 20 W/m^2 more instantaneous shortwave radiation to space, even when cloud-cover variations are accounted for. Therefore, mesoscale organization influences the trade-cumulus radiative effects through both horizontal and vertical dimensions.

Chapter 5 addresses whether—and how—trade-cumulus cold pools influence the top-of-the-atmosphere radiative budgets in the trades. To this end, we use two 19-member ensembles of large-domain, large-eddy simulations with boundary conditions characteristic of the trades: one allowing cold pools to form (CP), and one in which cold-pool formation is inhibited by homogenizing local rain-evaporation tendencies (NoCP). We find that cold pools have a weak impact on the cloud-radiative effect due to offsetting effects: on average, the CP ensemble features slightly deeper clouds with higher reflectivities but with smaller cloud cover. More importantly, in the NoCP ensemble, convection freely self-aggregates, whereas in the CP ensemble, it is arrested where cold pools suppress the mesoscale vertical ascents. This leads to the formation of strongly precipitating convective systems in the NoCP ensemble, which drive a mean drying of the trade-cumulus fields compared to the CP ensemble. As a result of this drying, the NoCP ensemble exhibits a more efficient escape of clear-sky longwave radiation to space, amounting to up to 1.88 W/m^2 when averaged over a day and the full ensemble. This indicates that cold pools influence the radiative budget of trade cumuli primarily through their impact on moisture fields, rather than through clouds.

The final chapter (Chapter 6) summarizes the main findings of the thesis and proposes a conceptual framework for the trade-cumulus system. This framework suggests that trade-cumulus self-organization is governed by two key processes: (i) mesoscale self-aggregation, a self-reinforcing mechanism driven by condensational heating anomalies at the cloud layer, which ultimately generates shallow circulations; and (ii) cold-pool dynamics, which suppress the continued growth of self-aggregation by interacting with clouds in the form of shallow squall lines. The interplay between these two mechanisms gives rise to a cyclic behavior in the mesoscale self-organization of trade cumuli. Building on insights developed throughout the thesis, this chapter further explains how large-scale and micro-scale CCFs influence characteristics of this cycle, such as its center, amplitude, and frequency. Guided by this conceptual framework, the chapter concludes by highlighting open questions for future research.

SAMENVATTING

Stapelwolken in passaatwindregio's zijn het meest voorkomende wolkentype op aarde en spelen een cruciale rol in het reguleren van de energiebalans van de planeet door zonnestraling terug de ruimte in te weerkaatsen. Ondanks hun belang blijven stapelwolken in passaatwindregio's een belangrijke bron van onzekerheid in klimaatprojecties. Dit komt grotendeels doordat klimaatmodellen moeite hebben om adequaat de processen weer te geven die deze wolken vormen, omdat die zich afspelen over een breed scala aan ruimtelijke en temporele schalen. Een belangrijk kennishiaat betreft de mesoschaalorganisatie van stapelwolken (vaak honderden kilometers groot) in passaatwindregio's, waarbij wolken spontaan opvallende, samenhangende patronen vormen. Deze structuren worden doorgaans niet door klimaatmodellen gezien. Er is nog veel onbekend over de relevantie van deze mesoschaalstructuren voor de terugkoppeling van veranderingen in lage bewolking op veranderingen in het globaal klimaat. Dit proefschrift heeft daarom als doel het begrip van de mesoschaalorganisatie van stapelwolken in passaatwindregio's te verbeteren, met bijzondere aandacht voor zelforganisatie — het spontane ontstaan van structuren die niet worden aangedreven door grootschalige of microfysische *cloud-controlling factors* (CCFs), maar door interacties binnen het systeem zelf (bijvoorbeeld tussen de wolken).

Na een introductie van stapelwolken in passaatwindregio's en de verschillende schalen die bijdragen aan hun ontwikkeling in hoofdstuk 1, onderzoekt hoofdstuk 2 de rol van neerwaartse luchtstromen gedreven door de verdamping van regen, zogenaamde koude poelen (ook wel cold pools genoemd), in het stimuleren van de zelforganisatie van stapelwolken in passaatwindregio's. De resultaten wijzen erop dat koude poelen sterk interageren met wolken in de vorm van structuren die lijken op ondiepe buienlijnen (lijnen van onweersbuien). Met behulp van een ensemble van 103 grootschalige large-eddy simulations (LES) analyseren we hoe de ruimtelijke eigenschappen van koude poelen reageren op grootschalige CCFs. Van deze factoren blijken de horizontale grootschalige windsnelheid, subsidentie en troposferische stabiliteit de belangrijkste invloeden te zijn. Daarnaast blijkt de dagelijkse cyclus van instraling — als een tijdsafhankelijke CCF — een sterke invloed te hebben op de evolutie van koude poelen, waarbij hun activiteit piekt tijdens de nacht door versterkte netto stralingsafkoeling, die de atmosfeer destabiliseert. Hoofdstuk 2 toont verder aan dat koude poelen het effect van wolken op de stralingsbalans aan de top van de atmosfeer moduleren via hun invloed op zowel de horizontale als verticale omvang van de wolken.

Hoofdstuk 3 behandelt de invloed van microschaalvariaties op de mesoschaal zelforganisatie van stapelwolken in passaatwindregio's. Door middel van LES variëren we de concentratie van wolkendruppeltjes en constateren we dat de zelforganisatie van stapelwolken in passaatwindregio's twee verschillende gedragspatronen vertoont als reactie op veranderingen op microschaal. In gevallen met lage druppelconcentraties is de regenefficiëntie hoog, wat leidt tot de snelle, verspreide vorming van koude poelen. Deze

koude poelen evolueren van een aanvankelijk willekeurig verspreide toestand naar grote, langlevende buienlijnen, die ontstaan door de botsing van koude poelen aan hun fronten. Dit regime wordt gekenmerkt door stabiele tijdreeksen met fluctuaties rond een stabiele toestand. Daarentegen vertonen gevallen met hoge druppelconcentraties sterke intermitterende dynamiek: koude poelen ontstaan, ontwikkelen zich, verzwakken en verdwijnen weer. In deze gevallen zijn interacties tussen koude poelen zeldzaam en ontwikkelen zich kleinere, kortlevende buienlijnen structuren. Dit hoofdstuk vergelijkt ook de impact van microschaalvariaties met de impact van grootschalige CCFs op stapelwolken in passaatwindregio's. De resultaten wijzen erop dat de concentratie van wolkendruppeltjes een even grote invloed heeft als de grootschalige horizontale wind en subsidentie op de albedo van velden van zelf-georganiseerde stapelwolken.

Hoofdstuk 4 onderzoekt of mesoschaalorganisatie de stralingseffecten van stapelwolken in passaatwindregio's beïnvloedt, onafhankelijk van variaties in wolkenfractie. Door gebruik te maken van het concept van partiële correlatie, en twintig jaar aan satellietwaarnemingen te combineren met een groot ensemble van LES, kwantificeren we het effect van variatie in stralingseffecten die niet komen door variaties in de wolkenfractie. De resultaten wijzen erop dat naarmate stapelwolken in passaatwindregio's meer clusteren, ze geometrisch dikker worden, meer wolkenwater bevatten en kleinere wolkendruppels bevatten. Dit betekent dat deze wolkenvelden optisch dikker zijn wanneer ze sterker geclusterd zijn. Gevolg hiervan is dat meer geclusterde wolkenvelden tot 20 W/m^2 meer kortgolvige straling weerkaatsen naar de ruimte, zelfs wanneer variaties in wolkenfractie in acht worden genomen. Mesoschaalorganisatie beïnvloedt daarmee de stralingseffecten van stapelwolken in passaatwindregio's via zowel de horizontale als verticale structuur van de wolken.

Hoofdstuk 5 richt zich op de vraag of, en op welke wijze, koude poelen het stralingsbudget aan de top van de atmosfeer in de passaatgebieden beïnvloeden. Hiervoor gebruiken we twee ensembles van respectievelijk 19 grootschalige LES met randvoorwaarden kenmerkend voor de passaatgebieden: één waarbij koude poelen vrij kunnen ontstaan (CP) en één waarbij de vorming van koude poelen wordt onderdrukt door lokale regenverdamping horizontaal te homogeniseren (NoCP). De resultaten wijzen erop dat koude poelen een beperkt effect hebben op het effect van wolken op de stralingsbalans aan de top van de atmosfeer vanwege compenserende mechanismen: gemiddeld toont het CP-ensemble iets diepere wolken met hogere reflectiviteit, maar met een kleinere wolkenfractie. Belangrijker is dat in het NoCP-ensemble stapelwolken vrij kunnen zelf-aggregeren, terwijl in het CP-ensemble mesoschalige circulaties worden onderdrukt door koude poelen. Dit leidt tot de vorming van sterk neerslagproducerende stapelwolksystemen in het NoCP-ensemble, die een gemiddelde uitdroging van de stapelwolksystemen in passaatwindregio's veroorzaken. Door deze uitdroging ontsnapt er meer langgolvige straling naar de ruimte, met een gemiddelde toename van maximaal 1,88 W/m^2 over een dag en het volledige ensemble. Dit geeft aan dat koude poelen het stralingsbudget van stapelwolken in passaatwindregio's primair beïnvloeden via hun impact op het vochtveld, en niet via veranderingen in de bewolking zelf.

Het afsluitende hoofdstuk (hoofdstuk 6) vat de belangrijkste bevindingen van dit proefschrift samen en stelt een conceptueel kader voor voor het systeem van stapelwolken in passaatwindregio's. Dit kader stelt dat de zelforganisatie van stapelwolken wordt gestuurd door twee kernprocessen: (i) mesoschaal zelf-aggregatie, een zelfversterkend mechanisme aangedreven door anomalieën in condensatieverwarming binnen de wolkenlaag, wat uiteindelijk leidt tot de vorming van ondiepe circulaties; en (ii) koude poelen dynamiek, die de verdere ontwikkeling van zelf-aggregatie onderdrukt door interactie met wolken in de vorm van ondiepe buienlijnen. De wisselwerking tussen deze twee mechanismen leidt tot een cyclusgedrag in de mesoschaalorganisatie van stapelwolken. Op basis van de in dit proefschrift ontwikkelde inzichten wordt verder toegelicht hoe grootschalige en microschaal CCFs kenmerken van deze cyclus beïnvloeden, zoals het centrum, de amplitude en de frequentie ervan. Afsluitend worden openstaande onderzoeksvragen voor toekomstig onderzoek besproken.

PERSIAN SUMMARY

چکیده به زبان پارسی

ابرهای کومولوس کم‌عمق شکل گیرنده بر روی اقیانوس ها در مناطق بادهای تجارتی (شرق وزان یا بسامان)، فراوان‌ترین نوع ابر روی زمین هستند و با بازتاب تابش خورشیدی به فضا، نقش مهمی در تنظیم تعادل انرژی سیاره ایفا می‌کنند. با وجود اهمیت بالای آن‌ها، کومولوس های تجارتی یکی از منابع اصلی عدم قطعیت در پیش‌بینی‌های اقلیمی به شمار می‌روند. دلیل اصلی این مسئله آن است که مدل‌های آب‌وهوایی و اقلیمی در شبیه‌سازی فرایندهایی که این ابرها را شکل می‌دهند – فرایندهایی که دامنه وسیعی از مقیاس‌های مکانی و زمانی را دربرمی‌گیرند – با چالش مواجه هستند. یکی از شکاف‌های کلیدی، به سازمان‌دهی هندسی میان‌مقیاس کومولوس‌های تجارتی (در ابعاد صدها کیلومتر) مربوط می‌شود، جایی که ابرها به‌طور خودبه‌خودی الگوهایی منسجم و قابل‌توجه تشکیل می‌دهند – ویژگی‌هایی که به طور کلی در مدل‌های اقلیمی نادیده گرفته می‌شوند. تاثیر این ساختارهای میان‌مقیاس در نقش کومولوس های تجارتی در سرعت بخشیدن یا کند کردن گرمایش جهانی حاصل از تغییر اقلیم، عمدتاً ناشناخته باقی مانده است. به همین دلیل، هدف این پایان‌نامه، بهبود درک ما از سازمان‌دهی هندسی میان‌مقیاس میدان‌های ابری کومولوس تجارتی، با تمرکز بر «خودسازمان‌دهی» است – یعنی پدیدار شدن ساختارهایی خودبه‌خودی که نه به‌واسطه عوامل کنترلی ابرها در مقیاس بزرگ یا میکروفیزیکی، بلکه بر اثر تعاملات درون‌سیستمی (مثلاً میان ابرها) ایجاد می‌شوند.

پس از معرفی ابرهای کومولوس تجارتی و مقیاس‌های مختلف مؤثر در شکل‌گیری آن‌ها در فصل مقدمه، فصل دوم به بررسی نقش جریان‌های نزولی ناشی از تبخیر باران، موسوم به «استخرهای سرد یا استخر هوای سرد»، در شکل گیری خودسازمان‌دهی هندسی میدان‌های کومولوس تجارتی می‌پردازد. نشان می‌دهیم که استخرهای سرد به شکلی پیچیده با ابرها درهم‌تنیده‌اند و به‌صورت ساختارهایی شبیه به خطوط کم‌عمق با آن‌ها تعامل می‌کنند. با استفاده از مجموعه‌ای شامل ۱۰۳ شبیه‌سازی جوی با دقت وضوح بسیار بالا (۱۰۰ متر) و با دامنه بزرگ (۱۵۰ کیلومتر) ، تحلیلی جامع از چگونگی واکنش ویژگی‌های فضایی استخرهای سرد به تغییرات درعوامل کنترلی مقیاس بزرگ ارائه می‌دهیم. در این میان، سرعت باد افقی در مقیاس بزرگ، سرعت جریان‌های بادی عمودی در مقیاس بزرگ و پایداری جو به‌عنوان کنترل‌کننده‌های اصلی ظاهر می‌شوند. افزون بر این، چرخه روزانه انرژی تابشی به‌عنوان یک کنترل‌کننده زمان‌متغیر، به طرز قابل توجهی بر تکامل استخرهای سرد کومولوس تجارتی اثر می‌گذارد، به‌طوری‌که فعالیت این استخرها در شب و در نتیجه افزایش سرمایش تابشی خالص – که موجب ناپایداری جو می‌شود – به اوج می‌رسد. در نهایت، فصل دوم نشان می‌دهد که استخرهای سرد، اثرات تابشی ابرها را از طریق تأثیرگذاری بر خواص هندسی آن‌ها در هر دو راستای افقی و عمودی تعدیل می‌کنند.

فصل سوم به بررسی تأثیر تغییرات ریزمقیاس (میکروفیزیکی) بر خودسازمان‌دهی هندسی میان‌مقیاس میدان‌های کومولوس تجارتی اختصاص دارد. با بهره‌گیری از شبیه‌سازی‌های بسیار دقیق جوی ، غلظت قطرات ابر را تغییر داده و مشاهده می‌کنیم که خودسازمان‌دهی هندسی کومولوس‌های تجارتی در برابر این تغییرات، دو رفتار متمایز از خود نشان می‌دهد. در مواردی که غلظت قطرات پایین است، راندمان بارش بالا بوده و استخرهای سرد وسیعی در سراسر دامنه شبیه‌سازی شکل می‌گیرند. این استخرها از یک توزیع اولیه تصادفی، به خطوط هوایی بزرگ، منظم و پایدار تبدیل می‌شوند که با برخورد متقابل استخرهای سرد در جبهه‌های پیشروی خود تداوم می‌یابند. این رژیم با سری‌های زمانی پایدار و نوساناتی تصادفی پیرامون یک وضعیت متعادل مشخص همراه است. در مقابل، در موارد غلظت بالای قطرات، چرخه‌ای متناوب مشاهده می‌شود: استخرهای سرد شکل می‌گیرند، گسترش می‌یابند، تحلیل می‌روند و ناپدید می‌شوند. در این حالت، تعاملات میان استخرهای سرد نادر است و ابرها در قالب ساختارهای خطی کوچک و گذرا با آن‌ها در تماس‌اند. این فصل همچنین تأثیر متقابل تغییرات عوامل کنترلی ریزمقیاس و بزرگ‌مقیاس را در میدان‌های ابری کومولوس تجارتی بررسی می‌کند.

نتیجه‌گیری ما این است که غلظت عددی قطرات ابر، تأثیری هم‌تراز با باد افقی و جریان‌های هوایی عمودی بزرگ‌مقیاس در میزانی که میدان های کومولوس تابش موج کوتاه خورشید را بازتاب می‌کنند دارد.

فصل چهار به بررسی این پرسش می‌پردازد که آیا سازمان‌دهی هندسی میان‌مقیاس، اثرات تابشی میدان‌های کومولوس تجارتی را مستقل از تغییرات پوشش ابری تحت تأثیر قرار می‌دهد یا خیر. با استفاده از مفهوم «همبستگی جزئی» و ترکیب داده‌های ماهواره‌ای بیست‌ساله با مجموعه‌ای گسترده از شبیه‌سازی‌های جوی دقیق با دامنه بزرگ، تغییرات پوشش ابری را کنترل کرده و دریافته‌ایم که با افزایش میزان خوشه‌بندی میدان‌های کومولوس تجارتی، ضخامت هندسی آن‌ها نیز افزایش می‌یابد، مقدار آب موجود در ابر در راستای عمودی بیشتر شده و شعاع قطرات ابر کوچک‌تر می‌شود. این امر نشان می‌دهد که میدان‌های ابری کومولوس کم‌عمق، در صورت خوشه‌بندی، از نظر نوری ضخیم‌تر هستند. در نتیجه، چنین میدان‌هایی می‌توانند تا حدود ۲۰ وات بر متر مربع تابش موج کوتاه آنی بیشتری را به فضا بازتاب دهند، حتی در صورت ثبات پوشش ابری. بنابراین، سازمان‌دهی هندسی میان‌مقیاس، از هر دو بُعد افقی و عمودی، بر اثرات تابشی ابرهای تجارتی تأثیرگذار است.

فصل پنجم به این پرسش می‌پردازد که آیا و چگونه استخرهای سردی که در رژیم بادهای تجارتی تشکیل می‌شوند بر بودجه‌های تابشی در بالای جو تأثیر می‌گذارند. برای بررسی این موضوع، از دو مجموعه‌ی ۱۹ عضوی شبیه‌سازی‌های دقیق جوی با دامنه‌های وسیع و با شرایط مرزی نمایانگر موقعیت جوی و هوایی رژیم بادهای تجارتی استفاده می‌کنیم: یک مجموعه با امکان شکل‌گیری استخرهای سرد (CP) و دیگری که در آن با همگن‌سازی تمایلات تبخیر باران محلی، شکل‌گیری استخرهای سرد متوقف می‌شود (NoCP) . نتایج نشان می‌دهد که استخرهای سرد به دلیل اثراتی که هم‌دیگر را خنثی می کنند، تأثیر محدودی بر اثرات تابشی ابر دارند: به‌طور میانگین، مجموعه‌ی CP شامل ابرهایی کمی عمیق‌تر با بازتاب‌پذیری بیشتر اما با پوشش ابری کمتر است. نکته مهم‌تر این‌که در مجموعه‌ی NoCP ، همرفت به‌صورت آزادانه پیش‌روی می‌کند، در حالی‌که در مجموعه‌ی CP ، استخرهای سرد از طریق سرکوب جریان های جوی میان‌مقیاس به سمت بالا در ابرها ، مانع ادامه‌ی همرفت می‌شوند. این امر در مجموعه‌ی NoCP منجر به شکل‌گیری سیستم‌های همرفتی با بارش شدید می‌شود که در مقایسه با مجموعه‌ی CP ، موجب خشکی بیشتر محیط کومولوس‌های تجارتی می‌گردد. در نتیجه‌ی این خشکی، مجموعه‌ی NoCP فراری مؤثرتر از تابش موج بلند در آسمان صاف به فضا نشان می‌دهد که در طول یک روز و به‌طور میانگین در کل مجموعه، به ۱٫۸۸ وات بر متر مربع می‌رسد. این یافته نشان می‌دهد که استخرهای سرد بیشتر از طریق تأثیر بر میدان‌های رطوبتی و نه از طریق ابرها، بودجه تابشی کومولوس‌های تجارتی را تحت تأثیر قرار می‌دهند.

فصل پایانی، یافته‌های کلیدی این پایان‌نامه را خلاصه کرده و چارچوبی مفهومی برای سیستم ابرهای کومولوس در میان مقیاس ارائه می‌دهد. این چارچوب نشان می‌دهد که خودسازمان‌دهی هندسی توده‌های تجارتی از طریق دو فرایند اصلی هدایت می‌شود: (۱) خودتجمعی میان‌مقیاس، که مکانیسمی خودتقویت‌شونده است و توسط ناهنجاری‌های گرمایش ناشی از میعان قطرات ابر در لایه‌ی ابری هدایت شده و در نهایت منجر به شکل‌گیری جریان‌های هوایی دوار کم‌عمق می‌شود؛ و (۲) دینامیک استخرهای سرد، که با تعامل با ابرها به‌صورت خطوط کم‌عمق، از رشد مداوم تجمعی میان‌مقیاس رطوبت و ابرها جلوگیری می‌کند. کنش متقابل میان این دو مکانیسم، منجر به بروز رفتاری چرخه‌ای در فرایند خودسازمان‌دهی هندسی میان‌مقیاس کومولوس‌های تجارتی می‌شود. با تکیه بر بینش‌های به‌دست‌آمده در طول این پایان‌نامه، این فصل همچنین تشریح می‌کند که چگونه عوامل کنترلی بزرگ‌مقیاس و ریزمقیاس، ویژگی‌های این چرخه نظیر مرکز، دامنه و فرکانس آن را تحت تأثیر قرار می‌دهند. در پایان، این چارچوب مفهومی کمک می کند که پرسش‌های بازمانده برای تحقیقات آینده، به عنوان افقی برای ادامه راه در این پژوهش‌ها، مطرح شوند.

PREFACE

My goal is to learn something new and I want to have fun doing it.
— William Phillips, Nobel Prize in Physics, 1997

One day during high school, my mathematics teacher showed us a short movie about Fibonacci numbers while teaching sequences and how to describe them. In the video, I was fascinated by the Golden Ratio and the fact that such *order* and *patterns* can be observed in nature, for example, in cyclones.

Ten years later, I feel incredibly fortunate to have had the opportunity to start my PhD journey on understanding the patterns of clouds and their relevance to the climate system.

Join me here as we travel into the world of clouds, their beautiful patterns, and the role these patterns play in the climate system. I hope that, like me, while reading parts of this thesis, you will not only appreciate the beauty of clouds but also learn new things and, above all, have fun — just as I did during my PhD!

Pouriya Alinaghi
Delft, May 2025

1

INTRODUCTION

1.1 Clouds: A beautiful source of inspiration that matters for climate

Clouds are both beautiful and striking. Not surprisingly, they have been a source of inspiration not only for climate scientists but also for artists (Fig. 1.1a). Painters are not the only artists captivated by clouds; Persian poets, for over a thousand years, have frequently used clouds as metaphors and symbols in their poems. This part of the introduction highlights two examples where clouds are featured in Persian poetry. Firstly, many Persian poets have associated clouds with rain (e.g., Fig. 1.1b). In the following lines, Hafez, a Persian poet who lived 800 years ago, offers a poetic explanation for why clouds produce rain:

“*When the spring cloud saw how time betrays its promises,*
It wept upon the jasmine, the hyacinth, and the wild rose.”

Secondly, Persian poets often noted that clouds influence sunlight. Consider the example below:

“*Do not keep company with the wicked,*
For their presence, though you're pure, will stain you.
Even the radiant sun, despite its brilliance,
Can be concealed by a small patch of cloud.”

This poem by Sanaei, who lived 900 years ago, clearly illustrates the interaction between clouds and solar radiation and that clouds “block” sunlight. Remarkably, these poetic insights by Hafez and Sanaei reflect what is now understood as two of the most crucial roles clouds play in the climate system: their influence on the Earth's water cycle and their modulation of incoming solar radiation, thereby influencing the Earth's energy budget.

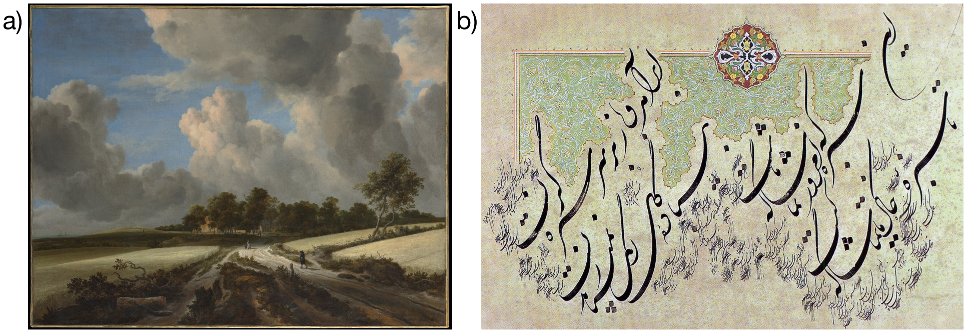

Figure 1.1: **Clouds in art and poems.** a) *Wheat Fields* by Jacob van Ruisdael, a renowned Dutch painter whose works are notably inspired by clouds. Clouds he painted appear especially realistic compared with many other artists. b) A typical example of Persian calligraphy in the Shekasteh Nastaligh style by Shahram Roohi, illustrating a poem consisting of clouds by Khayyam, a celebrated Persian poet who lived approximately 900 years ago. The poem starts with: “*The cloud arrived and wept anew upon the grass, Without rose-hued wine, life one must not pass.*”

Clouds cover 67–68% of the Earth—our home planet is not a blue planet, but a white one (Fig. 1.2). Despite this vast coverage, clouds contain only a significantly small amount of water. If we were to redistribute all the water in the clouds over the entire globe, it would form a puddle with a depth of only 0.1 mm, roughly the thickness of a human hair.

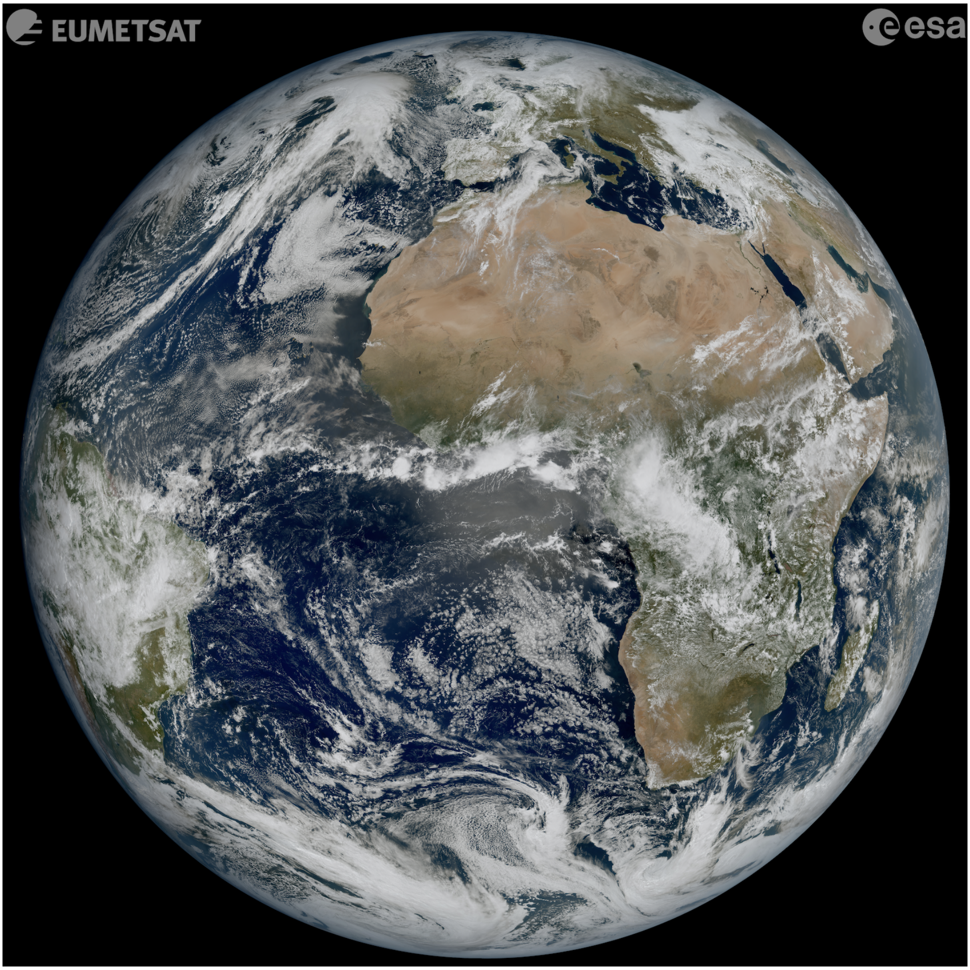

Figure 1.2: **Cloudy Earth.** This image is from Meteosat Third Generation – Imager 1 (MTG-I1) taken at 11:50 UTC on 18 March 2023 by the Flexible Combined Imager on MTG-I1. The figure emphasizes that Earth appears predominantly white rather than blue, primarily due to clouds, which cover 67-68% of our planet.

This amounts to 0.4% of total-water vapor, implying that clouds are really at the tail of the relative humidity distribution (Schneider et al., 2017).

As suggested by the poems, clouds are not merely tracers of atmospheric motions; rather, they are active components of the climate system. Clouds affect the climate system through their interaction with radiation in two ways. First, clouds reflect incoming solar, shortwave radiation back to space, cooling the Earth system, with a globally averaged value of -47.3 W/m^2 (IPCC AR6, 2023). Second, they act as a greenhouse gas, trapping heat by absorbing outgoing longwave radiation and re-emitting it towards the Earth's surface, warming the Earth system, with a globally averaged value of 26.2 W/m^2 (IPCC AR6, 2023). Thus, the net effect of clouds on Earth's radiation budget is to cool the planet, with a globally averaged value of −21.1 W/m^2 (IPCC AR6, 2023). Consequently, clouds influence the energy budget of the Earth system and, in turn, the global mean temperature. Of course, the magnitude of cooling and warming effects depends on the cloud regime, where cloud cover, cloud depth, cloud-top height and reflectivity can vary. For instance, shallow clouds have temperatures similar to the surface, resulting in a minimal longwave warming effect compared to their shortwave cooling effect. In contrast, deep clouds in the tropics, where cloud-top temperatures can become colder compared with shallow clouds, exhibit a longwave warming effect which is comparable to their shortwave cooling effect.

Shallow tropical clouds are at the heart of uncertainty in climate projections
The fact that clouds are an important component of the climate system does not immediately imply that they might respond to climate change and global warming[1]. If relative humidity remained fixed, and knowing that clouds form at the tail of the relative humidity distribution, why would clouds change in a warmer climate? Clouds often appear scattered, diffuse, and sometimes even random, changing so quickly—again, why would their climatology change? In fact, since Foote (1856) first noted the heat-trapping properties of CO_2, and later Arrhenius (1896) demonstrated that increases in CO_2 concentrations lead to higher surface temperatures, it took nearly a century for climate scientists to realize that clouds indeed could respond to global warming. Many years after Arrhenius's paper, Möller (1963) discovered that his analysis of the effect of increased CO_2 concentrations on surface temperature was highly sensitive to even small variations in cloudiness. Around two decades later, Paltridge (1980)'s analysis was the first to suggest that clouds would contain more liquid water in a warmer climate, implying that clouds counteract warming and slow it down.

A decade later, with the production of the first generation of global climate model intercomparisons, Cess et al. (1989) demonstrated for the first time that the inter-model spread in the climate sensitivity parameter—the response of global mean surface temperature to CO_2 doubling—among 14 global climate models was caused by the cloud feedback to climate change (Fig. 1.3a). Fifteen years later, Bony and Dufresne (2005) analyzed 15 existing climate models, splitting them into a low- and a high-sensitivity group. They showed that the spread in the estimated climate sensitivity originated in regions of strong large-scale subsidence. This stems from that fact that climate models strongly disagree about the response of shortwave and longwave cloud-radiative effects to warming in these regions in the tropics; i.e., where shallow tropical clouds form (Fig. 1.3b). These shallow tropical clouds include two regimes: (i) trade-wind cumulus and (ii) stratocumulus regimes. Despite significant improvements in observations, models, and our understanding of clouds within the decade following Bony and Dufresne (2005)'s work, Schneider et al. (2017) showed that the uncertainty in climate sensitivity among 30 climate models can be attributed to low-cloud feedback (Fig. 1.3c). Three years later, Sherwood et al. (2020) showed that among all cloud regimes, low marine clouds in the tropics, in addition to tropical anvils, are still the largest source of uncertainty in the total cloud feedback (Fig. 1.3d). In the latest IPCC report (IPCC AR6, 2023), the margins of uncertainty in climate feedback estimates remain determined by cloud feedbacks (Fig. 1.3e). Thus, to constrain the feedback of the climate system to anthropogenic climate change, we need to constrain cloud feedbacks, especially low-cloud climate feedbacks.

---

[1] This paragraph is inspired by Bjorn Stevens' presentation, Dispersing the Clouds Around Climate Change, delivered during the ceremony awarding the Buys Ballot Medal to Sandrine Bony.

All the reviews provided above suggest that we need to improve our understanding of clouds and their role in the climate system. This can help us identify exactly what climate models miss and fail to represent about clouds. An obvious explanation is that clouds are extremely challenging to model. The grid spacing of climate models is on the order of tens of kilometers, which is far coarser than the resolution needed to model clouds accurately. For simulating an individual trade-cumulus cloud, the required resolution is at least 100 m in the horizontal and 20 m in the vertical (Schneider et al., 2017). The immense computational time and costs have prevented climate scientists from performing climate-model simulations at such fine resolutions. So, clouds are not explicitly resolved in climate models with coarse resolutions. This limitation led to the development of physically motivated but statistical descriptions of clouds, referred to as “parameterization.” The spread in climate projections clearly indicates that clouds are far too complex to be accurately represented by these parameterizations, making clouds, specifically low clouds, a major source of uncertainty in climate projections (Nuijens and Siebesma, 2019; Schneider et al., 2017; Sherwood et al., 2020; Siebesma et al., 2020). Given the same computational power, a natural next step is to model clouds at high resolutions but over smaller domains. This is precisely what the modeling community pursued (Blossey et al., 2013; Zhang et al., 2013). They used detailed atmospheric models, such as large-eddy simulations (LES), which can directly resolve turbulent processes related to cloud formation (e.g., Heus et al., 2010). However, the challenge with LES studies lies in their relatively smaller domains, which require parameterizing the large-scale dynamics at the boundaries of the LES domain. This leads to a lack of proper and representative interactions between clouds and the large-scale environment. Recently, with increased computational power, LESs have become increasingly feasible on larger domains, allowing for improved representation of interactions between larger and smaller scales (e.g., Schulz and Stevens, 2023).

Combined observation–model studies constrained low-cloud climate feedbacks

Recently, observational studies have played an important role in constraining low-cloud climate feedback (Cesana and Del Genio, 2021; Myers et al., 2021; Scott et al., 2020). These studies assume that clouds are controlled by large-scale meteorological conditions, commonly referred to as “cloud-controlling factors” (CCFs) (Klein et al., 2018; Stevens and Brenguier, 2009). They further assume that the response of clouds to CCFs remains unchanged in a warmer climate. Using these two assumptions, cloud feedback, $\frac{\mathrm{d}C}{\mathrm{d}T_s}$, is estimated, where C represents shortwave cloud-radiative effect and T_s denotes global mean surface temperature. This estimation is carried out using the chain rule:

$$\frac{\mathrm{d}C}{\mathrm{d}T_s} = \frac{\mathrm{dCCFs}}{\mathrm{d}T_s} \times \frac{\partial C}{\partial \mathrm{CCFs}},$$

where the change in CCFs due to global warming, $\frac{\mathrm{d\,CCFs}}{\mathrm{d}T_s}$, is derived from climate models. Note that one cannot fully trust climate models for the term $\frac{\mathrm{d\,CCFs}}{\mathrm{d}T_s}$ because they do not accurately represent clouds. However, climate models remain our only source for this term, as it cannot be directly modeled or observed. The sensitivity of the cloud-radiative effect C to CCFs, $\frac{\partial C}{\partial \mathrm{CCFs}}$, is obtained from satellite and ERA5 reanalysis data (Hersbach et al., 2020).

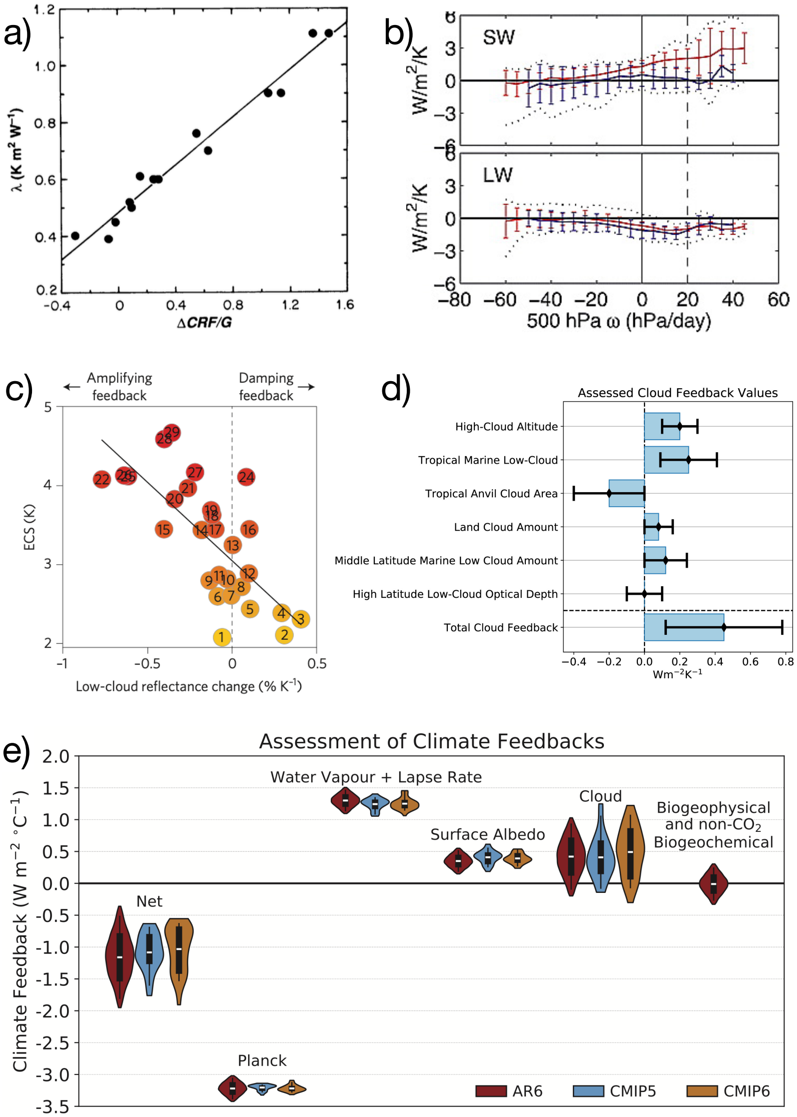

Figure 1.3: **Cloud-climate feedback throughout years 1989 to 2021.** a) The sensitivity of climate sensitivity parameter λ to cloud-radiative forcing (CRF) (Cess et al., 1989, their Fig. 1). b) The sensitivity of shortwave (SW) and longwave (LW) cloud feedback to different cloud regimes quantified by large-scale subsidence ω in low-sensitivity (blue) and high-sensitivity models (Bony and Dufresne, 2005, their Fig. 2), where the dotted lines show the minimum and maximum of these sensitivities among models. c) The scatter in the projected climate sensitivity among climate models and its dependence on low-cloud climate feedback (Schneider et al., 2017, their Fig. 1). d) The assessed values of cloud feedbacks for each individual component, adapted from Sherwood et al. (2020). e) The last climate feedback estimate from the sixth assessment report (AR6) of the IPCC report (IPCC AR6, 2023, their Chapter 7).

The cloud-radiative effect C can be written as $C = C_s + C_l$, where C_s and C_l are shortwave and longwave cloud-radiative effects, respectively. The shortwave cloud-radiative effect C_s is a function of the cloud cover f_c and cloud albedo α_c and can be written as $C_s \approx f_c \alpha_c S_\circ$, where $S_\circ$ represents the incoming shortwave radiation. With this, we can decompose the shortwave cloud feedback to contributions from cloud fraction f_c and cloud albedo α_c as:

$$\frac{\mathrm{d}C_s}{\mathrm{d}T_s} = \frac{\mathrm{dCCFs}}{\mathrm{d}T_s} \times \left(\frac{\partial f_c}{\partial \mathrm{CCFs}} \alpha_c + f_c \frac{\partial \alpha_c}{\partial \mathrm{CCFs}} \right) S_\circ.$$

The longwave cloud-radiative effect C_l is a function of the cloud cover f_c and cloud-top temperature T_c, and can be written as $C_l = f_c \epsilon_e \sigma T_c^4$, where ϵ_e is the effective emissivity, which measures the extent to which a partly cloudy pixel emits longwave radiation compared to a blackbody with emissivity of 1 and can be computed as $\epsilon_e = f_c \epsilon_c + (1 - f_c) \epsilon_{clrsky}$, where ϵ_c and ϵ_{clrsky} stand for the emissivity of clouds and the clear sky. The term σ is the Stefan-Boltzmann constant, with a value of $5.67 \times 10^{-8}\,\mathrm{W\,m^{-2}\,K^{-4}}$. With this, the longwave cloud feedback can be decomposed into contributions from cloud cover f_c and cloud-top temperature T_c:

$$\frac{\mathrm{d}C_l}{\mathrm{d}T_s} = \frac{\mathrm{dCCFs}}{\mathrm{d}T_s} \times \left(\frac{\partial f_c}{\partial \mathrm{CCFs}} (\epsilon_e \sigma T_c^4) + f_c \frac{\partial (\epsilon_e \sigma T_c^4)}{\partial \mathrm{CCFs}} \right).$$

Both cloud albedo α_c and cloud-top temperature T_c are functions of cloud-top height; the deeper the cloud, the larger the cloud albedo and the lower the cloud-top temperature. Conceptually, this means that both shortwave C_s and longwave C_l cloud radiative effects are functions of how wide clouds are in the horizontal and how deep they are in the vertical.

Specifically, the studies by Cesana and Del Genio (2021) and Myers et al. (2021) split the observation-based low-cloud climate feedback estimates into different cloud regimes, including stratocumulus, trade cumulus, tropical ascent, and midlatitudes. Their results show that the trade-cumulus feedback in global climate models is especially relevant, as this cloud regime covers approximately 18.2% of Earth system–second largest after the midlatitudes regime with the fraction of 19.7%–significantly affecting the total low-cloud feedback estimates (Myers et al., 2021). Thus, even a small fluctuation in this regime could significantly affect the global mean top-of-the-atmosphere radiation budget and in turn low-cloud climate feedback. A key finding from these studies is the considerable discrepancy between modelled and observed trade-cumulus feedback: global climate models tend to produce a large positive feedback, whereas observational data suggest a much weaker response. Motivated by this inconsistency, the present thesis focuses entirely on the trade-cumulus regime, with the primary aim of reducing cloud–climate uncertainty associated with this cloud type.

1.2 Trade-cumulus clouds over four spatiotemporal scales

One of the most significant challenges preventing the climate science community from accurately modeling clouds is their dependence on multiple spatial and temporal scales. From the microscale processes governing tiny cloud droplets, to the turbulent scales influencing individual clouds, to mesoscale dynamics, and further to synoptic-scale processes, all play a crucial role in determining the type of clouds that form and the spatial and temporal scales at which they evolve. This PhD thesis aims to advance our understanding of the interactions across these scales in the trade-wind regime. To this end, this section provides a brief overview of the various scales over which trade-cumulus clouds form and evolve. Understanding these scales and their interactions is crucial for constraining low-cloud climate feedback.

1.2.1 Synoptic scales: Tropical large-scale circulations determine where trade cumulus can form

Trade-cumulus clouds form in the trade-wind region of the tropics. Due to the Earth's curvature, more solar energy is received near the equator than at higher latitudes, which results in warm ascending air near the equator and a deeper column of air over the tropics. This creates a pressure gradient between the equator and higher latitudes, causing air to move from the equator towards higher latitudes at higher levels of the atmosphere. As this air reaches higher latitudes, it cools and sinks, increasing the pressure gradient between the equator and higher latitudes near the surface. The air then flows back towards the equator at lower altitudes. Due to the Coriolis force, caused by the Earth's rotation, the air is deflected to the right in the Northern Hemisphere. As a result, the air is deflected to the right as it approaches the equator. Consequently, the region near the equator experiences strong easterly winds, known as the "trade winds." Centuries ago, sailors observed and leveraged these winds for trade routes between Europe and the Americas across the Atlantic Ocean—hence the name "trade winds."

Due to the rotation of the Earth, the large-scale atmospheric circulation is divided into three cells, each spanning approximately 30° latitude in the meridional direction. The most well-known of these is the Hadley cell, which encompasses the trade-wind region. Its ascending branch is located near the equator, while its descending branch lies around 30° latitude (e.g., Hadley, 1735; Held and Hou, 1980). As illustrated in Fig. 1.4, shallow trade-cumulus clouds form in the subsiding regions of the Hadley cell over the subtropical oceans, while deep clouds, such as cumulonimbus, form near the equator. This conceptual picture also highlights that clouds are coupled to large-scale synoptic circulations. The richness of this coupling is of course more clear in Fig. 1.2, where clouds appear to follow large-scale circulations with intriguing patterns. In essence, this section highlights that synoptic-scale processes ($> 1000\,\mathrm{km}$) determine where trade-wind cumuli form, set the large-scale environment of the trades, and may modulate the characteristics of trade-wind cumuli.

1.2.2 Individual cloud scales: A cumulus cloud results from moist convection

In this section, the formation of a typical individual cumulus cloud in the trades is briefly explained. The following explanation takes us through the journey of an air parcel from the sea surface to the cloud top. Throughout this explanation, we will consider the properties of the parcel and its surrounding environment as the parcel moves upward.

Imagine a parcel of air near the sea surface. If this air parcel becomes warmer than its surrounding environment for any reason, it starts rising due to its positive buoyancy

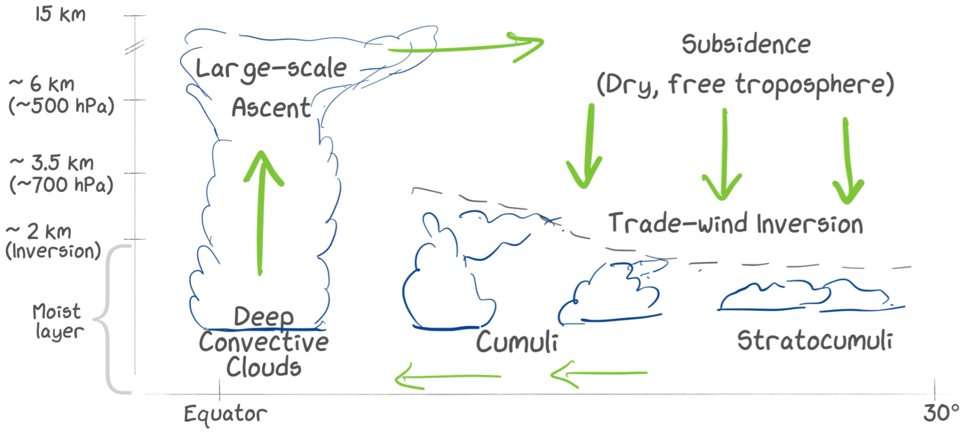

Figure 1.4: **Cloud types across Hadley cell.** The figure, adapted from George (2021), shows different cloud types and the coupling of clouds to the large-scale circulations across the Hadley cell.

and lower density. In the trade-wind region, the lowest 600 m of the atmosphere is generally well mixed, meaning that the properties (e.g., temperature, humidity, and wind) of the surrounding environment do not change with height. This means that if the parcel avoids exchanging heat with its environment, its temperature remains warmer than its surrounding environment as it rises and therefore it will ascend to a level called the lifting condensation level (LCL). The LCL is determined by the vertical profiles of temperature and total moisture content. While both temperature and moisture content generally decrease with height, the atmosphere's capacity to hold moisture decreases exponentially with decreasing temperature. Eventually, the air reaches a saturation point, which defines the LCL.

At the LCL, if the rising parcel has not exchanged heat or moisture with its surroundings to this level, the excess water vapor—beyond what the atmosphere can hold in vapor form, i.e. saturation vapor pressure—condenses into liquid water. This condensation releases heat, warming the parcel and making it lighter, thereby providing additional energy for it to continue rising. If the parcel remains warmer than its surroundings, it will rise further until all its kinetic energy, gained from the convective potential energy, is depleted. At this point, the parcel reaches the cloud-top height. If the parcel has enough convective potential energy, it may rise deep enough to reach the top of the trade-wind inversion layer (Fig. 1.4), where it stops ascending. Above this inversion layer lies the free-troposphere, characterized by dry, subsiding motions and a stable stratification, where temperature increases rapidly with height (Fig. 1.4). In the trade-wind regime, the top height of shallow trade-cumulus clouds typically ranges between 1 and 4 km, depending on various factors related to both the parcel and the environment. For instance, increased entrainment mixing can reduce the parcel's convective potential energy more rapidly with height, lowering the maximum height it can achieve. Similarly, a less unstable vertical structure of the surrounding environment at the cloud layer or stronger inversions can too inhibit the parcel's upward movement. Thus, this section has briefly described how an individual cumulus cloud develops vertically through moist convective processes occurring at scales of approximately 1–10 km.

1.2.3 MICROSCALES: WITHOUT AEROSOLS TRADE CUMULUS CANNOT FORM

Let us zoom in on our parcel exactly as it reaches the LCL. What would you expect to observe? Physically, water requires a surface to condense upon. You can easily test this by breathing twice in a room with normal temperature: once into the air and once onto the surface of your glasses or smartphone. You will notice that water vapor readily condenses on the surface but not in the air. The same principle applies to clouds—they require a surface for condensation. This surface is provided by aerosols. In the trade-wind region, these aerosols are predominantly sea salt, but they can also include dust transported from the Sahara to the North Atlantic, or even aerosols from ship exhaust. Thus, water condenses onto aerosol particles, forming cloud droplets with typical radii ranging from 10 to 20 micrometers.

The number of aerosols in an air parcel, or aerosol number concentration, determines two crucial aspects of clouds. Firstly, given the same amount of condensed liquid water, an increase in aerosol number concentration leads to a greater number of cloud droplets. This increases the surface area available to interact with radiation, thereby enhancing the cloud optical thickness. In turn, greater optical thickness directly increases the cloud albedo, resulting in more shortwave radiation being reflected back into space. This means, for a given liquid-water path, an increased number of cloud droplets leads to greater shortwave reflection, cooling the atmosphere. This effect is known as the Twomey effect (Twomey, 1974).

Secondly, for an individual cloud, increased cloud-droplet number concentration reduces the efficiency of collision-coalescence processes, which are critical for converting cloud droplets into rain droplets. This, in turn, decreases the efficiency of precipitation formation. This effect is known as Albrecht or lifetime effect (Albrecht, 1989). Two scenarios might arise as a result. First, if clouds do not rain out, they persist and grow deeper, potentially leading to more intense precipitation later. Because of the delay in precipitation formation, clouds live longer before they start raining, which is why this effect is called the “lifetime effect.” Second, for a given amount of cloud water, an increased number of cloud droplets reduces the size of individual droplets. This makes them more susceptible to evaporation at the cloud edges (Xue et al., 2008a). Depending on the cloud regime, deepening might outweigh cloud removal by evaporation, or vice versa. Thus, this section has highlighted that the formation and characteristics of trade-wind cumuli are fundamentally controlled by processes occurring at micrometer scales.

1.2.4 MESOSCALES: TRADE CUMULUS FIELDS ORGANIZE INTO MESOSCALE PATTERNS

This section so far has briefly covered scales involved in the formation of trade-cumulus clouds ranging from synoptic (> 1000 km) to cloud droplet ($\approx 10-20\,\mu$m). Obviously, there is a huge scale gap between the synoptic (> 1000 km) and individual cloud scale ($\approx 1-10$ km). Even under identical large-scale conditions in the trade-wind region and with a fixed aerosol number concentration, the resulting cloud structures can vary significantly from the classic cumulus form. This variability poses a fundamental challenge for how clouds are parameterized in climate models, in which clouds are often assumed to passively respond to the conditions imposed by synoptic scales. But is this assumption valid? Given identical large- and micro-scale conditions, do trade cumuli have the freedom to take forms other than classic puffy cumulus form?

A recent study by Stevens et al. (2020) reveals that trade-wind cumulus clouds can organize into strikingly beautiful mesoscale patterns—proving they are not always classic cumuli. The captivating nature of these patterns inspired Stevens et al. (2020) to assign poetic names to them: *Sugar*, *Gravel*, *Flowers*, and *Fish* (see Fig. 1.5). However, Schulz et al. (2021) demonstrated that over 60% of $10^{\circ}\times10^{\circ}$ cloud fields cannot be classified under one of these poetic names; they are often a mixture of these patterns. Furthermore, Janssens et al. (2021) conducted a comprehensive study revealing that the variability in trade-cumulus patterns is better represented as a continuous spectrum rather than as four discrete categories. These four categories appear to lie at the edges of this spectrum, likely because the human eye is more sensitive to striking outliers (Janssens, 2023a, Their Chapter 8). Regardless of the number of dimensions capturing the variability of these patterns, the scale of these remarkable structures highlights a key limitation of current climate models, which fail to represent them. In other words, because of the coarse resolution of climate models, they cannot resolve the scales at which these patterns form. This raises an important question: does the mesoscale organization of trade-cumulus fields influence trade-cumulus climate feedback? This question has significantly drawn attention from cloud scientists (Bony et al., 2020a, 2015; Nuijens and Siebesma, 2019).

As a first step, Bony et al. (2020a) showed that these patterns are not just beautiful and striking, but they feature different cloud cover and in turn different shortwave reflection. This means that the mesoscale organization of trade-cumulus cloud fields matters for their radiative effects. Thus, if the frequency of occurrence of more reflective patterns increases with climate change, they might slow down warming—and vice versa. This implies that the mesoscale patterning of trade-wind cumuli could play a role in their feedback to climate change. This necessitates understanding the drivers of mesoscale organization, which serves an important step towards understanding their relevance for cloud feedbacks. There have been crucial steps towards understanding the drivers of mesoscale organization, which are briefly explained below.

Mesoscale organization is partly controlled by large-scale conditions

Both Bony et al. (2020a) and Schulz et al. (2021) demonstrated that estimated inversion strength and near-surface wind speed can distinguish between mesoscale patterns in the trades. *Sugar* forms under very calm trade-wind conditions, while *Gravel* and *Flowers* are associated with windier environments. *Flowers*, in particular, develop under strong inversions. Additionally, Schulz et al. (2021) showed that *Sugar*, *Gravel*, and *Flowers* are local to the trades, arising from convective processes within the trade-wind region. In contrast, the *Fish* pattern results from extra-tropical intrusions into the trades. Collectively, the covariations between cloud patterns and environmental factors suggest that mesoscale variations are partly controlled by large scales.

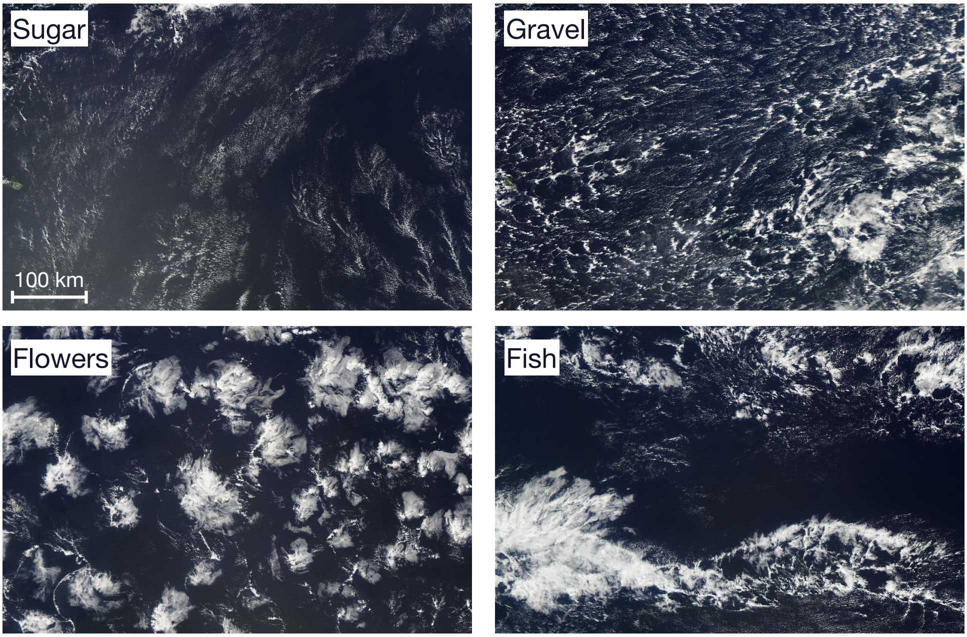

Figure 1.5: **Mesoscale cloud patterns in the downstream trades.** The subjectively identified cloud patterns by Stevens et al. (2020). Photos are from the NASA Worldview platform and are taken by either Aqua or Terra satellites on 2024/01/31 (Sugar), 2016/12/26 (Gravel), 2017/02/09 (Flowers), and 2024/01/14 (Fish), close to the east coast of Barbados over the North Atlantic Ocean.

Independent of large-scale variability, trade cumuli self-organize into mesoscale patterns

Here we describe whether, under time-invariant and spatially homogeneous large-scale external conditions, the trade-cumulus fields can still organize into mesoscale structures—arising, for instance, from interactions between system components such as clouds. We use the term *self-organization* to emphasize that these structures, independently of external variability, emerge from internal dynamics within the system. Similar internal interactions have been explored in stratocumulus (Glassmeier and Feingold, 2017) and deep convective regimes (Haerter et al., 2019; Nissen and Haerter, 2021), where mutual interactions between clouds lead to emergent structures at the scale of cloud fields. Importantly, these emergent structures cannot be explained by the individual components of the system, but rather by understanding how those components interact with each other. It is through these interactions that self-organization arises within the system (Pietronero, 2008).

Under large-scale conditions that are invariant in time and homogeneous in space, studies using large-eddy simulations have shown that non-precipitating trade-wind cumulus fields tend to aggregate into clustered structures (Bretherton and Blossey, 2017; Narenpitak et al., 2021). These modeling studies found that non-precipitating cumuli are inherently unstable to scale growth (Janssens et al., 2023). This scale growth occurs due to the presence of mesoscale overturning circulations that transport moisture from drier to moister regions in the field. As shallow cumulus clouds develop, dry regions become drier, and moist regions become moister. Clouds also grow both horizontally and vertically over these mesoscale moist regions. These studies highlight that clouds are not merely passively coupled to mesoscale circulations; rather, the clouds themselves—through shallow condensational heating, which destabilizes the cloud layer—drive mesoscale circulations (Janssens et al., 2024). Thus, cumulus self-aggregation is a self-reinforcing mechanism. The mesoscale circulations and their coupling to clouds were observed in the trade-wind region during the recent EUREC^{4}A field campaign (Bony et al., 2017; Stevens et al., 2021), which revealed a widespread presence of shallow mesoscale overturning circulations and its coupling to clouds across the trades (George et al., 2023; Vogel et al., 2022).

Non-precipitating trade cumuli continue to aggregate and deepen while simultaneously strengthening the shallow mesoscale circulations. As these clouds deepen, they eventually reach a point where precipitation begins. Naturally, this point depends on the microscale properties of cloud droplets, as explained earlier. Large-eddy simulations of trade-wind cumuli have shown that once precipitation starts, these clouds self-organize into ring-like structures, resembling the *Gravel* pattern illustrated in Fig. 1.5 (Lamaakel et al., 2023; Seifert and Heus, 2013; Vogel et al., 2016). These structures are linked to a process known as “cold pools.” Cold pools form when rain evaporates beneath clouds, creating a pocket of cold, dense air that drives strong downward motions. When this cold, dense air reaches the surface, it spreads out circularly due to mass conservation. As they expand, cold pools transport moisture from their interior to their edges. The strong convergence at their leading edges, combined with the moist air present there, actively triggers moist convection and the formation of clouds at their boundaries. This leads to an emergence of clear-sky areas that are enclosed by cloud rings, visible in the *Gravel* field of Fig. 1.5. There is observational evidence that trade-wind cumuli are frequently precipitating (Nuijens et al., 2009; Radtke et al., 2022), from which cold pools form (Zuidema et al., 2012). Recently, observations of Vogel et al. (2021) showed that there is a co-variability between the frequency of cold pools and the subjectively identified patterns of Fig. 1.5. Thus, in addition to models, observations suggest that cold pools are a process that organizes cloud fields into mesoscale structures.

1.3 AIMS OF THIS THESIS

The following sections outline the aims of this PhD thesis, which focuses on enhancing our understanding of the mesoscale self-organization of trade-wind cumulus cloud fields (Fig. 1.6, link 1), their response to large- and micro-scale processes (Fig. 1.6, links 2 and 3), and the radiative impacts of this (self-)organization—highlighting the influence of mesoscales on large scales (Fig. 1.6, link 4).

1.3.1 MESOSCALE SELF-ORGANIZATION OF PRECIPITATING TRADE CUMULI AND ITS DEPENDENCE ON LARGE- AND MICRO-SCALES

Although we know from previous studies that cold pools are associated with observed mesoscale patterns such as *Gravel* and *Flowers* (Vogel et al., 2021), we do not yet know how exactly cold pools evolve and interact with clouds in the trade-wind regime. An LES-based case study of *Flowers* shows that cold pools play a role in the formation of these patterns, similar to how cold pools organize deep mesoscale convective systems along squall lines (Dauhut et al., 2023). However, it remains unclear whether this squall-line analogy holds beyond a single case study. This is the question that will be investigated in **Chapter 2** where we explore what self-organizing roles cold pools play in trade-cumulus fields (Fig. 1.6, link 1). This chapter will be central in elucidating the role cold pools play in the evolution of scale growth after the non-precipitating aggregation phase. This will also be informative in showing how cold pools interact with and affect shallow circulation and cloud-circulation coupling in the trade-wind regime.

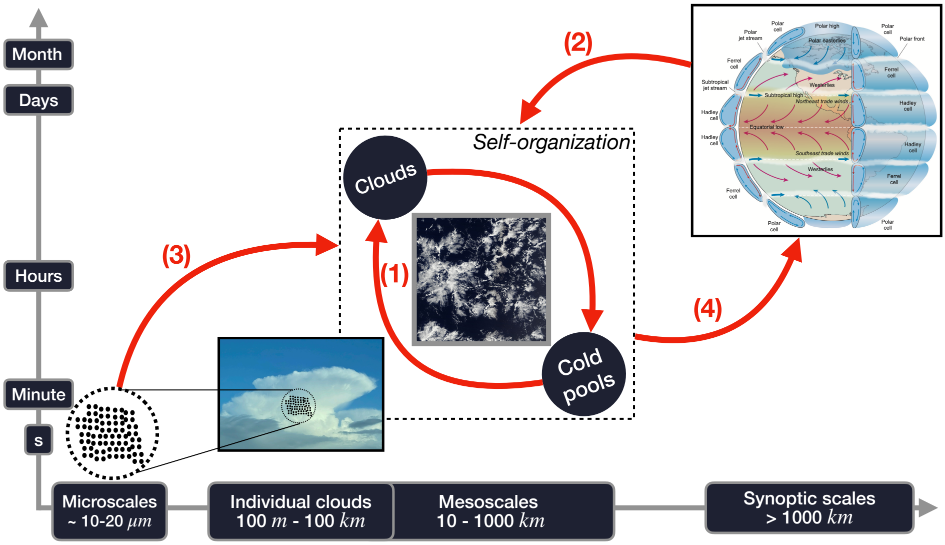
Month
Days
Hours
Minute
s
(2)
Self-organization
Clouds
(3)
(1)
(4)
Cold pools
Polar cell
Polar high
Polar jet stream
Polar easterlies
Polar cell
Polar front
Ferrel cell
Subtropical jet stream
Westerlies
Ferrel cell
Subtropical high
Northeast trade winds
Hadley cell
Hadley cell
Equatorial low
Hadley cell
Hadley cell
Southeast trade winds
Westerlies
Ferrel cell
Ferrel cell
Polar cell
Polar cell
Microscales ~ 10-20 μm
Individual clouds 100 m - 100 km
Mesoscales 10 - 1000 km
Synoptic scales > 1000 km

Figure 1.6: **Sketch of the dependence of mesoscale cloud (self-)organization on large- and micro-scale processes.** The horizontal and vertical axes represent spatial and temporal scales. The diagram summarizes the main foci of the thesis, where the response of mesoscale self-organization to variations in micro- and large-scale processes is explored. The large-scale figure is adapted from the book by Mathez and Smerdon (2018).

Mesoscale patterns of trade-cumulus fields have been shown to be influenced by variations in large-scale CCFs (Fig. 1.6, link 2), (Bony et al., 2020a; Schulz et al., 2021). Thus, the observed covariability between cold pools and mesoscale patterns of trade-cumulus fields (Vogel et al., 2021) suggests that cold pools should respond to variations in CCFs. Furthermore, cloudiness, precipitation, mesoscale organization, and cold pools in the trades were demonstrated to show diurnality in recent observational studies (Nuijens et al., 2009; Radtke et al., 2022; Vial et al., 2021; Vogel et al., 2021). Despite the aforementioned studies, no systematic investigation has yet been conducted to examine how large-scale CCFs influence the frequency and size of cold pools and in turn mesoscale organization in the trades. Chapter 2 fills this gap by presenting a comprehensive analysis of the cold-pool response to CCFs, using a large ensemble of large-domain LES simulations designed based on climatologically relevant large-scale conditions in the trade-wind regime. This quantification is crucial for understanding the extent to which cold pools, as a self-organizing process in the trades, have the freedom to evolve or change in the trade-wind regime. This chapter, therefore, investigates the extent to which mesoscale self-organization is affected by variations in large scales (Fig. 1.6, link 2).

As briefly explained above, a decrease in aerosol number concentration and, thereby, a decreased cloud-droplet number concentration (N_c) leads to a delay in precipitation formation (Albrecht, 1989) for individual clouds. LES-based studies of trade-cumulus fields showed that decreased N_c leads to a delay in precipitation formation, resulting in deeper cloud fields that, after a point, precipitate more intensely (Seifert et al., 2015; Yamaguchi et al., 2019). As cold pools are a result of rain evaporation, variations in N_c are expected to directly affect cold pools and, in turn, the mesoscale self-organization of trade-cumulus fields. However, the impact of N_c on the self-organization of trade-cumulus fields has not been quantified so far. **Chapter 3** thus sheds light on the dependence of mesoscale self-organization on micro-scale variations (Fig. 1.6, link 3) and compares this sensitivity with the impact of large scales (Fig. 1.6, link 2).

1.3.2 THE RELEVANCE OF MESOSCALE ORGANIZATION FOR THE RADIATIVE EFFECT OF TRADE-WIND CUMULUS CLOUD FIELDS

Bony et al. (2020a) demonstrated that the mesoscale patterning of trade-cumulus fields influences their ability to reflect shortwave radiation due to the co-variability between organization and cloud cover. However, Janssens et al. (2021)'s comprehensive statistical analysis of 21 cloud organization metrics indicated that, even though cloud cover co-varies with mesoscale organization metrics, it explains just a fraction of the total variability in mesoscale cloud patterns in the trades. This raises the question: To what extent does mesoscale cloud organization impact the radiative effects of trade-wind cumuli, independent of their cover? This question will be explored in **Chapter 4**. This chapter thus investigates the impact of mesoscales on the large scales (Fig. 1.6, link 4) through variations in the top-of-the-atmosphere cloud-radiative budgets.

Chapter 5 will investigate the impact of cold pools on the radiative budget of trade-wind cumulus fields. This chapter is motivated by two key challenges. First, cold pools suppress convection beneath them, forming cloud holes and expanding open-sky areas, thereby reducing cloud cover. At the same time, they trigger convection along their leading edges, enhancing cloud formation. However, the relative dominance of these opposing effects remains unquantified, leaving the net impact of cold pools on the cloud-radiative effect uncertain. Second, studies in deep convection showed that cold pools can suppress self-aggregation of moisture (Böing et al., 2012; Jeevanjee and Romps, 2013; Muller and Bony, 2015; Nissen and Haerter, 2021), a process that is shown to affect the top-of-the-atmosphere longwave clear-sky radiation in the tropics (Bony et al., 2020b). The effect of cold pools on moisture fields and in turn longwave clear-sky radiation had not yet been explored before **Chapter 5**. Using a denial experiment in which cold-pool formation is prevented (i.e., breaking link 1 in Fig. 1.6) by homogenizing rain-evaporation (Böing et al., 2012), **Chapter 5** comprehensively addresses these questions. **Chapter 5** thus will provide a quantitative estimate of the relevance of cold-pool-induced mesoscale self-organization for top-of-the-atmosphere radiative budgets of trade-wind cumulus fields across a range of climatologically relevant environmental conditions of the trades. This chapter therefore explores the impact of cold pools on the large-scale CCFs (Fig. 1.6, link 4) via regulating the top-of-the-atmosphere radiative budgets.

Finally, **Chapter 6** provides an overview of the entire thesis, summarizing its key findings in relation to the main objectives. It then proposes a conceptual picture of the trade-wind cumulus system, integrating the insights gained throughout the thesis. Building on this conceptual framework, the chapter also offers perspectives on future research directions shaped by these findings.

2

EXTERNAL DRIVERS AND MESOSCALE SELF-ORGANIZATION OF SHALLOW COLD POOLS IN THE TRADE-WIND REGIME

This chapter is published as 🗎 *Alinaghi, P., Siebesma, A. P., Jansson, F., Janssens, M., & Glassmeier, F. (2025). External drivers and mesoscale self-organization of shallow cold pools in the trade-wind regime. Journal of Advances in Modeling Earth Systems, 17(1), e2024MS004540..*

Abstract

Recent observations of the trade-wind regions highlight the covariability between cold-pool properties and mesoscale cloud organization. Given the covariability of organization with cloud cover and albedo, this suggests a potential impact of cold pools on the cloud radiative effect (CRE). To explore this, we use an ensemble of 103 large-domain, high-resolution, large-eddy simulations and investigate how the variability in cold pools is determined by large-scale external cloud-controlling factors (CCFs) and shaped by processes within the mesoscale. It is demonstrated that the size and frequency of occurrence of cold pools are strongly influenced by the near-surface horizontal wind speed and large-scale subsidence. The temporal evolution of cold pools is strongly correlated with the diurnality in radiation. Even without external variability, we find a strong intermittent behaviour in the evolution of cold pools, governed by a complex interplay between cold pools and clouds which expresses itself in the form of shallow squall lines. These squall lines result from precipitating downdrafts, cold pool outflows and the resulting gust fronts, reinforcing parent clouds. Cold pools influence the CRE of trade cumuli, but only when they exist during the day. This emphasizes the importance of the synchronization between cold-pool events and the diurnal cycle of insolation for the dependence of the CRE on cold pools.

2.1 Introduction

Cold pools are pockets of cold dense air that result from downdrafts associated with rain evaporation in the sub-cloud layer. When these downdrafts reach the surface, they expand circularly, forming mesoscale cloud arcs visible in satellite imagery (Zuidema et al., 2012, 2017). The local impact of cold pools is evident in both shallow and deep convection and consists of significantly altering the sub-cloud layer's thermodynamic structure and dynamics (Böing et al., 2012; Drager and van den Heever, 2017; Lochbihler et al., 2021a; Schlemmer and Hohenegger, 2016; Touzé-Peiffer et al., 2022; Vogel et al., 2021; Zuidema et al., 2012). Cold pools suppress the convection underneath clouds but can trigger new convective events by accumulating heat and moisture while maintaining a relatively higher wind speed at cold-pool fronts (Jeevanjee and Romps, 2013; Langhans and Romps, 2015; Tompkins, 2001; Torri et al., 2015; Vogel et al., 2021; Zuidema et al., 2012). When cold-pool fronts collide, they can even more forcefully trigger new convection, a feature described in the deep convective regime (Torri and Kuang, 2019) as well as in shallow cumulus (Xue et al., 2008b) and open-cell stratocumulus (Savic-Jovcic and Stevens, 2008). In these cases, such mutual interactions between cold pools give rise to a self-organization of the cloud fields that manifests in horizontal variability on the mesoscale (Glassmeier and Feingold, 2017; Haerter et al., 2019; Nissen and Haerter, 2021). Due to their interaction with ambient environmental shear, which invigorates and sustains the convection, cold-pool fronts can also evolve into squall lines, not only in deep convective systems (Moncrieff and Liu, 1999; Rotunno et al., 1988; Weisman and Rotunno, 2004), but also in case studies of shallow trade cumulus fields (Dauhut et al., 2023; Li et al., 2014).

Recent research on the climatology of trade-cumulus cold pools shows that the subjectively identified cloud patterns–*Sugar*, *Gravel*, *Flowers*, *Fish* (Stevens et al., 2020)– have distinct cold-pool statistics (Vogel et al., 2021). Given the effect of mesoscale cloud organization on cloud radiative effect (CRE) through its correlation with both cloud cover (Bony et al., 2020a) and albedo (Alinaghi et al., 2024a; Denby, 2023), these findings suggest that cold pools likely play a significant role in regulating the radiative effect of shallow cumulus clouds in the trades. However, the response of CRE to cold pools in the trades has not yet been directly explored. Therefore, this study aims to understand how cold pools can influence CRE. As illustrated in Fig. 2.1, this implies investigating (i) the underlying mechanisms through which cold pools evolve and interact with trade-cumulus clouds for fixed large-scale conditions, i.e. their self-organization on the mesoscale, and (ii) the extent to which this behavior is controlled by the large-scale conditions.

For large-scale conditions that are fixed in time and spatially homogeneous (dashed box in Fig. 2.1), large-eddy simulations (LESs) of non-precipitating trade cumuli tend to self-aggregate into clustered structures (Bretherton and Blossey, 2017; Janssens et al., 2023; Narenpitak et al., 2021), leading to growth in their horizontal length scales (Phase 1 in the time series of Fig. 2.1). Ultimately, the deepening alongside this increased clustering leads to the initiation of precipitation (Phase 2 in the time series of Fig. 2.1). As a result of rain evaporation, cold pools develop spontaneously from such conditions over domains of 50-300 km^2 (Anurose et al., 2020; Lamaakel et al., 2023; Seifert and Heus, 2013; Vogel et al., 2016). Formation of cold pools, in turn, leads to the presence of ring-like structures at the mesoscales. Throughout the manuscript, we use the term *self-organization* for the precipitating cumulus system because (i) these ring-like structures form under large-scale

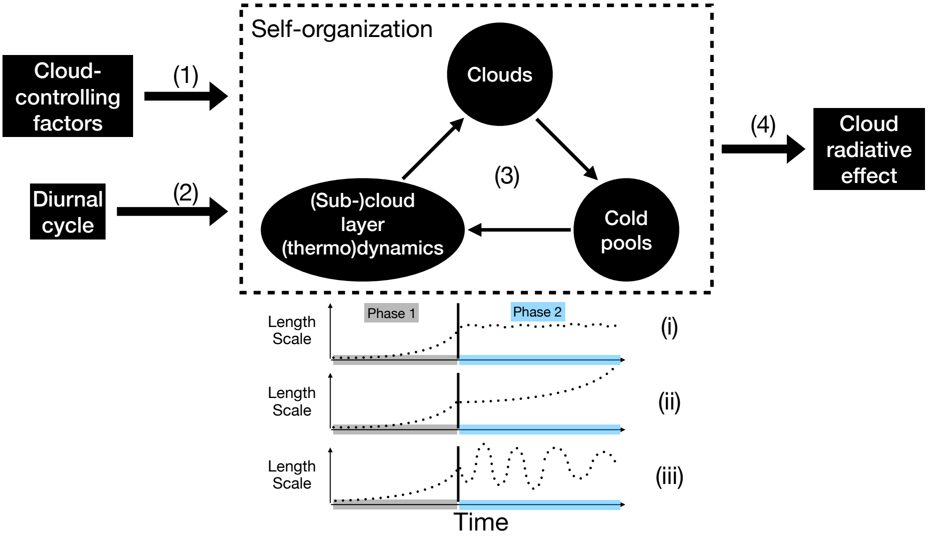

Figure 2.1: **A conceptual picture of the trade-cumulus cloud system.** The dashed rectangle box shows the trade cumulus system which is forced by (1) the large-scale CCFs and (2) the diurnal cycle. Having time-invariant and conducive CCFs, this system shows (3) self-organization via interaction between its components, i.e. clouds and cold pools. As a result of these interactions, this system might show (i) a time-invariant, (ii) an unstable, or (iii) an intermittent behaviour. The resulting (4) cloud-radiative effect is expected to depend on the details of links (1) to (3).

conditions that are invariant in time and space, and (ii) the interactions between cold pools and clouds mutually organize themselves into these ring-like structures at the mesoscale. A recent realistically forced LES case study of the so-called *Flowers* on Feb 2nd, 2020, highlighted the role of cold pools in shaping this pattern in shallow convection, similar to how deep mesoscale convective systems self-organize along squall lines thanks to cold pools dynamics (Dauhut et al., 2023). However, it remains unclear whether this "shallow squall line" analogy holds beyond this single case study. Thus, our first aim is to investigate the mechanisms through which cold pools in the trades self-organize and interact with clouds from their formation until their dissipation (Fig. 2.1, link 3). We will specifically explore, whether length-scale growth stabilizes under cold-pool activity (Phase 2, Option i), keeps increasing (Phase 2, Option ii), or shows an intermittent behavior (Phase 2, Option iii).

The next question is whether and how these self-organized fields of cold pools in the trades are controlled by the large-scale conditions, or cloud-controlling factors (CCFs). Variations in CCFs can be expected to directly control variations in convective triggering among mesoscale airmasses, and thus control fields of self-organized cold pools (Fig. 2.1, link 1). For example, forward shear is more effective than backward shear in triggering new cold-pool-driven convective events in LES experiments (Helfer and Nuijens, 2021). The diurnal cycle of insolation appears to consistently control characteristics of cold pools and their associated cloud patterns (Fig. 2.1, link 2), cloud cover and precipitation in observations (Radtke et al., 2022; Vial et al., 2021; Vogel et al., 2021). Furthermore, cold-pool-coupled trade cumulus patterns (Vogel et al., 2021) can be classified by their large-scale surface wind speed and inversion strength (Bony et al., 2020a, Fig. 3). Despite the expected response of trade-cumulus cold pools to CCFs, we do not yet know (i) the precise magnitude of this response, and (ii) which CCFs are the most important.

We comprehensively address these questions by means of a large ensemble of large-domain LESs. Such ensembles are becoming increasingly computationally feasible (Jansson et al., 2023). Their advantages compared to case studies lie not only in their greater generality but also in their amenability to statistical analyses, which facilitates model-measurement integration (Alinaghi et al., 2024a; Chen et al., 2024; Feingold et al., 2016; Glassmeier et al., 2019; Gryspeerdt et al., 2022; Hoffmann et al., 2020, 2023; Mapes, 2024). We specifically employ the *Cloud Botany* dataset, which includes 103 idealized, large-domain, LESs of shallow cumulus clouds (Jansson et al., 2023). These simulations were performed using the Dutch Atmospheric Large Eddy Simulation (DALES) model (Heus et al., 2010) and incorporate varying large-scale CCFs such as tropospheric stability, geostrophic wind, sea-surface temperature, and large-scale vertical velocity. The range of the used values of these CCFs are determined from ERA5 reanalysis data (Hersbach et al., 2020) and EUREC^{4}A field campaign (Bony et al., 2017; Stevens et al., 2021) and are therefore representative of the large-scale conditions of the trade-wind regions over the subtropical Northern Atlantic Ocean where cold pools frequently occur. This makes the *Cloud Botany* perfectly suitable for systematically exploring and categorizing the interplay between cold pools and the environmental conditions in which they form, develop, and decay.

In the remainder of the paper, we first introduce the data and methods, followed by a quantification of the response of cold pools to variations in large-scale CCFs (Fig. 2.1, link 1, sect. 2.3.1) as well as to the diurnal cycle of insolation (Fig. 2.1, link 2, sect. 2.3.2). To solely focus on the dependence of cold pools on self-organizing mechanisms (Fig. 2.1, link 3), the diurnality in radiation is switched off in sect. 2.3.3. We eventually present how the self-organization of cold pools manifests itself into 2D cloud patterns and how this affects CRE (Fig. 2.1, link 4) in sect. 2.3.4. We summarize our results in sect. 2.4.

2.2 METHODOLOGY & DATA

2.2.1 *CLOUD BOTANY* ENSEMBLE

The main data source for this study is the output of a large ensemble of LESs of shallow cumulus cloud fields, produced with the Dutch Atmospheric Large-Eddy Simulation (DALES) model (Jansson et al., 2023). This dataset, called *Cloud Botany*, consists of 103 simulations, each 60 hours long, over 150×150-km^2 domains with a horizontal resolution of 100 m and a vertical resolution of 20 m (which stretches by 1% with height). The *Botany* simulations were run for a range of different idealised large-scale forcings and environments, controlled by six parameters; we will refer to these parameters as cloud-controlling factors (CCFs) (Jansson et al., 2023, Fig. 2). These CCFs are the sea-surface liquid-water potential temperature (θ_{l0}), near-surface geostrophic wind speed (u_0), the moisture scale height (h_{q_t}), the temperature lapse rate in the free troposphere (Γ), large-scale vertical velocity variability (w_1), and the shear in the horizontal geostrophic wind (u_z). Each simulation was initialized with the profiles of temperature, humidity and wind that determine the large-scale environment. Table 2.1 provides information on the ensemble's mean and standard deviation of these CCFs.

The range of used values for the CCFs is based on the global ERA5 reanalysis data of the trade-wind environment (Hersbach et al., 2020). All *Botany* simulations feature constant large-scale tendencies for drying and cooling through advection as depicted by (Jansson et al., 2023, Fig. 3). Additionally, diurnality in incoming solar radiation is incorporated throughout the entire *Botany* simulations. The cloud-droplet number concentration is fixed and equal to $70 \times 10^6/\mathrm{m}^3$ in every grid cell of *Botany* simulations. For further details about the design and parameters of the *Botany* ensemble, we refer the readers to the dataset paper (Jansson et al., 2023).

Large-scale and initial conditions	**Parameters [units]**	**Ensemble's mean**	**Ensemble's standard deviation**
Sea-surface liquid-water potential temperature	θ_{l0} [K]	299	0.84
Near-surface geostrophic wind speed	u_0 [m/s]	-10.6	3.65
Temperature lapse rate in the free troposphere	Γ [K/km]	5	0.51
The moisture scale height	h_{q_t} [m]	1810	515
Large-scale vertical velocity variability	w_1 [cm/s]	0.0393	0.1906
Shear in the horizontal geostrophic wind	u_z [(m/s)/km]	2.22	1.79

Table 2.1: **Parameters of the *Botany* ensemble.** Overall statistics of the ensemble's parameters determining CCFs.

Each simulation member of the *Botany* ensemble is initialized from a homogeneous non-cloudy state, and the external CCFs are time-invariant throughout each simulation member. This means that the evolution of cloud fields is internally driven by, e.g. the interactions between the components of system, i.e. *self-organization.* This allows studying processes through which the system self-organizes. To illustrate their overall behaviour, we show Fig. 2.2a, which provides the time series of the domain-mean (cloud-)liquid-water path $\mathcal{L}$ and rain-water path $\mathcal{R}$ averaged over the entire ensemble. Figures 2.2b-e further show the albedo contour plots of the central reference simulation at 5, 23, 29, and 54 hours after the starting time of the simulation. All simulations in the *Botany* ensemble start from a homogeneous non-cloudy state (Fig. 2.2a). During the spin-up time of the first ≈ 10 hours, a majority of simulation members (87 out of 103) develop small cumuli (Fig. 2.2b) that due to self-reinforcing shallow circulations (Janssens et al., 2023) clump together and deepen (Fig. 2.2c). This marks phase 1 in Fig. 2.1. Once these aggregated clouds deepen sufficiently, they begin to precipitate ($\approx$ Hour 22; Fig. 2.2a) and form cold pools. This marks the beginning of phase 2 shown in Fig. 2.1. The cold pools can be visually diagnosed as relatively cloud-free areas surrounded by cloudy rings in Figs. 2.2d, 2.2e. The simulated cloud rings and cold pools are sometimes topped by stratiform anvils (Fig. 2.2d), which visually resemble *Flowers* (Stevens et al., 2020). Later, the cold pools organize into (semi-)cellular structures (Fig.

2.2e), which resemble Stevens et al. (2020)'s *Gravel.* Cloudiness and precipitation grow through the night and peak at sunrise (Fig. 2.2a). Afterwards, due to the stabilizing effect of daytime shortwave radiative heating, cloudiness and precipitation decline until around sunset, where they start to grow again. As cold pools result from rain evaporation, all our analyses throughout this paper focus on the second day of the *Botany* simulations, where the cumuli robustly precipitate (Fig. 2.2a), i.e. phase 2 of Fig. 2.1.

2.2.2 COLD POOLS DIAGNOSED BY THE MIXED-LAYER HEIGHT

Once clouds are raining, rain-evaporation cools the sub-cloud layer, while condensation warms the cloud layer, stabilizing the boundary layer. Consistently, cold pools in the trades often correspond to a drop in near-surface temperature (up to ≈ 1-2 K) and specific humidity (up to ≈ 1.5 g/kg), as observed by Zuidema et al. (2012). In this study, we diagnose cold pools using the (shallow) mixed-layer height (h_{mix}) from the 2D outputs of the *Botany* dataset, which is calculated according to the method proposed by (Rochetin et al., 2021, their Equation 1). The metric h_{mix} has been demonstrated as a reliable indicator for trade cumulus cold pools, with the area affected by cold pools exhibiting low values of h_{mix}, in both observations (Touzé-Peiffer et al., 2022) and models (Rochetin et al., 2021).

To illustrate how we diagnose cold pools from the horizontal field of h_{mix}, consider the snapshot in Fig. 2.3a. Figure 2.3b depicts the probability density distribution (PDF) of h_{mix} corresponding to Fig. 2.3a. The ansatz for our diagnosis of a cold pool is to imagine a symmetric mono-modal distribution in this PDF that would have occurred in the absence of cold pools; in this field, its mode is around 900 m. We approximate the upper boundary of this distribution as the 99$^{\text{th}}$ percentile of the 2D h_{mix}. Next, we mark its lower boundary by subtracting the difference between the mode and the upper boundary from the mode (blue line in Fig. 2.3b). Any pixel with an h_{mix} smaller than this height is considered a cold-pool pixel. The outline of the resulting cold-pool mask for this example is shown in Fig. 2.3a.

Using this cold-pool mask, we quantify spatial cold-pool characteristics, such as their fraction f_{cp}, number n_{cp}, and size $s_{cp} = \sum_{i=1}^{n_{cp}} \sqrt{A_i}/n_{cp}$, where A_i denotes the area of each individual cold-pool object within the simulation domain. Each cold-pool object is detected as 2D contiguous objects using the clustering technique. These metrics are calculated for all simulations every five minutes, which is the temporal resolution of the h_{mix} output in the *Botany* dataset.

Like previous studies (Drager and van den Heever, 2017; Rochetin et al., 2021), there are statistical assumptions in defining cold pools. However, the main results are not sensitive to these definition details. For instance, using the condition $h_{mix} < 400$ m for defining cold pools, as proposed by Touzé-Peiffer et al. (2022), yields very similar results (see section 2.3.1).

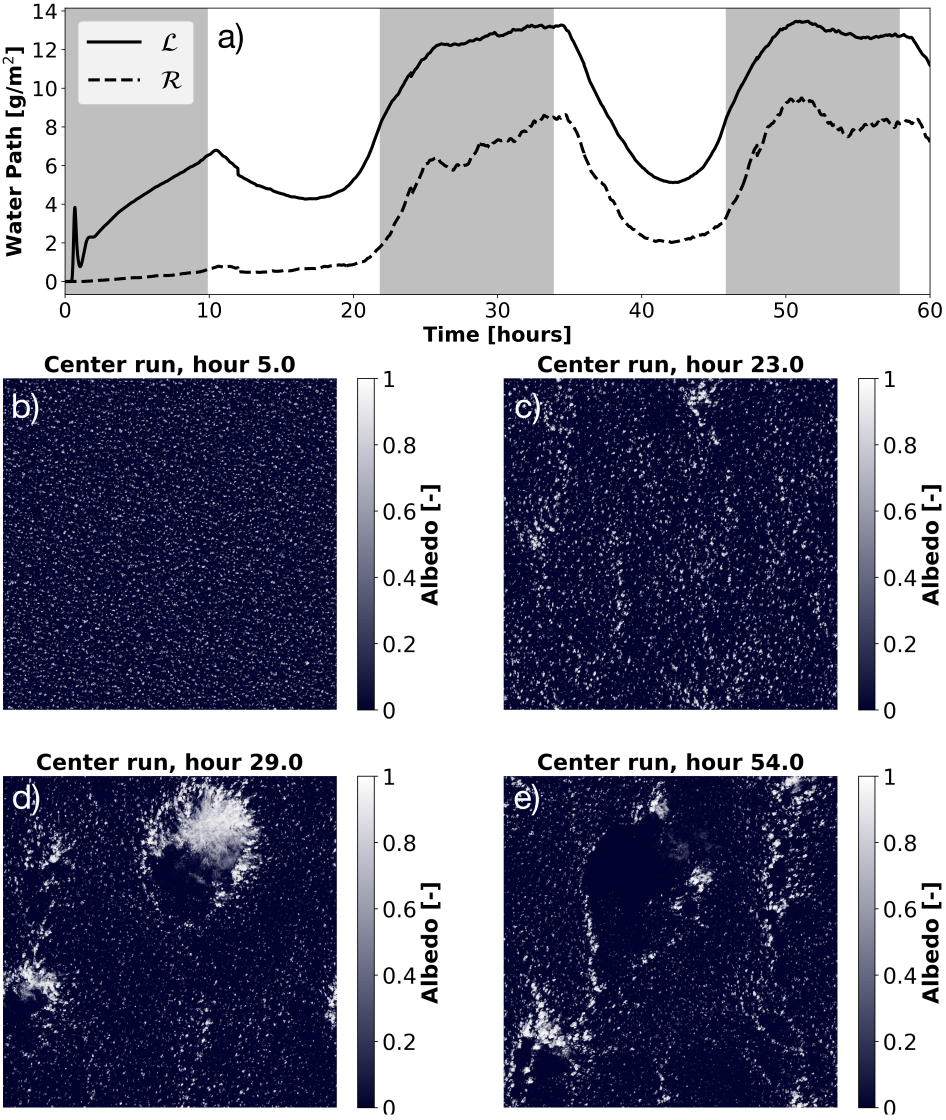

Figure 2.2: **Evolution of cumulus clouds in *Botany*.** (a) Time series of domain-mean liquid-water path ($\mathcal{L}$) and rain-water path ($\mathcal{R}$), averaged over the entire *Botany* ensemble. Grey-shaded areas correspond to nighttime. (b,c,d,e) Contour plots of cloud albedo for the central reference simulation (run 1) that has the mean CCFs of the entire ensemble.

Lastly, to explore the interactions between cold pools and clouds throughout the paper, particularly in sections 2.3.3 and 2.3.4, we use several cloud-field properties such as the domain-mean size of cloud objects (L_c), the mean fraction of open-sky areas (L_o) (Janssens et al., 2021), the domain-mean geometric thickness (h), and the domain-mean size of precipitation cells (L_p). The definitions of these metrics are detailed in the supplementary information.

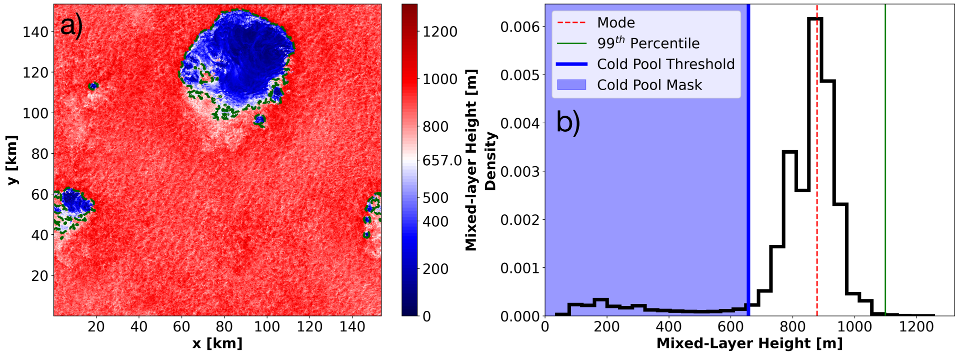

Figure 2.3: **Cold-pool mask definition.** (a) Contour plot of h_{mix} for hour 29 of the central reference simulation, which its cloud field is shown in Fig. 2.2. The cold-pool mask is shown by the green dashed contour line. (b) The probability density distribution of the h_{mix} shown in (a).

2.3 Results and Discussion

2.3.1 The dependence of cold pools on cloud-controlling factors

The dependence of cold pools on the CCFs (Fig. 2.1, link 1) is analyzed using a multivariate regression analysis

$$\overline{f}_{cp} \approx \sum_{i=1}^{6} \beta_i \times \widetilde{\mathrm{CCF}}_i \qquad \text{with} \qquad \widetilde{\mathrm{CCF}}_i := \frac{\mathrm{CCF}_i - \overline{\mathrm{CCF}}_i}{\sigma(\mathrm{CCF}_i)} \tag{2.1}$$

where $\overline{f}_{cp}$ is a vector where each elements stands for the average cold-pool fraction over the last two days of each simulation member of the ensemble when both precipitation and cold pools are present. Likewise, each CCF_i in the regression is a vector in which each element is the associated CCF_i of a simulation member of the ensemble. All the CCFs displayed in Table 1 are used as regressors. Regressors are standardized by subtracting their mean $\overline{\mathrm{CCF}}_i$ and through dividing by their standard deviation $\sigma(\mathrm{CCF}_i)$ across the entire ensemble. Therefore, β coefficients measure the relative significance of the CCFs with respect to each other with an equal weighting. Simulations without cold pools, i.e. $\overline{f}_{cp} < 0.001$, are excluded. Out of the 87 *Botany* simulations that develop into clouds, this selection criterion yields 82 simulations. In addition, we removed simulations 7 and 39 from the regression analysis as they do not fully contain the second day due to technical issues (Jansson et al., 2023). Therefore, our multiple regression analysis (Eq. 5.10) contains the target values and regressors, which are vectors (or 1D arrays) of size 80×1.

Figure 2.4a shows that the regression model based on *Botany*'s CCFs is well capable of explaining the variations of the mean cold pool fraction $\overline{f}_{cp}$ between the different simulations with $\mathrm{R}^2 = 0.87$. More specifically, Fig. 2.4b shows that the near-surface geostrophic wind speed and large-scale subsidence are the most important CCFs for explaining the variability of cold pools in the entire ensemble: Cold pools are favored by stronger $|u_0|$ and weaker cloud-layer subsidence (stronger w_1 corresponds to weaker subsidence (Jansson et al., 2023)). Weaker but still significant correlations are observed for Γ and u_z: stronger free-tropospheric stability and horizontal (backward) wind shear lead to a smaller $\overline{f}_{cp}$.

The cold pool fraction f_{cp} depends on both the number and size of cold-pool objects within each cloud field. Therefore, we also conduct the same regression analysis on $\overline{n}_{cp}$, the mean number of cold pools, and $\overline{s}_{cp}$, the mean size of cold pools. Figures 2.4c and 2.4e show that the CCFs are also well capable of explaining the variations of $\overline{n}_{cp}$ and $\overline{s}_{cp}$ with R^2 values of 0.82 and 0.69, respectively. Also here both wind speed u_0 and subsidence w_1 emerge as the most significant CCFs for explaining the variability of $\overline{n}_{cp}$ and $\overline{s}_{cp}$, consistent with the results of $\overline{f}_{cp}$ (Figs. 2.4d, 2.4f). Furthermore, the influence of Γ on $\overline{f}_{cp}$ appears to be primarily driven by the response of $\overline{s}_{cp}$ to Γ, as $\overline{n}_{cp}$ does not exhibit any significant response to Γ (Figs. 2.4d, 2.4f). The response of our simulated cold pools to θ_{l0} and h_{q_t} seems to not be significant. In addition, we test the extent to which our results are sensitive to the definition of cold pools: the same multivariate regression based on cold pools being defined as where $h_{mix} < 400$ m ends up in almost identical results (Fig. S3.1).

What are the underlying mechanisms through which cold pools respond to wind speed $|u_0|$, large-scale subsidence w_1, and stability Γ? In small-domain LESs of non-precipitating cumulus fields, Nuijens and Stevens (2012) showed that increased wind speed $|u_0|$ leads to stronger surface latent and sensible heat fluxes promoting deeper and more active cumulus convection. The deepening response to increased wind speed $|u_0|$ is also consistent with observations of the trades (Nuijens et al., 2009). Despite a modest response of the boundary-layer depth to wind speed $|u_0|$ perturbations in small-domain LESs of precipitating cases (Bretherton et al., 2013), similar regression analyses as Eq. 5.10 show that, in the *Botany* ensemble, increased wind speed $|u_0|$ leads to deeper cloud fields that contain larger amount of liquid water (Figs. S2, S3).

Weaker subsidence (larger w_1) reduces both the large-scale heating and drying of the cloud layer, allowing deeper cloud layers, consistent with observations (Nuijens et al., 2009). Likewise, increased stability prevents the deepening of the boundary layer, thereby limiting the growth of cloud fields' depth (Bellon and Stevens, 2012, Fig. 3). These responses are also consistent in the *Botany* dataset: regression analyses of the entire ensemble show that both cloud-top height and liquid-water path increase in response to decreased subsidence and stability (Figs. S3.2, S3.3).

Deeper trade cumuli with larger liquid-water paths eventually generate more intense precipitation, also in observations (Nuijens et al., 2009). Observational studies in the trades further showed that larger cold pools are associated with more vigorous precipitation-driven downdrafts (Vogel et al., 2021; Zuidema et al., 2012). Therefore, our *Botany*-based results mirror observations: deepening of the boundary-layer cloudiness leads to larger cold pools.

Most of the results of the regression analyses are also consistent with observations of mesoscale cloud patterns in the trades: the so-called *Gravel* and *Flower* patterns are strongly favored by windy environments (Bony et al., 2020a; Schulz et al., 2021). These distinct patterns are also reported to consist of a large number of cold pools (Vogel et al., 2021). However, *Gravel* and *Flowers* patterns are associated with larger subsidence (Schulz et al., 2021), which contradicts our LES-based results. *Fish* patterns were not simulated (Jansson et al., 2023) as these mesoscale structures are too large (> 1000 km) to be captured

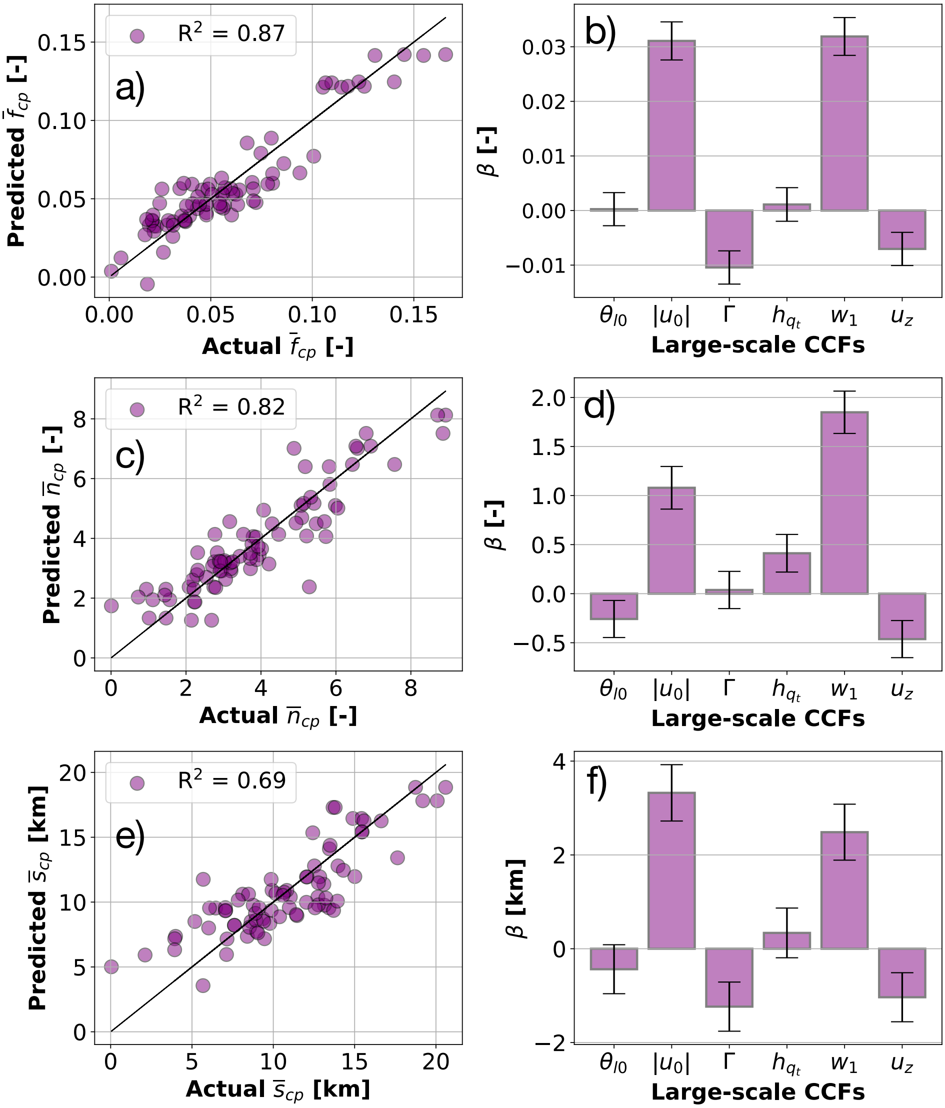

Figure 2.4: **Multivariate regression of CCFs to predict cold-pool statistics.** (a,c,e) The scatter plot of the results of multivariate regression analysis for $\overline{f}_{cp}$, $\overline{n}_{cp}$, and $\overline{s}_{cp}$ over the last two days of the *Botany* ensemble, where each purple circle stands for one simulation and the black line represents $y = x$. (b,d,f) The standardized beta coefficients (β) of the multiple regression analysis for predicting $\overline{f}_{cp}$, $\overline{n}_{cp}$, and $\overline{s}_{cp}$ as a function of *Botany*'s CCFs. Black error bars indicate the 95% confidence interval of each CCF. The greater the distance of the error bar from zero, the more significant the associated CCF in the regression model (smaller p-values). The p-values of the F-statistic test for all regression models are smaller than 10^{-17}.

in the simulation domains of the *Botany* simulations and stem from extra-tropical cold fronts that intrude into the trades (Schulz et al., 2021).

Therefore, theory, models, and observations, where available, confirm (i) the deepening of cloud fields in response to increased wind speed, decreased free-tropospheric stability, and decreased large-scale subsidence, and (ii) the increasing size of cold pools in response to this deepening.

2.3.2 THE DEPENDENCE OF COLD-POOL EVOLUTION ON THE DIURNAL CYCLE

Here, we investigate how the evolution of cold pools is modulated by the diurnal cycle (Fig. 2.1, link 2). Figure 2.5a shows the time series of the average cold-pool fraction of the entire *Botany* ensemble. As expected from the time series of clouds and rain (Fig. 2.2a), the dependence of cold pools on the diurnal cycle is clearly visible: there is a significantly larger cold-pool fraction during sunrise in comparison with sunset. This diurnality is due to the stronger radiative cooling during the nighttime that destabilizes the atmosphere, promoting stronger convection, more rain, and thereby more and larger cold pools. Despite the absence of diurnality in CCFs (e.g., subsidence, wind, sea-surface temperature) of the *Botany* simulations, it is noteworthy that these simulations featuring only diurnality in insolation can reproduce comparable evolution and range of variability in f_{cp} as reported in observations of the trades by Vogel et al. (2021).

To distinguish the cold-pool development forced by the daily cycle from any development due to pure self-organization, we select the central reference simulation (i.e., run 1 of the ensemble) which has the mean CCFs of the *Botany* hypercube, and conduct a simulation without diurnality in incoming solar radiation. To achieve this, we calculate the average solar radiation over 24 hours and determine the corresponding solar zenith angle. We then run DALES, keeping the zenith angle fixed at the calculated value (similar to Ruppert and Johnson (2016)), resulting in a simulation with the same total incoming solar radiation each day. This simulation is run over ten days, and its results are plotted in Fig. 2.5b.

Figure 2.5b still shows an intermittent behaviour in the time series of f_{cp}, even when the diurnality in insolation is absent. The fluctuations in fraction (Fig. 2.5b), number, and size (Fig. S3.4) of cold pools in the simulation without the diurnal cycle exhibit higher frequency but mostly with smaller amplitudes. The latter is due to the time-invariant shortwave radiative heating, constantly stabilizing the atmosphere, preventing clouds from getting as deep as nighttime, reducing the amplitude of cold-pool fluctuations. This is supported by the nighttime peaks in f_{cp}, which are about twice as large in the simulation with the diurnal cycle compared to the one without (Fig. 2.5b). This led us to ask: Why does the intermittent behaviour persist even in the simulation without the diurnal forcing? Answering this question sheds light on the dependence of cold pools on self-organizing mechanisms (Fig. 2.1, link 3).

2.3.3 THE DEPENDENCE OF COLD POOLS ON SELF-ORGANIZING MECHANISMS

As cold pools are the direct result of rain-evaporation-driven downdrafts, it is natural to expect a similar temporal behaviour of precipitation and other cloud properties that promote rain formation. Indeed, Fig. 2.6a shows that cloud fraction f_c, liquid-water path $\mathcal{L}$, and surface precipitation rate $\mathcal{P}$ (the latter two both conditioned on cloudy columns)

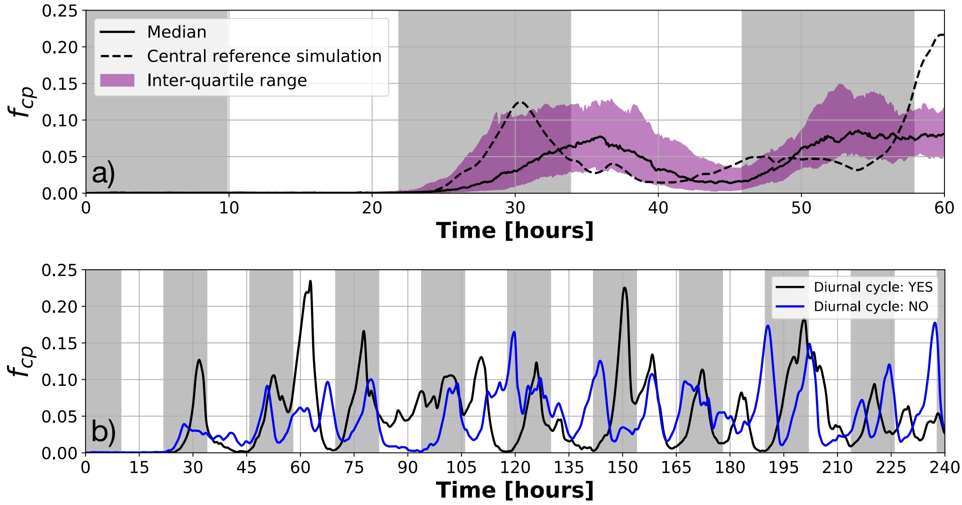

Figure 2.5: **Effect of the diurnal cycle on cold pools.** (a) The time series of the median f_{cp} (continuous line) accompanied by the interquartile range between the 25th and 75th percentiles of f_{cp} (purple shade) for the entire *Botany* ensemble. The f_{cp} time series of the central reference simulation is shown by the dashed line. (b) Time series of f_{cp} for the central reference simulation in the *Botany* dataset with (black) and without (blue) the diurnal cycle. Grey-shaded areas correspond to nighttime.

display a very similar intermittent behavior as the cold-pool fraction f_{cp}. This is further supported by Fig. 2.6b which shows strong correlations of the cloud field properties f_c, $\mathcal{L}$, and $\mathcal{P}$ with f_{cp} with lags of 0.5, 2.7, and 2.4 hours, respectively. These lag-correlations support the familiar sequence of events leading to cold pools: clouds grow deeper, increase their liquid-water content that promotes precipitation, leading to the formation of cold pools. The question now is what role cold pools play in driving this evolution.

Studies in deep convection (Haerter et al., 2019; Nissen and Haerter, 2021) showed that the interaction between cold pools through their collisions is an essential mechanism for the self-organization of deep convective cloud fields. Here, in our idealized simulation of trade cumulus, we hardly observe such interactions as the number and fraction of cold pools are too small for frequent collisions (Figs. 2.5b, S3.4). We speculate that this might be due to the structure of shallow mesoscale overturning circulations. Once these circulations aggregate cloud fields, their descending branches tend to separate the aggregated clouds from each other. Consequently, subsequent cold pools form far apart, preventing them from interacting with each other through collisions. This brings us to ask: what self-reinforcing feedback does govern the observed intermittent behaviour (Fig. 2.1, link 3)?

To answer this question, we suggest a mechanism through which cold pools play a role in the self-organization of the trade-cumulus cloud fields. Firstly, we begin by qualitatively describing these mechanisms using snapshots that depict the stages of a typical cold pool and its parent cloud's life cycle, referred to hereafter as the "cold-pool system"(sect. 2.3.3). We show these snapshots which, through visual inspection, are representative of nearly all cold pools forming in our simulation (Movie S1). Secondly, we offer statistical support for

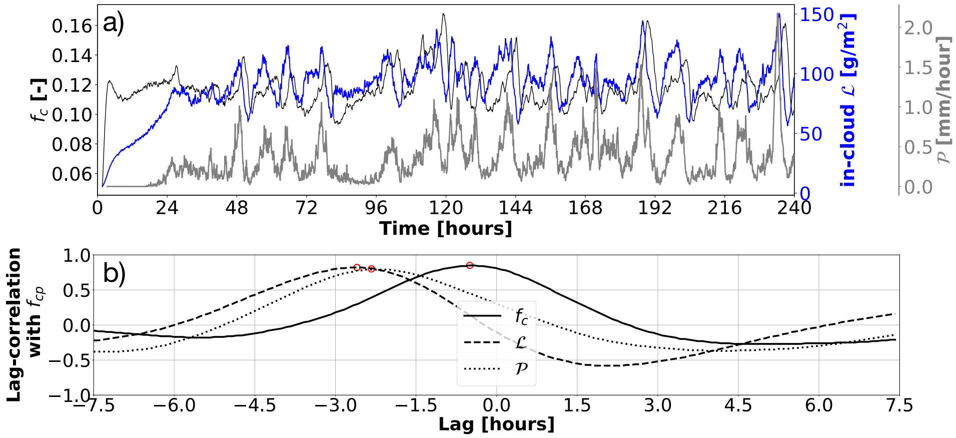

Figure 2.6: **Cloud-rain-cold-pool correlations.** (a) Time series of f_c, $\mathcal{L}$, and $\mathcal{P}$. (b) Lag-correlations of f_{cp} with f_c (continuous line), the in-cloud $\mathcal{L}$ (dashed line), and the in-rain $\mathcal{P}$. The highest correlations are marked by the red circle. The correlations are based on the last five days of the simulation without the diurnal cycle, during which the domain-mean total-water path has stabilized (Fig. S3.5).

the explained mechanisms throughout the simulation (sect. 2.3.3). Finally, we close this section by summarizing and discussing the points that are necessary to be considered in future research (sect. 2.3.3).

Three stages of self-organization of the cold-pool systems

Figure 2.7 shows the stages of the cold-pool system's life cycle, where we track one cold-pool system over hours 164-167 from both top and side views. This life cycle of the cold-pool system suggests a clear physical mechanism that governs the growth and decay of cold pools. Throughout the explanation of the life-cycle stages of cold pools below, we refer to the processes by numbers in the bold font that are also shown in Fig. 2.7.

Developing stage. Hour 164. During this developing stage, the cold-pool system (at $y \approx 80-90$ km) is relatively small in the horizontal (y direction) and displays self-reinforcing dynamics: precipitating downdrafts on the Southern part of the cold-pool system (**1**) suppress the mixed-layer height and induce a strong Northern outflow toward the boundary of the cold pool (**2**). Directly outside the cold pool, where the mixed layer still has a top close to the lifting condensation level (LCL), strong convergence of the outflow induces updrafts and the formation of active cumulus convection (**3**). These growing cumulus clouds appear to be pushed back into the cold-pool region by a strong convergence at the cloud base of the actively precipitating part of the system (**4**), where they reinforce the downdrafts through the precipitation that they produce. Finally, around the inversion at a height of 3 km, a region of strong divergence (an anvil outflow) can be observed (**5**).

Mature stage. Hour 165. At this stage, the cloud system has extended horizontally with the anvil outflow, partially covering the cold pool at $y \approx 79-95$ km (**5**). Underneath this outflow, a larger but also weaker precipitation band develops between $y \approx 80-90$ km, resulting in weaker downdrafts (**1**), a weaker surface outflow (**2**), and hence also a

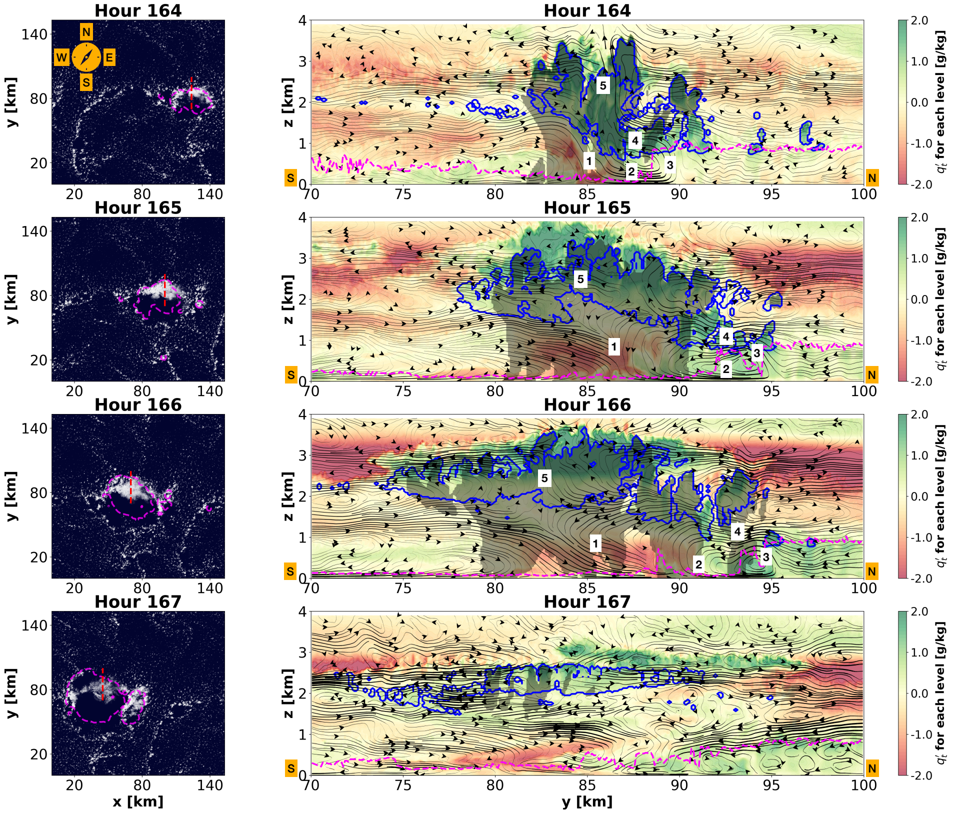

Figure 2.7: **Typical stages of the cold-pool system's life cycle.** The left column shows four contour plots of cloud albedo along with the cold-pool mask shown by the dashed, magenta contour lines for hours 164-167 of the simulation without the diurnal cycle. The right column shows y-z-cross-section contour plots of the total specific humidity anomalies associated with the dashed red line in snapshots shown in the left column. Cloud and rain boundaries are shown by the blue and grey contour lines. Circulations are made from the meridional (v) and vertical (w) velocity anomalies and are shown by black streamlines. To reduce the noise from the circulations, v, w are made from the medians of a 5-km window along the x dimension. The h_{mix} is shown by the dashed, magenta contour lines. The South (S), North (N), West (W), and East (E) directions are shown by orange labels.

weaker gust front with less vigorous updrafts into shallower cumulus clouds aloft (**3**). Yet, the connection with the cloudy updrafts at the gust front is still intact (**4**), such that the feedback from the developing stage remains sufficiently strong to sustain the system.

Decaying stage. Hours 166, 167. In the decaying stage (hour 166), the cloud extends further in the horizontal (**5**), mainly in the form of stratiform anvils. This leads to geometrically thinner clouds, which in turn contain less liquid water per cloudy column. Hence, the precipitation intensity reduces further (**1**), as do the diverging surface current (**2**) and the gust front (**3**), so that hardly any cumulus convection is formed on top of the updrafts (**4**). As a result, the moisture supply through the updrafts into the trailing anvils dwindles. The cold-pool system has now entered the decaying stage, after which at hour 167, the cloud object becomes thinner and vanishes quickly, leading to the presence of large clear-sky areas inside the cold-pool boundary (x-y cross-section).

Composite analysis of self-organization of the cold-pool system

To provide statistical support for the processes described above, we investigate the evolution of the most important parameters of all cold-pool systems that develop over the last five days of the simulation without the diurnal cycle. For clouds, we use the domain-mean liquid-water path $\mathcal{L}$ and cloud thickness h (both averaged over cloudy columns), and the average size of cloud objects L_c in the simulation domain. For precipitation, we use the in-rain domain-mean precipitation intensity $\mathcal{P}$ and the domain-mean size of precipitation cells L_p. For cold pools, we use the maximum near-surface horizontal velocity inside cold pools $u_{cp,max}$ to indicate the strength with which the cold pools diverge near the surface (see Fig. S3.6). In addition, we use $w_{P_{99.99}}$, the 99.99th percentile of the vertical velocity (at 200-m height) as an indication of the convergence strength at the gust front near the boundary of cold pools. We use this percentile because the width of the convergence area at the gust front is narrow, but features vigorous updrafts (see Fig. S3.6).

To highlight the evolution of the cold-pool system, we make a composite plot of the time series of all metrics mentioned above, i.e. $\mathcal{L}$, h, $u_{cp,max}$, $w_{P_{99.99}}$, L_c, and L_p during the last five days of the simulation without the diurnal cycle. To do so, we first find the corresponding time steps of the local minima of $\mathcal{P}$ time series. We find these local minima from the smoothed precipitation time series to avoid erroneously identifying very small noises as cold-pool events. As a result, for each cold-pool event i, we have a starting point t_i which is when precipitation starts, and an ending point t_{i+1} which is when precipitation stops. For each event i, we define a new time index

$$t^* = \frac{t - t_i}{t_{i+1} - t_i} \text{ where } t_i < t < t_{i+1}, \tag{2.2}$$

that ranges between 0 and 1. Since the length of cold-pool events may vary slightly throughout the simulation without a diurnal cycle, we linearly interpolate the time series of each event to ensure all cold-pool events have the same number of data points. Next, at each time step j in t^* for each cold-pool event i, we find the corresponding value C_{ij} of the metric $C \in \{\mathcal{L}, h, u_{cp,max}, w_{P_{99.99}}, L_c, L_p\}$ and calculate the mean of it for all cold-pool events by

$$\overline{C}_j = \frac{\sum_{i=1}^{N} C_{ij}}{N}, \tag{2.3}$$

where N is the total number of cold-pool events. We normalize the composited evolution of each metric $\overline{C}$ by their minimum and maximum as

$$\overline{C}_{j,\text{normalized}} = \frac{\overline{C}_j - \min(\overline{C})}{\max(\overline{C}) - \min(\overline{C})}. \tag{2.4}$$

Figs. 2.8a-c show the final normalized composited time series ($\overline{C}_{\text{normalized}}$). Figures 2.8a-c show that $\mathcal{P}$ features an almost symmetric evolution: it robustly increases during $0 < t^* < 0.45$, stabilizes during $0.45 < t^* < 0.65$, and robustly decreases during $0.65 < t^* < 1$. These time blocks respectively mark each stage of the life cycle of the cold-pool system described and visualized in sect. 2.3.3, i.e. *Developing*, *Mature*, and *Decaying*.

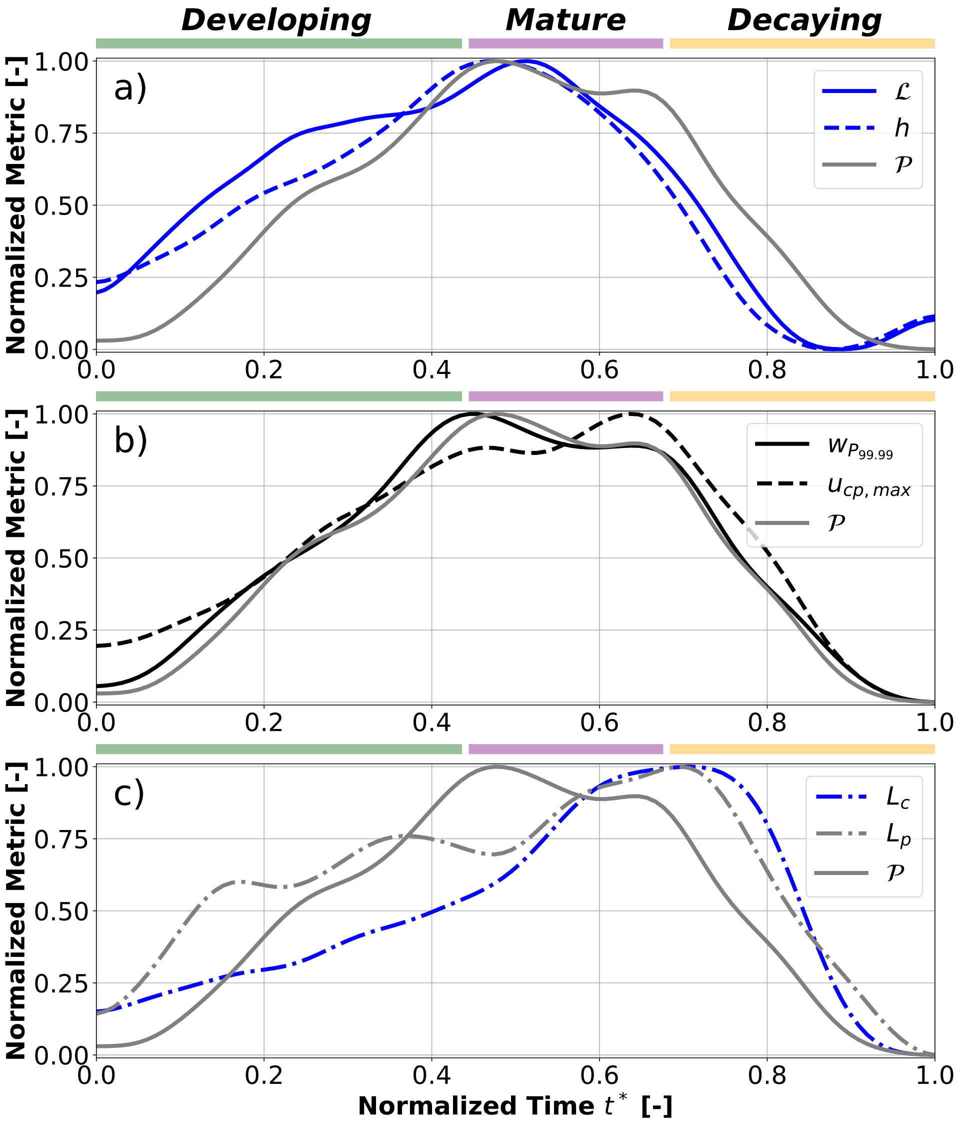

Figure 2.8: **Composite analysis of the evolution of the cold-pool system.** Composite time series of the evolution of the domain-mean precipitation intensity $\mathcal{P}$ with (a) the domain-mean liquid-water path $\mathcal{L}$ and cloud geometric thickness h, (b) maximum near-surface horizontal velocity at cold-pool areas $u_{cp,max}$ and the 99.99th percentile of vertical velocity $w_{P_{99.99}}$ at 200-m level, (c) domain-mean size of cloud objects L_c and precipitation cells L_p within the simulation domain for all life cycles of the cold-pool systems of the last five days of the simulation without the diurnal cycle. The stages of the cold-pool system *Developing, Mature, and Decaying* are marked by colors green, purple, and yellow, respectively. Composited time series were slightly smoothed using a Gaussian low-pass filter.

Figure 2.8a illustrates that at the beginning of the *Developing* stage ($t^* = 0$), clouds are already deep enough to start raining, which aligns with Fig. 2.6b. During this stage, Fig. 2.8b shows that as precipitation intensity $\mathcal{P}$ increases, the strength of the near-surface diverging outflows $u_{cp,max}$ and convergence at the cold-pool boundaries $w_{P_{99.99}}$ consistently increase. Simultaneously, clouds thicken, contain more liquid water (Fig. 2.8a), and the overall size of clouds and precipitation cells robustly increase (Fig. 2.8c). The growth of clouds both horizontally and vertically (Fig. 2.7, **4**,**5**), along with the increased precipitation downdrafts (Fig. 2.7, **1**), diverging outflows (Fig. 2.7, **2**), and converging updrafts (Fig. 2.7, **3**), are consistent with Fig. 2.7 (from hour 164) and imply the presence of circulations through which cold pools feed back to the parent clouds.

During the *Mature* stage, Fig. 2.8b shows that the time series of precipitation intensity $\mathcal{P}$, diverging outflows $u_{cp,max}$ and converging updrafts $w_{P_{99.99}}$ are quite stable. Figures 2.8a,c indicate that while clouds begin to shrink vertically ($t^* \approx 0.55$), as shown by a decrease in $\mathcal{L}$ and h, they expand horizontally, as shown by an increase in L_c. This is an indication of the formation of stratiform anvils that are vertically thin but horizontally large. Figure 2.8c further highlights that the size of precipitation cells L_p is also growing alongside the size of clouds. This means that the same amount of rain evaporation must be occurring over a larger region, which reduces the potential for the cold pool to drive the system. Formation of stratiform anvils during this *Mature* stage is consistent with the development of the cold-pool system shown in Fig. 2.7: from hour 164 to hour 165, both the width of the cloud and rain cells increase, while the average vertical thickness of the cloud decreases (Fig. 2.7, **5**).

Time series in Figs. 2.8a-c show that once clouds and precipitation cells reach their maximum size, the starting time of the *Decaying* stage is set; i.e. once stratiform anvils form, they lead to precipitation with larger cells L_p but weaker intensity $\mathcal{P}$, consistent with Fig. 2.7(**1**, during hours 164-166). As a result, Fig. 2.8b shows that the near-surface diverging outflows at cold pools $u_{cp,max}$ (Fig. 2.7, **2**) and the convergence at the cold-pool fronts $w_{P_{99.99}}$ (Fig. 2.7, **3**) get robustly weaker during the *Decaying* stage, such that they can hardly trigger formation of new clouds at LCL (Fig. 2.7, **4**, hour 166), consistent with what Fig. 2.7(hour 166) illustrates. Note that during the *Decaying* stage, the size of both clouds L_c and precipitation cells L_p drop quite fast (Fig. 2.8c) once $w_{P_{99.99}}$ reduces sufficiently, implying the quick disappearance of stratiform anvils after they detach from their convergence roots, as shown in Fig. 2.7(hour 167).

DISCUSSION AND OUTLOOK

In essence, the preceding analysis suggests that the role cold pools play in the trade-cumulus self-organization is through what we will call "shallow squall-line" dynamics. Thinking of the trade-cumulus cold-pool systems as squall lines has precedence in the analysis of mesoscale cloud rings without stratiform tops, visible in the so-called *Gravel* fields (Li et al., 2014). Yet, our findings suggest that the dynamics on a single cold pool edge also underlie the formation of the large anvils frequently found atop more clustered cloud systems. This resonates with the findings of Dauhut et al. (2023), who illustrated similar processes, though for a single case study, as in Fig. 2.7 and proposed that the so-called *Flowers* are shallow mesoscale convective systems. In fact, our results indicate that most cold pool systems in the trades develop through similar shallow squall-line dynamics, with only some growing as large as the case on Feb 2nd, 2020 (Narenpitak et al., 2021), and only some developing anvil clouds.

The difference between patterns with and without anvils might be related to inversion strength. In fields of *Flowers*, the inversion is strong (Bony et al., 2020a, Fig. 2), such that strong cold-pool-induced convection leads to large stratiform outflows when they impinge on the inversion. Another possibility is that the cloud-to-rain droplet auto-conversion is less efficient in *Flower* patterns, as shown by Radtke et al. (2023). For the same amount of cloud water content, this gives *Gravel* fields a larger number of precipitation cells compared to *Flowers*. In turn, *Gravel* features a larger number of cold pools (Vogel et al., 2021, Fig. 7a), which gives room for cold pools to collide with each other, triggering the formation of new clouds at their collision point (Nissen and Haerter, 2021). In *Flowers*, and in our simulation ensemble, such interactions are rare, as cold pools frequently form quite far from each other. Future studies might attempt to distinguish these regimes and mechanisms in more detail, including how microphysical properties affect cold pools and their interactions with clouds.

We hypothesize that the updrafts being sheared and pushed back to the parent clouds at the cloud-base height (orange arrow in Fig. 2.11) is due to a pressure gradient from the cold-pool front, where high pressure is induced by mechanically-driven updrafts, to the inside of cold pools, where evaporative downdrafts lead to lower pressures. This causes the updraft to deflect towards the cold-pool area at the cloud base. The sheared updrafts at the boundary of our shallow squall lines resemble those in deep mesoscale convective systems (Rotunno et al., 1988; Stensrud et al., 2005; Weisman and Rotunno, 2004). These cold-pool-induced circulations can reinforce their parent clouds if their induced wind shear is twice that of the ambient environment (Li et al., 2014, Fig. 15c). In addition, according to Li et al. (2014), we expect a “downwind triggering”, given our zonal wind is westward and features forward shear in the sub-cloud layer, resulting from the interplay between ambient environmental shear and cold-pool-induced shear. Although our simulations feature zero meridional geostrophic wind (south-north direction), we consistently observe triggering on the northern side of cold pools. Hence, further investigating the interaction between cold-pool-induced and environmental shear might help understand the causality of this cloud-cold-pool coupling, which we defer to future studies.

2.3.4 IMPLICATIONS FOR MESOSCALE CLOUD ORGANIZATION AND RADIATIVE EFFECT

Considering our conceptual picture (Fig. 2.1), we have shown how cold pools respond to CCFs (Fig. 2.1, link 1; sect. 2.3.1) and the diurnal cycle of radiation (Fig. 2.1, link 2; sect. 2.3.2). Keeping these CCFs time-invariant, we suggested that the cold pools organize trade-cumulus fields through shallow squall-line dynamics, which drives the self organization of cold-pool systems (Fig. 2.1, link 3; sect. 2.3.3). Here, we want to understand (i) how these self-organizing mechanisms manifest themselves as 2D cloud patterns (sect. 2.3.4), and (ii) whether and how they matter for trade-cumulus radiative effect (Fig. 2.1, link 4; sect. 2.3.4).

DEPENDENCE OF MESOSCALE ORGANIZATION ON COLD POOLS

To investigate the spatial organization of cloud fields throughout the cold-pool systems' life cycles, we use the average cloud size L_c and calculate the open-sky fraction L_o, the mean fraction of cloud-free areas in the simulation domain. These metrics effectively capture the mesoscale organization variability, in observations (Janssens et al., 2021) and in the *Botany* ensemble (Janssens, 2023a, chapter 7). Figure 2.9a shows the time series of these metrics over the ten-day period of the central reference simulation without the diurnal cycle: L_c grows fast during the first 24 hours of the simulation, when clouds are non-precipitating. This marks phase 1 from Fig. 2.1, where convergent moist areas with non-precipitating cumulus convection and divergent dry areas with less cumuli grow together. This phase is broken by rain and cold-pool formation around hour 24, after which the cloud scale L_c does not grow anymore but shows an intermittent behavior, comparable to the cold-pool fraction f_{cp} (Fig. 2.1, Option iii). This intermittency is also present in the time series of the open-sky fraction L_o. Figure 2.9b shows that L_c has a maximum correlation with f_{cp} with a lag of ≈ -1 hour, while L_o has its maximum correlation with a lag of ≈ +1 hour, consistent with the cold-pool systems' life cycle (Figs. 2.7,2.8): during both the *Developing* and *Mature* stages, the size of clouds L_c and cold pools f_{cp} grow until stratiform anvils form, which marks the beginning of the *Decaying* stage, during which the remaining anvils shrink in size, after which cold pools start to dwindle, raising the open-sky fraction L_o (Fig. 2.9c).

According to (Janssens et al., 2021, Fig. 3a); (Janssens, 2023a, Fig. 7.1a), L_c and L_o provide complementary information about shallow cumulus organization and, in combination, can explain most of the variability in organization observed in the trades. Figure 2.9d shows how the $L_c - L_o$ relationship evolves throughout one cold-pool cycle. Interestingly, our cross-correlation analysis in Figs. 2.9b,e shows that L_c and L_o are tightly lag-correlated, even though they are independent. This suggests that precipitating trade-cumulus organization can be captured by two dimensions: (i) one spatial organization or process-related metric, which can be one of f_c, $\mathcal{L}$, h, $\mathcal{P}$, f_{cp}, L_c, and L_o and (ii) one temporal organization metric, which measures the lag between, for instance, L_c and L_o; or equivalently how fast the first dimension evolves through one cold-pool system's life cycle.

Dependence of cloud-radiative effect on cold pools

Mesoscale organization affects the trade-cumulus radiative effect through variations in cloud cover f_c (Bony et al., 2020a) and optical thickness τ_c (Alinaghi et al., 2024a; Denby, 2023). So, since cold pools affect cloud organization (Fig. 2.9), we expect cold pools to affect CRE. To investigate this , we perform the same composite analysis of sect. 2.3.3 and Fig. 2.8 for the domain-mean CRE, f_c, and $\mathcal{L}$. In the *Botany* simulations, the cloud-droplet number concentration is fixed, so the variations in τ_c are fully determined by the variations in $\mathcal{L}$.

As a result, Fig. 2.10a highlights that during the *Developing* stage of the cold-pool systems, CRE gets stronger and reaches its maximum value once the system is in its *Mature* stage. During this stage when stratiform anvils are forming, f_c increases, while $\mathcal{L}$ decreases, which leads to CRE remaining stable at its maximum value. During the *Decaying* stage, cold-pool dynamics get weak and anvils vanish, leading to a decrease of f_c, $\mathcal{L}$, and therefore CRE. Our analysis demonstrates that cold pools influence CRE by modulating cloudiness both horizontally and vertically, as captured by f_c and $\mathcal{L}$. Furthermore, this analysis reveals that f_c and $\mathcal{L}$ evolve differently over the various stages of the cold pool system's life cycle. Therefore, to accurately assess the impact of cold pools on cloudiness, sampling at a single moment is insufficient. Instead, it is necessary to sample, e.g. by averaging, over all stages of cold-pool systems' life cycle.

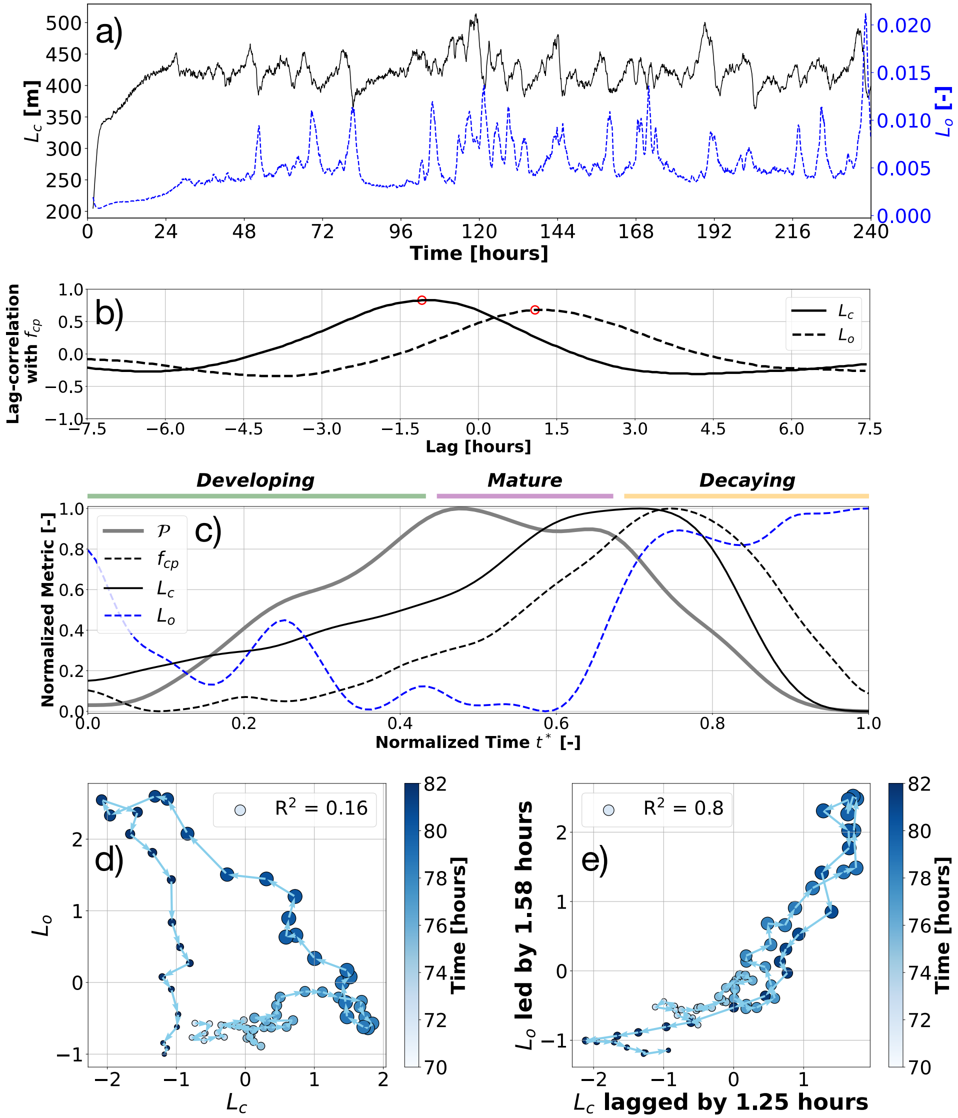

Figure 2.9: **Cold-pool-mesoscale organization relationships.** (a) Time series of L_c and L_o. (b) Lag-correlations of f_{cp} with L_c and L_o, with red circles showing the best correlations. (c) Similar composite analysis to Fig. 2.8 for $\mathcal{P}, f_{cp}, L_c$, and L_o of the simulation without the diurnal cycle. (d) The evolution of the standardized L_c and L_o (concerning their mean and standard deviations) through one cold pool's life cycle (hours 70-82). (e) The same relationship as (d) but with lags with respect to f_{cp} time series. The size of each circle in both plots is scaled by the value of f_{cp} at the corresponding time step. The correlations are based on the last five days of the simulation without the diurnal cycle.

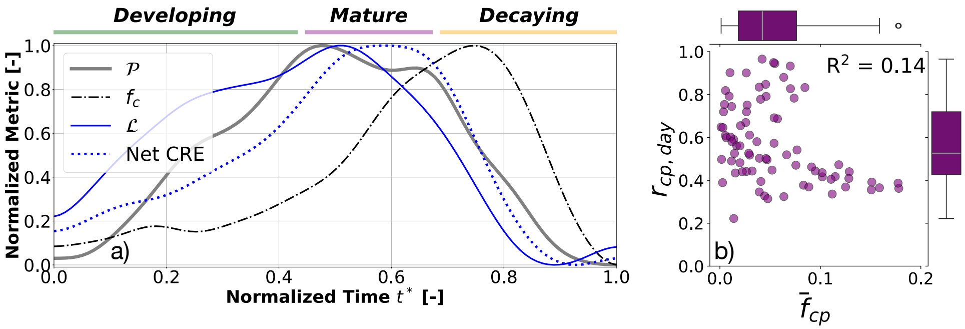

Figure 2.10: **Dependence of cloud-radiative effect on cold pools.** (a) Similar composite analysis to Fig. 2.8 for $\mathcal{P}, f_c, \mathcal{L}$, and net CRE (shortwave SW + longwave LW) of the simulation without the diurnal cycle. (b) The 2D scatter plot of the daily mean cold-pool fraction $\overline{f}_{cp}$ and the fraction of daytime contribution to this mean $r_{cp,day}$ quantified by Eq. 2.5 for the entire *Botany* ensemble.

Averaging over the daily time scale, along with the influence of the diurnal cycle, may lead to more intricate cold-pool-CRE relationships. Specifically, cold-pool events occurring at night contribute to the daily mean cold-pool fraction but do not affect shortwave radiative effects, which, by definition, only occur during the daytime (Fig. S3.7). This prompted us to ask the following questions: How frequently do cold pools occur during daytime? and, given the same daily mean cold-pool fraction, to what extent does the timing of cold pools influence their impact on CRE?

To answer these questions, we employ the data from the entire *Botany* ensemble and first introduce the metric $r_{cp,day}$

$$r_{cp,day} = \frac{\sum_{t=34}^{46} f_{cp,t}}{\sum_{t=22}^{46} f_{cp,t}} \tag{2.5}$$

where $\sum_{t=34}^{46} f_{cp,t}$ and $\sum_{t=22}^{46} f_{cp,t}$ are the sums of cold-pool fraction over the daytime (34-46 hrs) and the entire second day (22-46 hrs), respectively. Thus, $r_{cp,day}$ measures the daytime contribution of cold-pool events to the daily mean cold-pool fraction $\overline{f}_{cp}$ averaged over hours 22-46. Figure 2.10b shows $r_{cp,day} \approx 0.5$. This is consistent with Fig. 2.5a and with the fact that simulated cold pools tend to form during the night and peak slightly after sunrise. Fig. 2.10b further illustrates that while simulations with large $\overline{f}_{cp}$ ($\overline{f}_{cp} > 0.1$) feature similar $r_{cp,day}$ of around 0.4, there is significantly more variability in $r_{cp,day}$ ($\approx 0.2 - 1$) for simulations with relatively small $\overline{f}_{cp}$ ($0 < \overline{f}_{cp} < 0.1$): across the entire ensemble, $r_{cp,day}$ and $\overline{f}_{cp}$ are not strongly correlated (see also Fig. S3.8).

Therefore, both the factors that control the total cold-pool occurrence over a day ($\overline{f}_{cp}$) and those that control the relative distribution of f_{cp} between day and night ($r_{cp,day}$) have the potential to independently affect the CRE. Yet, we cannot quantify this effect here, e.g. through multivariate regression across the entire *Botany* ensemble, because the imposed variability in large-scale CCFs across the ensemble control variability both in the cold pools (as shown in sect. 2.3.1) and in the daily mean CRE (Janssens, 2023a; Janssens et al., 2025). Therefore, the relationship between daily mean cold-pool fraction and CRE across *Botany* is significantly confounded by CCFs. For example, the strength of imposed near-surface geostrophic wind $|u_0|$ appears to strongly control both cold-pool fraction (Fig. 2.4) and CRE (Janssens et al., 2025). Conversely, free-tropospheric humidity h_{q_t} relates strongly to CRE, but not to cold pools. Hence, to truly determine whether cold pools and their diurnal timing, independent of CCFs, affect the CRE, we are currently conducting a study to investigate how removing cold pools (Böing et al., 2012) affects CRE and its response to CCFs across the *Botany* ensemble.

2.4 SUMMARY

Observed covariations between cold pools and mesoscale organization (Vogel et al., 2021) suggest a potential impact of cold pools on radiative effects of clouds forming in the trade-wind regime. This led us to start this paper by asking three questions: (i) to what extent are cold pools controlled by the large-scale cloud-controlling factors (CCFs) (Fig. 2.1, link 1) and the diurnal cycle of insolation (Fig. 2.1, link 2)?; (ii) through what underlying mechanisms do trade-cumulus cold pools evolve and interact with clouds (Fig. 2.1, link 3)?; and (iii) what implications do these mechanisms have for mesoscale organization and cloud-radiative effect (Fig. 2.1, link 4)?

To answer question (i), we employed an ensemble of high-resolution LES simulations, *Cloud Botany* (Jansson et al., 2023), and showed that cold pools are largely regulated by CCFs (Fig. 2.4a). More specifically, cold pools are more frequent and larger in environments with stronger geostrophic wind speeds and weaker large-scale subsidence in the cloud layer (Fig. 2.4b). In addition, cold-pool evolution is tightly synced with the diurnality in incoming solar radiation (Fig. 2.5a).

To answer question (ii), we removed the diurnality in the insolation and found that cold pools show an intermittent behavior (Figs. 2.5b, 2.6), which is driven by a complex interaction between clouds and cold pools. We find that this interaction expresses itself through shallow squall lines, whose evolution we summarise in the conceptual Fig. 2.11. It is composed of precipitating downdrafts (blue arrows), near-surface diverging outflows (magenta arrows), and converging updrafts at cold-pool gust fronts (red arrows), which reinforce the parent clouds (Figs. 2.7, 2.8, and Fig. 2.11, orange arrows). This shallow mesoscale convective system develops and reaches a mature phase until stratiform anvils form, leading to stratiform precipitation, weakening the downdrafts, diverging outflows, and converging cold-pool-induced updrafts (Fig. 2.11, central panel), until they hardly trigger formation of new clouds, and the system decays (Fig. 2.8, and Fig. 2.11, right panel).

Finally, to answer question (iii), we quantified that cold pools affect mesoscale cloud organization by modulating the length scale and the open-sky fraction (Fig. 2.9). In the end, we showed that cold pools increase CRE once shallow squall lines are developing, until the point at which stratiform anvils form, when CRE stabilizes and reaches its maximum. Afterwards, the stratiform precipitation and the resulting decay in squall lines lead to a decrease in CRE (Fig. 2.10a). Moreover, we showed that the CRE dependence on cold pools is more complex when the diurnal cycle is present: to affect CRE, cold-pool events must occur during the day (Fig. 2.10b). This means that the synchronization of cold pools with the diurnal cycle of insolation affects the extent to which CRE is regulated by cold pools. Note that, unlike our idealized simulations, the diurnality in the trades is profound in the most important CCFs, i.e., wind speed and stability (Vial et al., 2021). Given the strong

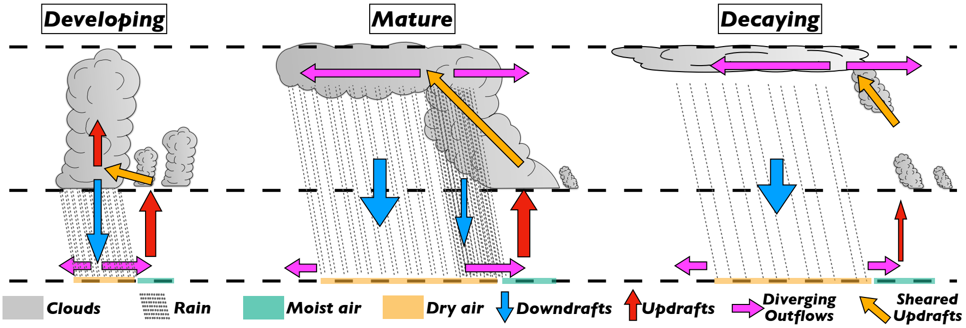

Figure 2.11: **Conceptual schematic of the cold-pool system.** Schematic of the cold-pool system evolution during the *Developing*, *Mature*, and *Decaying* stages as shown in sect. 2.3.3 under Figs. 2.7, 2.8.

dependence of cold pools on these CCFs (Fig. 2.4), investigating (i) how fast mesoscale cold pools adjust to these CCFs, and (ii) how synchronous this adjustment is with the diurnal cycle of insolation might improve our understanding of the effect of mesoscales on trade-cumulus feedback.

Last but not least, despite the efforts made within this study, we still face the question of whether cold pools, as a self-organizing process at the mesoscales, affect cloudiness independently of large scales (Janssens, 2023a; Janssens et al., 2025). We are currently working on addressing this question in our next study.

OPEN RESEARCH

The *Cloud Botany* dataset is accessible through the EUREC^{4}A intake catalog (https://howto.eurec4a.eu/botany_dales.html). The data is analyzed using Python (libraries: Numpy Harris et al. (2020), Xarray Hoyer and Joseph (2017), Pandas Wes McKinney (2010), Scipy Virtanen et al. (2020), Matplotlib Hunter (2007), Statsmodel Seabold and Perktold (2010), and Seaborn Waskom (2021)).

2.5 Supplementary Information

This file includes and represents figures, one movie, and detailed explanations about some cloud-field properties to additionally support the text.

Figures

Cloud-field properties

Within the paper, we use couple of cloud-field properties. Below, we elaborate on the details of calculating those parameters:

- **Cloudy columns** are defined where the liquid-water path $\mathcal{L}$ is larger than 0. Note that in DALES, $\mathcal{L}$ only contains the cloud-water specific humidity and does not contain rain water.

- **Geometric thickness** of clouds h is calculated from the 3D fields of liquid-water specific humidity q_l at each time step of the model outputs. We first identify a cloud mask in 3D by $q_l > 0$. Next, for each cloudy column, we sum up the vertical size of grid cells that are identified as cloudy. With this we get a 2D map of cloud geometric thickness. Next, we compute the domain-mean h by averaging over the cloudy columns.

- **Cloud organization metrics** such as domain-mean size of cloud objects L_c and the mean fraction of the open-sky areas L_o are calculated following Janssens et al. (2021) and the “cloudmetrics” github repository (webpage: https://github.com/cloudsci/cloudmetrics).

- **The domain-mean size of the rain cells** are defined based on the rain-water path $\mathcal{R}$ fields. The rain mask is defined where $\mathcal{R} > 1$ g/m^2. The size of rain cells are then computed similar to the size of cold pools and clouds.

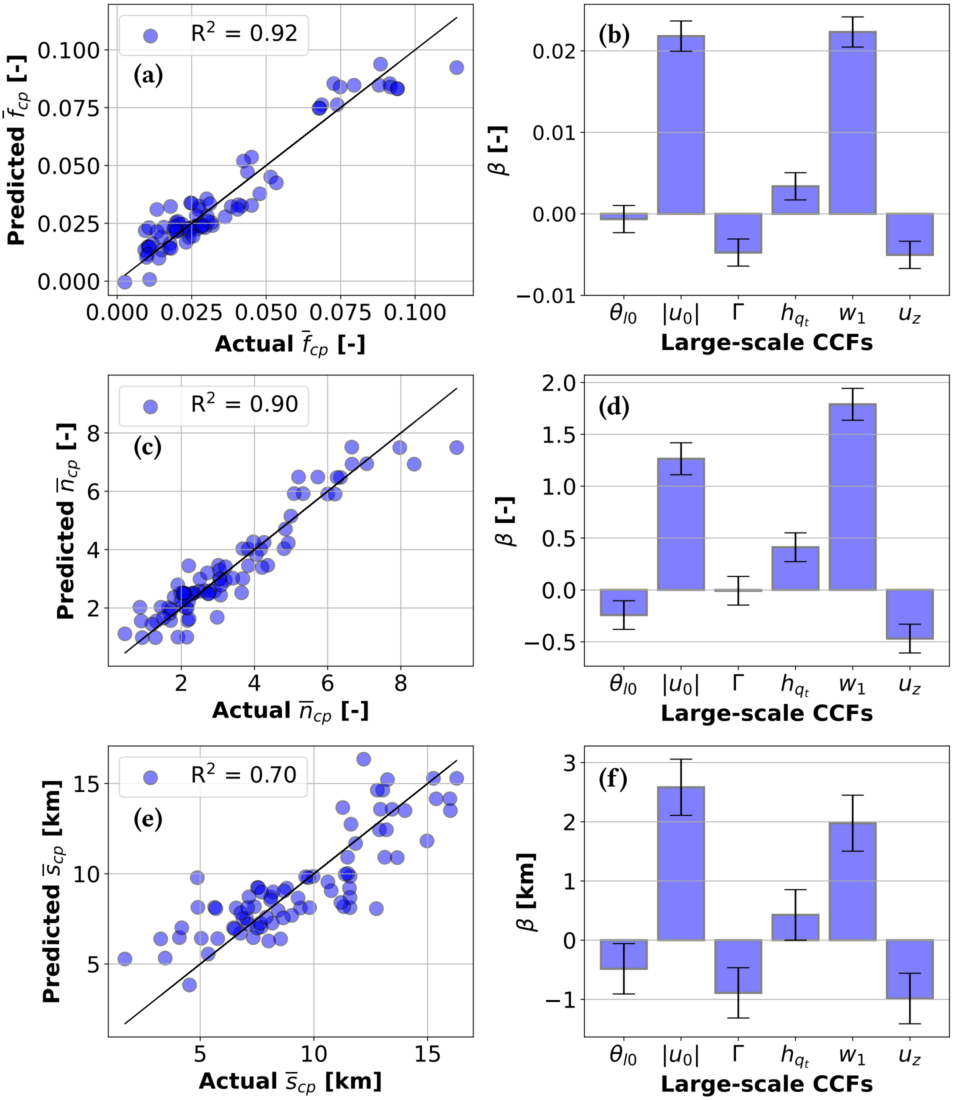

Figure S2.1: **Multivariate regression of CCFs to predict cold-pool statistics.** This plots is as same as the first figure of the results of section 3.1, but for cold pools being defined where $h_{mix} < 400$ m. Comparing two figures with each other, the number of cold pools and their response to CCFs are exactly the same. This analysis further shows that the definition ($h_{mix} < 400$ m) seems a bit stricter compared to our definition, which leads to cold pools being approximately 20% smaller. However, this does not affect the response of cold-pool sizes and fractions to CCFs; i.e., the relative significance of CCFs for cold-pool properties remains the same.

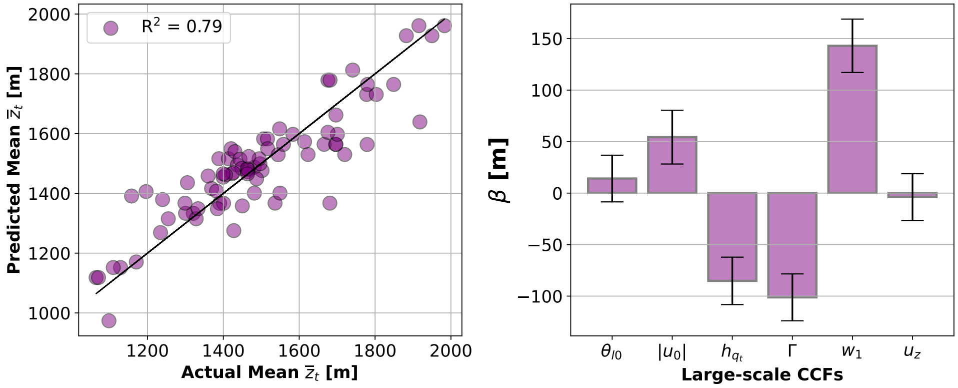

Figure S2.2: **Multivariate regression results of cloud-top height $\overline{z}_t$.** (a) The scatter plot of the results of multivariate regression analysis. (b) The standardized beta coefficients of the multiple regression analysis for predicting the domain-mean cloud-top height (z_t) as a function of large-scale CCFs of *Botany* simulations.

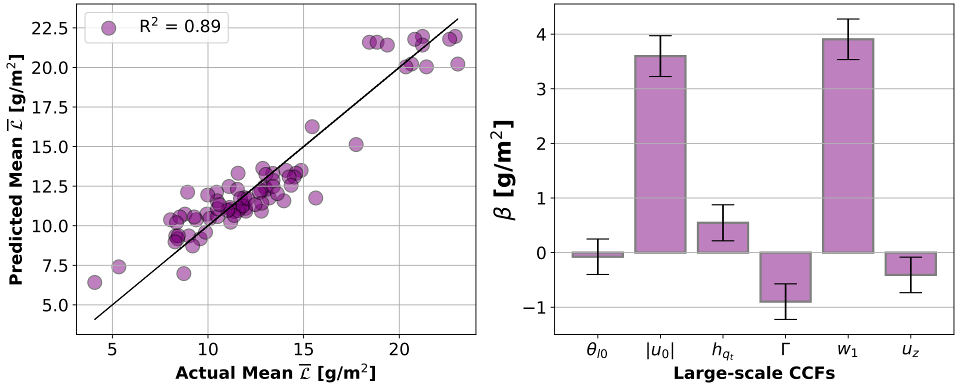

Figure S2.3: **Multivariate regression results of the liquid-water path $\overline{\mathcal{L}}$.** (a) The scatter plot of the results of multivariate regression analysis. (b) The standardized beta coefficients of the multiple regression analysis for predicting the domain-mean $\mathcal{L}$ as a function of large-scale CCFs of *Botany* simulations.

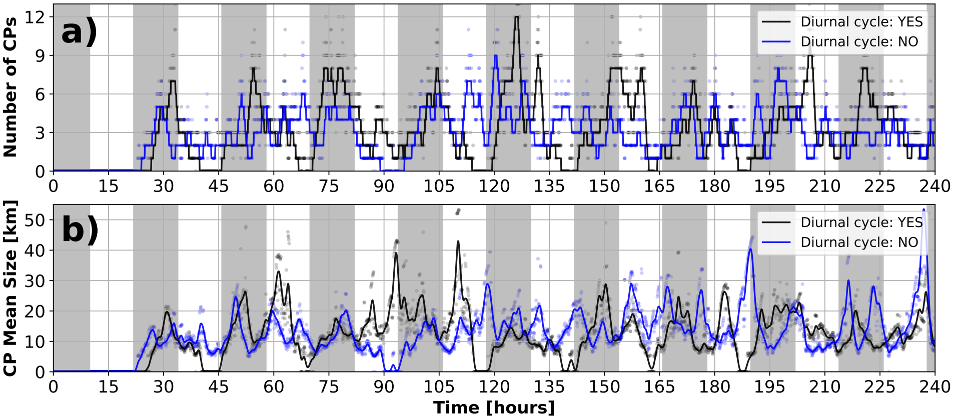

Figure S2.4: **Time series of cold-pool statistics including number and size.** Time series of (a) the number of cold-pool objects, and (b) the average size of cold-pool objects for the center run in the *Botany* dataset. These two metrics are only calculated for cold-pool objects featuring an area larger than 25 km^2. Due to this threshold, the time series of these two metrics are a bit noisy. To better see the signal, the noise in the scatter plot is filtered out in the line plot. The black (blue) line stands for the run with (without) the diurnal cycle. Grey-shaded areas correspond to nighttime.

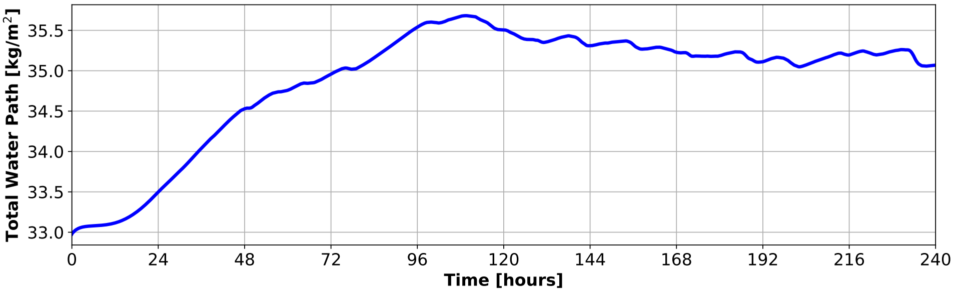

Figure S2.5: **Time series of domain-averaged total water path.**

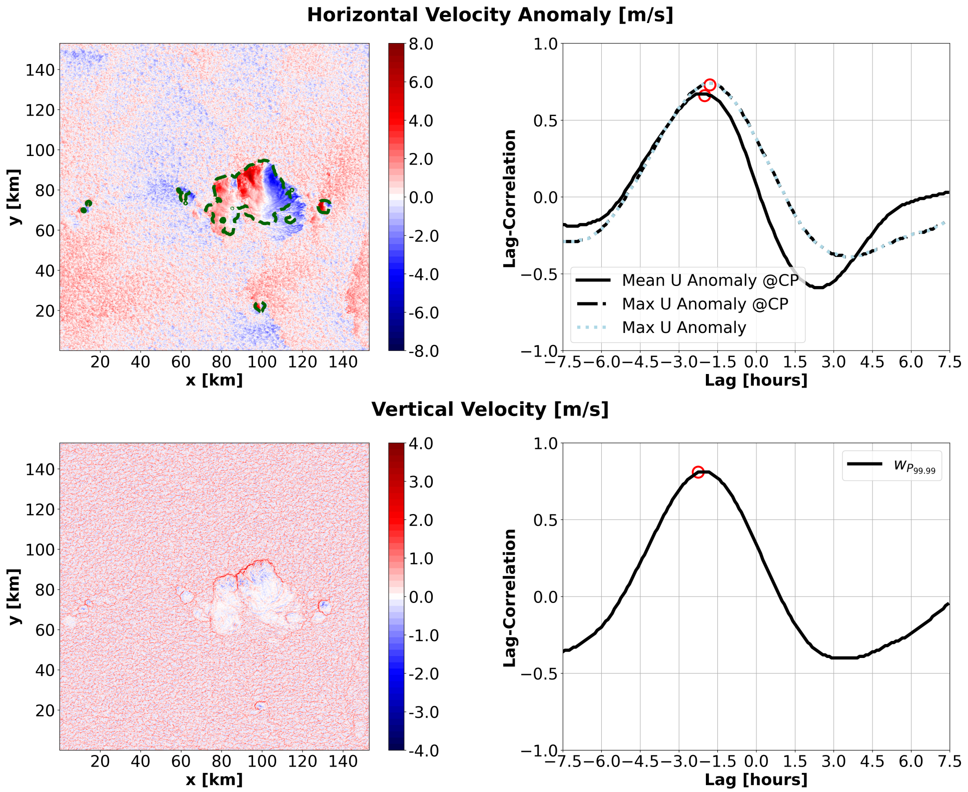

Figure S2.6: **Effect of cold pools on the sub-cloud layer in space and time. Contour plots** of: horizontal velocity (U) anomaly near the surface, and vertical velocity (w) at the 200-m level at hour 165 of the center simulation without the diurnal cycle. The cold-pool mask is shown by the green dashed contour line. **Cross-correlations** during the last five days: f_{cp} with mean and maximum horizontal velocity anomalies at cold pools, and f_{cp} with $w_{P_{99.99}}$ (99.99 th percentile of w). The red circles in the lag-correlations show where the correlation reaches its maximum absolute value. **Message of the figure:** This figure highlights that the dynamic properties of cold pools such as diverging outflows (as measures by the horizontal velocity anomalies) and the resulting convergence at their gust fronts (as measured by $w_{P_{99.99}}$) already reach their maximum values before cold pools reaching their maximum size as measured by f_{cp}.

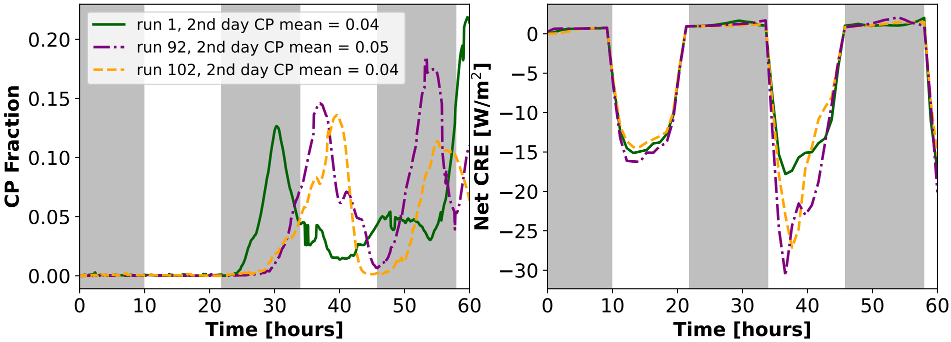

Figure S2.7: **Examples showing the importance of the timing of cold pools for their effect on CRE.** (a) Time series of f_{cp} for simulations 1, 92, and 102 of the *Botany* ensemble with the diurnal cycle. (b) Time series of the net CRE for the same simulations as in (a), with more negative values implying more cooling. Note that the magnitude of LW CRE is much smaller compared to that of SW CRE in our simulations as our focus is on shallow clouds.

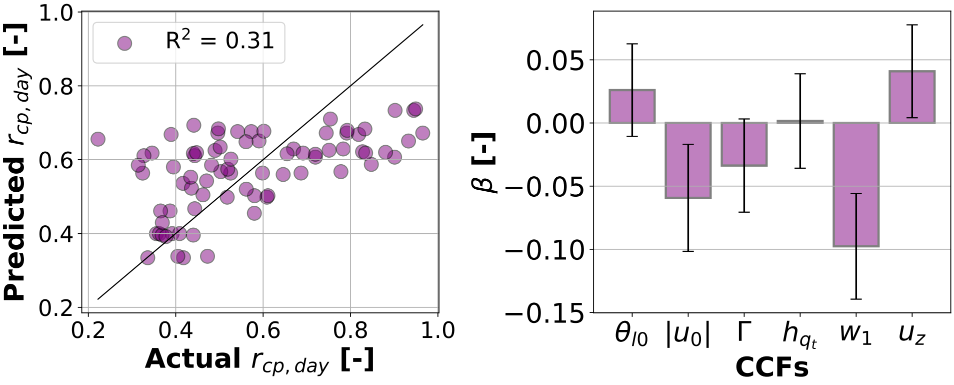

Figure S2.8: **Dependence of the cold-pools' daytime contribution to the daily mean cold-pool fraction $r_{cp,day}$ on cloud-controlling factors CCFs.** This plot shows the multivariate regression analysis for quantifying the extent to which $r_{cp,day}$ is controlled by CCFs. The results of this figure show that this metric is not fully controlled by CCFs, consistent with the scatter plot shown in Fig. 10b.

3

COLD POOLS MEDIATE MESOSCALE ADJUSTMENTS OF TRADE-CUMULUS FIELDS TO CHANGES IN CLOUD-DROPLET NUMBER CONCENTRATION

This chapter is published as *Alinaghi, P., Jansson, F., Blázquez, D. A., & Glassmeier, F. (2025). Cold pools mediate mesoscale adjustments of trade-cumulus fields to changes in cloud droplet number concentration. Atmospheric Chemistry and Physics, 25(12), 6121–6139. https://doi.org/10.5194/acp-25-6121-2025.*

Abstract

The mesoscale self-organization of trade-cumulus cloud fields is a major cloud-climate uncertainty. Cold pools, i.e. pockets of cold, dense air resulting from rain evaporation, are a key mechanism in shaping these dynamics and are controlled by the large-scale forcing. We study the microphysical sensitivity of cloud-field self-organization through cold pools by varying cloud-droplet number concentration N_c *from 20 to 1000* $/cm^3$ *in large-eddy simulations on large* $154 \times 154\ km^2$*-domains. We find that cold pools exhibit two distinct regimes of mesoscale self-organization. In very low* N_c*-conditions, cold pools transition from a stage where they are small and randomly distributed to forming large, long-lived structures that perpetuate due to the collisions of cold pools at their fronts. Under high-*N_c *conditions, cold pools display strongly intermittent behaviour and interact with clouds through small, short-lived structures. While* N_c *thus influences the number of cold pools and, in turn, mesoscale organization, cloud depth, and cloud albedo, we find its effect on cloud cover to be minimal. Comparing the microphysical sensitivity of cold-pool-mediated mesoscale dynamics to the external, large-scale forcing shows that* N_c *is as important as horizontal wind and large-scale subsidence for trade-cumulus albedo. Our results highlight that cold pools mediate adjustments of trade-cumulus cloud fields to changes in* N_c*. Such mesoscale adjustments need to be considered if we are to better constrain the effective aerosol forcing and cloud feedback in the trade-wind regime.*

3.1 INTRODUCTION

CLOUDS play a crucial role in the climate system by modulating the Earth's energy budget through their interactions with radiation. Their net effect is to cool the planet by reflecting incoming solar radiation back into space (Stephens et al., 2012). Clouds are one of the most important sources of uncertainty in climate projections. Firstly, the cloud feedback is the most uncertain feedback to the anthropogenic forcing of the climate system, which is mainly due to the uncertain response of shallow clouds to climate change (IPCC AR6, 2023; Nuijens and Siebesma, 2019; Schneider et al., 2017). Secondly, the complex interactions between clouds and aerosols lead to the process uncertainty that makes the effective radiative forcing due to aerosol-cloud interactions the most uncertain forcing in the climate system (Bellouin et al., 2020; IPCC AR6, 2023).

Aerosol perturbations change the concentration of cloud-condensation nuclei and in turn cloud-droplet number concentrations N_c. Assuming a fixed cloud-liquid-water path, increased N_c results in a larger number of smaller cloud droplets, leading to a larger surface area to interact with radiation, and in turn increased cloud-optical depth and cloud albedo, known as the *Twomey* effect (Twomey, 1977). In addition to this quasi-immediate effect that can be considered to occur on the spatiotemporal scales of individual cloud parcels, changes in N_c can also propagate to larger scales. On the single-cloud scale, increased N_c reduces the efficiency of collision-coalescence processes through smaller radii, decreasing the rain-formation efficiency, thereby delaying precipitation formation, known as the *Albrecht* or *lifetime* effect (Albrecht, 1989). This delay in precipitation formation allows clouds to live longer and in turn get deeper, which in the end precipitate more intensely. Such effects can lead to an internal re-organization on the cloud field, or mesoscale, which ranges from tens to hundreds of kilometers and evolves on timescales of hours to days. They can be considered a form of self-organization because they are not prescribed by a large-scale forcing. In addition to delayed precipitation formation, increased N_c has also been described to affect entrainment rates with effects on meso-timescales (Glassmeier et al., 2021).

For trade-cumulus cloud fields, large-eddy simulations (LESs) were first employed on small domains (6.4×6.4-12.8×12.8 km^2) to investigate the response of shallow cumuli to aerosol perturbations (Xue et al., 2008a; Zuidema et al., 2008). A decade later, LESs on larger domains (Seifert et al., 2015; Yamaguchi et al., 2019) showed that the compensating internal adjusting processes as proposed by Stevens and Feingold (2009) occur on the scales of 50×50 km^2 cumulus cloud fields, which is far beyond the scale of an individual cloud. While not their focus, these studies give a clear indication of cold-pool activity. Cold pools are pockets of cold, dense air resulting from downdrafts associated with rain evaporation. When these downdrafts reach the surface, cold pools spread outward in a circular pattern. Studies across various regimes—stratocumulus, shallow, and deep convection—indicate that cold-pool boundaries feature strong moist updrafts, which trigger cloud formation along their edges, forming cloud rings often visible in satellite imagery (Böing et al., 2012; Drager and van den Heever, 2017; Haerter and Schlemmer, 2018; Helfer and Nuijens, 2021; Jeevanjee and Romps, 2013; Langhans and Romps, 2015; Lochbihler et al., 2021b; Savic-Jovcic and Stevens, 2008; Schlemmer and Hohenegger, 2014; Torri et al., 2015; Touzé-Peiffer et al., 2022; Vogel et al., 2021; Xue et al., 2008a; Zuidema et al., 2012, 2017). When cold pools form in close proximity, their boundaries can collide (Torri and Kuang, 2019), which intensifies the next convective event. Such cold-pool interactions through collisions implement self-organization, as has been conceptually modeled for both open-cell stratocumulus (Glassmeier and Feingold, 2017) and deep convective regimes (Haerter et al., 2019; Nissen and Haerter, 2021).

Shallow cumuli in the trades are frequently precipitating (Nuijens et al., 2009; Radtke et al., 2022; Snodgrass et al., 2009), leading to the frequent presence of cold pools in the trade-wind regime (Touzé-Peiffer et al., 2022; Vogel et al., 2021; Zuidema et al., 2012). The size and frequency of occurrence of cold pools covary with the mesoscale organization of trade-cumulus clouds (Vogel et al., 2021). Even under large-scale conditions that are invariant in time and space, LES studies show that trade-cumulus cold pools self-organize and in turn pattern trade-cumulus fields into arc-shape structures (Seifert and Heus, 2013; Vogel et al., 2016). By generating strong moist updrafts at their fronts, cold pools affect and interact with clouds (Alinaghi et al., 2025d; Li et al., 2014; Vogel et al., 2021; Zuidema et al., 2012). On large-domain LESs of the trade-wind regime, Alinaghi et al. (2025d) recently showed that the cold-pool-cloud interaction expresses itself in the form of structures resembling shallow squall lines. Thus, cold pools are coupled to clouds through shallow circulations at the mesoscales which were frequently observed in the trades (George et al., 2023) and affect cloudiness (Alinaghi et al., 2025d; Janssens et al., 2023; Vogel et al., 2022).

The mesoscale dynamics of trade cumulus are typically discussed in the context of cloud feedback. The trade-cumulus feedback has long been a large source of uncertainty in climate projections (Cesana and Del Genio, 2021; Myers et al., 2021). Trade-cumulus fields pattern into structures at the mesoscales that influence cloud-radiative effect (Alinaghi et al., 2024a; Bony et al., 2020a; Denby, 2023). Therefore, it is crucial to explore processes through which these clouds organize and how these processes respond to the variations in large-scale cloud-controlling factors (CCFs). By employing a large ensemble of LESs, the *Cloud Botany* ensemble (Jansson et al., 2023), Alinaghi et al. (2025d) illustrated that cold pools in the trades are strongly controlled by the variations in the large-scale external CCFs. They particularly quantified the relative importance of CCFs with respect to each other. Additionally, diurnality in insolation, which acts as a time-varying CCF, was shown to strongly control the temporal evolution of cold pools throughout the entire *Cloud Botany* ensemble (Alinaghi et al., 2025d).

Given the direct impact of N_c on precipitation formation, it is expected that trade-cumulus cold pools respond to variations in N_c (Fig. 3.1, link 1), and thereby to feed back to cloud fields at the mesoscales (Fig. 3.1, link 2). Despite the previously investigated sensitivity of shallow cold pools to microphysics schemes (Li et al., 2015), the response of shallow cold pools to N_c has not been directly explored and quantified. Furthermore, it is unknown how such N_c variations change the interplay between cold pools and clouds in the trade-wind regime. This study explores this response by performing large-domain, large-eddy simulations in which we only vary cloud-droplet number concentrations N_c from 20 to 1000 /cm^3. The newly added dimension of variability in N_c here also enables us to systematically investigate the relative importance of N_c compared to the other CCFs (Fig. 3.1, link 3) for cold pools and the radiative effect of clouds in the trade-wind regime (Fig. 3.1, link 4). Hence, our work serves as a step towards understanding the significance of the aerosol forcing in comparison to the trade cumulus feedback and exploring the corresponding role of mesoscale dynamics.

This paper is structured as follows. Based on simulations discussed in section 4.2, we

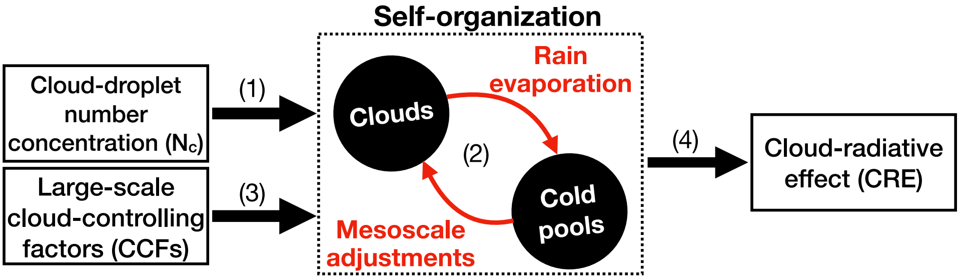
Self-organization
Cloud-droplet number concentration (Nc)
Large-scale cloud-controlling factors (CCFs)
(1)
(3)
Clouds
Rain evaporation
(2)
Cold pools
Mesoscale adjustments
(4)
Cloud-radiative effect (CRE)

Figure 3.1: **Conceptual picture of the study.** The diagram summarizes how (link 1) cloud fields respond to changes in N_c, and how (link 2) cold pools feed back to clouds (self-organization). The diagram further shows that the trade-cumulus system is forced by (link 3) the large-scale cloud-controlling factors (CCFs) whose relative importance for (link 4) the cloud-radiative effect will be quantified compared to N_c.

first investigate how trade-cumulus cold pools respond to N_c variability (Fig. 3.1, link 1; sections 3.3.1, 3.3.2) and how this response shapes the mesoscale organization of clouds (Fig. 3.1, link 2; section 3.3.2). Second, we explore how the diurnal cycle in insolation, as a time-varying CCF (Fig. 3.1, link 3), controls the evolution and response of cold pools to N_c (section 3.3.3). Next, we investigate the implications of our results for the cloud-field adjustments to N_c (Fig. 3.1, links 1, 2; section 3.3.4). Finally, we compare the effect N_c on cloud-field properties and radiative effects to that of large-scale external CCFs (Fig. 3.1, links 3, 4; section 3.3.5). Conclusions are presented in section 3.4.

3.2 Data and Methods

We perform large-eddy simulations (LESs) with the Dutch Atmospheric LES (DALES) model over domains of $153.6 \times 153.6\ \text{km}^2$, featuring a horizontal resolution of 100 m and a vertical resolution of about 20 m. All simulations are forced by the same large-scale CCFs. These follow the central reference simulation of the *Cloud Botany* ensemble (Jansson et al., 2023), which corresponds to the mean large-scale conditions of the winter trades as derived from the ERA5 reanalysis data (Hersbach et al., 2020). The corresponding profiles, which are also used for initialization are shown in Fig. 3.2. Moreover, all simulations feature the same horizontal tendencies of cooling and drying through advection as shown in the *Cloud Botany* paper (Jansson et al., 2023, their Fig. 3). Most of the simulations feature diurnality in the solar incoming radiation, while all other CCFs are fixed in time. Thus, the variability and evolution in the simulations are driven by the interaction between the components of the system, allowing the study of processes via which the system self-organizes. For more details on the design of the *Cloud Botany* simulations, including the selection of parameters for the large-scale forcing, refer to Jansson et al. (2023).

Simulations utilize the two-moment cloud-microphysics scheme of Seifert and Beheng (2001) with a constant cloud-droplet number concentration N_c. We conduct six, 72-hour simulations with varying N_c values in the set $\{20, 50, 70, 100, 200, 1000\}\ /\text{cm}^3$. The selected range of N_c variability, from 20 to 100, is similar to that used by Seifert et al. (2015), which is based on observations of the trades (Colón-Robles et al., 2006; Gerber et al., 2008; Hudson and Noble, 2014). We also included N_c values of 200 and 1000, as recent observations from

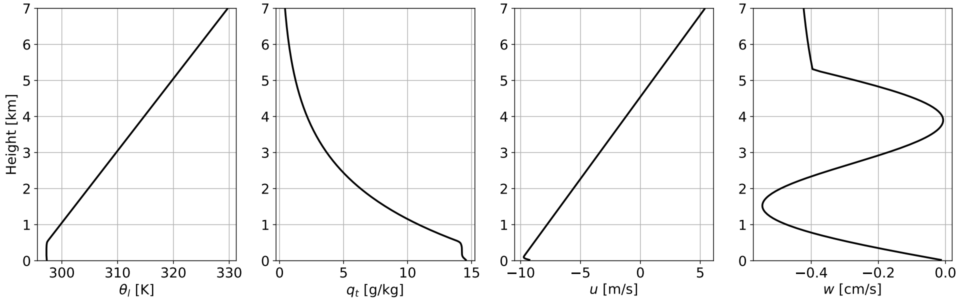

Figure 3.2: **Large-scale and initial conditions of the simulation** for potential temperature θ_l, total moisture q_t, horizontal wind u, and updraft w following the assumptions of the *Cloud Botany* ensemble (Jansson et al., 2023) with parameter values of sea-surface (potential) temperature $\theta_{l0} = 299$ K, near-surface wind speed $u_0 = -10.6$ m/s, moisture scale-height $h_{q_t} = 1810$ m, temperature lapse-rate $\Gamma = 5$ K/km, large-scale vertical velocity variability $w_1 = 0.0393$ cm/s, and the horizontal wind shear $u_z = 0.0022$ (m/s)/m.

the EUREC^{4}A field campaign (Bony et al., 2017; Stevens et al., 2021) report $\mathrm{N_c}$ values as high as 1000/cm^3, primarily due to the presence of dust (see Fig. 9 in Quinn et al., 2021, and Figs. 9 and 10 in Bony et al., 2022). Note that since $\mathrm{N_c}$ is fixed in time and space and does not evolve in our simulations, our study excludes microphysical adjustments. To gauge this limitation, we compare our results to cases from the literature with more complex microphysics.

Figure 3.3 visualizes that all these simulations start from a homogeneous non-cloudy state and develop into randomly distributed cumulus clouds. Afterward, clouds self-aggregate due to the presence of self-reinforcing shallow mesoscale overturning circulations (Bretherton and Blossey, 2017; Janssens et al., 2023; Narenpitak et al., 2021). As clouds aggregate, they deepen and eventually start to precipitate, leading to the presence of mesoscale arc-like structures, indicating the presence of cold pools in the field.

Alinaghi et al. (2025d) showed that the evolution of cold pools across the entire *Botany* ensemble is strongly controlled by the diurnality of insolation, mirroring observations of the trades (Vial et al., 2021; Vogel et al., 2021). To investigate how the evolution of cold pools is affected by variations in $\mathrm{N_c}$ independently of the diurnal cycle, we switch off the diurnality in insolation. To this end, we re-run simulations with $\mathrm{N_c}$ values of 20, 70, and 1000 /cm^3, while keeping the solar zenith angle time-invariant, ensuring that the total incoming solar radiation over the entire 24-hour period is equal to that of the simulations with the diurnal cycle (Alinaghi et al., 2025d, their section 3.2).

To diagnose cold pools, we use the 2D outputs of the mixed-layer height h_{mix}, as h_{mix} has been shown to be a reliable indicator for trade-cumulus cold pools in both models (Rochetin et al., 2021) and observations (Touzé-Peiffer et al., 2022). We identify cold pools following Alinaghi et al. (2025d): for each cloud field, we find the mode and the upper boundary (99th percentile) of an assumed symmetric probability density function (PDF) of h_{mix} that would have been observed in the absence of cold pools. The lower boundary of h_{mix} is calculated by first determining the difference between the upper boundary and the mode, and then subtracting this difference from the mode. Cold pools are identified where h_{mix} is smaller than the lower boundary of h_{mix} (see Fig. 3 in Alinaghi et al. (2025d)). In

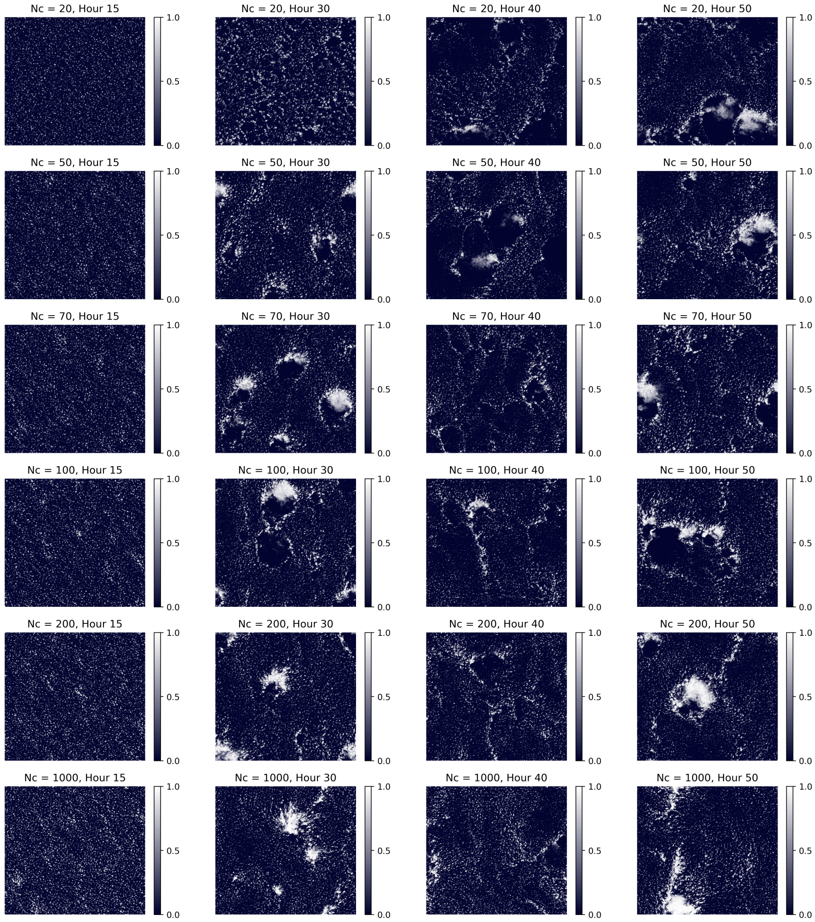

Figure 3.3: **Cloud-field albedo examples.** The figures show how cloud fields develop in our LES simulations featuring the diurnal cycle of insolation with N_c of 20 (1st row), 50 (2nd row), 70 (3rd row), 100 (4th row), 200 (5th row), and 1000 /cm^3 (6th row), at hours 15 (1st column), 30 (2nd column), 40 (3rd column), and 50 (4th column) after the start of simulations.

essence, this method identifies cold pools where h_{mix} is relatively shallower compared to other parts of the field. Alinaghi et al. (2025d) showed that the response of cold pools to CCFs is not sensitive to the details of the cold-pool diagnosis performed with this method.

Using the identified cold-pool mask and a clustering method, we define cold-pool objects as 2D contiguous structures within the simulation domain at each model time step. We then quantify the number of cold pools, n_{cp}, within the domain. Additionally, we compute the domain-mean cold-pool size as $s_{cp} = \sum_{i=1}^{n_{cp}} \sqrt{A_i}/n_{cp}$, where A_i denotes the area of each cold-pool object i within the domain.

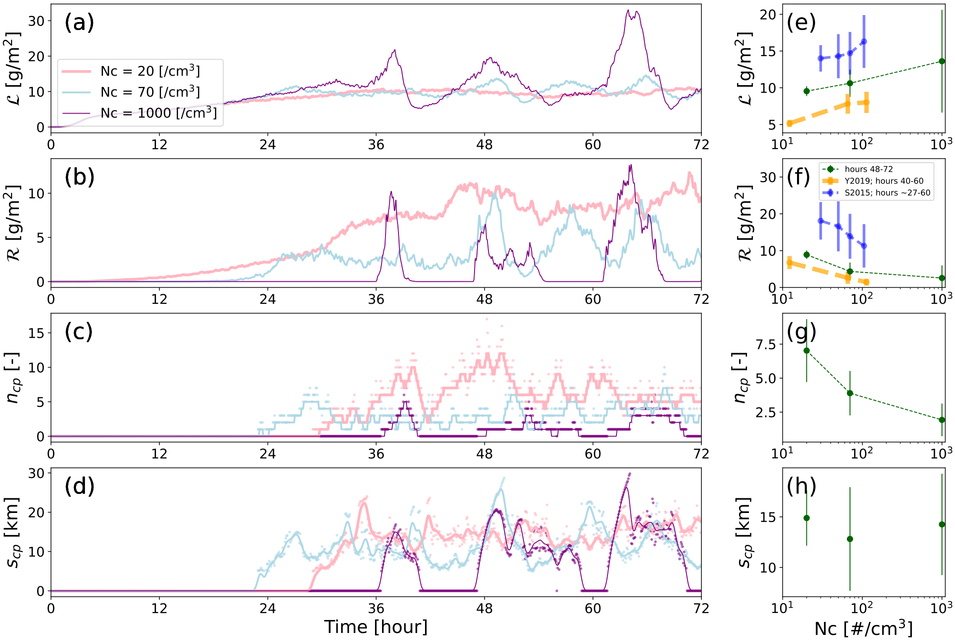

Figure 3.4: **Time series of clouds, rain, and spatial properties of cold pools in simulations without the diurnal cycle.** Panels (a-d) show time series of $\mathcal{L}$, $\mathcal{R}$, n_{cp}, and s_{cp} for simulations without the diurnal cycle of solar incoming radiation, where solid lines shown for cold-pool number and size provide a guide to the eye obtained through Gaussian filtering of the original data points. Note that there is significant precipitation in the $\mathrm{N_c} = 20$ /cm^3 case before cold pools with diameters larger than the 5-km threshold appear. Panels (e-h) show the response of $\mathcal{L}$, $\mathcal{R}$, n_{cp}, and s_{cp} to $\mathrm{N_c}$. The results from Yamaguchi et al. (2019) averaged over the last 20 hours of their simulations are shown in orange. The results from Seifert et al. (2015) for their near-equilibrium state are shown in blue. Dashed lines are added as a visual guide where the mean values show a trend.

3.3 Results and Discussion

3.3.1 Cloud-droplet number concentration affects the spatial and temporal properties of trade-cumulus cold pools

In this section, we investigate how the spatial and temporal properties of cold pools are influenced by $\mathrm{N_c}$ (Fig. 3.1, link 1, 2). As cold pools result from rain-evaporation (Fig. 3.1, link 2), we first examine how clouds and rain respond to $\mathrm{N_c}$ in simulations without diurnal cycle, which feature $\mathrm{N_c}$ values of 20, 70, and 1000 /cm^3. According to theory (Albrecht, 1989) and previous LES studies (Seifert et al., 2015; Yamaguchi et al., 2019), increased $\mathrm{N_c}$ reduces the efficiency of auto-conversion, delaying rain formation and allowing clouds to deepen and persist longer. Consistent with this, increased $\mathrm{N_c}$ leads to the accumulation of liquid water $\mathcal{L}$ (Fig. 3.4a), eventually resulting in the production of more intense rain $\mathcal{R}$ (Fig. 3.4b). Furthermore, the amplitude of fluctuations of $\mathcal{L}$ and $\mathcal{R}$ increases with increasing $\mathrm{N_c}$, while their frequency decreases (Figs. 3.4a,b).

We quantitatively compare our results to those of Yamaguchi et al. (2019) and Seifert et al. (2015) (Figs. 3.4e,f). Results of Yamaguchi et al. (2019) were obtained on ten times smaller domains but using a microphysics scheme with prescribed aerosol and prognostic cloud-droplet number concentrations. The latter converges to a certain value after approximately 20 hours (Yamaguchi et al., 2019, their Fig. 5e). We therefore compare our fixed-N_c results to averages of the last 20 hours of their simulations. The systematic difference between the values of cloud-field properties is expected due to differences in the large-scale cloud-controlling factors; notably, their geostrophic wind speed is 60% smaller than that of our simulations (Yamaguchi et al., 2019, their Table 1). Similarly, we present the results from Seifert et al. (2015), which feature a domain size similar to that of Yamaguchi et al. (2019) but fixed N_c as in our simulations. We selected their simulations with interactive radiation and prescribed large-scale advective cooling to match our setup as closely as possible. It is worth noting that the cloud fields in Seifert et al. (2015) have larger cloud- and rain-water paths (Figs. 3.4e,f), which we mainly attribute to their larger meridional geostrophic wind.

Consistent with Yamaguchi et al. (2019) and Seifert et al. (2015), increased N_c leads to an increased domain-mean liquid-water path, $\mathcal{L}$ (Fig. 3.4e). As shown by the error bars, the temporal variance in $\mathcal{L}$ increases in response to increased N_c in our simulations. In addition, Fig. 3.4f illustrates that the domain-mean rain-water path, $\mathcal{R}$, decreases with increasing N_c in all studies. Similar to $\mathcal{L}$, the temporal variations in $\mathcal{R}$ increase with increasing N_c in our simulations. This is in contrast to the small-domain LESs of Yamaguchi et al. (2019, 50×50 km^2) and Dagan et al. (2018, 12×12–50×50 km^2), where increased N_c was found to reduce the amplitude of fluctuations in the time series of $\mathcal{R}$. The temporal variance of liquid- and rain-water path in simulations of Seifert et al. (2015) do not show a systematic response to N_c. The response of the temporal variations of cloud-field properties to N_c thus appears markedly different in our large domains.

The temporal variations of cold-pool characteristics follow those of the rain-water path, $\mathcal{R}$ (Figs. 3.4b-d). Notably, in the simulation with $N_c = 20/\text{cm}^3$, once cold pools form around hour 30, they grow until around hour 36 and persist until the end of the simulation. In contrast, cold pools in the simulation with $N_c = 1000/\text{cm}^3$ form, develop, reach a maximum, decay, and completely vanish. Therefore, increased N_c enhances the intermittency in the evolution of cold pools. Averaged over the last day, increased N_c leads to a smaller number of cold pools, n_{cp} (Fig. 3.4g), while the domain-mean size of cold pools, s_{cp}, shows a muted response to N_c variations (Fig. 3.4h).

3.3.2 COLD-POOL EVOLUTION SHOWS TWO DISTINCT MESOSCALE BEHAVIOURS FOR LOW AND HIGH CLOUD-DROPLET NUMBER CONCENTRATIONS

To understand the difference in cold-pool dynamics for different cloud-droplet number concentrations, Fig. 3.5 contrasts the extreme N_c cases. Consistent with observations (Vogel et al., 2021; Zuidema et al., 2012), both have in common that cold pools alter the spatial pattern of moisture in the sub-cloud layer. Cold pools are characterized by relatively dry air inside but relatively moist air at their fronts. Cold pools further modify the spatial pattern of horizontal velocity in the sub-cloud layer, thereby altering the spatial pattern of convergence and, in turn, vertical velocity. Cold pools feature large values of downward vertical velocity inside but strong updrafts at their fronts. Therefore, cold-pool fronts actively contribute to moist convergence and cloud formation. In contrast, the downward motions inside cold pools can potentially suppress convection and lead to cloud-free

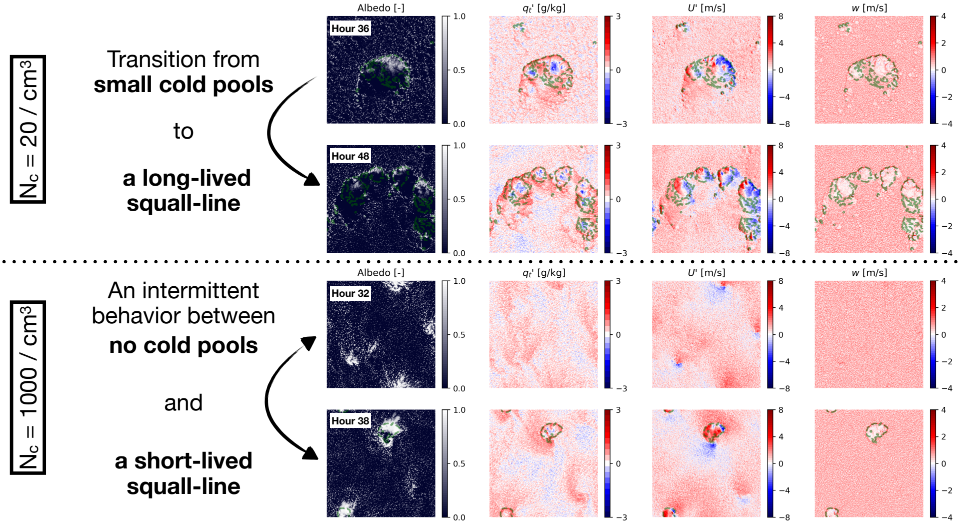

Figure 3.5: **Effects of cold pools on the organization of the (sub-)cloud layer properties for the simulations without diurnal cycle and with $\mathbf{N_c} = 20/\mathbf{cm}^3$ and $\mathbf{N_c} = 1000/\mathbf{cm}^3$.** For each condition, columns 1-4 indicate the 2D top-views of cloud albedo, total moisture anomalies (q_t') at the 200-m level, the horizontal wind speed anomalies (U') at the first level of the model, and the vertical velocity (w) at the 200-m height. The green dashed contour line marks the cold-pool boundaries quantified from the mixed-layer height fields. In the U' fields, red indicates that cold pools accelerate the wind, while blue indicates they decelerate it.

regions.

Despite the similar evolution of individual cold pools independent of N_c, there are notable differences in the collective, i.e. self-organization, behavior. In the low-N_c simulation (i.e., $N_c = 20/\text{cm}^3$), cold pools tend to form in close proximity. As their fronts converge, they trigger the formation of new cold pools at their collision points. This triggering mechanism occurs due to (i) the collision of anomalously moist cold-pool fronts, which mechanically forces the moist air upward due to mass conservation, and (ii) the high efficiency of rain formation, where a small amount of cloud water quickly turns into rainwater, leading to the formation of a new cold pool at the collision point. Consequently, the small, space-filling cold pools at hours 30-36 collide and transition into a stage where they become organized into a large front, sustained by the interaction (collision) of its cold pools at its fronts (see Fig. 3.5, $N_c = 20/\text{cm}^3$, hour 48). This is consistent with the time series of cold-pool number n_{cp} and size s_{cp} shown in Figs. 3.4c,d, which show that after around hour 38, the metrics of cold pools stabilize: s_{cp} remains around 15±5 km, and n_{cp} around 6±4. This behaviour of cold pools resembles the mathematical toy model of colliding circle cold pools presented by Nissen and Haerter (2021, their Fig. 5), which demonstrates (i) similar transitions from randomly distributed cold pools to a band-like structure, and (ii) that cold-pool collision is the key mechanism for the self-organization of the system. Notably, their model was motivated by cold pools in the regime of deep convection.

In contrast, cold pools do not interact as readily in the high-N_c simulation (i.e., $N_c = 1000/\text{cm}^3$). This is attributable to two factors. First, the efficiency of rain formation and, consequently, cold-pool formation, is significantly lower in high-N_c than in low-N_c

simulations. Second, cold pools form at greater distances from each other. We speculate that this distance is determined by the horizontal length scale of the self-reinforcing shallow circulations that lead to moisture aggregating in the absence of rain (Bretherton and Blossey, 2017; George et al., 2023; Janssens et al., 2023; Narenpitak et al., 2021). As Janssens et al. (2023) showed, the aggregation of non-precipitating cumuli develops atop such anomalous mesoscale moist regions, whose size expands in tandem with the growth of anomalous mesoscale dry regions. The scale growth of dry regions in the descending branch of circulations effectively separates moist regions—and consequently, their associated aggregated clouds—preventing interactions between their subsequent cold pools, which form at greater distances from each other. Consistently, Fig. 3.5 ($N_c = 1000/cm^3$, hour 38) suggests that the downward branches of these circulations are so large that they effectively separate two cloud clusters and cause their cold pools to form at a distance from each other, thus preventing their interactions.

The intermediate case of $N_c = 70/cm^3$ exhibits a cold-pool evolution similar to that of the high-N_c case with $N_c = 1000/cm^3$: (i) cold pools in the $N_c = 70/cm^3$ case also form far apart, resulting in very infrequent cold-pool interactions, and (ii) its cold-pool evolution displays strong intermittency, as shown by Figs. 3.4c,d. The self-organization dynamics of this case were recently discussed by Alinaghi et al. (2025d) , where cold pools are characterized in analogy to squall lines in deep mesoscale convective systems (Rotunno et al., 1988; Stensrud et al., 2005; Weisman and Rotunno, 2004). In this regime, cold pools reinforce and sustain their parent clouds due to the convergence of moist air at their fronts. Once cold pools get mature, their moist updrafts at their fronts become so strong such that they impinge on the inversion, leading to the formation of stratiform anvils with stratiform precipitation. This weakens the cold-pool-induced updraft, ultimately causing parent clouds to detach from their cold-pool children (Alinaghi et al., 2025d, their Figs. 7, 8, 11). This self-organizing behaviour of cold pools and clouds in simulations where they cannot interact is also evident in the cold-pool time series (Fig. 3.4cd), which exhibit an intermittent behaviour with large amplitudes and low frequencies for both $N_c = 70$ and $1000/cm^3$.

An interesting observation is that rain and cold pools tend to develop more rapidly once the initial event has occurred. For instance, the time series shown in Fig. 3.4b-d demonstrates that it takes approximately 36 hours for the $N_c = 1000/cm^3$ simulation to produce rain and cold pools. However, subsequent cold-pool events occur within about 8 hours, indicating a faster formation of rain and cold pools. In this simulation, the next convective event takes place precisely where the fronts of the previous cold-pool event had accumulated moisture, thereby expediting the development of subsequent convection. We hypothesize that cold pools in the high-N_c simulation act as a “moisture memory” similar to deep convection (Colin et al., 2019), facilitating aggregation over shorter timescales compared to when cold pools are absent. This suggests that the moisture variance induced by cold pools decreases the induced delay in rain formation associated with increased N_c.

As the final point in this section, we investigate how the two N_c-induced regimes of cold-pool self-organization dynamics relate to the mesoscale organization of trade-cumulus cloud fields (Fig. 3.1, link 2). To address this, we quantify several metrics based on the geometry of clouds that effectively capture the variability in the mesoscale organization of cloud fields in the trades (Janssens et al., 2021). These include the domain-averaged size of cloud objects, the mean fraction of open-sky areas, the domain-mean depth of clouds, and the degree of organization I_{org}. The details of these metrics and their calculations are explained by Janssens et al. (2021). In addition to geometry-based cloud metrics, we further compute more organization metrics that are based on spatial distribution of cloud-liquid-water and total moisture fields. First, we quantify the spatial standard deviation of the liquid-water path $\sigma\mathcal{L}$. Second, following Radtke et al. (2023), we consider the metric ΔQ, which quantifies the moisture aggregation at the mesoscales. This metric is calculated as the difference between the 5^{th} and 95^{th} percentiles of the mesoscale total moisture anomaly fields, derived by coarse-graining the total moisture anomaly fields as outlined by Janssens et al. (2023, see their Fig. 3).

Interestingly, the geometry-based organization metrics quantifying the mean size of cloud objects and the open-sky areas, which were shown to explain most of the variability within the mesoscale organization of trade cumuli (Janssens et al., 2021), do not capture the two distinct behaviours of cold pools at low-and high-N_c regimes discussed in the context of Fig. 3.5 (Fig. S3.1). However, Fig. 3.6a,b shows that the spatial variance in cloud-liquid-water path $\sigma\mathcal{L}$ is strongly affected by N_c. First, increased N_c translates into a strong intermittent behaviour in $\sigma\mathcal{L}$ evolution (Fig. 3.6a). Second, Fig. 3.6b indicates that, when averaged over 24-48 and 48-72 hour intervals, increased N_c leads to greater spatial heterogeneity in liquid-water content: shallow cumuli become more aggregated in response to increased N_c, as visually evident in the snapshots of cloud fields shown in Figs. 3.3 and 3.5. The $\sigma\mathcal{L}$-N_c relationship suggests that a reduced number of cold pools, in response to increased N_c, enhances cloud aggregation. This echoes Radtke et al. (2023)'s findings, which also show that rain (auto-conversion) is less efficient in more aggregated fields of trade cumuli (Radtke et al., 2023, their Fig. 2).

With the delay in precipitation formation due to increased N_c, moisture is expected to continue aggregating through shallow circulations driven by latent heating from condensation in the non-precipitating cumulus layer (Bretherton and Blossey, 2017; Janssens et al., 2023). Fig. 3.6c shows that this is exactly what happens in simulations with high N_c. In simulations with N_c of 70 and 1000 /cm^3, the moisture aggregation metric ΔQ keeps growing until cold pools start to form, after which ΔQ stabilizes and shows an intermittent behaviour. In contrast, in the lowest case of N_c, the moisture does not aggregate at the mesoscales until hour 30, where cold pools start to form, after which the moisture aggregation metric ΔQ starts developing and keeps increasing until the end of the simulation. This implies that this metric of moisture aggregation at the mesoscales is intriguingly able to encapsulate the contrasts between these distinct behaviours of cold pools at low- and high-N_c. Averaged over hours 24-48, ΔQ associated with the low-N_c is by 50% smaller than of that of the high-N_c cases (Fig. 3.6d). However, as the simulations progress into hours 48-72, cold pools in low-N_c simulations develop into large squall lines, increasing their moisture aggregation and reducing the sensitivity of ΔQ to N_c (Fig. 3.6d).

In summary, the evolution of cold pools and trade-cumulus fields is significantly influenced by N_c, exhibiting two distinct behaviours at low and high N_c (Fig. 3.1, links 1, 2). In simulations with $N_c = 20/\text{cm}^3$, cold pools form in close proximity, leading to interactions and collisions that trigger the formation of clouds and due to high rain efficiency formation of new cold pools at the collision points. This results in persistent long-lived structures resembling squall lines. Conversely, in simulations with higher N_c values (70

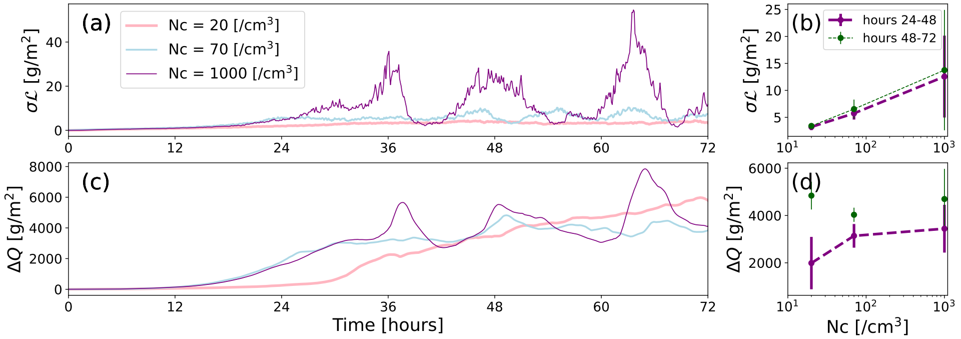

Figure 3.6: **Dependence of mesoscale organization of cloud fields on N_c.** The panels (a,c) show the time series of the spatial standard deviation of the liquid-water path σL and the difference between the 5^{th} and 95^{th} percentiles of the mesoscale total moisture anomaly fields ΔQ for the simulations without the diurnal cycle of insolation. Panels (b,d) show their responses to N_c for hours 24-48 in purple and hours 48-72 in green. Dashed lines are added as a visual guide where the mean values have a trend.

and 1000/cm^3), cold pools form at greater distances, preventing interactions and resulting in intermittent behaviour. Cold pools in such cases are short-lived structures resembling squall lines, hypothetically facilitating convection by providing moisture anomalies at their fronts, thereby decreasing N_c-induced delays in subsequent cold-pool formation. This N_c-driven contrast in cold-pool dynamics affects moisture and cloud-water variance, with higher N_c leading to more aggregated trade-cumulus cloud fields.

3.3.3 DIURNAL CYCLE SYNCHRONIZES THE PHASES OF COLD-POOL EVOLUTION ACROSS SIMULATIONS WITH PERTURBED N_c

We have shown that the temporal evolution of cold pools, and the trade-cumulus system in general, is controlled by N_c (Fig. 3.1, links 1, 2). Observations have shown that the evolution of trade-cumulus fields, their mesoscale organization, precipitation, and cold pools in the trades feature diurnality (Nuijens et al., 2009; Radtke et al., 2022; Vial et al., 2021; Vogel et al., 2021). This raises the question: to what extent does the diurnal cycle of insolation, as a time-varying external forcing, control or affect the influence of N_c on the evolution of cold pools (Fig. 3.1, link 3)?

To answer this question, we plot the time series of the domain-mean rain-water path $\mathcal{R}$, the number n_{cp}, and the size s_{cp} of cold pools in our simulations with the diurnal cycle, featuring N_c values of 20, 50, 70, 100, 200, and 1000 /cm^3. As expected, Figs. 3.7a-c show that, across all simulations, the evolution of rain and cold pools follows the diurnal cycle of radiation, peaking around sunrise and reaching a minimum around sunset. This pattern is due to the absence of solar radiation combined with longwave radiative cooling during the night. This strong nighttime radiative cooling destabilizes the atmosphere, stimulating convection and leading to the formation of deeper clouds that precipitate more intensely. In contrast, during the daytime, radiative heating from solar radiation stabilizes the atmosphere, suppressing convection and causing a notable decrease in rain, and in the number and size of cold pools in almost all simulations. Thus, the diurnal cycle serves as an external forcing (Fig. 3.1, link 3) that synchronizes the periodicity and amplitude of

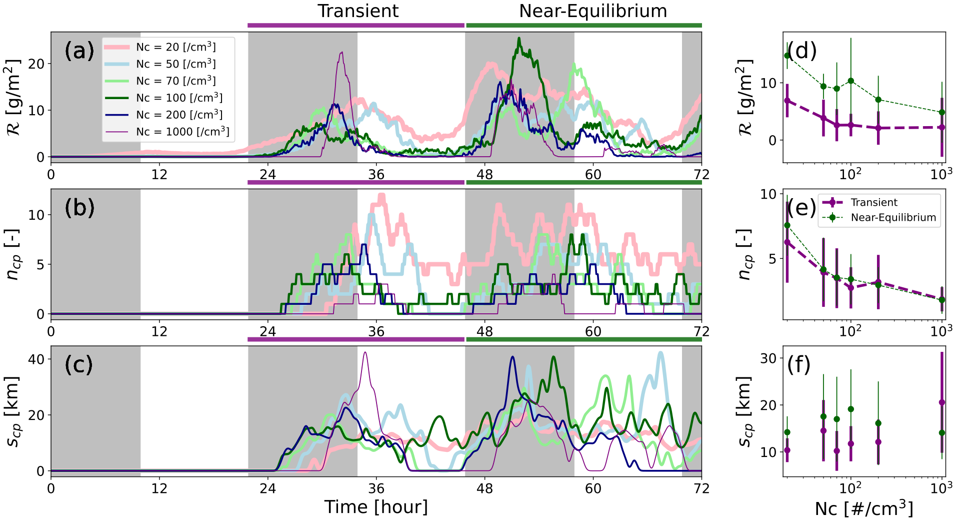

Figure 3.7: **Effects of the diurnal cycle of insolation on the evolution and $\mathrm{N_c}$-response of rain and cold pools.** Panels (a-c) show time series of rain-water path $\mathcal{R}$, cold-pool number n_{cp}, and cold-pool size s_{cp} for simulations with the diurnal cycle of solar incoming radiation. Nighttime is shown by the grey color. Solid lines shown for cold-pool number and size provide a guide to the eye obtained through Gaussian filtering of the original data points. Note that there is significant precipitation in the $\mathrm{N_c} = 20$ /cm^3 case before cold pools with diameters larger than the 5-km threshold appear. Panels (d-e) show the response of $\mathcal{R}$, n_{cp}, and s_{cp} to $\mathrm{N_c}$ during the transient (purple), and near-equilibrium (green) phases, which are marked in the time series plots (a-c). Dashed lines are added as a visual guide where there is a trend.

cold-pool variability that were discussed in the context of Fig. 3.4 across simulations with different $\mathrm{N_c}$. The simulated diurnal cycle in precipitation and cold pools is consistent with observations of the trades (Nuijens et al., 2009; Radtke et al., 2022; Vial et al., 2021; Vogel et al., 2021).

Although all simulations show evolution synchronized with the diurnal cycle, the cold pools in the simulation with the lowest $\mathrm{N_c}$ continue to persist even during the daytime when convection suppression due to reduced net radiative cooling is at its peak. This behaviour is notable as it indicates that the mesoscale self-organization of cold pools through collisions, as discussed in Section 3.3.2, outweighs the externally imposed suppressive effect of the diurnal cycle during the day. Consequently, cold pools in the $\mathrm{N_c} = 20/\mathrm{cm}^3$ simulation remain active throughout the day. However, the duration of cold-pool's persistence during the day decreases with increasing $\mathrm{N_c}$. Specifically, during daytime hours around 34-46, increased $\mathrm{N_c}$ leads to an earlier disappearance of cold pools and a more delayed formation of the next generation of cold pools, as shown in Fig. 3.7c. To summarize, we find that the diurnal cycle externally synchronizes the mesoscale self-organization dynamics of cold pools, which is in turn modulated by the details of microphysics and rain formation.

The synchronization of cold-pool events by the diurnal cycle enables us to compare the responses of rain-water path $\mathcal{R}$ and cold pools to $\mathrm{N_c}$ during the same time window across all simulations. In all simulations, except for $\mathrm{N_c} = 20/\mathrm{cm}^3$, rain and subsequently cold pools begin to form after hour 24 (Figs. 3.7a-c), with the evolution of cold pools following the diurnal cycle of net radiative cooling. We refer to the day starting at hour 22 as the "transient" phase and the subsequent day beginning at hour 46 as the "near-equilibrium" phase. We selected these hours based on the development of the total-water (cloud and water vapor) path in our simulations, which consistently increases until hour 48 across all simulations, after which it stabilizes and becomes time-invariant (Fig. S3.2).

All simulations consistently show a higher daily mean rain-water path $\mathcal{R}$ during the near-equilibrium phase compared to the transient phase (Fig. 3.7d). This is because, in the near-equilibrium phase, our simulations are more developed and feature deeper boundary layers with larger total water that can develop more rain. Consistent with our results based on the last 24 hours of simulations without the diurnal cycle (Figs. 3.4f-h), Figs. 3.7d,e illustrate that during the both transient and near-equilibrium phases, rain-water path $\mathcal{R}$ and the number of cold pools n_{cp} decrease with increasing $\mathrm{N_c}$. Also, the size of cold pools s_{cp} do not show a notable change in response to $\mathrm{N_c}$ (Fig. 3.7f).

3.3.4 Twomey effect primarily controls the dependence of cloud-radiative effect on $\mathrm{N_c}$

In this section, we investigate the sensitivity of the relative cloud-radiative effect (Xie and Liu, 2013), rCRE = $f_c \cdot \mathcal{A}_c$, to $\mathrm{N_c}$ (Fig. 3.1, link 4), with f_c and $\mathcal{A}_c$ as cloud fraction and albedo. Assuming the plane-parallel approximation (Lacis and Hansen, 1974), cloud albedo is given by $\mathcal{A}_c = \frac{\tau}{\tau+7.7}$ with the cloud-optical thickness $\tau \approx {\mathrm{N_c}}^{1/3}\mathcal{L}^{5/6}$ following Zhang et al. (2005). Therefore, we explore the response of cloud fraction f_c, domain-mean liquid-water path $\mathcal{L}$, mean cloud albedo $\mathcal{A}_c$ over the cloudy columns where the cloud-liquid-water path is larger than zero, and the relative cloud-radiative effect rCRE to $\mathrm{N_c}$. These sensitivities are explored during different phases of the simulations with the diurnal cycle: non-precipitating (hours 5-15), transient (hours 22-46), and near-equilibrium (hours 46-72). For comparison, we also include results from Seifert et al. (2015) and Yamaguchi et al. (2019) , where the latter features more comprehensive microphysics than our study with its fixed cloud-droplet number concentration.

During the non- (or weakly) precipitating phase, the response of the cloud fraction f_c and liquid-water path $\mathcal{L}$ to $\mathrm{N_c}$ is negligible (Figs. 3.8a,b). Thus, the relative cloud-radiative effect (rCRE) is influenced by $\mathrm{N_c}$ primarily through the cloud albedo response, or the Twomey effect (Figs. 3.8c,d). During both the transient and near-equilibrium phases, the cloud fraction f_c decreases very slightly with increasing $\mathrm{N_c}$, though this response is much smaller than the temporal variance of f_c within each simulation (Fig. 3.8a). Additionally, the liquid-water path $\mathcal{L}$ shows a small increase with increased $\mathrm{N_c}$ (Fig. 3.8b). However, similar to the non-precipitating phase, the Twomey effect continues to strongly control the response of rCRE to $\mathrm{N_c}$ during both the transient and near-equilibrium phases (Figs. 3.8c,d).

The response of the liquid-water path in the near-equilibrium phase is consistent with the results of Yamaguchi et al. (2019) and Seifert et al. (2015). This small positive sensitivity of the liquid-water path in our simulations does not significantly affect the impact of $\mathrm{N_c}$ on rCRE compared to the Twomey effect. Cloud fraction f_c decreases with increasing $\mathrm{N_c}$ in the simulations of Yamaguchi et al. (2019). Similarly, our simulations and those of Seifert et al. (2015) both show a decrease in f_c in response to increased $\mathrm{N_c}$. However, this decrease seems to be smaller compared with the f_c response in Yamaguchi et al. (2019)'s simulations.

3

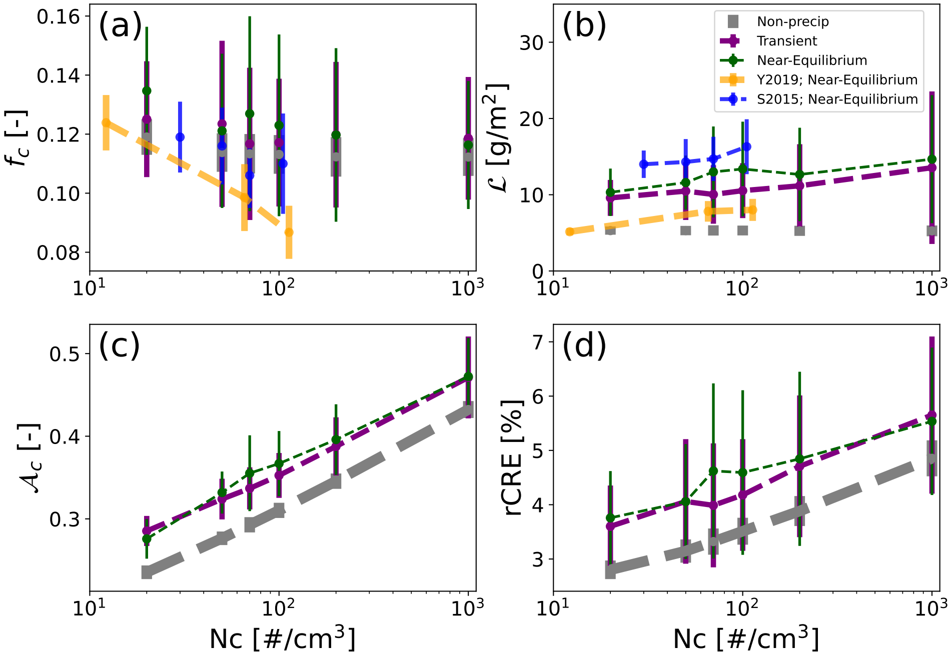

Figure 3.8: **Sensitivity of relative cloud-radiative effect to cloud-droplet number.** Panels (a-d) show the response of cloud fraction f_c, domain-mean liquid-water path $\mathcal{L}$, cloud albedo $\mathcal{A}_c$, and relative cloud-radiative effect rCRE to N_c during the non-precipitating (dark grey), transient (purple), and near-equilibrium (green) phases. The results from Yamaguchi et al. (2019) averaged over the last 20 hours of their simulations are shown in orange. The results from Seifert et al. (2015) for their near-equilibrium state are shown in blue. Note that Seifert et al. (2015); Yamaguchi et al. (2019) do not report on the cloud albedo and rCRE in their studies. Dashed lines are added as a visual guide where there is a trend.

It would be interesting to revisit this difference with a cloud microphysics scheme that does not fix cloud-droplet number as in the current study but allows for full microphysical adjustments.

It is worth noting that although variations in N_c modulate the number of cold pools and in turn, mesoscale self-organization of trade-cumulus fields, cloud fraction f_c is very weakly affected. Our results here resonate with Janssens et al. (2025) who hypothesize that circulations associated with self-organization symmetrically distribute cloudiness at the mesoscales such that the increased cloudiness at their ascending branch is compensated by the decreased cloudiness at their descending branch. This implies that although decreased N_c increases the number of cold pools, the increased cloudiness at their fronts, where convection is triggered, appears to be buffered by the decreased cloudiness at their interiors, where convection is suppressed. Future studies are encouraged to explicitly investigate this.

3.3.5 $\mathrm{N_c}$ INDUCES COMPARABLE VARIATIONS IN CLOUD-RADIATIVE EFFECT TO THE LARGE-SCALE CLOUD-CONTROLLING FACTORS

In this section, we quantify the relative importance of $\mathrm{N_c}$ (Fig. 3.1, link 1) compared with the large-scale cloud-controlling factors (CCFs; Fig. 3.1, link 3) for driving changes in cloud-field properties and radiative effects (Fig. 3.1, links 2, 4). Using the data from the *Botany* dataset (Jansson et al., 2023) as well as our new simulations of this study, we employ a multivariate regression model

$$\overline{C} \approx \sum_{i=1}^{7} \beta_i \times \widetilde{\mathrm{CCF}}_i \qquad \text{with} \qquad \widetilde{\mathrm{CCF}}_i := \frac{\mathrm{CCF}_i - \overline{\mathrm{CCF}_i}}{\sigma(\mathrm{CCF}_i)},$$

where, the vector $\overline{C}$ represents the mean of the metric $C \in \{\mathcal{A}_c, \mathrm{rCRE}\}$, averaged over the last 2 days (hours 12–60) for each member of the *Botany* ensemble. Each regressor $\widetilde{\mathrm{CCF}}_i$ is a vector containing the associated CCF_i values for the simulation members of the *Botany* ensemble. The regressors (CCFs) include sea-surface (potential) temperature (θ_{l0}), near-surface wind speed (u_0), moisture scale height (h_{q_t}), temperature lapse rate (Γ), large-scale vertical velocity variability (w_1), and horizontal wind shear (u_z). In addition, we consider $\mathrm{N_c}$ as a 7^{th} regressor. For the regressor $\mathrm{N_c}$, we use the simulations with the diurnal cycle over hours 12-60 to be consistent with the simulations of the *Botany* ensemble. All regressors are standardized by subtracting their mean $\overline{\mathrm{CCF}}$ and dividing by their standard deviation $\sigma(\mathrm{CCF})$ across the ensemble, which allows the comparison of CCFs and $\mathrm{N_c}$ with an equal weighting. In our regression analysis, we only include simulations that develop clouds and run for at least 48 hours. This leaves us with 80 simulations out of the initial 103 in the *Botany* ensemble. Including the simulations with the diurnal cycle from this study (six in total) and noting that the simulation with $\mathrm{N_c} = 70/\mathrm{cm}^3$ being already part of the ensemble as the central reference simulation, our regression analysis features 85 data points in total. This means that the target value $\overline{C}$ and regressors $\widetilde{\mathrm{CCF}}_i$ of the regression model are vectors of size 85×1.

Figure 3.9 shows the results of the multivariate regression for cloud albedo $\mathcal{A}_c$ and rCRE. Note that the response of cloud albedo $\mathcal{A}_c$ and rCRE to CCFs of the *Botany* ensemble has already been addressed and discussed by Janssens (2023a); Janssens et al. (2025), to which we refer for details. Figure 3.9a illustrates that the effect of $\mathrm{N_c}$ on cloud albedo $\mathcal{A}_c$, known as the Twomey effect, is comparable to that of large-scale subsidence as quantified by w_1. Additionally, the effect of $\mathrm{N_c}$ on trade-cumulus brightening is about 75% of the effect of horizontal wind speed, 150% of the effect of stability, and 300% of the effects of free-tropospheric humidity and vertical wind shear. Eventually, the response of rCRE to $\mathrm{N_c}$ is statistically significant at the 95% level and accounts for about 66%, 28%, and 25% of the response of rCRE to free-tropospheric humidity, wind speed, and large-scale subsidence, respectively (Fig. 3.9b). Note that the sensitivity of rCRE to $\mathrm{N_c}$ is smaller than that of cloud albedo to $\mathrm{N_c}$ in our regression analysis, which is due to the very weak impact of $\mathrm{N_c}$ on cloud fraction f_c (Fig. 3.8a). Similar regression results for other cloud-field and cold-pool properties are presented in Fig. S3.3.

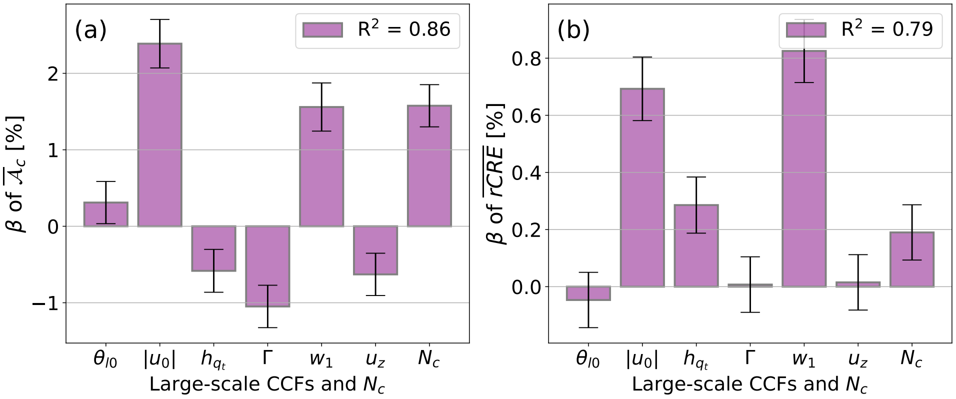

Figure 3.9: **Cloud-field response to large-scale cloud-controlling factors and cloud-droplet number concentration.** The standardized β coefficients of the multiple regression analysis for (a) cloud albedo $\mathcal{A}_c$ and (b) relative cloud-radiative effect rCRE, all averaged over the last two days of the LESs of the *Botany* ensemble. The error bars show the 95% confidence interval for each regressor. The p-values of the F-statistic test of all models are smaller than 10^{-22}.

3.4 CONCLUSIONS & OUTLOOK

Cold pools, resulting from rain-evaporation, affect the mesoscale organization of trade-cumulus fields (Alinaghi et al., 2025d; Seifert and Heus, 2013; Vogel et al., 2021, 2016; Zuidema et al., 2012). We have used an ensemble of large-domain LESs to investigate the sensitivity of mesoscale organization to cloud-droplet number concentration N_c and the role of cold pools therein as conceptualized in Fig. 3.1.

Investigating the sensitivity of mesoscale cold-pool dynamics to microphysics (Fig. 3.1, link 1), we find that cold pools show two distinct behaviours at low and high N_c. In low-N_c cases, there are many cold pools within the simulation domain, which form in close proximity (Figs. 3.4c,d,g,h, 3.5). This allows them to interact with each other through collisions. Efficient rain formation then leads to the swift triggering of new cold pools at collision points. Consequently, cold pools organize into a large long-lived front with a resemblance to a squall line that perpetuates through collisions of cold pools at its leading edge. In contrast, high-N_c cases feature sparsely distributed cold pools, which prevents their interaction. In this regime, cold pools exhibit an intermittent behaviour, manifesting as small, short-lived fronts resembling squall lines that form, develop, decay, and vanish (Figs. 3.4c,d,g,h, 3.5).

For the effect of N_c on the interaction between clouds and cold pools (Fig. 3.1, link 2), our analysis shows that increased N_c suppresses the formation of cold pools (Figs. 3.4g,h, 3.5), while enhancing the self-aggregation of cloud fields (Figs. 3.6). In other words, by delaying precipitation formation, increased N_c allows non-precipitating cumulus fields to aggregate moisture (Fig. 3.6c,d) through self-reinforcing mesoscale overturning circulations (Bretherton and Blossey, 2017; Janssens et al., 2023; Narenpitak et al., 2021). We quantified this effect, which clearly influences the mesoscale organization of cloud fields, particularly by increasing the spatial variance in the cloud-liquid-water path (Fig. 3.6a,b). Interestingly, despite the suppression of cold pools and the boost in aggregation due to increased N_c

(Figs. 3.6a-d), the overall daily mean responses of cloud fraction and liquid-water path are notably small (Figs. 3.4e, 3.8a,b). This echoes recent findings of Janssens et al. (2025) that shallow mesoscale circulations appear to symmetrically modulate cloudiness within trade-cumulus fields such that the increased cloudiness at their ascending branch is compensated by the decreased cloudiness at their descending branch. This suggests that although by increasing N_c, mesoscale organization is affected by the variations in cold pools, the increased cloudiness at the edges of cold pools appears to be buffered by the decreased cloudiness at their interiors.

For the effect of the diurnal cycle as an external forcing on the microphysical sensitivity (Fig. 3.1, link 3), we find that the diurnal cycle synchronizes the self-organization dynamics of cold pools on the mesoscale across simulations with varying N_c (Fig. 3.7). Cold pool activity is thus controlled by both, the external forcing as well as the self-organization dynamics. The contribution of self-organization dynamics increases with decreasing N_c as showcased by the fact that cold-pool activity survives the day-time suppression for the lowest N_c case (Figs. 3.7b,c).

To compare the importance of microphysical and large-scale controls on the cold-pool dynamics (Fig. 3.1, links 1 and 3) occurring on the intermediate mesoscale, we have made use of the *Cloud Botany* ensemble (Jansson et al., 2023). We demonstrate that the Twomey effect is as significant as the primary cloud-controlling factors for the brightening of trade-cumulus fields (Fig. 3.9a). Despite the very small response of cloud fraction to N_c (Fig. 3.8a), the response of the relative cloud-radiative effect to N_c (Fig. 3.1, link 4) is about 25% as significant as the response of rCRE to horizontal wind speed and large-scale subsidence (Fig. 3.9b).

We have obtained these results using a prescribed cloud-droplet number as a proxy for microphysical influences. This assumption excludes microphysical adjustments. Despite a broad agreement between our results and those of Yamaguchi et al. (2019) that are based on more detailed microphysics scheme with prognostic N_c, Li et al. (2015) showed that cold pools are sensitive to choices of microphysics schemes. We therefore encourage future research, such as the cold-pool model intercomparison project (Kazil et al., 2025, CP-MIP), to focus on the sensitivity of mesoscale cold-pool dynamics to such microphysical choices if we truly want to understand rain-evaporation, cold pools, and their relevance for trade-cumulus fields.

Irrespective of its idealizations, this study clearly highlights that aerosol-cloud interactions are affected by processes happening at multiple spatial and temporal scales, ranging from the microscale via the mesoscale to the large scales. For shallow cloud fields in the trades, we demonstrate that variations in the microscale can manifest themselves at the mesoscale to a degree that is comparable to the influence of large-scale controls. We consider these findings a valuable step towards understanding the mesoscales as a pre-requisite for constraining trade-cumulus climate feedbacks as well as trade-cumulus mediated aerosol forcings.

Data Availability

The *Cloud Botany* dataset is publicly accessible through the EUREC^{4}A intake catalog (https://howto.eurec4a.eu/botany_dales.html). The simulation outputs of Yamaguchi et al. (2019) are publicly available from the NOAA dataset platform (https://csl.noaa.gov/groups/csl9/datasets/data/cloud_phys/2019-Yamaguchi-Feingold-Kazil/). The data is analyzed using Python (libraries: Numpy (Harris et al., 2020), Xarray (Hoyer and Joseph, 2017), Pandas (Wes McKinney, 2010), Scipy (Virtanen et al., 2020), Statsmodel (Seabold and Perktold, 2010), Matplotlib (Hunter, 2007), and Seaborn (Waskom, 2021)). The basic profiles and time series associated with cloud-field properties, cloud organization metrics, and cold-pool properties as well as a movie of simulations are publicly available by Alinaghi et al. (2024b) and from the link https://zenodo.org/records/13868738. The coarse-graining of the total-water path anomaly fields is done using the code (SMOCs.ipynb) by Janssens (2023b) which is publicly available (https://doi.org/10.5281/zenodo.8089287).

3.5 Supplementary Information

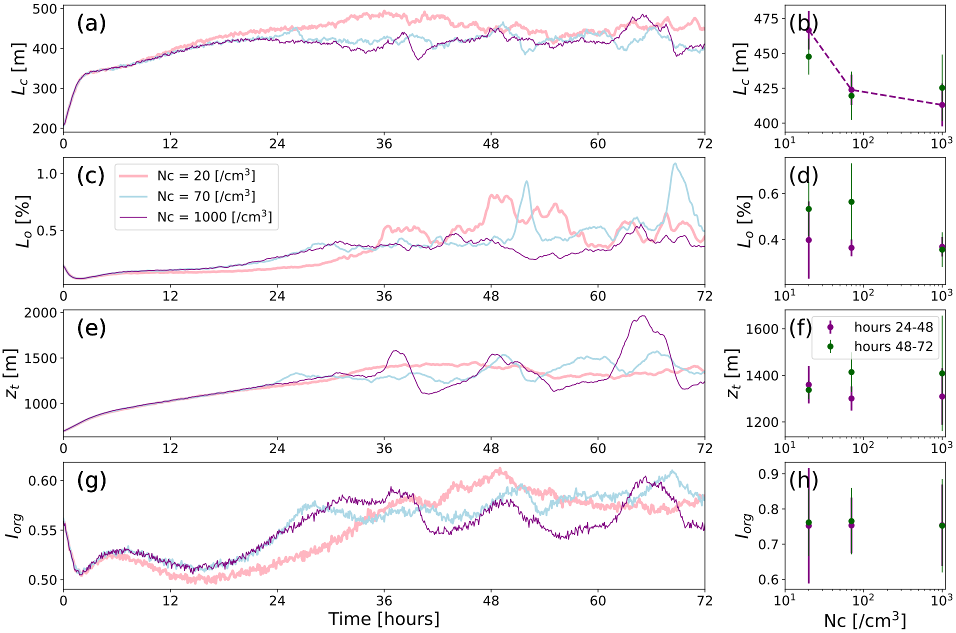

Figure S3.1: **Dependence of several mesoscale cloud organization metrics on $\mathbf{N_c}$.** The panels (a,c,e,g) show the time series of the domain-mean size of cloud objects L_c, the mean fraction of the open-sky areas L_o, the domain-mean of cloud-top height z_t, and the degree of organization I_{org} for the simulations without the diurnal cycle of insolation. Panels (b,d,f,h) show their mean responses to N_c for hours 24-48 in purple and 48-72 in green. The dashed line is shown as a visual guide where there is a trend.

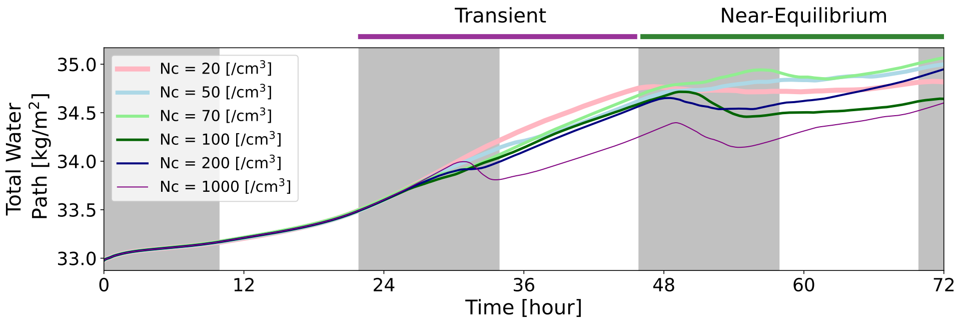

Figure S3.2: **Total-water path time series for several N_c.** The figure shows the development of the domain-mean total-water path, which is the sum of both cloud-water and water-vapor paths. The transient and near-equilibrium phases are marked by purple and green.

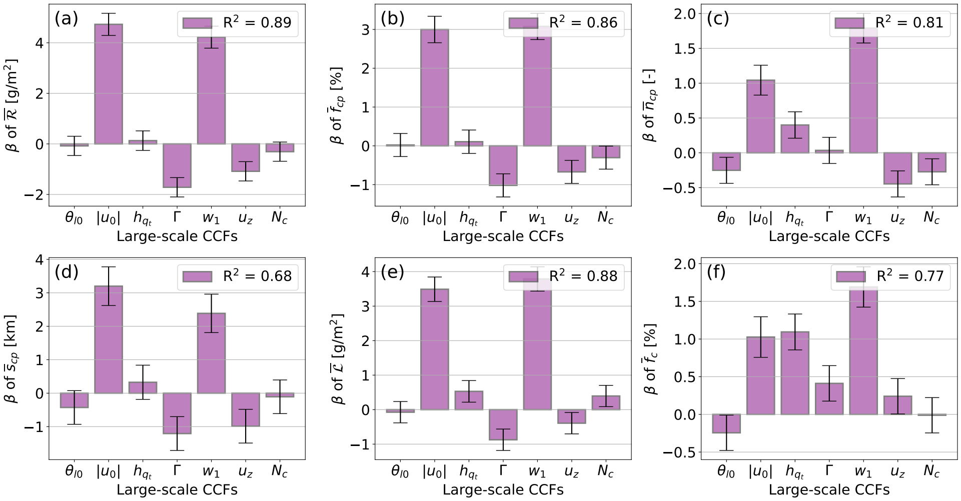

Figure S3.3: **Cloud-field response to large-scale cloud-controlling factors and cloud-droplet number perturbations.** The standardized β coefficients of the multiple regression analysis for (a) rain-water path $\overline{\mathcal{R}}$, (b) cold-pool fraction $\overline{f}_{cp}$, (c) cold-pool number $\overline{n}_{cp}$, (d) cold-pool size $\overline{s}_{cp}$ (e) liquid-water path $\overline{\mathcal{L}}$, and (f) cloud fraction $\overline{f}_c$, all averaged over the last two days of the LESs of the *Botany* ensemble. The error bars show the 95% confidence interval for each regressor. The larger the distance of the confidence interval with zero, the more significant the corresponding regressor. The p-values of the F-statistic test of all models are smaller than 10^{-15}.

4

SHALLOW CUMULUS CLOUD FIELDS ARE OPTICALLY THICKER WHEN THEY ARE MORE CLUSTERED

This chapter is published as 🗎 *Alinaghi,P., Janssens, M., Choudhury,G., Goren,T., Siebesma,A.P. & Glassmeier,F. (2024) Shallow cumulus cloud fields are optically thicker when they are more clustered. Quarterly Journal of the Royal Meteorological Society,150(763),3566–3577. Available from: https://doi.org/10.1002/qj.4783.*

Abstract

Shallow trade cumuli over subtropical oceans are a persistent source of uncertainty in climate projections. Mesoscale organization of trade cumulus clouds has been shown to influence their cloud radiative effect (CRE) through cloud cover. We investigate whether organization can explain CRE variability independently of cloud cover variability. By analyzing satellite observations and high-resolution simulations, we show that more clustered cloud fields feature geometrically thicker clouds with larger domain-averaged liquid water paths, smaller cloud droplets, and consequently, larger cloud optical depths. The relationships between these variables are shaped by the mixture of deep cloud cores and shallower interstitial clouds or anvils that characterize cloud organization. Eliminating cloud cover effects, more clustered clouds reflect up to 20 W/m^2 *more instantaneous shortwave radiation back to space.*

4.1 INTRODUCTION

MARINE shallow cumulus clouds, as the most prevalent cloud type (Johnson et al., 1999), play a vital role in the climate system by reflecting incoming solar radiation back to space (Bony and Dufresne, 2005; Bony et al., 2004, 2015). Alongside the uncertain response of cloud-controlling factors to climate change, the response of these clouds to changes in cloud-controlling factors is a long-standing uncertainty of model-based climate projections (Nuijens and Siebesma, 2019; Schneider et al., 2017). Recently, observations of contemporary climate have constrained this response (Cesana and Del Genio, 2021; Myers et al., 2021) but also emphasised the importance of the mesoscales, which climate models do not correctly represent (Vogel et al., 2022).

Shallow cloud fields in the trades exhibit a diverse range of mesoscale patterns (Bony et al., 2020a; Stevens et al., 2020). A comprehensive analysis by Janssens et al. (2021) shows that the quantification of such patterns needs at least two effective dimensions. Cloud fraction f_c as a bulk 1D measure and the organization index I_{org}, which quantifies the level of non-randomness in cloud spatial distribution within a cloud field (Tompkins and Semie, 2017; Weger et al., 1992) are an example of a suitable variable choice to represent these two dimensions. How relevant this mesoscale organization is for the low-cloud climate feedback remains an open question.

The shortwave (SW) and longwave (LW) radiative effect of trade cumulus clouds is sensitive to organization (Denby, 2020). The daily mean cloud radiative effect (CRE) varies by approximately 10 W/m^2, primarily due to differences in f_c, with a variability of about 5 W/m^2 at a fixed f_c (Bony et al., 2020a, Fig. 5). Contrary to the case of deep convective clouds (Tobin et al., 2012), where outgoing LW radiation increases with clustering, Luebke et al. (2022) suggest a correlation between increased I_{org} values and *reduced* LW warming. No influence of clustering on SW cooling is observed in their study. For stratocumulus cloud decks, McCoy et al. (2022) demonstrate that different morphologies, indicative of differences in the horizontal organization of the cloud decks, modulate the relationship between albedo and f_c.

We aim to investigate whether – independent of f_c variability – the horizontal organization of shallow cumulus cloud fields has an impact on the their net CRE. To do so, we combine satellite data with a large ensemble of large-eddy simulations by Jansson et al. (2023) (section 4.2). After removing the confounding effect of cloud fraction (section 4.3.1), we show that clustered cloud fields feature optically thicker clouds (section 4.3.2). This stems from clouds in clustered fields containing more liquid water and smaller retrieved cloud droplets (section 4.3.2). In turn, analyzing the simulations establishes that the increases in liquid-water path with clustering primarily results from increases in cloud geometric thickness (section 4.3.3). Section 4.4 concludes.

4.2 METHODOLOGY AND DATA

To disentangle the effects that spatial organization may have on the CRE independently of f_c, we adopt the following, simple model. Firstly, CRE consists of SW and LWCRE at the top of the atmosphere. In a single cloudy column, SWCRE depends on both f_c and cloud albedo A_c, approximately as

$$\mathrm{SWCRE} \approx f_c A_c S_0 \tag{4.1}$$

where S_0 is the incoming solar radiation (Ramanathan et al., 1989). Three-dimensional radiative effects could significantly alter the SWCRE, yet Singer et al. (2021) demonstrated that neglecting these effects are small at the top of the atmosphere for trade cumulus clouds. We therefore relate A_c to cloud optical depth τ_c through the plane-parallel assumption (Lacis and Hansen, 1974)

$$A_c = \frac{\tau_c}{\tau_c + 7.7}. \tag{4.2}$$

The cloud optical depth τ_c is related to the liquid-water path $\mathcal{L}$ and cloud-droplet effective radius r_e through (Han et al., 1994)

$$\tau_c = \frac{9}{5}\frac{\mathcal{L}}{r_e}. \tag{4.3}$$

The liquid-water path $\mathcal{L}$, in turn, depends on the cloud geometric thickness h and degree of adiabaticity f_{ad}, approximately given by (Feingold et al., 2017; Wood, 2006)

$$\mathcal{L} \approx f_{ad} h^2. \tag{4.4}$$

LWCRE is primarily determined by the cloud-top temperature T_c and its emissivity ϵ, following the Stefan-Boltzmann law, with

$$\text{LWCRE} \approx \epsilon \sigma T_c^4, \tag{4.5}$$

where σ represents the Stefan-Boltzmann constant (Ardanuy et al., 1991). Since T_c can be approximated by cloud-top height z_t, deeper clouds tend to be colder, emitting less LW radiation to space, thereby resulting in more LW radiative warming. Since our focus is on shallow clouds, the LWCRE variability is minimal, and SWCRE variability will govern the net CRE variability; we show this in section 4.3.1. In the following sections, we will therefore use the relations above to interpret how remotely sensed and simulated f_c, τ_c, $\mathcal{L}$, r_e, f_{ad} and h make up variations in SWCRE, due only to the spatial patterning of clouds.

Following previous studies (Bony et al., 2020a; Janssens et al., 2021; Stevens et al., 2020), we focus on clouds over the tropical Atlantic Ocean to the east of Barbados (10°-20°N, 48°-58°W), which have been shown to be representative for the trades (Medeiros and Nuijens, 2016). Our analysis covers December to May of 2002 to 2020. The satellite dataset used here combines data from NASA's Moderate Resolution Imaging Spectroradiometer (MODIS) aboard the Aqua satellite, with data from the Clouds and the Earth's Radiant Energy System (CERES) instrument. We compute organization metrics from MODIS' cloud masks with 1 km spatial resolution. For each cloudy scene, we calculate two metrics - cloud fraction (f_c) and degree of organization (I_{org}). The metric I_{org} is derived based on the distribution of the nearest neighbor distances (Janssens et al., 2021; Weger et al., 1992), which characterizes cloud fields as clustered when $I_{org} > 0.5$, random at $I_{org} = 0.5$, and regular for $I_{org} < 0.5$. The preprocessing of MODIS' cloud masks follows Janssens et al. (2021): Scenes with > 20% cirrus coverage (≈5% of the total data) are excluded, as are cloud fields with solar zenith angles > 45° (≈15% of the total data). In line with the analysis of Bony et al. (2020a, Fig. 5), we use the full 10° × 10° domain, which leads to excluding about 50% of the total data due to the satellite swath not covering the whole 10° × 10° domain. Following Schulz et al. (2021), we focus solely on shallow clouds by excluding scenes with cloud-top heights $z_t > 4\,\text{km}$, which excludes about 5% of the total data. After preprocessing, out of about 3200 cloud

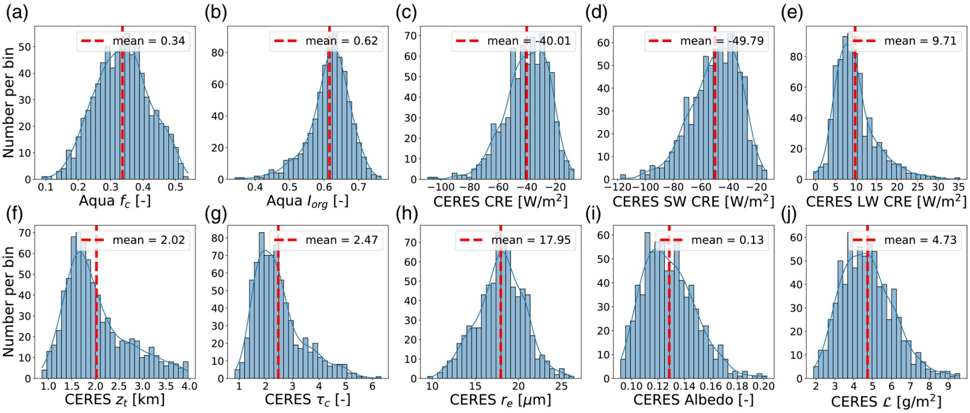

Figure 4.1: **Distribution of cloud field properties from Aqua MODIS and CERES satellite data.** (a) cloud fraction f_c, (b) degree of organization I_{org}, (c) domain-mean net cloud radiative effect (CRE), (d) domain-mean SWCRE, (e) domain-mean LWCRE, (f) domain-mean cloud-top height z_t, (g) domain-mean cloud optical depth τ_c, (h) domain-mean cloud effective radius r_e, (i) domain-mean cloud field albedo, and (j) domain-mean liquid-water path $\mathcal{L}$.

scenes, approximately 750 cloud fields remain for analysis, which is about 25% of the total data. Nevertheless, the distributions of f_c and I_{org} shown in Figs. 4.1(a, b) confirm that the remained data still covers a rich spectrum of patterns, and is similar to distributions shown by Bony et al. (2020a).

CERES provides hourly top-of-the-atmosphere SW and LW radiative fluxes for all-sky and clear-sky conditions, as well as τ_c, A_c, z_t, $\mathcal{L}$, and r_e. The CERES dataset features a spatial resolution of 1°. We select CERES data around 13:30 local time, which corresponds to the overpass time of the Aqua satellite. SWCRE and LWCRE are calculated as the difference between the all-sky and clear-sky radiative fluxes at the top of the atmosphere. For each cloud scene, we calculate domain-mean values of cloud properties provided by CERES. The distribution of CERES data is shown in Figs. 4.1(c-j).

We extend our satellite analysis with the *Cloud Botany* dataset (Jansson et al., 2023). This is a large ensemble (ca. 100 members) of high-resolution (100 m) large-eddy simulations (LES) of shallow cumulus clouds with a domain size of 150 km by 150 km. It was initialized with a variety of conditions derived from ERA5 reanalysis data (Hersbach et al., 2020) of trade cumuli that cover the climatological conditions of the area under consideration. We refer to the dataset paper, Jansson et al. (2023), for details. Our motivation for employing the *Botany* simulations is twofold. Firstly, considering that satellite retrievals of liquid-water path $\mathcal{L}$ (and effective radius r_e) might be underestimated (overestimated) in broken cloud fields containing small clouds (Cho et al., 2015; Coakley et al., 2005; Painemal and Zuidema, 2011; Seethala and Horváth, 2010; Zhang and Platnick, 2011), the simulations support that our results are physical. Secondly, the simulations provide data on cloud-base height (z_b) and cloud geometric thickness (h) so that we can investigate how those vertical characteristics are correlated to organization. The distributions of lifting-condensation level as well as z_b (Fig. S2.1) show qualitative agreement with those of Barbados-Cloud Observatory data as shown in (Albright et al., 2023, Figs. 2, 3). We use hourly data from hours 37-43 of the simulations (574 cloud fields in total). These times are chosen because they approximately align with the daily overpass times of the Aqua satellite to match the diurnal phase. To determine the geometric thickness h of each cloudy column, we calculate the difference between the altitudes of the highest and lowest cloudy pixels where the liquid water specific humidity is larger than zero. Subsequently, for each cloud field, we compute the domain-averaged h. We further compute the mean size of cloud objects within each cloud field using: $L_c = (\sum_1^n \sqrt{A_i})/n$, where A_i represents the area of each individual cloud object i, and n corresponds to the total number of cloud objects within the field.

4.3 RESULTS & DISCUSSIONS

4.3.1 CLOUD CLUSTERING IMPACTS CRE INDEPENDENTLY OF f_c VARIABILITY

Bony et al. (2020a) showed that trade cumulus mesoscale organization affects CRE through variations in f_c: scenes with organisation types of higher cloud cover have a larger, negative CRE. In this section, we aim at investigating whether mesoscale organization still affects CRE, independently of f_c. Figures 4.2(a-c) show that more clustered clouds (higher I_{org}) reflect less SW radiation towards space (smaller magnitude of SWCRE). In addition, increased clustering is also correlated to decreased LWCRE. Overall, the warming effect induced by the SW component is partially compensated by the reduced LW warming. Consequently, enhanced clustering of clouds results in diminished net cloud radiative cooling.

It is crucial to emphasize that the relationships illustrated in Figs. 4.2(a-c) are confounded by the variability of f_c, as f_c is correlated with I_{org} ($R^2 = 0.61$), SWCRE ($R^2 = 0.51$), and LWCRE ($R^2 = 0.34$) (see also Fig. S2.2, Fig. 4.2, d, e). To better understand how f_c controls the relationships between organization and radiation, Figs. 4.2(d-f) present the same data as Figs. 4.2(a-c), but grouped into quartiles of f_c. Figure 4.2(d) shows that although I_{org} and SWCRE exhibit a positive correlation across the entire dataset (Fig. 4.2, a), they demonstrate a negative correlation within each f_c bin. Hence, the relationship between I_{org} and SWCRE presented in Fig. 4.2(a) emerges because I_{org} itself depends on f_c (purple to yellow lines in Figs. 4.2, d-f). Once we remove this correlation between I_{org} and f_c, e.g. by binning on f_c, we observe that the SWCRE becomes more negative when the cloud fields become more clustered (lines at constant f_c have a negative slope). Similarly, Fig. 4.2(e) shows that the strong negative I_{org}-LWCRE correlation (Fig. 4.2, b) is almost entirely due to variations in f_c; it almost vanishes upon grouping the data by f_c. The net CRE is dominated by its SW component (Fig. 4.2, f), and therefore follows the results from Fig. 4.2(d). Hence, Figs. 4.2(a-c) essentially capture the findings by Bony et al. (2020a): They show that variations in f_c to first order control variations in SWCRE.

To eliminate the confounding effect of f_c on the I_{org}-CRE relationship, we employ the concept of partial correlation analysis (Baba et al., 2004). For any given metric (e.g., X), we eliminate the variability associated with f_c using a regression analysis,

$$X = c \cdot f_c + X|f_c, \tag{4.6}$$

where f_c serves as the regressor, c represents the coefficient, and $X|f_c$ denotes the remaining variability in X that cannot be explained by f_c. It should be noted that Eq. 4.6 does not

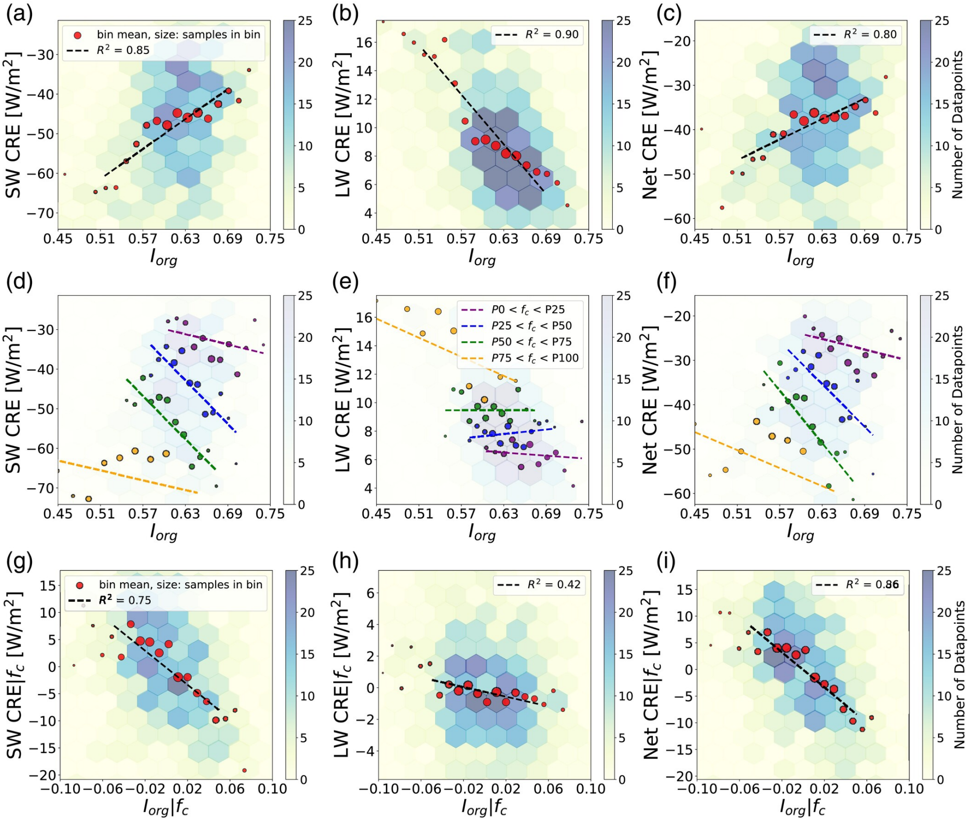

Figure 4.2: **Dependence of domain-mean CRE on clustering.** In the first row (a-c), the relationships between I_{org} and SWCRE (a), LWCRE (b), and net CRE (c) are illustrated. The second row (d-f) presents the same relationships, but the data is grouped into four classes based on the 0^{th} (P0), 25^{th} (P25), 50^{th} (P50), 75^{th} (P75), and 100^{th} (P100) percentiles of f_c, indicated by colors ranging from purple to yellow, representing low to high f_c, respectively. The third row (g-i) shows the same relationships but with removing the f_c variability through partial correlation analysis (Eq. 4.6). The mean values of I_{org} (for the 3^{rd} row, $I_{org}|f_c$) in each bin are denoted by red (purple, blue, green and yellow for the 3^{rd} row) circles, with their size proportional to the number of points in the bin. The dots are fitted with a dashed line. Values below the 5^{th} and above the 95^{th} percentile of I_{org} (for the 3^{rd} row, $I_{org}|f_c$) are excluded from the fit.

keep f_c constant. In a scatter plot with a linear fit $c \cdot f_c$, $X|f_c$ instead measures the distance from the regression line (Fig. S2.3). Partial correlation is conceptually similar to grouping data by a confounding variable, as in Figs. 4.2(d-f), but it continuously controls for the confounder across the whole dataset. This gives more statistically significant correlations compared to simple grouping, where the number of data points can drastically decrease after the grouping has been performed. The different colors in Figs. 2(d-f) correspond to subtracting different offsets $c \cdot f_c$ from X. By measuring the distance from the central fit line, the method thus collapses all the lines in Figs. 2(d-f) into a single line.

Figs. 4.2(g-i) present the variables, with their partial correlation to f_c removed. Fig. 4.2(g) shows that as $I_{org}|f_c$ increases, SWCRE$|f_c$ becomes more negative, i.e., as clouds cluster, they reflect more incoming SW radiation. Quantitatively, as $I_{org}|f_c$ varies between -0.05 to 0.05, the radiative cooling induced by SW reflection increases by approximately 20 W/m^2. This confirms that the positive correlation observed in Fig. 4.2(a) is due to I_{org} and SWCRE being negatively correlated to f_c (Fig. 4.2, d). Similarly, after elimination of f_c variability, the response of LWCRE to cloud clustering is strongly reduced to about 1 W/m^2 (Fig. 4.2, h), indicating that the correlation between I_{org} and LWCRE in Fig. 4.2(b) is almost solely due to their mutual correlation with f_c (Fig. 4.2, e). The variability in LWCRE due to clustering is thus similar in magnitude to the LW radiative effect (≈ 0.75 W/m^2) of the “cloud twilight zone” (Eytan et al., 2020). Ultimately, as Fig. 4.2(i) illustrates, the dependence of net CRE on $I_{org}|f_c$ arises almost exclusively from the dependence of the SW component on cloud clustering. In summary, our findings of this section emphasize that mesoscale organization affects CRE, even after controlling for f_c variability.

4.3.2 CLUSTERING AND CLOUD OPTICAL THICKNESS ARE POSITIVELY CORRELATED

In the previous section, we eliminated the impact of f_c on the I_{org}-SWCRE relationship. The remaining variability in SWCRE after controlling for f_c is primarily due to variations in A_c (Eq. 4.1): A bi-linear regression with f_c and A_c as regressors can explain 94% of variability in SWCRE in our dataset (Fig. S2.4). This confirms that the impact of 3D radiative effects is small compared to f_c and A_c in these large cloud fields. Having 3D effects excluded, the remaining variability in SWCRE primarily corresponds to changes in cloud albedo and equivalently cloud optical depth τ_c (Eq. 4.2).

Figure 4.3(a) displays the variability of cloud patterns in a plane spanned by $\tau_c|f_c$ and $I_{org}|f_c$. This figure shows a continuous range of patterns, ranging from small, unclustered clouds in the lower left corner to large, highly-clustered clouds in the upper right corner. On average, $\tau_c|f_c$ increases with increasing $I_{org}|f_c$ (Fig. 4.3, b). Quantitatively, a 0.1 increase in $I_{org}|f_c$ corresponds to a 0.5 increase in $\tau_c|f_c$, which is about 10% of the total τ_c variability (Fig. 4.1, g). Such a 0.1 increase in $I_{org}|f_c$ results in an approximately 0.01 increase in the domain-mean albedo (Fig. S2.5). In trade-wind regimes, even such small albedo variability makes up a non-negligible portion (roughly 10%, Fig. 4.1, i) of the total albedo variability, consistent with Denby (2023). The relationship between $I_{org}|f_c$ and $\tau_c|f_c$ indicates that horizontal cloud field organization, as measured by I_{org}, is linked to its optical properties, as captured by τ_c: trade cumuli are optically thicker when they are more clustered.

As theoretically expected (Eq. 4.3), τ_c is proportional to $\mathcal{L}/r_e$ in our dataset (Fig. S2.6). Figure 4.4 shows that both, $\mathcal{L}$ and r_e, contribute to mediating the relationship between clustering and optical depth. With the f_c effect eliminated, there is a positive correlation between the degree of cloud clustering and the amount of liquid water present within the clouds (Fig. 4.4, a). Similarly, as the level of clustering increases, clouds tend to exhibit smaller radii r_e (Fig. 4.4, b).

Stevens et al. (2020) introduced a subjective classification of patterns, which they termed *Sugar*, *Gravel* and *Flowers*. *Sugar* consists of small randomly distributed clouds. *Gravel* is associated with ring-like structures. Their organization is not as random as for the *Sugar* type but still features values of I_{org} that indicate an unclustered state. *Flowers* are commonly highly-clustered groups of circular clouds with clear-sky regions between them. Our $\mathcal{L}$-I_{org} relationship seems to be in contrast to Schulz et al. (2021) who show that individual

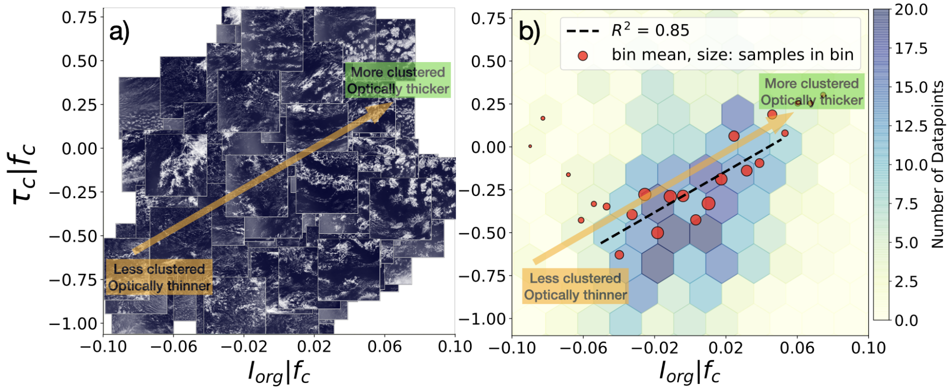

Figure 4.3: **Dependence of domain-mean cloud optical depth on clustering.** The scatter plot of MODIS cloud features (a) and the 2-dimensional histogram (b) depict the $I_{org}|f_c$–$\tau_c|f_c$ relationship. Specifically, for the scatter plot in (a), instead of displaying individual points, the entire cloud field is visualized to enhance pattern visualization. Clouds are represented in white, while the blue background represents the ocean color (MODIS true-color images). For plot (b), the mean values of $I_{org}|f_c$ in each bin are denoted by red circles, with their size proportional to the number of points in the bin. The red dots are fitted with a dashed black line. Values below the 5^{th} and above the 95^{th} percentile of $I_{org}|f_c$ are excluded from the fit.

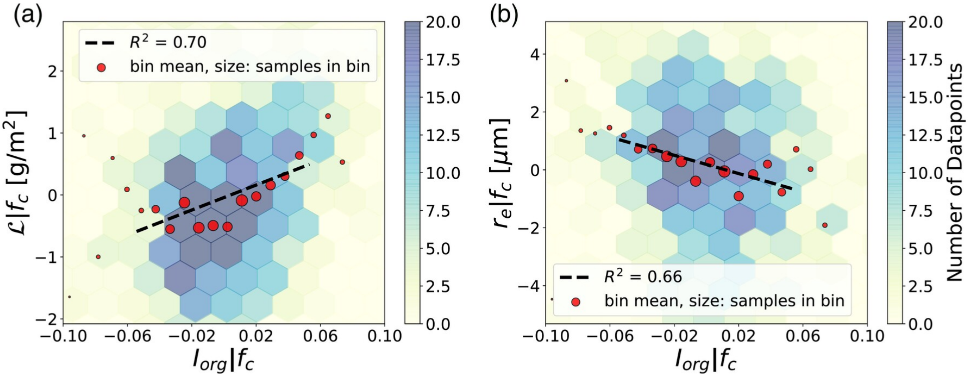

Figure 4.4: **Dependence of domain-mean liquid water path and effective radius on clustering.** The figure shows the 2D histograms of the relationships between $I_{org}|f_c$ and $\mathcal{L}|f_c$ (a), and between $I_{org}|f_c$ and $r_e|f_c$ (b). The mean values of $I_{org}|f_c$ in each bin are denoted by red circles, with their size proportional to the number of points in the bin. The red dots are fitted with a dashed black line. Values below the 5^{th} and above the 95^{th} percentile of $I_{org}|f_c$ are excluded from the fit.

clouds in unclustered *Gravel* configuration have higher liquid-water path $\mathcal{L}$ compared to individual clouds in *Flowers* configuration, which is highly-clustered. To reconcile this with our results, we need to remind ourselves that the large cloud scenes analyzed here contain a mixture of different clouds. Stevens et al. (2020) report that *Gravel* clouds tend to coexist with *Sugar*. For *Flowers* such a coexistence is less pronounced. Instead, *Flowers* feature anvils, stratiform outflows that form once the updrafts encounter stable layers such as the inversion, causing the cloud to grow horizontally. Such shallow cumulus anvils

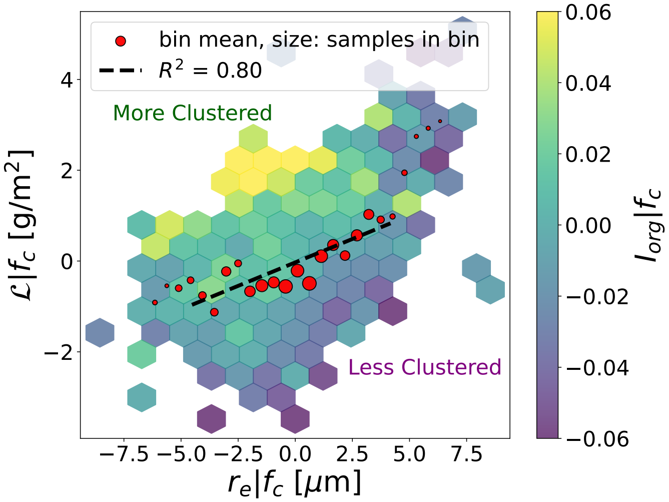

Figure 4.5: **Relationship between domain-mean liquid-water path and effective radius**. This figure shows that $\mathcal{L}|f_c$ is positively correlated to $r_e|f_c$. The figure further shows that with increased clustering $I_{org}|f_c$, i.e., going from lower right corner to upper left corner, r_e decreases, while $\mathcal{L}$ increases. The mean values of $r_e|f_c$ in each bin are denoted by red circles, with their size proportional to the number of points in the bin. The red dots are fitted with a dashed black line. Values below the 5^{th} and above the 95^{th} percentile of $r_e|f_c$ are excluded from the fit.

have notable geometric thickness (up to 600 m (Dauhut et al., 2023)). This means that anvil cloudiness is optically thicker and more reflective than typical *Sugar*. When considering two cloud fields with identical f_c, it therefore seems reasonable that a *Flower*-dominated field features a larger domain-averaged $\mathcal{L}$ as compared to a field dominated by *Sugar* and *Gravel*.

Similarly, the relationship between I_{org}, $\mathcal{L}$ and r_e might seem unexpected: Based on adiabatic parcel lifting, we would expect $\mathcal{L}$ and r_e to be positively correlated, while Fig. 4.4 suggests a negative correlation. When directly correlating $\mathcal{L}$ versus r_e we find the expected positive correlation, as shown in Fig. 4.5. However, Fig. 4.5 further shows that with increasing $I_{org}|f_c$, $\mathcal{L}$ increases while r_e decreases, indicating that more clustered cloud fields contain more liquid water with smaller effective radius. To hypothesize why, we use an example snapshot from a scene (Fig. S2.7, a) at the high end of the $I_{org}|f_c$ values: In such scenes, clouds have substantially smaller r_e in their veils compared to their core updrafts. In contrast, unclustered cloud fields exhibit a more homogeneous r_e with relatively larger values (Fig. S2.7, b). These snapshots suggest that for highly-clustered cloud fields, the average $\mathcal{L}$ is primarily influenced by their cores, while the average r_e is influenced by their veils. This is consistent with the fact that $\mathcal{L}$ is proportional to r_e^6 (Goren et al., 2022), resulting in a more pronounced contrast between the core and veils in $\mathcal{L}$ compared to r_e. This could well explain why the average $\mathcal{L}$ of highly-clustered cloud fields is larger compared to that of unclustered cloud fields, while their average r_e is smaller in comparison to unclustered cloud fields.

It is of utmost importance to recognize that satellite retrievals of $\mathcal{L}$ and r_e over broken clouds come with uncertainties, as documented in previous studies (Painemal and Zuidema, 2011; Seethala and Horváth, 2010; Zhang and Platnick, 2011). These uncertainties can result in an overestimation of r_e and an underestimation of $\mathcal{L}$, especially for small clouds, such as *Sugar* and *Gravel.* This is because these clouds might feature smaller sizes compared to the resolution of satellites ($\approx$ 1 km), leading to more frequent partially filled pixels (Cho et al., 2015; Coakley et al., 2005). By utilizing standard satellite products, which exclude highly uncertain pixels associated with very small clouds (see Fig. S2.7, b), these biases are mitigated to some extent and enhance the reliability of our analysis of r_e and $\mathcal{L}$. Nonetheless, it is essential to note that this analysis urges the need for further modeling or in-situ observational studies exploring the relationship between the organization and microphysics of trade cumulus clouds.

It is interesting to contrast the small droplets in relatively thick anvils described here to the very large droplet sizes and optically thin veil clouds that have been reported in the context of the stratocumulus-to-cumulus transition (Wood et al., 2018). While O et al. (2018b) report an increase in the corresponding ultra-clean conditions with boundary layer height, this relationship is unlikely to extend to deep trade cumulus *Flowers*, which can be considered shallow mesoscale convective systems with complex outflow dynamics (Dauhut et al., 2023). On the microphysical process level, ultra clean conditions have been associated with strong precipitation scavenging (O et al., 2018a), while Radtke et al. (2023) discuss that the conversion efficiency to precipitation decreases with increasing clustering in trade cumulus.

Overall, our discussion of the relationship between liquid-water path and effective radius to clustering and the resulting effects on optical depth highlight that organized cloud fields cannot be conceptualized with a single, typical profile of cloudiness. Instead, addressing horizontal spatial variability necessitates the consideration of at least two distinct cloud types, associated with horizontal variations in the profiles of liquid water and droplet sizes (see sketches in Fig. 4.7).

4.3.3 MEAN CLOUD GEOMETRIC THICKNESS INCREASES WITH CLUSTERING

For an entraining lifting parcel, liquid-water path $\mathcal{L} \propto f_{ad}h^2$ (Eq. 4.4). To explain the observed I_{org}-$\mathcal{L}$ relationship, we therefore investigate the relationships of I_{org} to geometric cloud depth h and degree of adiabaticity f_{ad} in the *Botany* simulations. We repeat the analysis from Sects. 4.3.1 and 4.3.2 for the *Botany* dataset. We notice that the correlation between f_c and I_{org} is smaller (R of 0.1) in the *Botany* dataset that features smaller domain size compared to our satellite data (Fig. S2.8, a). This is in line with the results of Janssens et al. (2021) on satellite data over 500 km domains in which the f_c-I_{org} correlation (R) is about 0.3 (their Fig. S2 in the supplementary information). This shows that the f_c-I_{org} correlation decreases with reducing the domain size. We hypothesize that reducing the domain size increases the variability in f_c, with f_c potentially reaching values of 1 (Fig. S2.9). Conversely, reducing the domain size decreases the probability of a cloud field featuring more than one type of pattern, thus reducing the variability in I_{org} (Fig. S2.9). Therefore, with increased f_c towards 1, I_{org} cannot decrease less than a limit, as reduced domain size shrinks its variability. This potentially decreases the covariance between f_c and I_{org}, weakening the strength of the f_c-I_{org} correlation. f_c and I_{org} being almost orthogonal in the *Botany* data (Fig. S2.8, a) implies that combinations of f_c and I_{org} explain most patterns that develop in the *Botany* dataset, and their relation to τ and the CRE might be understood without controlling for f_c (Janssens, 2023a, Chapter 7). Here, we still remove the effect of f_c from both CRE and I_{org}, to solely investigate the effect of I_{org} on CRE independent of f_c variations and remain consistent with the analysis in Sect. 4.3.1.

Repeating the analysis for the simulation data shows qualitative agreement with the observations (Fig. S2.10(a-c) and Fig. S2.11) and thus justifies using the simulations to further analyse the relationships between I_{org}, h and f_{ad}. Note that the discrepancy in the response of r_e to clustering between simulations and satellite data (Fig. S2.10, d) is expected from the fixed cloud droplet number in the simulations but does not fundamentally affect our discussion of $\mathcal{L}$ here.

Figure 4.6(a) shows that the domain-averaged geometric thickness increases by more than 100 m as cloud fields become more clustered (increasing $I_{org}|f_c$). Additionally, compared to f_{ad}, the variability in h has a significantly larger influence on the value of $\mathcal{L}$ (Fig. S2.12). Thus, our LES-based results indicate that the simulated increase in $\mathcal{L}$ due to enhanced clustering (Fig. S2.10, c) primarily stems from the geometric thickening of cloud fields.

Figure 4.6(b) further explores the relationship between horizontal and vertical cloud field properties and shows that the average size of cloud objects (L_c) increases with $I_{org}|f_c$. This positive correlation shows that cloud horizontal extent as quantified by L_c, is positively correlated to cloud vertical extent as quantified by h, consistent with the findings of Feingold et al. (2017). The figure moreover illustrates that an increase in $I_{org}|f_c$ corresponds to a rise in the domain-average cloud-base height (z_b). Note that z_b is not the lifting condensation level; instead, it represents the lowest height of a cloudy pixel within each column. This means that a higher domain-mean z_b is an indication of the presence of more anvils in the field. Overall, Fig. 4.6 demonstrates that enhanced clustering is correlated to a higher occurrence of larger cloud objects with elevated domain-mean z_b, indicating a larger anvil extent.

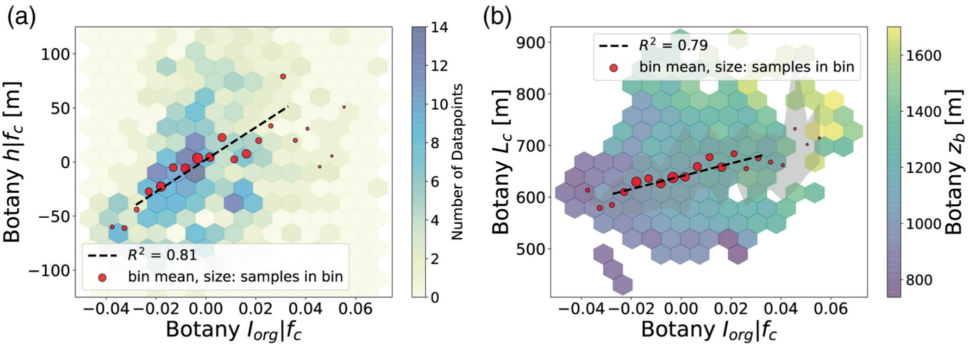

Figure 4.6: **Dependence of domain-mean geometric thickness, average size of cloud objects, and domain-mean cloud-base height on clustering.** (a) The figure shows the 2D histogram of the relationship between $I_{org}|f_c$ and $h|f_c$. (b) The plot shows the relationship between $I_{org}|f_c$ and the mean-field cloud object size (L_c) with contour colors representing the values of domain-averaged cloud-base height (z_b). The gray shade indicates the inter-quartile range variability of L_c in each bin of $I_{org}|f_c$. For both plots, the mean values of $I_{org}|f_c$ in each bin are denoted by red circles, with their size proportional to the number of points in the bin. The red dots are fitted with a dashed black line. For both plots, values below the 5^{th} and above the 95^{th} percentile of $I_{org}|f_c$ are excluded from the fit.

4.4 Conclusions & Outlook

We have explored the impact of shallow cumulus cloud field organization on cloud radiative effects, where confounding variability of f_c was removed through partial correlation analysis (Eq. 4.6). Based on satellite data, our analysis shows that an increased level of clustering ($I_{org}|f_c$) results in up to 20 W/m^2 higher SW reflection to space (Fig. 4.2, g, i). We observe that, irrespective of f_c variations, more clustered cloud fields exhibit, on average, higher liquid water path (Fig. 4.4, a), smaller cloud droplets (Fig. 4.4, b), and consequently, greater optical thickness (Fig. 4.3). A complementing ensemble of large-eddy simulations indicates that increased clustering corresponds to geometrically thicker cloud fields that feature increased anvilness (Fig. 4.6). Figure 4.7 summarizes these results. Collectively, they suggest that, eliminating the effect of f_c, the distribution of horizontal cloud sizes ultimately relates to the vertical extent of clouds, subsequently influencing liquid-water path and cloud optical depth, and ultimately albedo and SWCRE.

What do our results mean in terms of the cloud feedback of trade cumulus? To translate the potential impact of increased SW radiative cooling from organization (independently of f_c) into cloud feedback estimates, a worthwhile follow-up effort would be to repeat our analysis for all trade-wind regions. Such global statistics would contribute to a comprehensive quantification of the sensitivity of CRE to I_{org}. Considering the sensitivity of mesoscale organization to cloud-controlling factors, Myers et al. (2021) (their Supplementary Information) show that in addition to an increase in sea-surface temperature, which is not expected to trigger a notable response in trade cumulus cloudiness (Cesana and Del Genio, 2021; Myers et al., 2021), Estimated Inversion Strength (EIS) *is* projected to moderately increase, and surface wind to slightly decrease. According to Bony et al. (2020a) such an increase in EIS would favor high-cloud-fraction *Flowers* over *Gravel* and *Sugar* with lower cloud fractions. In contrast, the decreasing surface wind would favor *Sugar*.

While our results highlight the tight relationship between horizontal cloud organization and geometric thickness, whether cloud fraction and optical depth interact positively or negatively in response to drivers of organization remains an open question. To address this interplay, we need to further explore how mesoscale processes (George et al., 2023; Janssens et al., 2023; Vogel et al., 2021) modulate cloud fraction, liquid-water path, effective radii, and anvil extent.

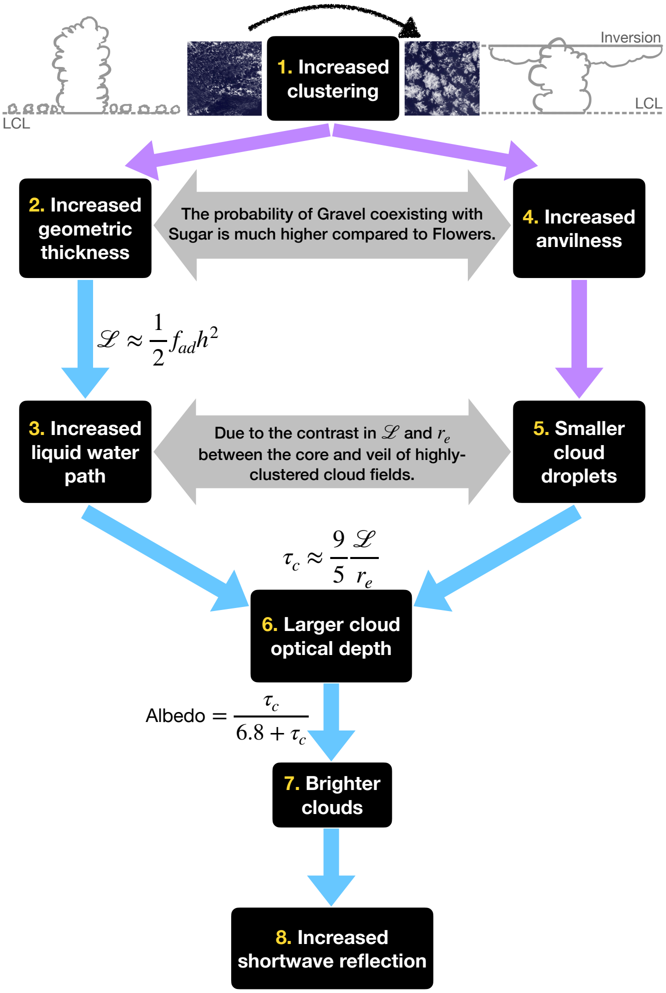
Inversion
LCL
LCL
1. Increased clustering
2. Increased geometric thickness
The probability of Gravel coexisting with Sugar is much higher compared to Flowers.
4. Increased anvilness
$\mathscr{L} \approx \frac{1}{2} f_{ad} h^2$
3. Increased liquid water path
Due to the contrast in $\mathscr{L}$ and r_e between the core and veil of highly-clustered cloud fields.
5. Smaller cloud droplets
$\tau_c \approx \frac{9}{5}\frac{\mathscr{L}}{r_e}$
6. Larger cloud optical depth
Albedo $= \frac{\tau_c}{6.8 + \tau_c}$
7. Brighter clouds
8. Increased shortwave reflection

Figure 4.7: **Summary of results.** Comparing two cloud fields with identical cloud cover, the highly-clustered cloud field features a larger domain-averaged geometric thickness, a higher liquid water path, more frequent anvils with smaller cloud droplets, and consequently, brighter clouds and therefore larger SW reflection in comparison to the unclustered cloud field. Blue arrows and corresponding equations are supported by theory and thus imply causality. Purple arrows are main results of our study, which only indicate correlations. The gray arrows illustrate apparent paradoxes which are discussed in section 4.3.2.

Data Availability

The cloud masks, provided by Aqua satellites, related to NASA's MODIS instrument, can be extracted from level-1 Atmosphere Archive & Distribution System Distributed Active Archive Center (http://dx.doi.org/10.5067/MODIS/MYD06_L2.061). The data set related to CERES instrument is made available by Synoptic TOA and surface fluxes and clouds (SYN1deg - level 3) at https://ceres.larc.nasa.gov/data/#syn1deg-level-3. Preprocessing of cloud masks alongside calculation of organization metrics were done using the cloud metrics Github repository available at https://github.com/cloudsci/cloudmetrics. The Botany dataset was downloaded using the EUREC^{4}A intake catalog (https://howto.eurec4a.eu/botany_dales.html). The data was analyzed utilizing Python (used libraries: Numpy (Harris et al., 2020), Pandas (Wes McKinney, 2010), Scipy (Virtanen et al., 2020), Matplotlib (Hunter, 2007), and Seaborn (Waskom, 2021)). ChatGPT (OpenAI: https://openai.com/blog/chatgpt) has been used for copy-editing during the preparation of the manuscript.

4.5 Supplementary Information

This file includes some additional figures for supporting the main text of our paper (First part). Additionally, the detailed calculation of adiabaticity is presented (Second part).

Supplementary Figures

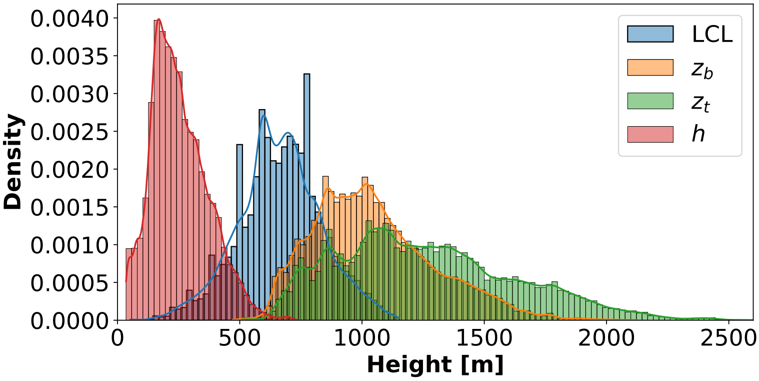

Figure S4.1: The distribution of lifting-condensation level (LCL), domain-mean cloud-base height (z_b), domain-mean cloud-top height (z_t), and domain-mean cloud geometric thickness (h) along the entire *Botany* ensemble.

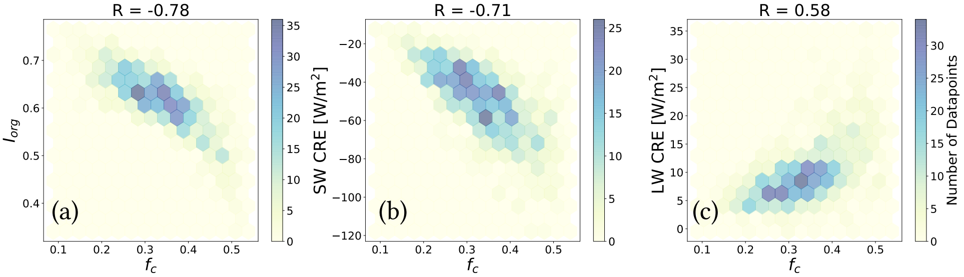

Figure S4.2: The 2D histograms of the relationships between f_c and (a) I_{org}, (b) SWCRE, and (c) LWCRE with the reported Pearson's correlation (R).

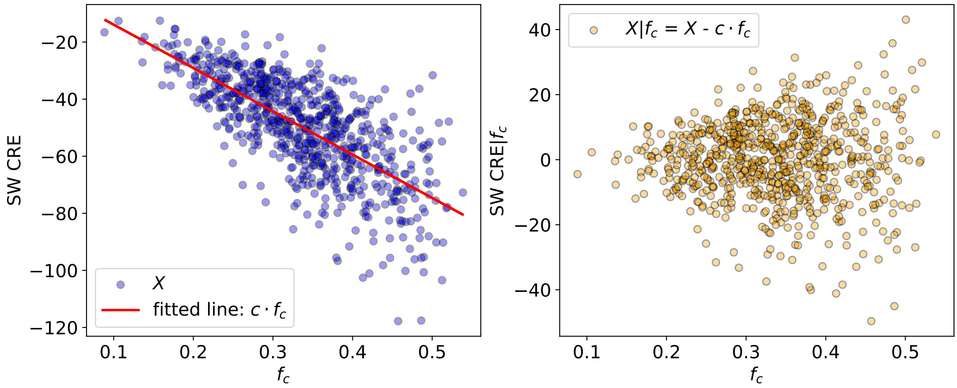

Figure S4.3: The figure illustrates Eq. 4.6 and emphasizes that we do not fix but control for f_c. Here, we show the example for X =SWCRE. The term $X|f_c$ quantifies variability in SWCRE that cannot be explained by f_c.

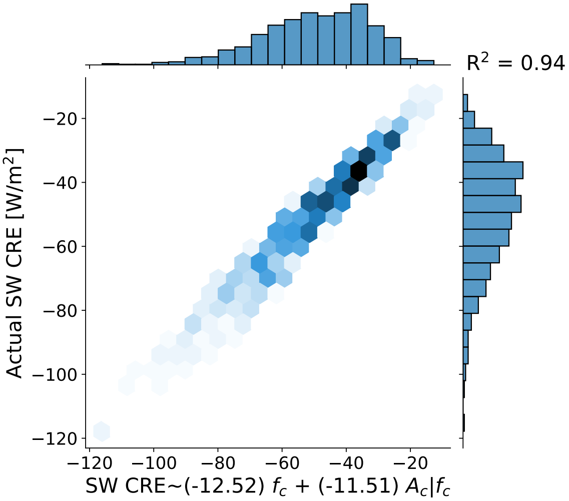

Figure S4.4: The result of the bi-linear regression analysis in which the target value is SWCRE and the regressors are f_c and Ac|f_c (Ac: cloud albedo observed by CERES). The reported coefficients are for the standardized f_c and Ac|f_c. This plots ensures that the derived f_c from MODIS cloud masks in addition to the observed albedo by CERES can significantly capture the variability in SWCRE.

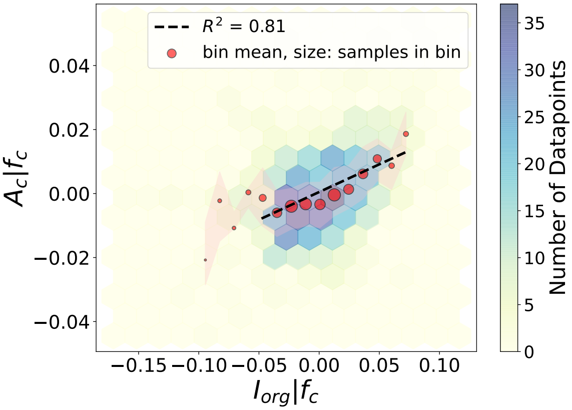

Figure S4.5: The relationship between I_{org} and cloud albedo (A_c), having the effect of f_c eliminated.

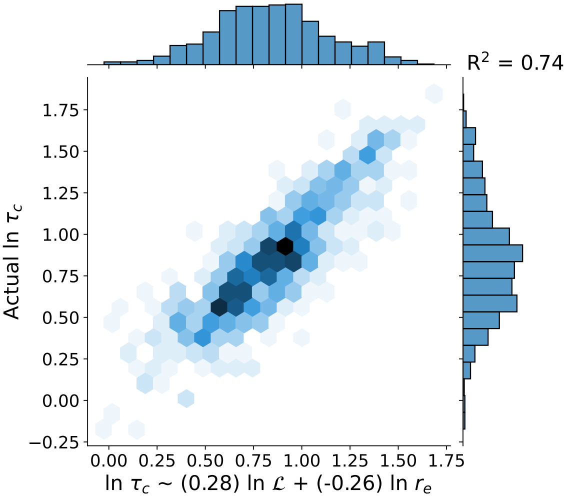

Figure S4.6: The result of the bi-linear regression analysis in which the target value is ln τ_c and the regressors are ln $\mathcal{L}$ and ln r_e. The reported coefficients are for the standardized ln $\mathcal{L}$ and ln r_e. This plots ensures that ln $\mathcal{L}$ and ln r_e can significantly capture the variability in ln τ_c, in line with theory.

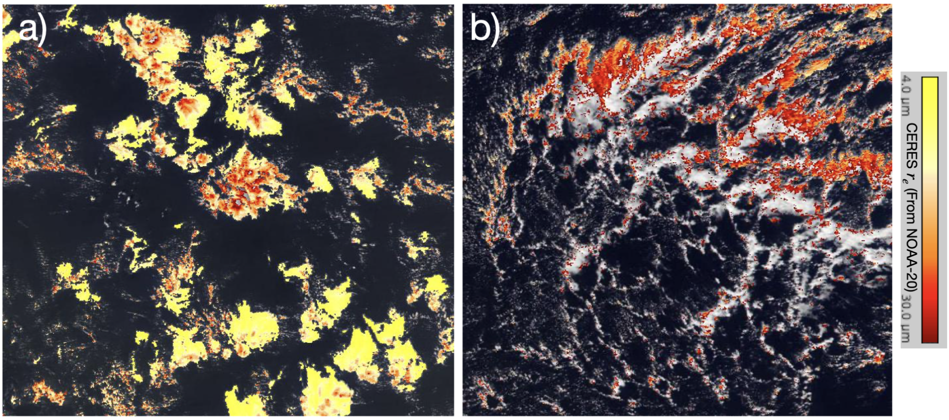

Figure S4.7: **Satellite snapshots of cloud-droplet effective radius.** A highly-clustered (a) and an unclustered cloud field snapshots (from NASA Worldview) taken by NOAA-20 satellite on 03/Feb/2021 (10°-16°N, 51°-57°W) and 19/Dec/2021 (14°-18°N, 48°-53°W), respectively. The cloud fields are colored by the value of standard effective radius r_e product, which goes from 4 (yellow) to 30 (red) μm. Note that in the standard satellite product of the field shown in (b), smaller clouds (pixels with low cloud fractions) are already removed from the scene due to high uncertainty in their retrievals. Therefore, to some extents, it assures that our analysis of effective radius is not considerably affected by retrieval issues of these small clouds.

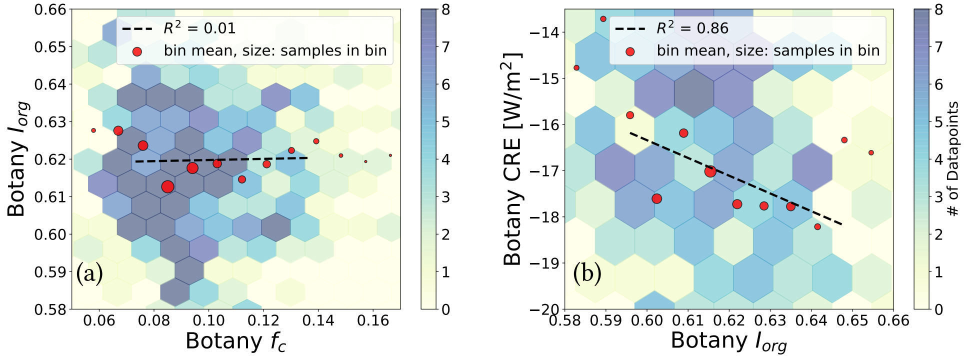

Figure S4.8: The figure shows the relationships between a) f_c and I_{org} and b) I_{org} and (net) CRE in Botany simulations. This figure shows that as the domain size decreases from ≈1100 km (in satellites) to ≈150 km (in *Botany*), the correlation between f_c and I_{org} drastically decreases, meaning that f_c and I_{org} do not share information in smaller domains. As a result, the correlation between I_{org} and net CRE does not change after removing the f_c variability (see the difference between plot (b) and Fig. S4.10, a). Nevertheless, in section 3.3, we removed the f_c variability from both CRE and I_{org}, as still CRE variability is primarily controlled by f_c.

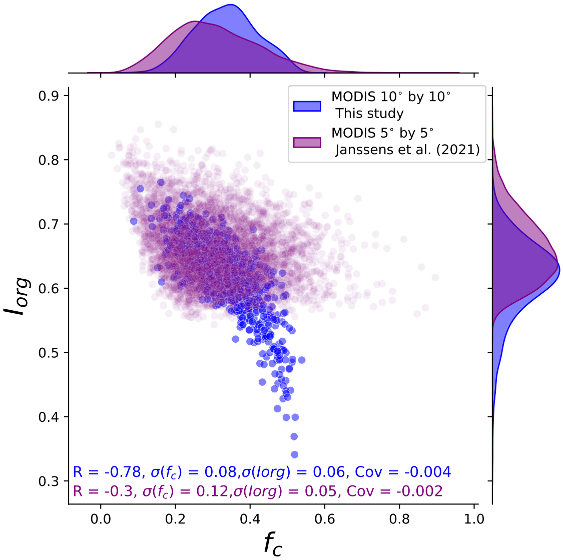

Figure S4.9: This figure shows how the $f_c - I_{org}$ correlation changes with reducing the domain size from $10^\circ \times 10^\circ$ to $5^\circ \times 5^\circ$. For the latter, we use the dataset which is publicly shared by Janssens et al. (2021).

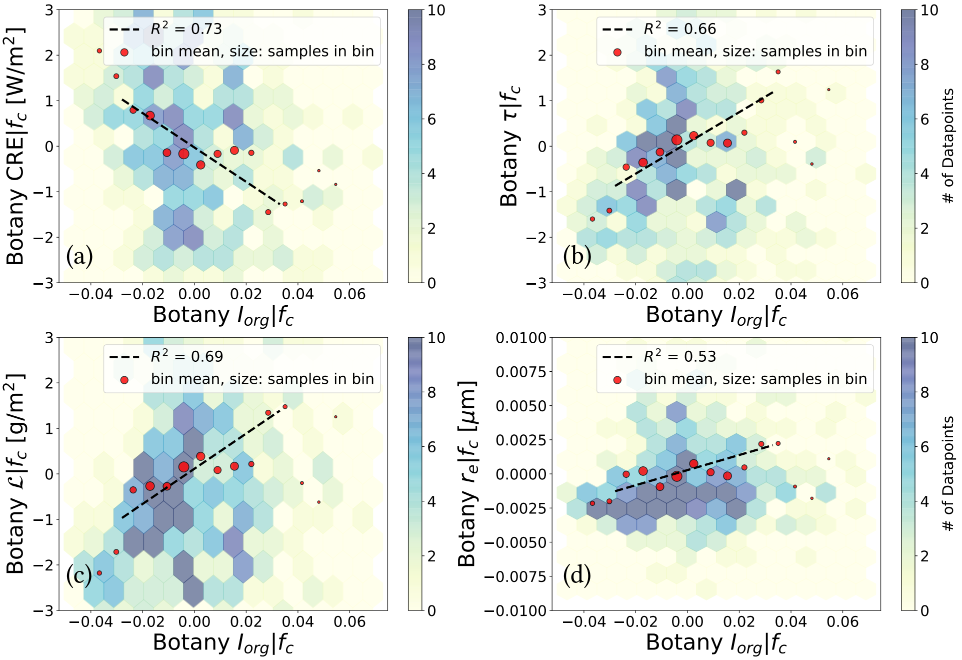

Figure S4.10: All results derived from the hourly analysis of the Cloud Botany dataset during the second day between the 37th and 43rd hours. Values below the 5th and above the 95th percentile of $I_{org}|f_c$ are excluded from the fitting.

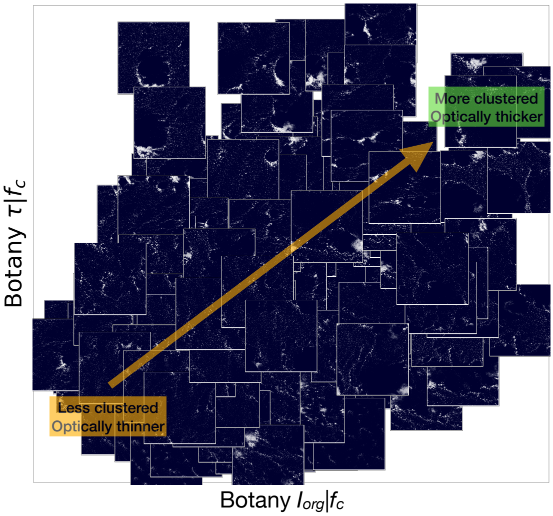

Figure S4.11: Similar to Fig. 4.3(a) but for the Botany dataset during hours 37-43.

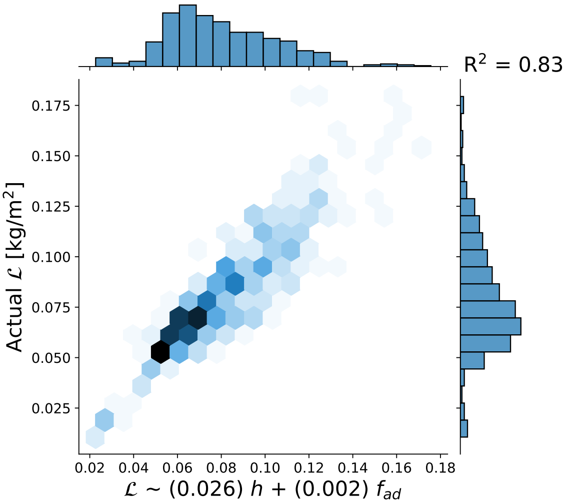

Figure S4.12: The result of the bi-linear regression analysis in which the target value is the in-cloud $\mathcal{L}$ and the regressors are h and f_{ad}. The reported coefficients are for the standardized h and f_{ad}.

Calculation of the degree of adiabaticity

The degree of adiabaticity is computed using the following equation:

$$f_{ad} = \frac{\int_{z_b}^{z_t} \rho(z) q_l(z) dz}{\int_{z_b}^{z_t} \rho(z) \Gamma_{ad}(z) z dz} \tag{4.7}$$

where, z represents the height, $\rho(z)$, $q_l(z)$, and $\Gamma_{ad}(z)$ denotes density, liquid water specific humidity, and the moist adiabatic lapse rate of q_l at each model height. To ensure a more precise estimation, f_{ad} is computed only for columns where the associated z_b is in proximity to the lifting condensation level (<850 m) and the cloud thickness exceeds 150 m.

The calculation of Γ_{ad} is determined by the following equation Eytan et al. (2021); Schmeissner et al. (2015):

$$\Gamma_{ad} = \frac{c_p}{L_v}\left(\Gamma_m + \frac{g}{c_p}\right) \tag{4.8}$$

Here, c_p represents the specific heat constant, g denotes the acceleration due to gravity, L_v stands for the latent heat of vaporization. The moist adiabatic lapse rate for temperature, Γ_m, is computed as:

$$\Gamma_m = \frac{g}{c_p}\left(\frac{1 + \dfrac{L_v}{R_d T} q_s}{1 + \dfrac{\beta L_v}{c_p} q_s}\right) \tag{4.9}$$

In the above equation, R_d corresponds to the gas constant for dry air, T represents temperature, β is the constant in the Clausius-Clapeyron equation ($e_s = A\exp(\beta(T - T_0))$), and q_s denotes the saturation specific humidity, which can be approximated as $\approx 0.622\frac{e_s}{P}$ where P represents pressure.

For simplicity, we calculate Γ_{ad} for the middle of the cloud layer (at $z' = \frac{z_b + z_t}{2}$) and assume that it linearly changes with height through the cloud layer. This assumption leads to the equation below:

$$f_{ad} = \frac{\int_{z_b}^{z_t} \rho(z) q_l(z) dz}{\Gamma_{ad}(z') \int_{z_b}^{z_t} \rho(z) z dz} \tag{4.10}$$

where, a f_{ad} value of 1 in each column indicates a fully adiabatic cloud, while values smaller than 1 and larger than 0 indicate non-adiabatic clouds. In the final step, after obtaining f_{ad} for each column, we proceed to calculate the domain-mean f_{ad} for the entire cloud field.

5

COLD POOLS WARM THE TRADES IN LARGE-EDDY SIMULATIONS

This chapter is in preparation to be submitted as as 🗎 *Alinaghi, P., Janssens. M, Jansson, F. (2025). Warming from cold pools: A pathway for mesoscale organization to alter Earth's radiation budget.* The preprint of a slightly different version is publicly available by Alinaghi et al. (2025b).

Abstract

In this paper, we aim at understanding the impact of cold pools—results of rain-evaporation that pattern clouds at the mesoscales—on the top-of-the-atmosphere radiation budgets in the trade-wind regime. To do so, we perform a denial experiment by creating two 19-member ensembles of large-eddy simulations, both forced by the same large-scale conditions characteristic of the trades: one with cold pools (CP) and one where cold-pool formation is prevented by homogenizing rain-evaporation (NoCP). As a result, we find that the CP ensemble features clouds with smaller coverage but greater albedo compared to the NoCP ensemble. These effects compensate for each other, leading to a weak impact of cold pools on the shortwave cloud radiative effect. However, by suppressing mesoscale ascent and thereby arresting the mesoscale self-aggregation of moisture, cold pools reduce the moisture loss via precipitation in the CP ensemble. At nearly every time step, this explains the total moisture difference between the CP and NoCP ensembles. Consequently, the NoCP ensemble exhibits a daily mean of 1.88 W/m^2 *more efficient escape of clear-sky longwave radiation, implying more cooling when cold pools are absent. Thus, cold pools affect the net radiative budget in the trades through modulating moisture fields and not clouds.*

5.1 INTRODUCTION

Cold pools form when raindrop evaporation creates pockets of cold, dense air, driving downdrafts. Upon reaching the surface, these downdrafts spread horizontally, generating cellular cloud structures across various convective regimes, from stratocumulus (Glassmeier and Feingold, 2017; Savic-Jovcic and Stevens, 2008; Xue et al., 2008a) to shallow trade-wind cumulus (Alinaghi et al., 2025d; Anurose et al., 2020; Dauhut et al., 2023; Helfer and Nuijens, 2021; Lamaakel et al., 2023; Seifert and Heus, 2013; Touzé-Peiffer et al., 2022; Vogel et al., 2021, 2016; Zuidema et al., 2012, 2017) and deep convection (Böing et al., 2012; Drager and van den Heever, 2017; Haerter and Schlemmer, 2018; Jeevanjee and Romps, 2013; Langhans and Romps, 2015; Lochbihler et al., 2021b; Moncrieff and Liu, 1999; Schlemmer and Hohenegger, 2014; Stensrud et al., 2005; Tompkins, 2001; Torri et al., 2015; Weisman and Rotunno, 2004). These structures arise from cold-pool-induced negative buoyancy beneath precipitating clouds, which suppresses convection. Conversely, cold pools enhance convection by generating strong vertical wind convergence at their leading edge, where heat and moisture accumulate, forming cloud rings that enclose negatively buoyant clear-sky regions.

Over the past decade, observations and models have established cold pools as a fundamental organizing mechanism in trade-cumulus cloud fields (Alinaghi et al., 2025c,d; Dauhut et al., 2023; Seifert and Heus, 2013; Vogel et al., 2021, 2016; Zuidema et al., 2012). Since the trades play an important role in cooling Earth, so may therefore its cold pools. Specifically, we are motivated by three questions on how cold pools may affect the top-of-atmosphere radiation budget.

First, by suppressing convection and increasing open-sky fraction, cold pools reduce cloudiness, while by triggering convection, they enhance cloudiness. Thus, cold pools might directly influence the cloud-radiative effect (CRE). Yet, the extent to which CRE is affected by cold pools in the trades has not been directly quantified.

Second, in deep convection, several studies indicate that cold pools hinder mesoscale self-aggregation of moisture (Jeevanjee and Romps, 2013; Muller and Bony, 2015; Nissen and Haerter, 2021), a process known to directly affect the long-wave clear-sky radiative effect (Bony et al., 2020b). Thus, cold pools may have a direct impact on long-wave clear-sky radiation. However, their influence on the clear-sky radiation and moisture budget of the trades remains largely unexplored.

Third, Alinaghi et al. (2025d) showed that fields with more and larger cold pools reflect more shortwave radiation to space in large-eddy simulations. But this might be driven by large-scale cloud-controlling factors (CCFs), as large-scale conditions that favor cold-pool formation also promote development of more clouds and more aggregated convection (Alinaghi et al., 2025d; Janssens et al., 2025). As a result, disentangling the actual impact of cold pools on the top-of-atmosphere radiative budget remains challenging.

Therefore, this study aims to isolate the impact of cold pools on the top-of-atmosphere radiative budget, independent of CCF-induced variability. To achieve this, we perform a cold-pool denial experiment, in which cold-pool formation is prevented by homogenizing rain-evaporation. Specifically, instead of allowing rain-evaporation to *locally* modify moisture and in turn temperature fields—thereby generating cold pools—we redistribute its effects evenly across the entire simulation domain at each level. This prevents the cold-pool formation which would have otherwise patterned clouds at the mesoscales. The denial experiment is conducted using two 19-member large-domain large-eddy simulations: one with cold pools (CP) and one without (NoCP), both forced by various CCFs of the trade-wind regime derived from ERA5 reanalysis data (Hersbach et al., 2020).

The paper is organized as follows: First, we explain the design of our ensemble and the method used to prevent formation of cold pools (Section 5.2). Next, we present the impact of homogenizing rain evaporation on top-of-the-atmosphere shortwave and longwave radiative effects (Section 5.3.1). Sections 5.3.4–5.3.3 investigate how homogenizing rain evaporation influences cloud cover and albedo, which regulate shortwave radiative effects, as well as the moisture budget of trade-wind cumulus fields, which governs longwave radiative effects. Finally, we discuss the implications of our results for trade-cumulus climate feedback (Section 5.3.5), before concluding (Section 5.4).

5.2 INHIBITING COLD-POOL FORMATION BY HOMOGENIZING RAIN EVAPORATION

To investigate the relevance of cold pools to the radiative budgets of trade-cumulus fields, we select a subset of simulations from the *Cloud Botany* dataset. *Cloud Botany* is a large ensemble of large-eddy simulations (LESs) with 100-m resolution over 156 × 156 km^2–domains, designed by varying large-scale cloud-controlling factors (CCFs). These CCFs are defined by six parameters: the sea-surface liquid-water potential temperature (θ_{l0}), near-surface geostrophic wind speed (u_0), the moisture scale height (h_{q_t}), the temperature lapse rate in the free troposphere (Γ), large-scale vertical velocity variability (w_1), and the shear in the horizontal geostrophic wind (u_z).

Alinaghi et al. (2025d) quantified the relative importance of these CCFs for the daily mean cold-pool properties across the *Cloud Botany* ensemble. To first order, the near-surface wind speed ($|u_0|$) and large-scale subsidence (w_1) control the daily mean number and size of cold pools across the ensemble, with second-order contributions from stability (Γ) and wind shear (u_z). These four factors also strongly influence the CRE across the ensemble (Janssens et al., 2025). Thus, for our denial experiment, we focus on these four dimensions of variability, whose ranges are shown in Table 5.1. With exception of the diurnality in insolation, the CCFs are time-invariant in the *Cloud Botany* ensemble. Although this limits us to study the effect of cold pools in conditions without externally imposed heterogeneity, it allows isolating the impact of cold pools on mesoscale cloud fields over a range of climatologically relevant conditions.

Our model employs the two-moment microphysics scheme of Seifert and Beheng (2001), with a fixed cloud-droplet number concentration in both time and space. Normally, its rain-evaporation is parameterized following the approach of Seifert (2008). Various methods have been proposed to suppress cold-pool formation in large-eddy simulations (Böing et al., 2012). Since cold pools originate from rain-evaporation, a natural way to prevent their formation is to entirely disable the rain-evaporation tendency by setting it to zero. This directly and locally reduces relative humidity by eliminating the evaporative cooling and moistening effects of rain-evaporation, resulting in higher cloud-base heights and deeper mixed layers (Helfer and Nuijens, 2021). Although we want to understand the impact of preventing cold-pool formation on the mean state of the system, setting rain-evaporation tendency to zero *directly* influences the mean state of the atmosphere in

Large-scale and initial conditions	**Parameters [units]**	**Number of simulations**	**Range of variability**
Near-surface geostrophic wind speed	u_0 [m/s]	5	from 5 to 15
Temperature lapse rate in the free troposphere	Γ [K/km]	5	from 4.5 to 7.5
Large-scale vertical velocity variability	w_1 [cm/s]	4	from -0.002 to 0.001
Shear in the horizontal geostrophic wind	u_z [(m/s)/km]	4	from -4 to 4

Table 5.1: **Parameters of the LES ensemble.** Overall information about the ensemble's parameters determining CCFs. Note that in addition to simulations above, the ensemble has a central reference simulation with the mean of CCFs above. This means our ensemble features 19 simulations in total.

terms of temperature and moisture. This, in turn, could directly impact our comparison of top-of-the-atmosphere radiation, as the domain-averaged moisture plays a key role in regulating the amount of outgoing longwave clear-sky radiation (Fildier et al., 2023; Janssens et al., 2025).

Thus, instead of completely disabling rain-evaporation, we suppress cold-pool formation by homogenizing it throughout the model. Specifically, at each model level where rain evaporation would locally affect moisture and, in turn, temperature, we take the evaporation tendency value and redistribute it uniformly across all grid cells at the corresponding level (Böing et al., 2012). Homogenizing rain evaporation only within the sub-cloud layer yields similar results. This approach ensures that the overall impact of rain-evaporation on the mean atmospheric state remains unchanged, as it solely redistributes the local, heterogeneous effects of rain-evaporation at each height.

As a result, we have two 19-member ensembles: one with cold pools (hereafter referred to as CP) where cold pools normally form due to local rain-evaporation and one without cold pools (NoCP) where rain-evaporation is evenly redistributed across the whole domain at each level. Each simulation is run for a period of five days. Figure 5.1a shows the temporal evolution of the cloud- and rain-water paths, averaged over the entire CP and NoCP ensembles. Both ensembles start from a non-cloudy, homogeneous state. During the non-precipitating phase, the behavior of both ensembles is identical, as non-precipitating cumuli self-aggregate due to shallow circulations that are self-reinforcing (Bretherton and Blossey, 2017; Janssens et al., 2023; Narenpitak et al., 2021).

As the cumuli aggregate, they deepen until they begin to precipitate. At this point, cold pools form in the CP ensemble, where clouds organize into cloud rings enclosing clear-sky areas (Fig. 5.1b). The formation of cold pools is also evident in the development of very shallow mixed-layer heights (h_{mix}) in Fig. 5.1b, consistent with models (Rochetin et al., 2021) and observations (Touzé-Peiffer et al., 2022). In contrast, while the NoCP ensemble also precipitates, no cold pools form. This is reflected in the mixed-layer height (h_{mix}) not being suppressed in the NoCP ensemble (Fig. 5.1c). Instead, the NoCP ensemble features clustered cloud structures without the development of open-sky areas. Cloud patterns alongside non-suppressed mixed-layer heights suggest that our method for preventing

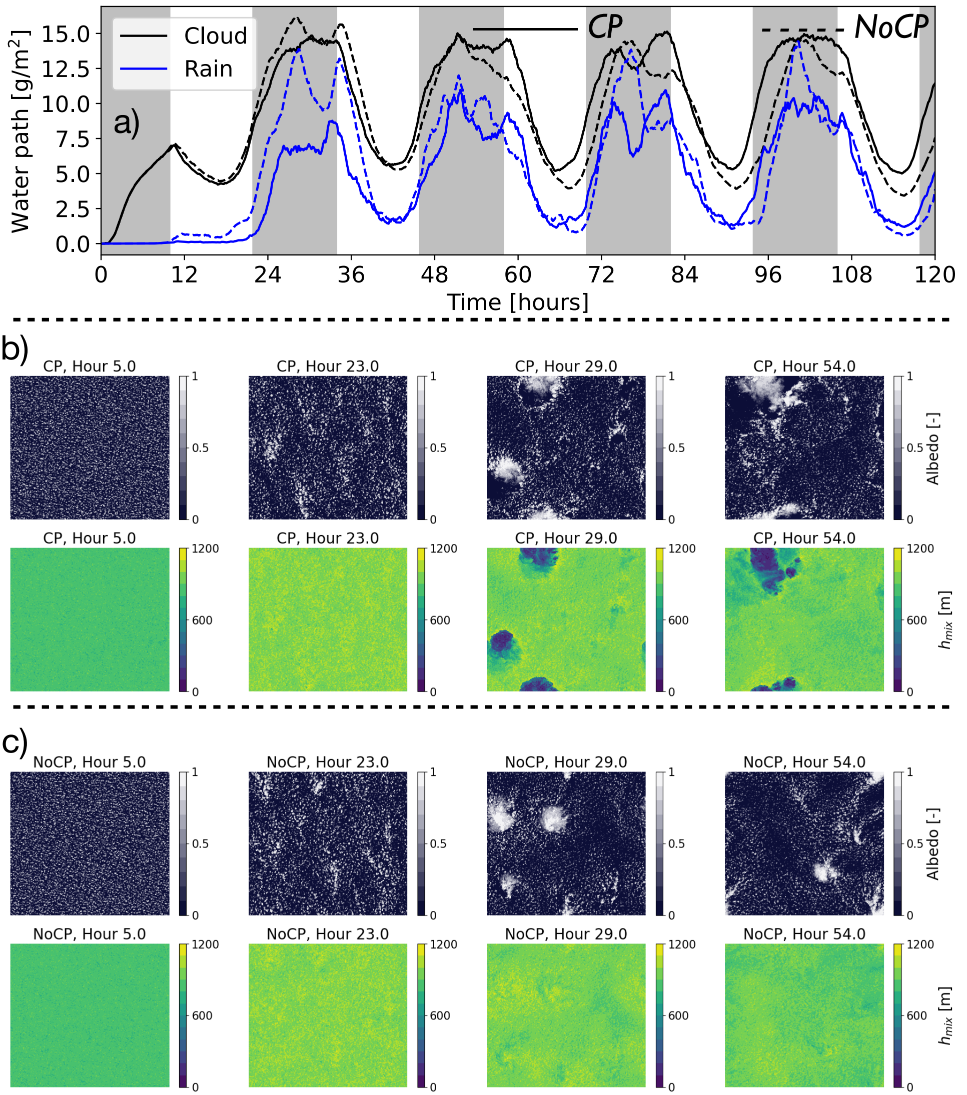

Figure 5.1: **Temporal evolution of cloud fields in both the CP and NoCP ensembles.** a) Time series of cloud- and rain-water paths averaged over the entire CP (continuous) and NoCP (dashed) ensembles. Grey shades show nighttime. b) and c) are the top-view fields of cloud albedo (first row) and mixed-layer height (second row) for the central reference simulation of the CP and NoCP ensembles, respectively.

cold-pool formation is promising.

The evolution of clouds and precipitation in both ensembles follows the diurnality of net radiative cooling: clouds and rain develop during the night, peak around sunrise, and reach their minima around sunset. This cycle repeats throughout the five-day simulations across all members, mirroring observations (Nuijens et al., 2009; Radtke et al., 2022; Vial et al., 2021; Vogel et al., 2021).

5.3 RESULTS AND DISCUSSION

5.3.1 COLD POOLS WARM THE TRADES BY REDUCING THE OUTGOING LONGWAVE, CLEAR-SKY RADIATION AT THE TOP OF THE ATMOSPHERE

The net radiative budget N at the TOA is expressed as $N = F_s^{\downarrow} + C_s + C_l - F_{s,c}^{\uparrow} - F_{l,c}^{\uparrow}$, where $F_s^{\downarrow}$ is the solar (shortwave) incoming radiation, C_s and C_l represent the shortwave and longwave cloud-radiative effects, respectively, while $F_{s,c}^{\uparrow}$ and $F_{l,c}^{\uparrow}$ are the outgoing shortwave and longwave clear-sky fluxes. Thus, a positive N indicates energy accumulation in the system, which implies warming. These terms are computed as domain- and time-averaged values for each member of the CP and NoCP ensembles over the 5^{th} day. Averaging over the last three days of simulations give comparable results (not shown).

Figure 5.2a shows that the mean TOA net radiative budget N for the CP ensemble exceeds that of the NoCP ensemble by 1.88 $\mathrm{W/m^2}$. The relative warming of the CP ensemble ($N_{\mathrm{CP}} - N_{\mathrm{NoCP}} > 0$) is robust for 18 out of 19 ensemble members. This warming effect of cold pools is primarily due to reduced outgoing longwave clear-sky radiation $F_{l,c}^{\uparrow}$ of the CP ensemble, as the differences in C_s and C_l between the CP and NoCP ensembles are negligible. Similarly, the shortwave outgoing radiation through clear skies $F_{s,c}^{\uparrow}$ is nearly identical in both cases.

Figure 5.2b further illustrates that the muted response of the shortwave cloud-radiative effect C_s to homogenizing rain evaporation arises from compensating factors: a reduced shortwave cooling due to a smaller cloud fraction $F_s^{\downarrow}\alpha_c\Delta f$ in the CP ensemble is offset by increased shortwave cooling from their higher cloud albedo $F_s^{\downarrow} f \Delta\alpha_c$. It is worth mentioning that there is approximately a 1.5 $\mathrm{W\ m^{-2}}$ spread around the mean difference between C_s of the CP and NoCP ensembles. This spread arises from the CP ensemble's higher albedo and lower coverage, with their relative impact differing across models. Including more ensemble members with different CCFs would lead to a more representative estimation of the effect of cold pools on C_s in the trade-wind regime.

The same cloud response helps explain the minimal difference in C_l: the CP ensemble features clouds with a smaller horizontal extent and f but greater depth. Since albedo is strongly influenced by cloud depth across the *Cloud Botany* ensemble (Alinaghi et al., 2024a), the reduced warming from C_l due to the smaller f is offset by the increased warming from C_l caused by deeper clouds. Deeper clouds feature colder cloud layer temperatures, which less efficiently emit longwave radiation to space, giving less cooling.

The greatest cooling from homogenized rain evaporation stems from a rise in $\Delta F_{l,c}^{\uparrow}$. It can be attributed to the difference in the horizontally and temporally averaged total water (cloud + vapor) I between these cases, $\Delta F_{l,c}^{\uparrow} \approx \partial_I F_{l,c}^{\uparrow} \Delta I$. That is, cold pools keep the trade-wind layer moist, preventing the emission of longwave radiation to space from near the surface.

The results of this section motivate an investigation into the causes and mechanisms underlying the differences in cloud fraction f, cloud albedo α, and total water I between the CP and NoCP cases, as they significantly explain the difference in the shortwave and longwave radiative fluxes at the TOA of the CP and NoCP ensembles.

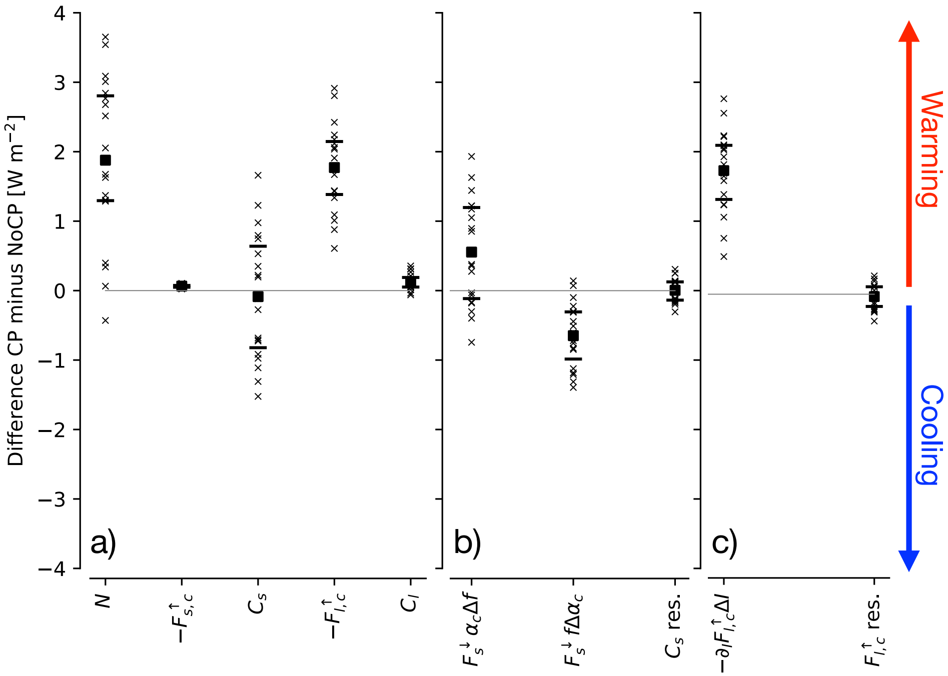

Figure 5.2: **Effects of cold pools on the daily mean net radiative budget at the top of the atmosphere.** a) Decomposition of the net radiative flux at the TOA into shortwave C_s and longwave C_l cloud radiative effects, and the shortwave $F^{\uparrow}_{s,c}$ and longwave $F^{\uparrow}_{l,c}$ outgoing clear-sky fluxes at the TOA. For each component, the y-axis shows the associated TOA radiation of CP ensemble minus that of NoCP ensemble. b) Decomposition of C_s to effects from cloud fraction $F^{\downarrow}_s \alpha_c \Delta f$ and albedo $F^{\downarrow}_s f \Delta\alpha_c$. c) Dependence of $\Delta F^{\uparrow}_{l,c}$ on the difference between the mean total-water path ΔI between the CP and NoCP ensembles.

5.3.2 Cold-pool simulations remain moister because they precipitate less

Figures 5.2a,c demonstrate that the main difference between the net TOA radiative fluxes of the CP and NoCP ensembles is due to the CP ensemble being moister, which leads to smaller outgoing LW radiative cooling of 1.88 W/m^2 in the CP ensemble. In this section, we investigate the source of difference between the total moisture of the CP and NoCP ensembles. To this end, we define I as the mass-weighted vertical average of the total-water specific humidity q_t, given by:

$$I = \langle q_t \rangle = \frac{\int_0^{z_\infty} \rho(z) q_t(z) dz}{\int_0^{z_\infty} \rho(z) dz}, \tag{5.1}$$

where $\rho(z)$ denotes the reference density profile, and z_∞ is the domain top at 7 km. Applying the mass-weighted averaging operator, defined as

$$\langle \circ \rangle = \frac{\int_0^{z_\infty} \rho(z) \circ dz}{\int_0^{z_\infty} \rho(z) dz}, \tag{5.2}$$

to all terms in the moisture budget equation, we obtain the bulk moisture budget:

$$\begin{aligned}\frac{\partial I}{\partial t} = \underbrace{\frac{\partial \langle q_t \rangle}{\partial t}}_{\text{Bulk moisture tendency}} &= -\underbrace{\left\langle \frac{\partial \left(\overline{w' q_t'}\right)}{\partial z} \right\rangle}_{\text{Vertical flux convergence}} \\ &\quad - \underbrace{\left\langle u_j^{LS} \left(\frac{\partial q_t}{\partial x_j}\right)^{LS} \right\rangle}_{\text{Large-scale advection and subsidence}} - \underbrace{\langle P(z) \rangle}_{\text{Precipitation}} + \underbrace{\langle N \rangle}_{\text{Nudging}},\end{aligned} \tag{5.3}$$

where u_j^{LS} represents the large-scale velocity in the j-direction, $\overline{w' q_t'}$ is the slab-mean total moisture flux at height z with

$$X' = X - \overline{X}, X \in \{w, q_t\}, \tag{5.4}$$

where X' is anomaly of variable X with respect to the slab-mean average $\overline{X}$. $P(z)$ is the domain-mean total precipitation flux at height z. Specifically, $P(z)$ is the sum of auto-conversion, accretion, and rain-evaporation fluxes. Note that the moisture profile in each member of the *Cloud Botany* ensemble is nudged towards its initial horizontally-averaged value with the nudging term in Eq. 5.3 (Jansson et al., 2023).

Figure 5.3a presents the differences between the components of the total moisture budget for the CP and NoCP cases of the central reference simulation. Among all components, the difference in precipitation fluxes between the CP and NoCP cases accounts for the total moisture difference at nearly every time step of the simulations. As shown in Fig. 5.3a, CP cases remain moister almost entirely because they precipitate less compared to NoCP cases.

Figure 5.3b breaks down the total moisture change rate due to precipitation fluxes into contributions from auto-conversion (cloud-to-rain drop), rain-evaporation, and accretion. Since this analysis focuses on the precipitation-induced changes in q_t, which in our LES model excludes rain water, auto-conversion and accretion appear as negative contributions (sinks of q_t), while rain-evaporation is positive. Figure 5.3b shows that the difference in accretion and rain-evaporation rates dominate the difference in total precipitation fluxes between CP and NoCP cases, while auto-conversion and the residual term (a correction for negative rain in the microphysics scheme) have minor effects. Comparing CP and NoCP cases in the central reference simulation reveals that differences in total precipitation flux are primarily explained by the difference in accretion rate at nearly every time step (Fig. 5.3b). That is, CP cases precipitate less than NoCP cases, because they less efficiently produce rain through accretion. Figures 5.3c,d confirm that the results discussed for the central reference simulation (Figs. 5.3a,b) hold consistently across the entire ensemble.

The rate of change in rain due to accretion in our model's microphysics scheme $\partial_t q_r|_{accretion} \approx q_r q_l$ (Seifert and Beheng, 2001), where q_r and q_l represent rain-water and cloud-water specific humidity, respectively. Thus, to understand why the accretion rate in the NoCP cases is larger than in the CP cases, we need to determine why the production of rain- and cloud-water content is greater in the NoCP ensemble.

To understand the differences in rain- and cloud-water content between the CP and NoCP ensembles, we need to identify what controls them. For rain formation, clouds

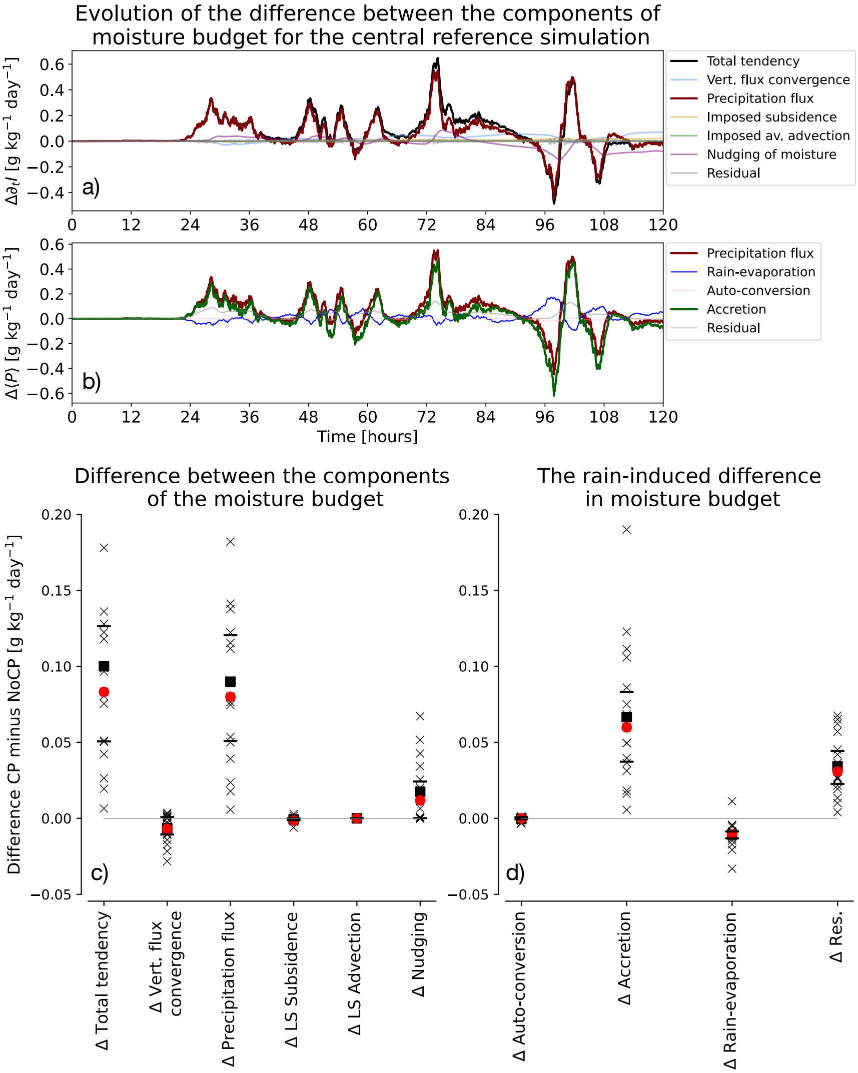

Figure 5.3: **Effects of cold pools on the total-water budget.** a) Difference in moisture budget components (Eq. 5.3) between CP and NoCP cases, with CP minus NoCP tendencies on the y-axis. b) Decomposition of precipitation-induced moistening into rain-evaporation, auto-conversion, and accretion rates for the central reference simulation. c,d) Same decomposition as a,b for the full ensemble. Components are averaged over hours 12-36, when simulations start diverging in total moisture. Each simulation's mean is marked by a cross (×), the ensemble mean by squares, interquartile range edges by horizontal bars, and the central reference simulation mean by a red circle.

must deepen. In the trade-cumulus regime, cloud deepening is correlated with horizontal widening due to the relationship between cloud horizontal and vertical extent (Alinaghi et al., 2024a; Feingold et al., 2017). The scale growth of trade cumuli occurs through self-reinforcing shallow mesoscale circulations driven by condensational heating atop anomalously moist mesoscale regions (Bretherton and Blossey, 2017; Janssens et al., 2023; Narenpitak et al., 2021). Therefore, we investigate how cloud- and rain-water contents are influenced by the spatial standard deviation of the total moisture I' across both CP and NoCP ensembles.

To achieve this, we create a so-called “moisture-space" plot following e.g. Muller and Bony (2015); Schulz and Stevens (2018). This plot is generated by first dividing the entire CP and NoCP ensembles into 10-km mesoscale blocks. Next, for each block, we compute the term I (using Eq. 5.3) averaged over the entire block and call it I_m. Then, we calculate the term total moisture anomaly at the mesoscales I' for each block as $I' = I_m - \overline{I}$, where $\overline{I}$ is the domain-mean I. Next, we group these blocks into bins of I'. Finally, for each bin, we calculate the average cloud- and rain-water content (q_l and q_r) as well as the total-water content anomaly (q_t') of all blocks associated with that bin.

Figs. 5.4a,b shows the moisture space of the total-water content anomaly q_t'. It is consistently positive across all heights where $I' > 0$, and vice versa. Specifically, the mesoscale q_t anomalies reside in the (upper) cloud layers, where they can be decisive for the growth of rain droplets. Moreover, Figs. 5.4c,d demonstrate that in both ensembles, blocks with higher I' contain deeper clouds with greater cloud- and rain-water content, where total-water content anomaly is high. Thus, it is in these blocks where accretion will more efficiently produce rain. Consistently, Figs. 5.4f,h show that the 10-km block-averaged rain-water path, $\mathcal{R} = \int_{z=0}^{z=z_\infty} q_r(z)dz$, and surface precipitation, $\mathcal{P}$ non-linearly increase with rising I' in both ensembles, giving leverage to very moist mesoscale regions in setting the mean $\mathcal{R}$ and $\mathcal{P}$, even though there are relatively few such columns. However, the CP ensemble lacks blocks with I' greater than ≈1.5 g/kg, which do develop in the NoCP ensemble. Indeed,Figs. 5.4c,e reveal that it is the presence of these very moist blocks in the NoCP ensemble ($1.5 < I' < 2.5$ g/kg) which explains why the overall mean $\mathcal{R}$ and $\mathcal{P}$ of the NoCP cases is approximately 1 g/m^2 and 0.15 mm/day higher than those of the CP ensemble.

5.3.3 COLD POOLS ARREST RUNAWAY MESOSCALE SELF-AGGREGATION OF MOISTURE

The preceding analysis (Figure 5.4) demonstrates that the CP ensemble retains moister boundary layers than the NoCP ensemble, because they do not develop extremely moist 10-km blocks, in which rain is efficiently produced and rained out. This implies that the cold pools prevent the mesoscale self-aggregation of moisture into these moist blocks in the CP ensemble.

To investigate how cold pools inhibit mesoscale moisture self-aggregation, we conduct a moisture budget analysis for the 10-km blocks of both the CP and NoCP ensembles. In addition to the terms in Eq. 5.3, which apply to the full domain, the 10-km blocks also experience horizontal moisture fluxes at their boundaries with adjacent mesoscale blocks.

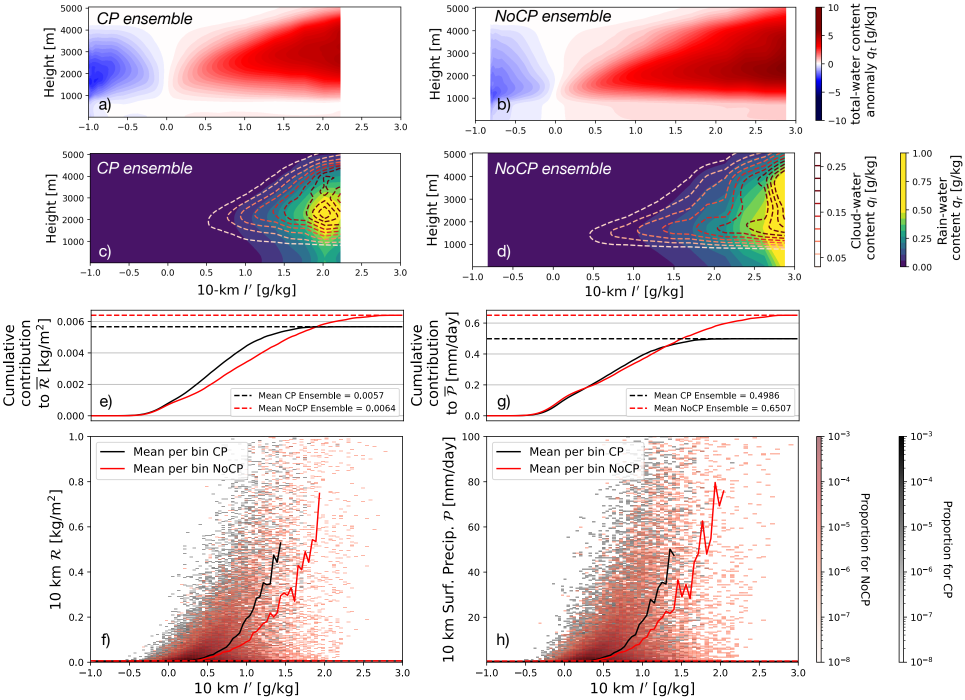

Figure 5.4: **Effects of cold pools on rain and surface precipitation flux.** Moisture space of the total-water content anomaly q_t' (a,b) cloud- and rain-water contents q_l and q_r (c,d) for the CP and NoCP ensembles. q_l is shown by the dashed, white-to-red contour lines. Plots d) and f) show the 2D histogram of 10-km total-water anomalies I' vs. 10-km rain-water path $\mathcal{R}$ and surface precipitation flux $\mathcal{P}$, with c) and e) showing the cumulative contribution of I' bins to the mean $\mathcal{R}$ and $\mathcal{P}$ of each ensemble.

Thus, the bulk moisture budget for the 10-km blocks can be expressed as

$$\frac{DI}{Dt} = \frac{D\langle q_t\rangle}{Dt} = -\underbrace{\left\langle \frac{\partial(U'_{h_j} q_t)}{\partial x_j}\right\rangle}_{\text{i}} - \underbrace{\left\langle \frac{\partial(w' q_t)}{\partial z}\right\rangle}_{\text{ii}} - \underbrace{\left\langle u_j^{LS}\left(\frac{\partial q_t}{\partial x_j}\right)^{LS}\right\rangle}_{\text{Large-scale advection and subsidence}} - \underbrace{\langle P(z)\rangle}_{\text{Precipitation}} + \underbrace{\langle N\rangle}_{\text{Nudging}}, \tag{5.5}$$

where the first (i) and second (ii) terms on the right-hand side represent the total q_t flux in the horizontal and vertical, respectively. Here, U'_{h_j} and w' denote the horizontal and vertical components of the anomalous velocity vector with respect to the domain mean. This means that the horizontal advection with the domain-mean horizontal wind is absorbed in the left-hand side of Eq. 5.5, which means our budget analysis follows the mesoscale blocks as they move with the larger-scale wind.

To understand the contributions from the mesoscales and sub-mesoscales, we decompose variables $\phi \in \{U'_{h_j}, w'\}$ to contributions from the mesoscales ϕ_m and sub-mesoscales ϕ_s. The mesoscale contributions ϕ_m are calculated by averaging ϕ over each 10-km block. For each 100-m grid cell inside a 10-km block, sub-mesoscale contributions ϕ_s is anything that remains after filtering the mesoscale contributions, i.e. $\phi_s = \phi - \phi_m$. By applying the product rule to the first two terms (i and ii) of Eq. 5.5, we obtain

$$\langle \mathrm{i}_m \rangle = -\left\langle U'_{h_{j,m}} \frac{\partial q_{t,m}}{\partial x_j} \right\rangle - \left\langle q_{t,m} \frac{\partial U'_{h_{j,m}}}{\partial x_j} \right\rangle - \left\langle \frac{\partial (U'_{h_{j,s}} q_{t,s})_m}{\partial x_j} \right\rangle, \tag{5.6}$$

$$\langle \mathrm{ii}_m \rangle = -\left\langle w'_m \frac{\partial q_{t,m}}{\partial z} \right\rangle - \left\langle q_{t,m} \frac{\partial w'_m}{\partial z} \right\rangle - \left\langle \frac{\partial (w'_s q'_{t,s})_m}{\partial z} \right\rangle. \tag{5.7}$$

The mass conservation at the mesoscales implies that $q_{t,m} \frac{\partial U'_{h_{j,m}}}{\partial x_j} + q_{t,m} \frac{\partial w'_m}{\partial z} = 0$. Substituting this relation, we obtain

$$\begin{aligned} \langle \mathrm{i}_m \rangle + \langle \mathrm{ii}_m \rangle = \; & \underbrace{-\left\langle U'_{h_{j,m}} \frac{\partial q_{t,m}}{\partial x_j} \right\rangle}_{\text{mesoscale horizontal advection}} \; \underbrace{-\left\langle \frac{\partial (U'_{h_{j,s}} q_{t,s})_m}{\partial x_j} \right\rangle}_{\text{sub-mesoscale horizontal transport}} \\ & \underbrace{-\left\langle w'_m \frac{\partial q_{t,m}}{\partial z} \right\rangle}_{\text{gradient production}} \; \underbrace{-\left\langle \frac{\partial (w'_s q'_{t,s})_m}{\partial z} \right\rangle}_{\text{sub-mesoscale vertical transport}} . \end{aligned} \tag{5.8}$$

Because the 10-km blocks in both ensembles experience the same external large-scale subsidence and advection and are similarly nudged towards their initial state, we include both terms in the residual and rewrite Eq. 5.5 as

$$\frac{DI_m}{Dt} = \frac{D\langle q_{t,m} \rangle}{Dt} = \langle \mathrm{i}_m \rangle + \langle \mathrm{ii}_m \rangle - \langle P_m(z) \rangle + \mathrm{Residual}_m. \tag{5.9}$$

To analyze moisture aggregation in the very moist blocks of both ensembles, we calculate the terms of Eq. 5.9 for these blocks at each hour for each ensemble member. At every time step, the terms are averaged over blocks where mesoscale moisture anomaly I'_m exceeds the 90^{th} percentile of its distribution for that time step. This condition closely resembles averaging over blocks where the rain-water path exceeds the 90^{th} percentile of its distribution.

As a result, Fig. 5.5a presents the difference (CP minus NoCP) between the terms of Eq. 5.9, averaged over very moist (rainy) blocks. Consistent with the moisture-space plots in Fig. 5.4, Fig. 5.5a shows that in 18 out of 19 ensemble members, the very moist mesoscale blocks in the NoCP ensemble experience a higher moistening rate—on average approximately 0.31 g/kg/day more than in the CP ensemble. The primary contributor to this moistening is the larger gradient production term in the NoCP ensemble with an ensemble average of approximately 3.21 g/kg/day. To a lesser extent, differences in precipitation (1.28 g/kg/day) and mesoscale horizontal advection (0.87 g/kg/day) lead to slightly greater moistening in the CP ensemble.

This analysis suggests that cold pools prevent the mesoscale aggregation of moisture in the very moist blocks primarily by suppressing the gradient production term. At the mesoscales, the variability in the gradient production term is strongly governed by the variability in the vertical motion w'_m almost everywhere (Fig. S5.1). This implies that cold pools strongly suppress vertical motion in the very moist mesoscale blocks of the CP ensemble.

To investigate this, we calculate the mean of w'_m over the very moist (rainy) blocks of both CP and NoCP ensembles over the lower 5-km layer. As a result, Figure 5.5b illustrates that on the first non- or weakly precipitating day, when cold pools are absent, w'_m in both CP and NoCP ensembles evolve very similarly. However, after this, once cold pools start to form over day 2, w'_m of the NoCP ensemble can develop to nearly twice the magnitude of that in the CP ensemble (Fig. 5.5b). This is also shown in the vertical profile of w'_m by Fig. 5.5c,d: While the NoCP ensemble-averaged w'_m freely develops up to 0.1 m/s in the cloud layer, its CP counterpart does not exceed 0.05 m/s.

To assess direct cold-pool contributions to this vertical motion suppression in the CP ensemble, we separate their effects into contributions from three regions: (i) cold-pool edges, (ii) inside cold pools, and (iii) outside cold pools. The ensemble-averaged time series (Fig. 5.5b) shows that the overall mean w'_m is primarily controlled by regions outside cold pools. Although cold-pool edges enhance w'_m through convective triggering, this effect is counteracted by suppressed w'_m inside cold pools, leading to a net weak impact by cold pools.

To determine at which levels cold pools influence w'_m, Fig. 5.5e-g presents the temporal evolution of w'_m across these three regions, weighted by their respective fractions (Fig. 5.5h). The unweighted profiles are shown in Fig. 5.5i-k. First, while cold-pool edges exhibit strong upward w'_m of up to 0.2 m/s (Fig. 5.5i), their small fractional area (Fig. 5.5h) weakens their contribution to the overall mesoscale ascent within 10-km blocks (Fig. 5.5e).

Second, Fig. 5.5j highlights that cold pools generate strong mesoscale downdrafts in the sub-cloud layer, while above 1 km, they sustain updrafts inside cold pools. This structure mirrors squall-line dynamics discussed by Alinaghi et al. (2025d), where cold-pool-induced shear displaces the updrafts at the edge of cold pools toward the cold-pool interiors, reinforcing parent clouds (Fig. S5.2). However, since cold-pool coverage remains below 30% of the very moist blocks (Fig. 5.5h), their impact on the overall mean mesoscale w'_m remains limited (Fig. 5.5f).

Ultimately, the cancellation between updrafts at cold-pool edges and downdrafts inside cold pools means that regions outside cold pools dictate the final mean w'_m in the CP ensemble. Fig. 5.5k shows that outside cold pools, w'_m evolves similarly to the NoCP ensemble, even reaching 0.09 m/s. However, because the presence of cold pools reduces their area fraction (Fig. 5.5h), their weighted mean ascent remains below 0.05 m/s (Fig. 5.5g).

In summary, this section highlights that preventing cold pools by homogenizing rain-evaporation allows mesoscale ascent to develop freely, whereas in the presence of cold pools, it is strongly suppressed (visualization in Fig. S5.2). Preventing cold-pool formation, in turn, enables the undisturbed development of the gradient production of moisture in the NoCP ensemble, which strongly drives the self-aggregation of moisture and the presence of very moist blocks in the NoCP ensemble. The absence of these very moist blocks in the

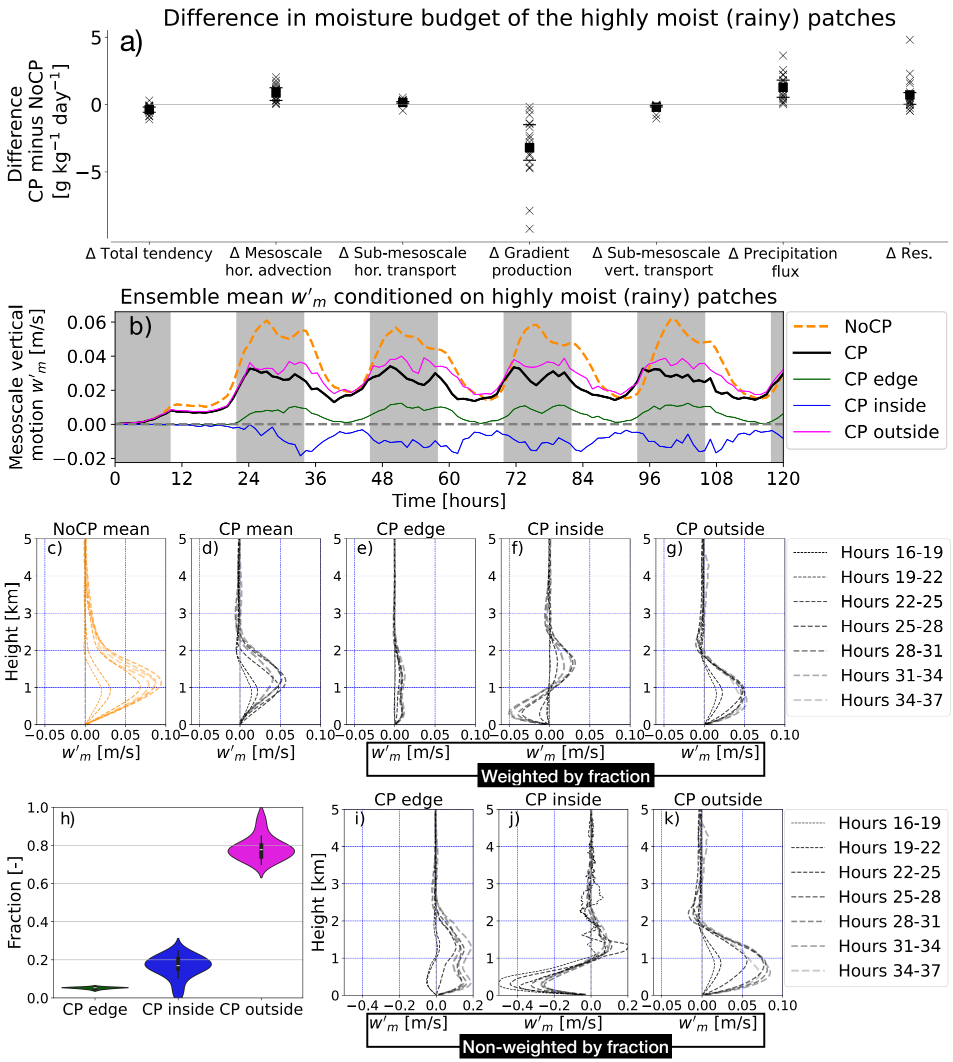

Figure 5.5: **Impact of cold pools on mesoscale self-aggregation of moisture.** (a) Differences between terms in Eq. 5.9 for the CP and NoCP ensembles. At each time step, components are averaged over 10-km blocks where I' exceeds the 90th percentile. Time averages are taken over hours 12–36, when the simulations begin to diverge in total moisture. Crosses (×) indicate individual simulation means, squares show the ensemble mean, and horizontal bars mark the interquartile range. (b) Ensemble-averaged time series of mesoscale 10-km vertical motion (w'_m) in the lowest 5 km for NoCP (orange) and CP (black), with CP contributions from cold-pool edges (green), inside (blue), and outside (magenta). (c-g) Vertical profiles of (b) for hours 16-37. (i-k) Same as (e-g), but without weighting by (h), which shows the distribution of the fractions of cold-pool regions within highly moist (rainy) 10-km blocks.

CP ensemble is key to explaining its smaller surface precipitation flux and, consequently, its lower drying rate, which results in the lower clear-sky outgoing longwave radiation in the CP ensemble, and its relative warming.

5.3.4 Cold pools lead to slightly deeper clouds with smaller coverage

The small offsetting effects of cold pools on cloud fraction f and albedo α in determining shortwave cloud-radiative effect C_s are extensively investigated in the supplementary information. Since these effects are small, we only provide a brief summary of these effects below.

Clouds generally form through both thermodynamical and dynamical processes. The self-aggregation of clouds over anomalously moist mesoscale regions during the non-precipitating phase (Bretherton and Blossey, 2017; Janssens et al., 2023; Narenpitak et al., 2021), as well as convective triggering by cold pools through modifications of moisture and temperature fields (Schlemmer and Hohenegger, 2016; Tompkins, 2001), are thermodynamic processes. Dynamic triggering by cold pools, which generate strong upward motions at their leading edges, dynamically controls cloudiness (Jeevanjee and Romps, 2013).

First, homogenizing rain evaporation in the NoCP ensemble leads to the development of highly moist mesoscale regions, which are absent in the CP ensemble (see also Section 5.3.3). These regions also exhibit very high relative humidity. Since cloud cover f is strongly influenced by relative humidity, the absence of these anomalously moist mesoscale regions in the CP ensemble explains their smaller cloud cover compared to the NoCP ensemble (Fig. S5.3).

Second, given the same degree of moisture aggregation, the CP ensemble exhibits stronger mesoscale vertical ascent (Fig. S5.4a,b), leading to the formation of deeper clouds (Fig. S5.4c,d). Cloud depth strongly controls cloud-water path across the Botany ensemble (Alinaghi et al., 2024a). Since cloud-droplet number is fixed in time and space in our simulations, cloud-water path directly controls cloud-optical depth and, consequently, cloud albedo. As a result, clouds in the CP ensemble are more dynamically driven, leading them to be deeper, contain more cloud water, have greater optical depth, and appear brighter (Fig. S5.4e,f).

5.3.5 Impact of cold pools in comparison with large-scale CCFs

So far, we have shown that cold pools—mainly through modulating the moisture budget—play an important role in TOA clear-sky longwave radiation, with an effect of approximately 1.88 W/m^2 averaged over a day and entire ensemble. Now, the question is: how significant is this daily mean 1.88 W/m^2 cold-pool-induced warming compared to the effects of varying the larger-scale forcings on trade-cumulus fields? Answering this question will directly help us understand the relevance of cold pools for trade-cumulus feedback.

To answer this question, we perform a multivariate regression analysis on the ensemble's CCFs

$$\overline{Y} \approx \sum_{i=1}^{4} \beta_i \times \widetilde{\mathrm{CCF}}_i \qquad \text{with} \qquad \widetilde{\mathrm{CCF}}_i := \frac{\mathrm{CCF}_i - \overline{\mathrm{CCF}_i}}{\sigma(\mathrm{CCF}_i)} \tag{5.10}$$

with the target value $Y \in \{C_s, -F^{\uparrow}_{l,c}\}$, which is the domain-mean TOA shortwave cloud radiative effect or the longwave clear-sky outgoing radiation averaged over they 5^{th} day of simulations. Regressors are CCFs $\in \{|u_0|, \Gamma, w_1, u_z\}$, which are by design are time-invariant throughout each simulation. Note that regressors are standardized by subtracting their mean and dividing by their standard deviation to quantify their impact on Y with an equal weighting. So, our regression of Eq. 5.10 consists of the target value Y and regressors CCFs that are vectors of size 18, the number of simulations in each CP and NoCP ensembles.

Figure 5.6 shows the results of the multivariate regression of Eq. 5.10 for C_s (Fig. 5.6a,b) and $-F^{\uparrow}_{l,c}$ (Fig. 5.6c,d) for both CP and NoCP ensembles. The response of both C_s and $-F^{\uparrow}_{l,c}$ to CCFs and their comparison with observational studies were already discussed by Janssens et al. (2025). Here, our regression analysis for C_s (Fig. 5.6a,b) shows that in both CP and NoCP ensemble, increased near-surface wind speed $|u_0|$ and reduced large-scale subsidence (increased w_1) lead to more negative shortwave reflection with approximately the same magnitude. Compared with $|u_0|$ and w_1, stability Γ has a smaller effect on C_s; increased Γ leads to increased shortwave reflection, due to increased cloud cover in response to increased Γ. Unlike NoCP ensemble, the C_s of the CP ensemble seems to be insensitive to variations in wind shear. Comparing the CP and NoCP ensemble, homogenizing rain-evaporation has a significantly smaller effect on C_s compared with the C_s response to the unit of change in CCFs. This confirms an earlier hypothesis (Alinaghi et al., 2025d): Although there is significant co-variability in the presence of cold pools and C_s, this is not caused by the presence of cold pools, but by the larger-scale forcing's general translation into cloudiness.

Moreover, our regression analysis for $-F^{\uparrow}_{l,c}$ (Fig. 5.6c,d) shows that stability Γ is by far the most important CCF that controls $-F^{\uparrow}_{l,c}$: for a given mixed-layer temperature profile, the more stable the (free-)troposphere, the warmer the (free-)troposphere, and in turn the larger the longwave cooling rate. Comparing the impact of homogenizing rain-evaporation with that of CCFs on $-F^{\uparrow}_{l,c}$ highlights that cold pools play a more important role for modulating the longwave clear-sky radiation feedback compared with a unit of change in near-surface wind $|u_0|$, large-scale subsidence w_1, and wind shear u_z. It is only stability parameter Γ whose unit of change has a larger impact on $-F^{\uparrow}_{l,c}$ than cold pools.

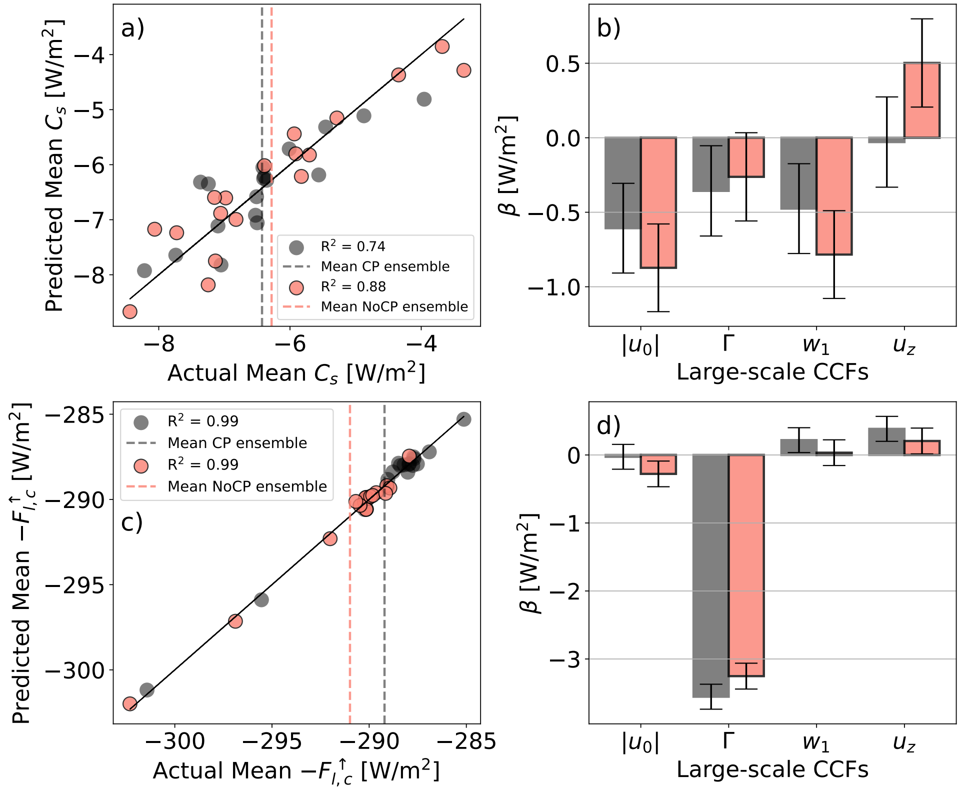

Figure 5.6: **Effects of cold pools on the response of the TOA radiative fluxes to CCFs.** a,b) Results of multiple regression analysis for the TOA shortwave cloud radiative effect C_s with the beta coefficients shown in b). c,d) Results of multiple regression analysis for the TOA longwave clear-sky radiative effect $-F^{\uparrow}_{l,c}$ with the beta coefficients shown in d). The p-values of the F-statistic of both models are smaller than 10^{-12}.

5.4 Conclusion

Within this paper, we aimed at understanding the impact of cold pools on the top-of-the-atmosphere radiative fluxes in the trade-wind regime. To this end, we perform a denial experiment consisting of two 19-member ensemble of large-eddy simulations (LESs): one with cold pools (CP) and one without (NoCP). Both ensembles are forced by the same large-scale environments. In the NoCP ensemble, rain-evaporation is homogenized; therefore, the NoCP ensemble cannot develop cold pools that would have otherwise patterned cloud fields at the mesoscales (Fig. 5.1b,c). Thus, this denial experiment helps us understand given the same CCFs, what impact cold pools have on clouds and in turn the radiative budget at the top of the atmosphere.

We first find that the impact of cold pools on cloudiness is minimal in both horizontal and vertical dimensions (Figs. S5.3, S5.4). Clouds in the CP ensemble are slightly deeper but exhibit slightly smaller coverage compared to those in the NoCP ensemble. Thus, the larger cloud albedo in the CP ensemble is offset by smaller cloud coverage, resulting in the shortwave cloud radiative effect being insensitive to cold pools (Fig. 5.2a,b). Therefore, the impact of cold pools on the response of clouds to CCFs is minimal (Fig. 5.6a,b).

Second, we find that cold pools significantly influence the mesoscale aggregation of moisture (Fig. 5.5a). This is mainly due to cold pools suppressing the mesoscale vertical ascent (Fig. 5.5b-k), thereby arresting the gradient production of moisture (Fig. 5.5a). Consequently, the NoCP ensemble develops mesoscale blocks with a higher level of moisture aggregation that do not exist in the CP ensemble (Fig. 5.5). As precipitation falls into these very moist mesoscale blocks in both ensembles (Fig. 5.4a,b), the NoCP ensemble produces significantly more rain than the CP ensemble (Fig. 5.4c,d). The large amount of rain, combined with the very high relative humidity in the moistest blocks of the NoCP cases, explain why surface precipitation is larger in the NoCP cases.

By decomposing the total moisture budget into all its terms (Eq. 5.3), we find that the precipitation flux almost entirely accounts for the difference in total moisture between the CP and NoCP ensembles (Fig. 5.3a,b). The greater total moisture present in the CP ensemble fields leads to more heat being trapped in their atmosphere, resulting in approximately 1.88 W/m^2 less outgoing longwave radiation at the top of the atmosphere compared to the NoCP ensemble (Fig. 5.2a,c). This indicates that cold pools warm the trades by a daily mean of 1.88 W/m^2 compared to when rain evaporation is homogenized. We showed that the resulting impact of homogenizing rain-evaporation on the TOA radiative budget is comparable to the impact of varying the CCFs across a climatologically representative range (Fig. 5.6c,d).

Overall, our denial experiment of cold pools highlights that cold pools symmetrically increase cloudiness vertically while reducing it horizontally. This symmetrical cloud response results in a buffered impact of cold pools on the cloud radiative effect. This finding aligns with the hypothesis of Janssens et al. (2025), which suggests that mesoscale circulations symmetrically increase and decrease cloudiness in their ascending and descending branches, respectively.

In contrast, the effect of homogenizing rain-evaporation on moisture fields is significantly asymmetric. By eliminating the disturbances cold pools induce to mesoscale ascent, their absence allows moisture to freely accumulate in already moist patches. Given the strong nonlinear response of precipitation to moisture anomalies, preventing cold-pool formation leads to more drying of trade-cumulus system, which in turn drives more efficient longwave clear-sky radiative cooling. This also resonates with deep convective studies who found (i) cold pools weaken moisture self-aggregation (Jeevanjee and Romps, 2013; Muller and Bony, 2015; Nissen and Haerter, 2021) and that (ii) mesoscale aggregation dries the convective system, allowing more efficient escape of longwave radiation (Bony et al., 2020b).

DATA AVAILABILITY

Datasets from the large-eddy simulation ensembles, along with the Python scripts used to generate the figures in this manuscript, are publicly available by Alinaghi et al. (2025a) at https://doi.org/10.5281/zenodo.15544026. The version of the Dutch Atmospheric Large-Eddy Simulation for homogenizing rain-evaporation is publicly available at https://github.com/dalesteam/dales/tree/botany-homogenization.

5.5 Supplementary Information

This file includes and represents explanations and figures to additionally support the text.

Bi-linear regression of the gradient production term

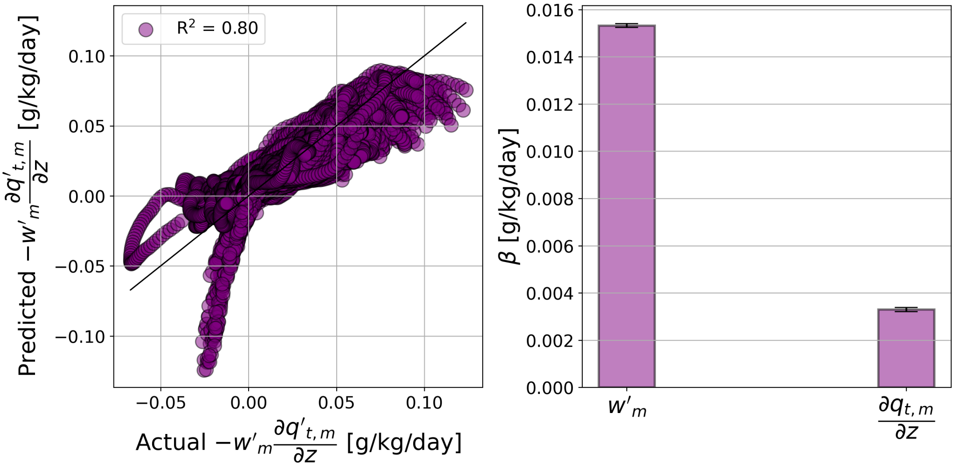

Figure S5.1: **Multivariate regression results of the gradient production term $-w'_m\frac{\partial q_{t,m}}{\partial z}$.** (Left) The scatter plot of the results of multivariate regression analysis with around 130 k points from the mesoscale blocks of the entire ensemble in 3D. (Right) The standardized beta coefficients of the multiple regression analysis for predicting the gradient production term ($-w'_m\frac{\partial q_{t,m}}{\partial z}$) as a function of mesoscale vertical ascent w'_m and gradient of mesoscale moisture $\frac{\partial q_{t,m}}{\partial z}$. The error bars show the confidence intervals at the 99.99th level of confidence. **Message** is that the gradient production term is strongly controlled by the mesoscale vertical motion and the effect of w'_m is around five times larger than that of moisture gradient in height.

Cloud-circulation coupling in the CP vs. NoCP ensembles

Figure S5.2 shows example snapshots for comparing the difference between the overall structures of the circulations between the (central reference simulation of the) CP and NoCP ensembles.

Detailed analysis for the impact of cold pools on cloudiness

Figure 5.2a,b shows that cold pools do not appear to affect the shortwave cloud-radiative effect C_s. Despite a rather large disagreement across the ensemble regarding the impact of cold pools on C_s, this model spread seems to be symmetrically distributed around zero (Fig. 5.2a). Figure 5.2b indicates that this symmetry around zero is primarily due to the opposing impacts of cold pools on cloud fraction f and cloud albedo α_c. In the following two parts of this section, we will explore how homogenizing rain-evaporation affects both f (section 5.5) and α_c (section 5.5).

To quantify the impact of cold pools on cloudiness, we analyze how the homogenization of rain evaporation modulates the response of clouds to their drivers through both

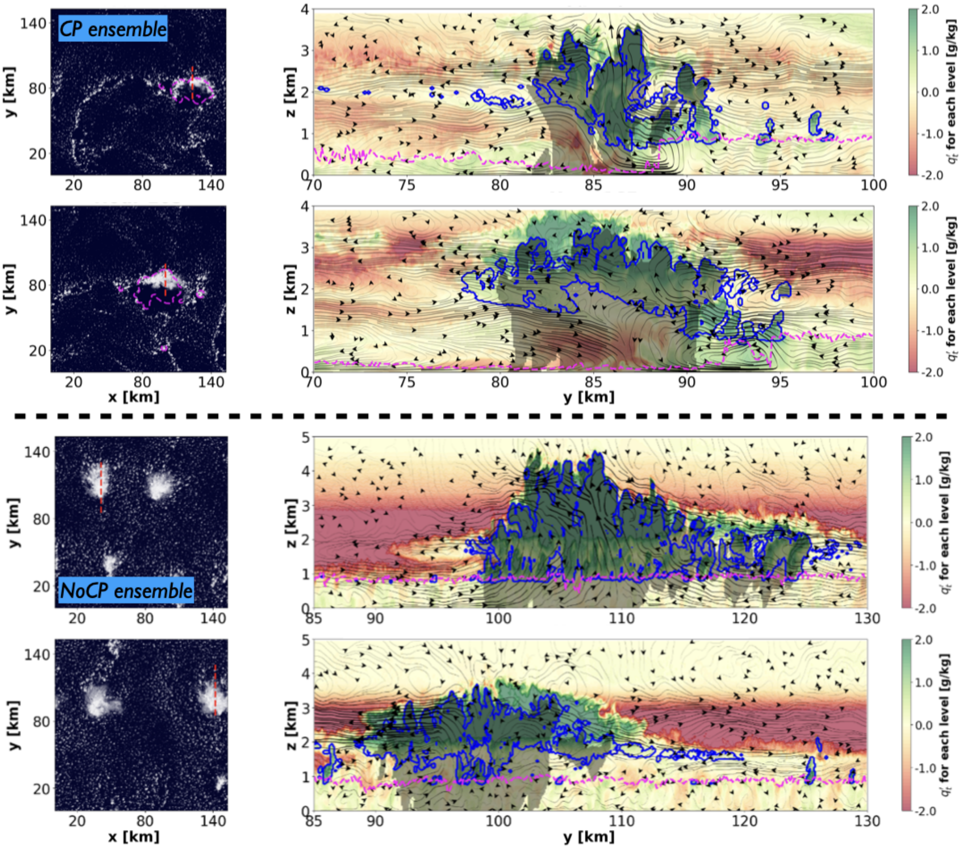

Figure S5.2: **Cloud-circulation coupling in CP vs. NoCP ensembles.** The left column shows four contour plots of cloud albedo along with the cold-pool mask shown by the dashed, magenta contour lines for two time steps of CP (upper part) and NoCP (lower part) ensemble. The right column shows y-z-cross-section contour plots of the total specific humidity anomalies associated with the dashed red line in snapshots shown in the left column. Cloud and rain boundaries are shown by the blue and grey contour lines. Circulations are made from the meridional (v) and vertical (w) velocity anomalies and are shown by black streamlines. To reduce the noise from the circulations, v, w are made from the medians of a 5-km window along the x dimension. The h_{mix} is shown by the dashed, magenta contour lines. The South (S), North (N), West (W), and East (E) directions are shown by orange labels.

thermodynamic and dynamic processes at the mesoscales. First, previous research shows that clouds tend to self-aggregate within anomalously moist mesoscale regions (Bretherton and Blossey, 2017; Janssens et al., 2023; Narenpitak et al., 2021). Once clouds begin to form, condensation anomalies generate latent heating. Due to the validity of the weak-temperature-gradient approximation in the trades, this heating drives mesoscale vertical motions. Thus, we consider mesoscale total-water anomalies, I, as the first driver, primarily representing a thermodynamic control on clouds.

Second, cold pools can suppress cloud formation by disrupting convection beneath existing clouds, but they can also trigger convection at their edges through both thermodynamic and dynamic processes (Alinaghi et al., 2025d; Seifert and Heus, 2013; Vogel et al., 2016). Thermodynamically, cold pools promote convection by accumulating heat and moisture at their fronts (Schlemmer and Hohenegger, 2016; Tompkins, 2001). Dynamically, they trigger convection as their leading edges featuring strong wind convergence and vertical motions. Therefore, in this section, we consider mesoscale vertical motion evaluated at the (near) cloud-base height, w', as the second driver of cloudiness in our analysis.

To compute both drivers I and w' at the mesoscales, we coarse-grain them by calculating their average within 10-km blocks present in every domain across both CP and NoCP ensembles. These blocks are made by splitting our 153×153 km^2 domains into 16×16 blocks with the size of 9.6×9.6 km^2. In the following subsections, these 10-km blocks enable a comprehensive statistical analysis of how rain-evaporation homogenization influences the response of both cloud fraction f and cloud albedo α to their respective drivers, I and w'.

Cold-pool ensemble lacks very humid columns, reducing cloud coverage

To investigate the difference in cloud fractions f between the CP and NoCP ensembles, we analyze all the 10-km blocks across all members of both ensembles. We group these blocks into bins based on I', similar to the moisture-space plots made by (Muller and Bony, 2015; Schulz and Stevens, 2018). For each bin of I, we compute the mean cloud fraction of all 10-km blocks within that bin. Consequently, Figs. S5.3a,b present the 2D histograms of 10-km I' and cloud fraction f for both ensembles during their last four days.

Figure S5.3b illustrates that the 10-km cloud fraction f increases as the mesoscale moisture anomaly grows. In the very moist blocks of the CP ensemble ($0 < I' < 1.5$ g/kg), the CP ensemble exhibits a larger mean cloud fraction than the NoCP ensemble, for the same I. The formation of more trade cumuli at a lower mesoscale moisture aggregation in the CP ensemble suggest convective triggering by cold pools at for instance their edges. It can also be due to formation of anvil outflows resulting from shallow mesoscale convection systems near the inversion of the CP ensemble (Alinaghi et al., 2025d). In contrast, in the NoCP ensemble, the mean cloud fraction continues to increase with higher I in the very moist blocks which do not exist in the CP ensemble. Quantifying the contribution of I bins to the mean cloud fraction of the entire ensemble, Fig. S5.3a reveals that the NoCP ensemble contains a higher frequency of blocks in the range $0 < I' < 2.5$ g/kg. This results in the mean cloud fraction of the NoCP ensemble being 0.01 larger than that of the CP ensemble. Due the weak temperature gradient at the mesoscales, a larger total moisture I of a block implies a higher relative humidity. This means that the higher frequency of blocks with higher relative humidity in the NoCP ensemble might be the reason for their 0.01 larger mean cloud fraction compared with the CP ensemble.

Here, we emphasize that the analysis of Figs. S5.3a,b and the associated discussion is for comparing the *mean* cloud fraction across both ensembles. We showed in Fig. 5.2b that although the majority of simulations agrees on cloud fraction of the CP ensemble being smaller, still around 25% of our ensemble shows the opposite, i.e. cloud fraction of the NoCP cases are smaller. Statistically, this suggests that the claim “the cloud fraction of CP cases is smaller than that of NoCP cases” cannot be considered significant at confidence levels exceeding 75%.

The statistical analysis shown here demonstrates the persistence of trade-cumulus cloudiness to even completely homogenizing rain-evaporation and cold pools. By binning

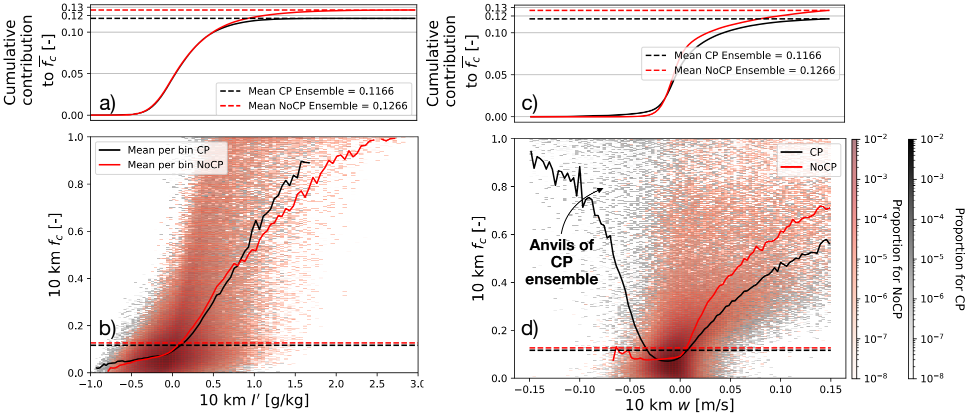

Figure S5.3: **Impact of cold pools on cloud fraction.** 2D histograms of (b) 10-km total-water anomalies (I) vs. cloud fraction (f_c) and (d) 10-km vertical velocity (w) vs. cloud fraction. Cumulative contributions to the mean f_c are shown in (a) and (c), respectively.

the 10-km blocks based on their block-averaged vertical velocity w at 1000-m height, similar to Janssens et al. (2025), Figs. S5.3c,d reveal that for blocks with overall mesoscale ascent, stronger ascent corresponds to larger cloud fractions. Figure S5.3d further demonstrates that for blocks with $w > 0$, the NoCP ensemble consistently produces a higher cloud fraction at a given ascent strength, likely due to higher relative humidity in those columns. Moreover, Fig. S5.3d indicates significant cloud coverage in the descending branch of mesoscale circulations when cold pools are present. This is attributed to blocks with anvil cloudiness, where stratiform clouds are disconnected from the updraft root at the cloud base. In these blocks, the cloud-base features downdrafts, while the inversion feature stratiform cloudiness.

COLD POOLS LEAD TO DEEPER CLOUDS WITH GREATER ALBEDO

Assuming a plane-parallel approximation, cloud albedo is given by $\alpha_c = \frac{\tau_c}{7.7+\tau_c}$, where τ_c is the cloud optical thickness, computed as $\tau_c = \mathcal{L}^{5/6} N_c^{1/3}$. Here, $\mathcal{L}$ represents the cloud-liquid-water path, and N_c denotes the cloud-droplet number concentration. Since N_c remains constant in both time and space in our model, we focus on differences in $\mathcal{L}$ between the CP and NoCP ensembles. Alinaghi et al. (2024a) demonstrated that $\mathcal{L}$ is strongly influenced by cloud geometric thickness h, or equivalently, cloud depth z_t in the *Botany* ensemble. Theoretically, we expect $\mathcal{L} \propto h^2 \approx z_t^2$ (Feingold et al., 2017; Wood, 2006). As cloud depth z_t is closely tied to the strength of updrafts, we first examine how the cloud-base mass flux $\mathcal{M}$ differs between the CP and NoCP ensembles. The mass flux for each 10-km block is calculated as the mean vertical velocity w at the cloud base, averaged over cloudy pixels where cloud-water specific humidity is greater than zero.

Figs. S5.4a,b show that while the cloud-base mass flux $\mathcal{M}$ remains insensitive to I in dry regions ($I' < 0$), it increases almost linearly with I' in mesoscale moist regions ($I' > 0$). Furthermore, these figures highlight that the primary difference in mass flux between the CP and NoCP ensembles arises from the anomalously moist mesoscale regions. Since cold pools tend to form in blocks with aggregated moisture, Fig. S5.4b suggests that, for the same level of moisture aggregation, cold pools enhance the cloud-base mass flux $\mathcal{M}$. This implies that the vertical updrafts in the CP ensemble are more dynamically driven compared with the updrafts of the NoCP ensemble.

Following the response of $\mathcal{M}$ to I', cloud depth z_t also increases linearly with I' (Fig. S5.4d). Moreover, given the same I', the higher mass flux in the CP ensemble leads to deeper clouds compared to the NoCP ensemble (Fig. S5.4c,d). Since the cloud-water path $\mathcal{L} \propto z_t^2$, Fig. S5.4f shows that $\mathcal{L}$ exhibits a nonlinear increase with I' in mesoscale moist regions ($I' > 0$). Consequently, the deeper clouds in these regions within the CP ensemble result in a greater cloud-water path compared with the NoCP ensemble (Fig. S5.4e,f).

Fig. 5.2b indicates that 17 out of 19 members of our ensemble support the statement that “the CP ensemble features deeper clouds with a larger cloud-water path." It is worth noting that the $\Delta\alpha_c$ shown in Fig. 5.2b is based on the last day of the ensemble, where the differences between the CP and NoCP ensembles are more pronounced compared to those in Fig. S5.4 which is based on data from the last four days of the ensemble.

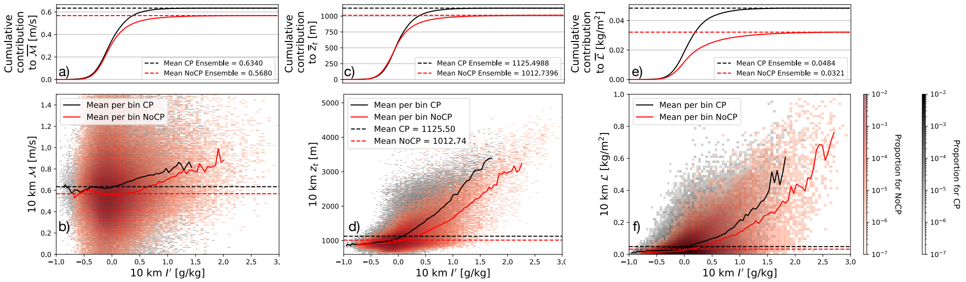

Figure S5.4: **Impact of cold pools on liquid-water path.** 2D histograms of 10-km total-water anomalies (I') vs. 10-km (b) cloud-base mass flux ($\mathcal{M}$), (d) cloud-top height (z_t), and (f) cloud-liquid-water path ($\mathcal{L}$). Cumulative contributions of I bins to the mean values are shown in (a), (c), and (e), respectively.

6

CONCLUSIONS AND OUTLOOK

The primary goal of this thesis is to advance our understanding of the mesoscale organization of trade-cumulus fields and its impact on radiative effects, low-cloud climate feedback, and the effective radiative forcing due to aerosol-cloud interactions. First, the key findings of this thesis will be summarized (section 6.1). Then, this section proposes a conceptual framework for the trade-cumulus system, integrating the findings of this thesis to provide a structured perspective followed by open questions (section 6.2).

6.1 Summary of thesis findings

Trade-wind cumulus clouds are a major source of uncertainty in climate projections (Bony and Dufresne, 2005; Myers et al., 2021). These cloud fields tend to organize into mesoscale patterns spanning tens to hundreds of kilometers. Due to coarse resolutions, climate models lack the capability to resolve such mesoscale patterns. Therefore, the relevance of these mesoscale patterns for the low-cloud climate feedback remains essentially unknown. That is, we do not yet know how these patterns respond to climate change by accelerating or decelerating global warming. This thesis aims to improve our understanding of the mesoscales and their response to large- and micro-scale variations. Specifically, it focuses on understanding the mesoscale *self-organization* of trade-cumulus fields—that is, the emergence of mesoscale patterns not driven by the external variability in the large or micro scales, but arising from inherent interactions among the components of the system itself.

The self-organization of trade-cumulus fields in the non-precipitating phase arises from condensational heating anomalies within the cloud layer, which drive shallow circulations that, in turn, govern cloud formation and further condensational heating (Bretherton and Blossey, 2017; Janssens et al., 2021; Narenpitak et al., 2021). This self-reinforcing mechanism leads to the horizontal scale growth and deepening of cloud fields in the non-precipitating phase. Once clouds reach a certain height and depth, rain eventually begins to form. As a result of rain evaporation, the air becomes colder and denser, creating cold pools that drive strong downdrafts. Once these downdrafts reach the surface, cold pools expand horizontally. Cold-pool fronts are characterized by moist air and strong convergence, triggering cloud formation at cold-pool edges. Thereby, cold pools play an important role in organizing trade-cumulus fields into mesoscale cloud rings in the precipitating phase (Seifert and Heus, 2013; Vogel et al., 2021, 2016). Throughout this thesis, we explored (i) what role cold pools play in the self-organization of trade-cumulus fields and how the scale growth of cloud fields evolves during the precipitating phase influenced by cold pools; (ii) the extent to which cold pools and mesoscale organization of trade-cumulus fields are affected by the external, large- and micro-scale cloud-controlling factors (CCFs); and (iii) the relevance of (self-)organization for the trade-cumulus radiative budgets and the effective radiative forcing due to aerosol–cloud interactions.

6.1.1 Cold pools are coupled to clouds in the form of shallow squall lines in the trades

Chapter 2 investigates the role of cold pools in the self-organization of trade-cumulus fields and their influence on the scale-growth phase. This is examined using large-eddy simulations (LESs) forced by large-scale CCFs characteristic of the trades, which remain fixed in time and homogeneous in space. This chapter demonstrates that once cold pools form, they inhibit the scale growth of cloud fields. At this stage, the trade-cumulus system enters a phase in which all cloud-related properties—such as rain, precipitation, and cold pools—exhibit strong intermittent behavior. This behavior arises from the complex coupling between clouds and cold pools, resembling the the structure of squall lines in deep mesoscale convective systems. **Chapter 2** shows that cold pools self-reinforce their parent clouds until they become strong enough to impinge on the inversion, leading to the formation of stratiform clouds and associated precipitation. This process weakens the squall-line dynamics, ultimately driving the decay of the shallow mesoscale convective systems.

6.1.2 Mesoscale organization of precipitating cumuli is strongly controlled by the large-scale conditions

After establishing the role of cold pools in the self-organization of trade-cumulus fields, **Chapter 2** examines the extent to which they are regulated by large-scale CCFs. Using a large ensemble of large-domain LESs (*Cloud Botany* from Jansson et al., 2023), **Chapter 2** demonstrates that cold pools are strongly influenced by CCFs. Specifically, their behavior is primarily governed by the strength of horizontal wind speed and large-scale subsidence. To a lesser extent, atmospheric stability and horizontal wind shear also play a role in modulating cold pools in the trades.

In essence, conditions such as increased wind speed and decreased large-scale subsidence, stability, and wind shear promote the deepening of the cloud layer. For instance, increased wind speed results in increased surface fluxes, leading to deeper boundary layers that allow formation of deeper clouds. Cloud-layer deepening leads to a higher liquid-water path in clouds, which in turn enhances the rain-water path and the development of cold pools. Furthermore, the diurnal cycle of insolation exerts a significant control over cold-pool evolution by modifying atmospheric stability. The transition from night to day reduces the net radiative cooling, strengthening atmospheric stability and thereby weakening cold pool dynamics.

6.1.3 Cold-pool evolution is controlled by the micro-scale variability

Cold pools originate directly from the evaporation of rain droplets. Since microphysical variations influence the collision-coalescence processes and in turn the onset of rain formation, they are expected to have a direct impact on cold-pool dynamics. **Chapter 3** investigates this relationship by varying cloud-droplet number concentrations N_c in the central reference simulation of the *Cloud Botany* ensemble.

This chapter shows that under low-N_c conditions (20 cm^{-3}), cold pools are more frequent and form in close proximity to one another. As a result, cold-pool interactions through their collisions become more common, leading to convective triggering at their collision points. Due to a fast formation of rain droplets in low-N_c conditions, even a small amount of triggered cloud water at the collision points is sufficient to initiate precipitation and, subsequently, cold-pool formation. In such cases, cold pools develop into a long-lived shallow squall line which perpetuates due the cold-pool collisions at its front. In such cases, cold-pool evolution exhibits minimal intermittency.

In contrast, at higher N_c values (70 and 1000 cm^{-3}), cold pools are more dispersed. In these cases, a slow formation of rain droplets prolongs the non-precipitating phase, during which cloud fields aggregate due to shallow mesoscale overturning circulations driven by condensational heating. When clouds cluster over anomalously moist regions, shallow circulations transport moisture from dry areas into already moist areas, reinforcing the contrast between moist and dry regions. This process effectively separates cloud clusters and their associated cold pools. In such cases, cold pools develop and dissipate in the form of shallow squall lines, as discussed in **Chapter 2**.

Chapter 3 further compares the effects of microphysical variations induced by N_c with those of large-scale CCFs on cloud-field properties. This chapter demonstrates that the influence of N_c is as significant as that of the most dominant CCFs in determining trade-cumulus albedo and radiative effect. This chapter, therefore, represents one of the first quantitative, systematic comparisons between the large- and micro-scale effects on trade-cumulus mesoscale organization and radiative effects.

6.1.4 MESOSCALE ORGANIZATION AFFECTS CLOUD-RADIATIVE EFFECT BY MODULATING BOTH CLOUD FRACTION AND OPTICAL THICKNESS

Chapter 4 answers the question of whether mesoscale organization affects cloud-radiative effects solely through variations in cloud fraction as shown by Bony et al. (2020a). **Chapter 4** quantifies the extent to which the organization of trade-cumulus fields influences their radiative effect, independent of cloud-cover variations. Using concepts from partial correlation analysis, **Chapter 4** removes any variability in cloud-radiative effect and organization that can be explained by cloud cover. After eliminating cloud-fraction variations, this chapter demonstrates that more clustered cloud fields can still reflect up to 20 W/m^2 more instantaneous shortwave radiation to space, based on approximately 20 years of satellite data. Data from a large ensemble of large-eddy simulations (LESs) complement these satellite-based findings, showing that more clustered fields reflect more radiation to space because they are geometrically thicker, contain more liquid water, and have smaller cloud droplets. As a result, they exhibit greater optical depth and albedo, making them brighter. As shown in this chapter, mesoscale organization affects clouds in both horizontal and vertical dimensions, controlling the extent to which clouds reflect shortwave radiation to space.

6.1.5 COLD POOLS AFFECT RADIATIVE BUDGETS IN THE TRADES BY AFFECTING FIELDS OF MOISTURE AND NOT CLOUDS

Chapter 5 investigates the relevance of cold-pool-induced self-organization for the radiative budget of the trades. Using a large ensemble of LESs, **Chapter 5** inhibits cold-pool formation by homogenizing rain evaporation and quantifies its effect on the radiative budget. As a result, **Chapter 5** shows that simulations with cold pools feature clouds with slightly higher albedo and slightly smaller coverage. This results in a very weak impact of cold pools on shortwave radiative effects. In contrast, inhibiting cold pools by homogenizing rain evaporation allows moisture to self-aggregate freely through shallow circulations governed by condensational heating. This leads to the formation of very moist mesoscale regions that would not have developed in the presence of cold pools. The runaway moisture self-aggregation in the absence of cold pools results in deep clouds that precipitate intensely. The difference in precipitation explains the divergence in bulk moisture budgets between simulations with and without cold pools at nearly every time step. A lower drying rate due to reduced precipitation flux in simulations with cold pools leads to less efficient outgoing clear-sky longwave radiation, amounting to 1.88 W/m^2 when averaged over a day and the ensemble. Thus, the mesoscale self-organization due to cold pools in the trades affects the radiative budgets primarily by modulating moisture fields rather than clouds.

6.2 A CONCEPTUAL FRAMEWORK FOR THE TRADE-WIND CUMULUS SYSTEM

Collectively, the results in this thesis suggests a conceptual framework for understanding the trade-wind cumulus system. In this section, we first propose this framework based on the combined findings of this thesis regarding the self-organization of the trade-cumulus system, i.e. its evolution under time-invariant and spatially homogeneous large-scale forcings. Second, we summarize how the diagram of the conceptual model responds to variations in micro- and large-scale forcings, as well as to the diurnal cycle as a cyclic large-scale forcing mechanism. Third, we discuss what the proposed conceptual diagram implies for the radiative budgets of the trade-wind cumulus fields. Finally, the conceptual framework shows the remaining open questions and knowledge gaps regarding the trade-cumulus system and its climate feedback.

6.2.1 TRADE-CUMULUS SELF-ORGANIZATION TENDS TO EXHIBIT A CYCLIC BEHAVIOR

The combined insights from Bretherton and Blossey (2017); Janssens et al. (2023) and **Chapters 2,3** suggest that trade-cumulus evolution is primarily governed by two key processes. The first, which we call mesoscale self-aggregation, is the result of the condensation of cloud droplets and the associated latent heating, which drives shallow circulations and the scale growth of moisture fluctuations and clouds. In **Chapter 3**, we quantified this process using the difference in total moisture between the high and low percentiles of the coarse-grained moisture fields, denoted as ΔQ. The second process is driven by the evaporation of rain droplets, which cools the atmosphere and generates density currents, thereby governing cold-pool dynamics, denoted as $\mathcal{D}_{cp}$. The metric $\mathcal{D}_{cp}$ quantifies the strength of cold pools within the simulation domain. This strength can be assessed based on the intensity of the horizontal wind within the cold pools and/or the magnitude of convergence at cold-pool edges. **Chapter 2** demonstrated that these dynamic metrics are positively (lag-)correlated with the size of cold pools within the simulation domain.

Building on Bretherton and Blossey (2017); Janssens et al. (2023) and **Chapters 2,3,5**, mesoscale cloudiness C_m in the trades can be conceptually modeled as

$$\partial_t C_m = f_1(\Delta Q) + f_2(\mathcal{D}_{cp}), \tag{6.1}$$

where C_m represents a mesoscale (mean-field) cloud-related variable such as cloud fraction f_c or cloud-water path $\mathcal{L}$. The functions f_1 and f_2 translate the effects of mesoscale self-aggregation ΔQ and cold-pool dynamics $\mathcal{D}_{cp}$ into changes in mesoscale cloudiness, respectively.

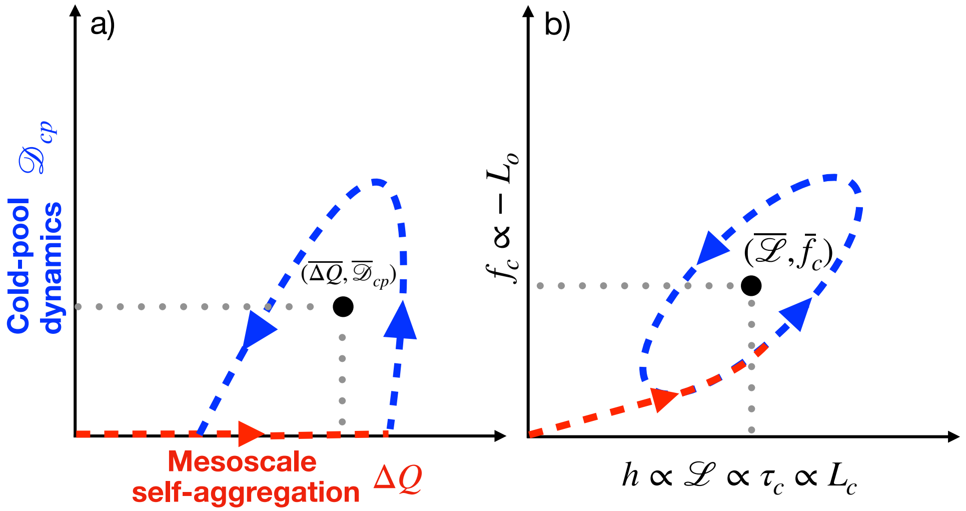
a)
Cold-pool dynamics $\mathscr{D}_{cp}$
$(\overline{\Delta Q}, \overline{\mathscr{D}}_{cp})$
Mesoscale self-aggregation ΔQ
b)
$f_c \propto -L_o$
$(\overline{\mathscr{L}}, \bar{f}_c)$
$h \propto \mathscr{L} \propto \tau_c \propto L_c$

Figure 6.1: **Conceptual diagram of the evolution of the trade-cumulus system.** Plots show diagram sketches of the temporal evolution of the a) process space spanned by the mesoscale moisture (self-)aggregation ΔQ and cold-pool dynamics $\mathcal{D}_{cp}$ and b) mesoscale organization space spanned by the geometry-based organization metrics. The mean of (near-)steady state is shown by the black dot in both process space $(\overline{\Delta Q}, \overline{\mathcal{D}}_{cp})$ and organization space $(\overline{\mathcal{L}}, \bar{f}_c)$.

Following **Chapters 2,3**, we construct a conceptual diagram illustrating the interplay between mesoscale self-aggregation ΔQ and cold-pool dynamics $\mathcal{D}_{cp}$ in the trade-cumulus system. Figure 6.1a presents a plane spanned by these two processes, which we refer to as the process space. Based on findings from **Chapters 2,3,5**, the trade-cumulus system initially self-aggregates through shallow circulations before cold pools form. Once cold pools emerge, they arrest further self-aggregation of moisture (see also Fig. S6.1). **Chapters 2,3** demonstrate that cold-pool dynamics exhibit intermittent time series, driven by complex interactions between clouds and cold pools in the form of shallow, short-lived squall lines. When cold pools dissipate, self-aggregation resumes, leading to further scale growth and deepening, which in turn facilitates the reformation of cold pools. This cyclic interplay between mesoscale self-aggregation and cold-pool dynamics manifests as a cyclic behavior, as illustrated in Fig. 6.1a.

Chapters 2,3 further show that the cyclic behavior observed in the process space of Fig. 6.1a similarly governs a cyclic pattern in the evolution of mesoscale cloudiness C_m, as depicted in Fig. 6.1b, which represents the mesoscale cloud organization space (see also Fig. S6.1). Here, variations in C_m can be described using various process- and geometry-based metrics. Janssens et al. (2025, 2021) identified two geometry-based dimensions—namely, the mean size of cloud objects (L_c) and the mean (or maximum) fraction of open-sky areas (L_o)—as key variables capturing a significant portion of variability in the trades. Complementary analyses from **Chapter 4** and Janssens et al. (2025) indicate that L_c is correlated with cloud geometric thickness (h), due to the positive relationship between horizontal and vertical extents. Cloud geometric thickness, in turn, strongly influences the domain-mean cloud-water path $\mathcal{L}$ and, consequently, the optical depth τ_c. Additionally, L_o is negatively correlated with cloud fraction.

Janssens et al. (2023) demonstrated that during the scale-growth phase, both cloud size (L_c) and depth (h) develop while cloud fraction remains only weakly affected, which is illustrated in Fig. 6.1b showing a larger increase in cloud length scale compared with their coverage in the self-aggregation phase. **Chapters 2,3** explain how clouds interact with cold pools and evolve over a cold-pool life cycle. These findings illustrate that cold-pool-cloud interactions in the form of shallow squall lines affect mesoscale organization. This leads to mesoscale cloud organization too exhibits a cyclic behavior, driven by the evolution in the process space.

6.2.2 WHAT CONTROLS THE CENTER, SIZE, AND THE FREQUENCY OF THE CYCLIC BEHAVIOR?

Multivariate regression analyses throughout this thesis indicate that variations in large-scale conditions by CCFs determine the daily average degree of mesoscale aggregation of moisture (see Fig. S6.2), cold-pool dynamics, and in turn mesoscale organization of trade-cumulus fields (**Chapters 2,3**). This means that CCFs strongly control the position of the center of the cycle in both the process space ($\overline{\Delta Q}, \overline{\mathcal{D}}_{cp}$) and the mesoscale organization space ($\overline{\mathcal{L}}, \overline{f}_c$) across a broad range of climatologically relevant conditions of the trades.

Regression analyses further suggest that large-scale conditions also influence the amplitude of the cycle (see Figs. S6.3, S6.4). The amplitude of these fluctuations can be quantified by subtracting the long-term average of a time series from its maximum value. Alternatively, the standard deviation of cloud-field properties over time can serve as a proxy for the cycle's amplitude, where a larger standard deviation indicates a stronger deviation from the mean evolution (i.e., the center) of the cycle. For instance, stronger wind speeds and greater atmospheric instability enhance the degree of mesoscale aggregation (Fig. S6.2), leading to deeper clouds and stronger cold pools compared to the mean long-term state. Stronger cold pools afterward create larger open-sky areas. Thus, the increased strength of these processes manifests in larger horizontal and vertical cloud extents, which also exhibit larger fluctuations. Figure 6.2a,b accordingly, shows the sketch of how both dimensions in both process and organization space change in response to variations in the large scales. It should be noted that our analysis of the impact of CCFs on the amplitude of fluctuations (in Figs. S6.3, S6.4) is based on the *Cloud Botany* ensemble, which features a diurnal cycle of insolation. Since the diurnal cycle affects atmospheric stability and, thereby, influences the amplitude of the time series of cloud fields (**Chapters 2,3**), it is important to assess the impact of CCFs on the cycle's amplitude in an ensemble similar to *Cloud Botany* but with the diurnal cycle of insolation switched off.

In addition, **Chapter 3** demonstrates that variations in cloud-droplet number concentrations, do not significantly influence the mean state (i.e., they do not shift the center of the cycle). However, they do affect the size of the cycle, since increased cloud-droplet number concentration leads to larger amplitudes in fluctuations of mesoscale self-aggregation, cold-pool dynamics as well as almost all cloud-field properties. More interestingly, **Chapter 3** shows that when $\mathrm{N_c}$ decreases further, approaching cloud-droplet number concentrations of $\mathrm{Nc} = 20/\mathrm{cm}^3$, the behavior of the cycle itself changes. In cases with very low $\mathrm{N_c}$, aggregation does not strongly develop initially. Instead, due to the early onset of rain

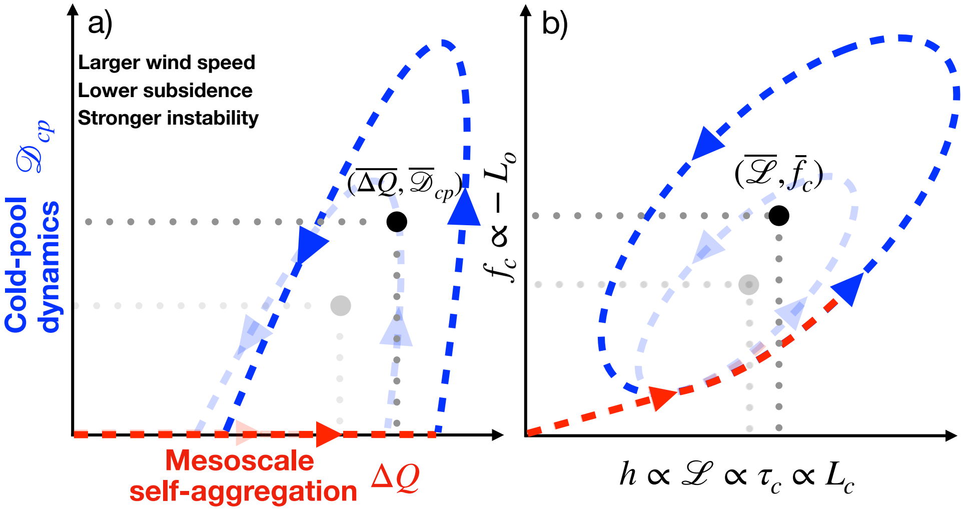
a)
Larger wind speed
Lower subsidence
Stronger instability
$(\overline{\Delta Q}, \overline{\mathscr{D}}_{cp})$
Cold-pool dynamics $\mathscr{D}_{cp}$
Mesoscale self-aggregation ΔQ
b)
$f_c \propto -L_o$
$(\bar{\mathscr{L}}, \bar{f}_c)$
$h \propto \mathscr{L} \propto \tau_c \propto L_c$

Figure 6.2: **Conceptual diagram of the trade-cumulus system and its dependence on large-scale conditions.** The figures illustrate changes in the cyclic behavior of trade-cumulus self-organization in response to increased large-scale wind speed, instability, and subsidence. Low-transparency diagrams indicate the reference evolution (Fig. 6.1), while high-transparency curves show the new evolution.

formation, cold pools form from the very beginning (Fig. 6.3a). Over time, these cold pools transition from a randomly distributed state to a large, elongated squall line, which persists due to cold-pool collisions at its leading edge. During this phase, both cold pools and mesoscale aggregation of moisture grow together, as the large squall line appears to enhance mesoscale moisture aggregation (Fig. 6.3a). Under these conditions, the system tends to converge toward a quasi-stationary state, where all cold-pool and cloud-related properties, including mesoscale organization metrics, reach a time-invariant value, albeit with small fluctuations around this point (Fig. 6.3b). It is important to note that, despite the increased strength of cold pools (Fig. 6.3a), the mean state of the mesoscale cloudiness itself remains unchanged (Fig. 6.3b).

Furthermore, **Chapters 2,3** demonstrate that the evolution of the trade-cumulus system is strongly influenced by the diurnal cycle of insolation; so, the diurnal cycle of insolation acts as a cyclic forcing and in turn imposes strong control over the frequency of the cycle. It cyclically affects the trade-cumulus system by enhancing instability at night due to increased net radiative cooling. Since stability—as a large-scale CCF—sets the center of the system's cycle, the diurnal variation in insolation shifts this center by modulating the system's stability. In response to these changes in stability, the self-organizing processes—namely self-aggregation and cold-pool dynamics—synchronize with the diurnal cycle of net radiative cooling, evolving cyclically with a 24-hour frequency around this central state. The results of **Chapters 2, 3** show that the center of the system does not appear to shift when the diurnal cycle is turned off. However, the amplitude of the fluctuations increases when the diurnal cycle is present. In the absence of the diurnal cycle, the frequency of oscillations seems to depend on microscale properties. Specifically, an

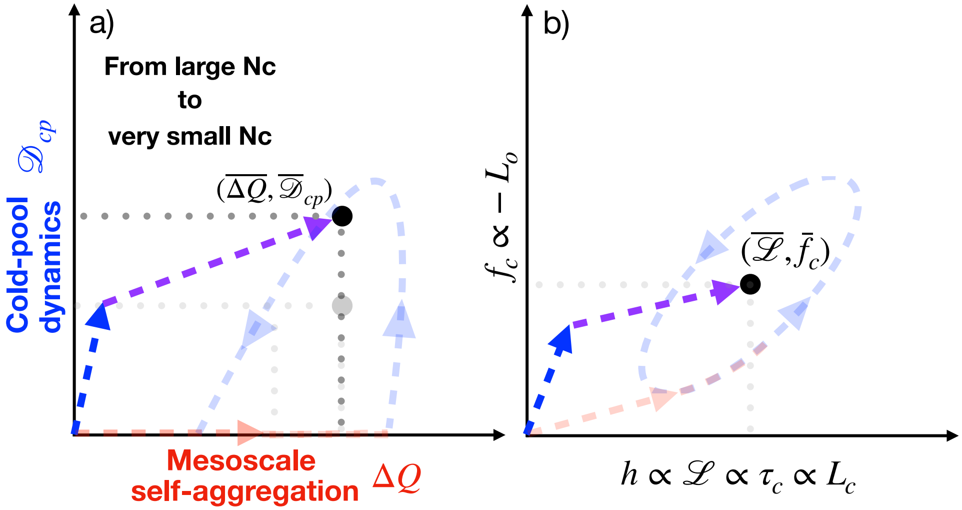
a)
From large Nc
to
very small Nc
$(\overline{\Delta Q}, \overline{\mathscr{D}}_{cp})$
Cold-pool dynamics $\mathscr{D}_{cp}$
Mesoscale self-aggregation ΔQ
b)
$(\overline{\mathscr{L}}, \bar{f}_c)$
$f_c \propto -L_o$
$h \propto \mathscr{L} \propto \tau_c \propto L_c$

Figure 6.3: **Conceptual diagram of the trade-cumulus system and its dependence on cloud-droplet number concentration.** The figures illustrate changes in the behavior of trade-cumulus self-organization in response to variations in cloud-droplet number concentration N_c. Low-transparency diagrams indicate the reference evolution with $N_c > 50\ /\mathrm{cm}^3$ (Fig. 6.1), while high-transparency curves show the new evolution with decreased N_c to concentrations of $20/\mathrm{cm}^3$. The purple arrow here means that both cold pools (blue) and mesoscale aggregation (red) are growing together.

increase in N_c leads to a noticeable decrease in the frequency of the system's evolution (**Chapter 3**). Based on the findings of this thesis, we cannot draw definitive conclusions regarding the influence of large-scale properties on the frequency of the cycle. This remains an open question for future studies.

6.2.3 How does the system evolve if it is initialized from an already organized state outside the cycle?

Throughout this thesis, all simulations begin from a non-cloudy state where all fields related to the thermodynamic and dynamic properties are homogeneous in space. It would be valuable to initialize LES simulations from a point outside the cycle–where the initial condition of the system features mesoscale structures–to explore whether the large-scale CCFs of the system drive its evolution back toward the cycle. We have conducted similar simulations and found that the system tends to return to the cycle defined by micro- and large-scale CCFs (e.g., see Fig. S6.5). This suggests that the cycle is an attractor for the trade-cumulus system. Nevertheless, a comprehensive analysis based on a systematically initialized ensemble of simulations with varied initial conditions would be necessary to test this hypothesis more robustly. A similar ensemble of stratocumulus system with varied initial conditions was performed by Glassmeier et al. (2019).

Initial conditions with organized structures are especially relevant because air masses in the trade-wind regime follow trade winds and therefore mostly originate from the stratocumulus regime, as shown by the preliminary analysis of geostationary satellite data (Meier, 2024) and previous studies (Schulz et al., 2021). Initial conditions are also important in cases like *Fish* pattern (Stevens et al., 2020), which appears to form following the intrusion of extra-tropical air masses into the trades (Schulz et al., 2021). Conducting ensembles with varying initial conditions in terms of the organization and structure of the system would be valuable for understanding the extent to which aggregation and cold-pool processes influence and shape these already available or intruding patterns to the trades.

6.2.4 What does the cyclic behaviour imply for trade-cumulus radiative budgets?

The studies of Janssens et al. (2025) and **Chapter 5** show that when assessing the impact of mesoscale organization on the radiative or energy budget of the trades, we should not focus solely on clouds. In addition to clouds, which determine the shortwave cloud radiative effect, the system's moisture budget ultimately controls the longwave outgoing clear-sky radiation (Bony et al., 2020b; Fildier et al., 2023). This means that the space shown in part (b) of all diagrams in this section is relevant only for the cloud radiative effect and overlooks the longwave clear-sky radiative fluxes, where mesoscale organization also plays an important role.

To understand the impact of mesoscale self-organization on the climate feedback of trade-cumulus fields, two denial experiments were performed on the *Cloud Botany* ensemble. First, Janssens et al. (2025) re-performed the entire ensemble on smaller domains where mesoscale aggregation and cold-pool dynamics (the process space in Figs. 6.1-6.3) cannot develop and remain negligible. In such an ensemble, where mesoscales cannot develop, clouds are almost entirely controlled by large-scale conditions. This means that the mesoscale organization space (diagram b of Figs. 6.1-6.3) collapses into a single point whose location is determined by the CCFs. As a result, the system resembles the *Sugar* pattern, with almost negligible precipitation. Since the center of the cycle is controlled by the CCFs, Janssens et al. (2025) consistently show that the mean state of cloudiness remains nearly unchanged when both mesoscale processes are suppressed. This indicates that–independently of CCFs–mesoscale self-organization has a very weak impact on the mean cloud-radiative effect.

Janssens et al. (2025) demonstrate that the reason for the weak impact of self-organization on cloudiness is that the mesoscale organization appears to symmetrically affects cloudiness horizontally: increased cloudiness in the ascending branch of circulations is compensated by decreased cloudiness in the descending branch. Similarly, our proposed cyclic behavior of trade-cumulus self-organization suggests that mesoscale processes symmetrically distribute cloudiness around the mean state—determined by the CCFs—over time as well: mesoscale aggregation and cold-pool dynamics together evolve such that the system oscillates around a mean state set by the large-scale CCFs. This means that by averaging over time scales similar to the dominant period of the cycle, the effect of mesoscale self-organization on cloudiness cancels itself out, implying a weak impact of self-organization on cloudiness over longer time scales. The second denial experiment, in which only cold-pool dynamics were suppressed, led to the same conclusion: given CCFs, cold pools also have a very weak impact on the daily mean cloud-radiative effect in the trades (**Chapter 5**).

Preventing both the scale-growth mechanism and cold-pool dynamics also appears to have a very weak impact on the moisture budget and, in turn, on the clear-sky longwave outgoing radiation of the trades (Janssens et al., 2025). However, preventing only cold-pool dynamics allows moisture aggregation to develop freely (**Chapter 5**). This leads to the generation of intense precipitation fluxes that drive the drying of the system. Consequently, given the same CCFs, preventing cold-pool dynamics affects the mean state of the system in terms of moisture and influences the radiative effects related to clear-sky longwave radiation. This results in an increase of approximately 1.88 W/m^2 in the daily mean escape of longwave radiation when cold-pool formation is prevented. Thus, results of **Chapter 5** shows that cold pools do not change the mean of the system in terms of mesoscale cloudiness, but it does change the mean of the system in terms of moisture, which is relevant for the longwave clear-sky radiation budget.

6.2.5 OPEN QUESTIONS AND OUTLOOK

Guided by the proposed conceptual framework, we list and elaborate on some of the open questions, followed by suggestions on how to address them.

An explicit theory for the proposed cyclic behavior is missing

The first question concerns the weighting functions f_1 and f_2 in Eq. 6.1. For f_1, previous studies (Bretherton and Blossey, 2017; Janssens et al., 2023; Narenpitak et al., 2021) have started developing a theory on the interaction between cloudiness and mesoscale self-aggregation in the trades. However, despite the efforts within this thesis, an explicit theory on the interaction between clouds and cold pools is still lacking. To address this gap, future research should investigate through what underlying mechanisms rain-evaporation-driven cold pools inhibit moisture self-aggregation in the trades—a pathway already initiated in **Chapter 5**. Given the similarities between the shallow squall lines explored in this thesis and their deep counterparts, theories from deep squall-line studies (Rotunno et al., 1988; Stensrud et al., 2005; Weisman and Rotunno, 2004) are possibly good starting points for developing theories for the impact of cold pools on self-aggregation and their coupling with clouds.

After bringing rain evaporation and cold pools into the moisture-convection framework, the next step is to develop simple conceptual models, such as the "bulk model for instability" proposed by Janssens et al. (2023). This bulk model—which applies to moist mesoscale regions in the cloud layer—follows from Equations 30a and 30b of Janssens et al. (2023):

$$\frac{\partial \langle q'_{t_m} \rangle}{\partial t} \propto \langle q'_{t_m} \rangle \overline{\theta}_l w^* \frac{\partial}{\partial z}\left(\frac{\Gamma_{q_t}}{\Gamma_{\theta_{lv}}}\right) \tag{6.2}$$

where $\langle q'_{t_m} \rangle$ represents bulk mesoscale moisture fluctuations, $\overline{\theta}_l$ is the slab-averaged liquid-water potential temperature, w^* is the domain-mean vertical velocity conditioned on cloudy grid points, and Γ_{q_t} and $\Gamma_{\theta_{lv}}$ are the lapse rates of moisture and liquid-water virtual potential temperature, respectively. A possible starting point is to understand the role that rain evaporation and cold pools play in modulating the terms (i) the vertical velocity scale w^* and (ii) $\frac{\partial}{\partial z}\left(\frac{\Gamma_{q_t}}{\Gamma_{\theta_{lv}}}\right)$. **Chapter 5** already highlights that, at the mesoscales, cold pools strongly damp vertical velocity because the overall mesoscale vertical velocity in areas influenced by cold pools is zero, due to the cancellation between updrafts at cold-pool edges and downdrafts in their interiors. However, how cold pools affect the lapse rates of total moisture and liquid-water virtual potential temperature remains unclear and warrants further investigation.

The cyclic behaviour might be sensitive to the microphysical choices and the spatial resolution in models

We began this thesis by criticizing climate models for their failure to parametrize shallow convection and clouds accurately. LESs (albeit on small domains) with 100-meter resolution, which can resolve convection, help address this issue. However, rain evaporation—one of the central themes of this thesis and a crucial component of the cyclic behaviour—is still highly parameterized in such high-resolution models. Li et al. (2015) also showed that cold pools are sensitive to the choice of microphysics schemes in LESs. In response, the scientific community initiated the Cold-Pool Model Intercomparison Project (Kazil et al., 2025). The first results of this comparison between several LESs highlight that models with different microphysics schemes generally agree well on the evolution and magnitude of cloud and rain-water paths. However, the amount of surface precipitation—or in other words, the extent to which rain evaporates—varies significantly among models. This implies that cold-pool characteristics differ across models. Since cold pools play a crucial role in shaping moisture fields and, consequently, in determining how much heat is trapped in the atmosphere (**Chapter 5**), it is essential to identify the most suitable microphysics scheme. Observational data on rain evaporation would be valuable in refining and potentially unifying these microphysics schemes.

Another important consideration is that all conclusions drawn in this thesis regarding the impact of micro-scale variations on cold pools are based on simulations with fixed cloud-droplet number concentrations. This limitation prevents us from assessing the real-world, full microphysical adjustments of cloud fields to aerosol perturbations. A logical next step would be to extend the analysis of **Chapter 3** using more realistic cloud microphysics schemes–such as those of Yamaguchi et al. (2019) on small domains–that explicitly account for the activation of cloud droplets from aerosols.

An important point emerging from **Chapter 5** concerns the representation of cold pools in climate models. As climate-model resolutions improve, mesoscale processes are increasingly well captured. However, the results of **Chapter 5** indicate that even if km-scale climate models–to some extent–partly represent mesoscale aggregation, they may over-dry the atmosphere if cold pools are not adequately represented to suppress mesoscale vertical motions. The absence of cold pools, as shown in **Chapter 5**, can result in an additional 1.88 W/m^2 of cooling on a daily average. This issue is particularly relevant because recent research suggests that mesoscale features begin to develop at a resolution of approximately 1 km (Saffin et al., 2023), while cold pools require resolutions of at most 100 m to properly trigger convection at their edges (Fiévet et al., 2023).

How does the domain size affect the cycle properties?

The simulations in this thesis and the resulting insights summarized in the sketch diagrams of this chapter are all based on domains with a size of 150 by 150 km^2. Comparison of our simulations with those of Seifert et al. (2015) and Yamaguchi et al. (2019) in **Chapter 3** showed that LES-based responses of the frequency and amplitude of fluctuations to N_c are clearly sensitive to domain size when the domain length is smaller than 150 km. We have performed simulations with domains four times larger (i.e. 300 by 300 km^2), and the results remain consistent with those obtained from 150 by 150 km^2 domains (see Fig. S6.6). Although this is promising, we still do not know how large a domain needs to be to truly capture the mesoscale processes shaping the trades. Regarding this point, the fact that simulations on 300 by 300-km^2 domains still show strong intermittency suggests that the phases of several existing shallow mesoscale convective systems within the simulation domain appear to be synchronized, even in the absence of the diurnal cycle. The underlying reason for this synchronization of shallow squall-line events is not trivial and therefore remains to be explored.

LESs with open-boundary conditions (e.g., Liqui Lung et al.., 2024) can be particularly useful, as they are not constrained by the limitations of small-domain simulations. For instance, in LESs with doubly periodic boundary conditions and relatively small domains, once a cloud system aggregates, its subsequent cold pools may collide with themselves, leading to artificial and unrealistic cold-pool interactions. Such unrealistic collisions can result in erroneous mechanical triggering of convection that would not occur in nature. Additionally, open-boundary LES setups provide a more realistic representation of the interactions between large- and mesoscale processes, and they even allow for studying the extent to which mesoscales influence larger scales.

How fast does the trade-cumulus system respond to variations in micro- and large-scale?

Vial et al. (2023) used the diurnal cycle as a testbed to assess which climate models best represent trade-wind cumuli in the climate system. Their results show that climate models that better capture the transition from shallow to deep clouds overnight also exhibit the weaker trade-cumulus climate feedback found in both observational data (Cesana and Del Genio, 2021; Myers et al., 2021) and LESs (Janssens et al., 2025). This suggests that the response time of the mesoscales to variations in large-scale features, such as the diurnal cycle, matters for the climate feedback of the trade-wind regime.

Due to diurnality, clouds exhibit higher coverage and albedo during the middle of the night or near sunrise in both observations (Vial et al., 2021) and the LESs conducted or used in this thesis (**Chapter 2,3**). As discussed in **Chapter 2**, the distribution of cloudiness between day and night plays a crucial role in determining the amount of sunlight reflected back into space. For instance, in our idealized simulations, colder sea-surface temperatures or drier environments appear to slow down the deepening rate at night, causing the peak in cloudiness to occur during the day (**Chapter 2**). This shift leads to up to twice the shortwave reflection compared to simulations with warmer sea-surface temperatures, where convection develops faster and peaks in the middle of night.

Unlike our idealized simulations, there is also a diurnal cycle in large-scale CCFs in the trades, such as the horizontal wind speed (Meier, 2024; Vial et al., 2021). Therefore, it is important to understand how quickly mesoscale cloudiness responds to variations in CCFs and to what extent the time scale of this response influences the distribution of cloudiness between day and night. This could have implications for low-cloud climate feedback: if, in a warmer climate, CCFs evolve in a way that accelerates cloud deepening overnight while leading to an earlier cloud shrinkage during the day, the overall shortwave reflection may decrease. While this might seem like a second-order effect, future studies should at least make an effort to quantify its relevance for low-cloud climate feedback.

6.3 SUPPLEMENTARY INFORMATION

This section provides figures to additionally support the text in the conclusions.

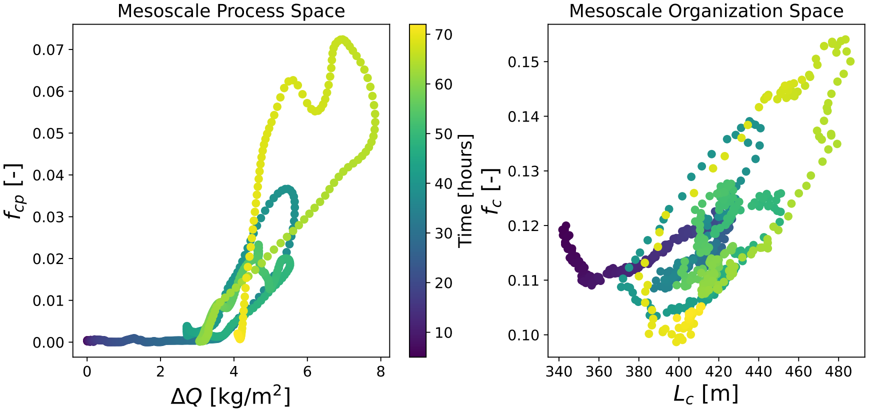

Figure S6.1: **Temporal evolution of mesoscale processes shaping organization of trade-cumulus fields.** The left plot shows the temporal evolution of the mesoscale moisture self-aggregation metrics ΔQ and cold-pool fraction f_{cp} as processes shaping the mesoscale self-organization of trade-cumulus fields. The right plot shows how the domain-mean size of cloud objects within the simulation domain L_c and cloud fraction f_c, as proxies for mesoscale self-organization of trade-cumulus fields, evolve temporally. The time series are from the central reference simulation of the *Cloud Botany* ensemble with the cloud-droplet number concentration of 1000 /cm^3.

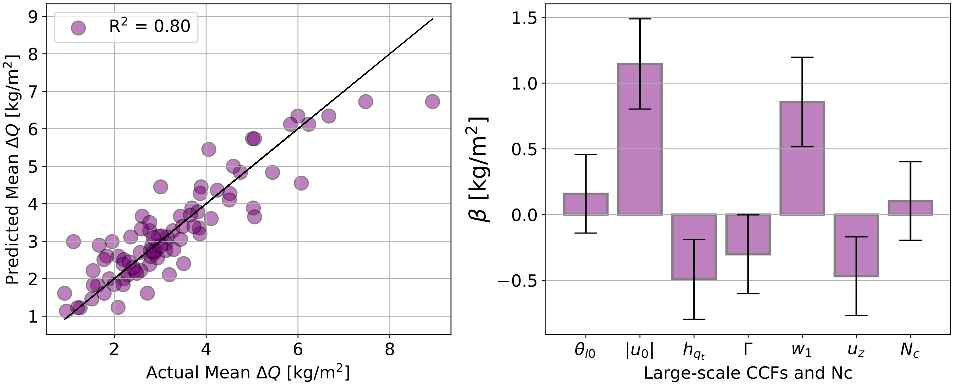

Figure S6.2: **Dependence of the mesoscale moisture aggregation metric on CCFs.** Multivariate regression results of the mesoscale moisture aggregation metric ΔQ with CCFs as regressors. The results are based on the simulations of the *Cloud Botany* Ensemble.

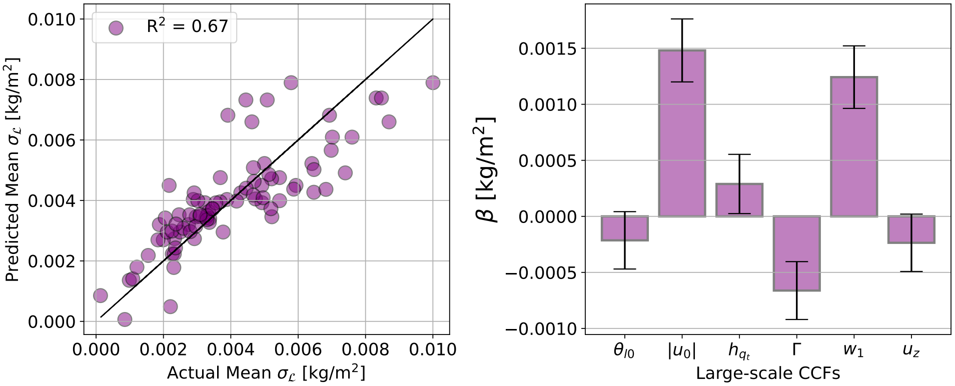

Figure S6.3: **Dependence of liquid-water path standard deviation in time $\sigma_{\mathcal{L}}$ on CCFs.** Multivariate regression results of the liquid-water path $\mathcal{L}$ standard deviation in time $\sigma_{\mathcal{L}}$ with CCFs as regressors. The results are based on the simulations of the *Cloud Botany* Ensemble.

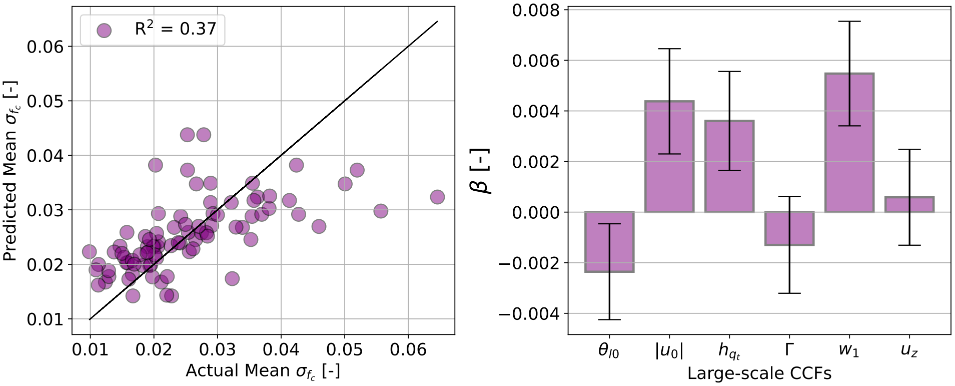

Figure S6.4: **Dependence of cloud-cover standard deviation in time σ_{f_c} on CCFs.** Multivariate regression results of the cloud-cove standard deviation in time σ_{f_c} with CCFs as regressors. The results are based on the simulations of the *Cloud Botany* Ensemble.

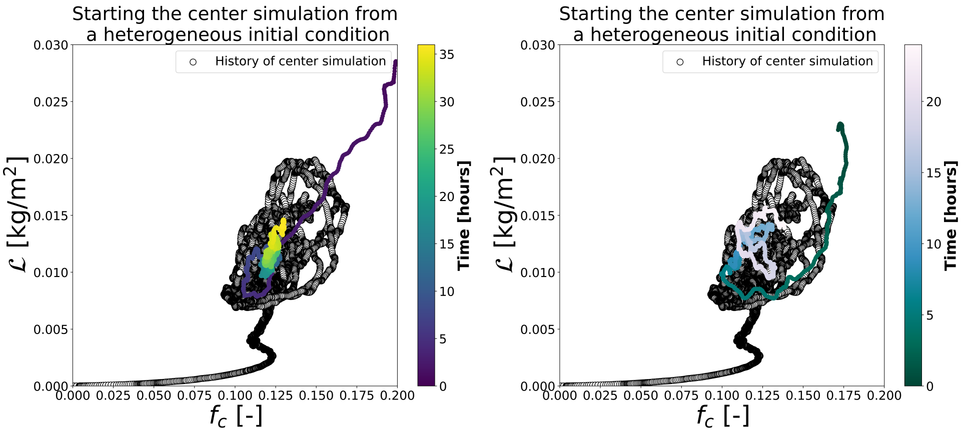

Figure S6.5: **Initializing the central reference simulation of the *Cloud Botany* ensemble from a non-homogeneous cloudy state.** The figure presents two experiments designed to investigate how the central reference simulation, without a diurnal cycle (explored in Chapter 2), evolves when initialized from an organized, precipitating cloud state with existing cold pools. White circles represent points from the central reference simulation when started from a homogeneous, non-cloudy state. The left and right plots illustrate the evolution of the simulation when initialized from a point outside the cycle. In both cases, the system tends to return to the cycle, whose center and size appear to be dictated by large-scale factors. The x- and y-axes show the cloud fraction f_c and liquid-water path $\mathcal{L}$.

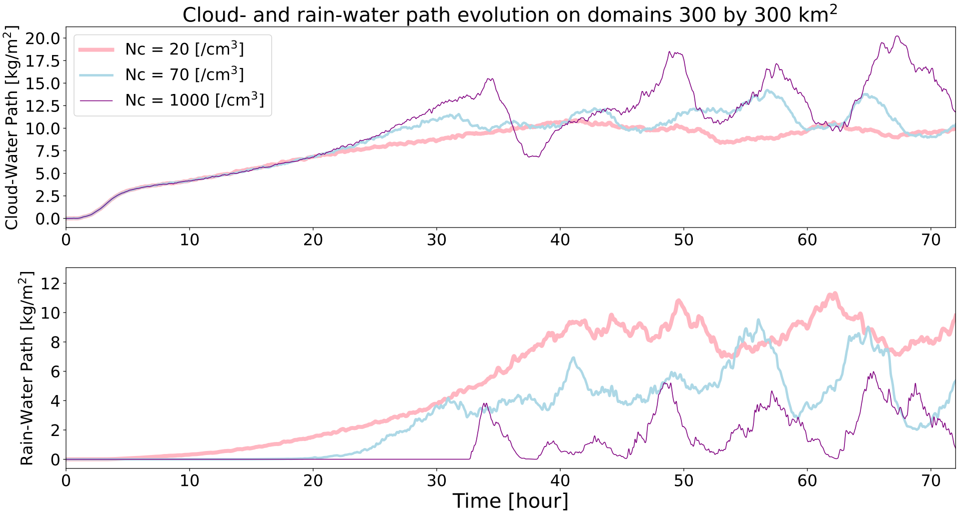

Figure S6.6: **Evolution of cloud-and rain-water path on 300 by 300 km^2 domains.** Domain-size sensitivity of the response of cloud- and rain-water path evolution to cloud-droplet number concentrations N_c in comparison with results of **Chapter 3**.

BIBLIOGRAPHY

BIBLIOGRAPHY

Albrecht, B. A. (1989). Aerosols, cloud microphysics, and fractional cloudiness. *Science*, 245(4923):1227–1230.

Albright, A. L., Stevens, B., Bony, S., and Vogel, R. (2023). A new conceptual picture of the trade wind transition layer. *Journal of the Atmospheric Sciences*, 80(6):1547–1563.

Alinaghi, P., Janssens, M., Choudhury, G., Goren, T., Siebesma, A. P., and Glassmeier, F. (2024a). Shallow cumulus cloud fields are optically thicker when they are more clustered. *Quarterly Journal of the Royal Meteorological Society*, 150(763):3566–3577.

Alinaghi, P., Janssens, M., and Jansson, F. (2025a). Dataset for the cold-pool denial experiment in a large ensemble of large-domain, high-resolution large-eddy simulations.

Alinaghi, P., Janssens, M., and Jansson, F. (2025b). Warming from cold pools: A pathway for mesoscale organization to alter earth's radiation budget.

Alinaghi, P., Jansson, F., A. Blázquez, D., and Glassmeier, F. (2024b). Datasets and the movie for the manuscript "Cold pools mediate mesoscale adjustments of trade- cumulus fields to changes in cloud-droplet number concentration".

Alinaghi, P., Jansson, F., Blázquez, D. A., and Glassmeier, F. (2025c). Cold pools mediate mesoscale adjustments of trade-cumulus fields to changes in cloud droplet number concentration. *Atmospheric Chemistry and Physics*, 25(12):6121–6139.

Alinaghi, P., Siebesma, A. P., Jansson, F., Janssens, M., and Glassmeier, F. (2025d). External drivers and mesoscale self-organization of shallow cold pools in the trade-wind regime. *Journal of Advances in Modeling Earth Systems*, 17(1):e2024MS004540. e2024MS004540 2024MS004540.

Anurose, T. J., Bašták Ďurán, I., Schmidli, J., and Seifert, A. (2020). Understanding the moisture variance in precipitating shallow cumulus convection. *Journal of Geophysical Research: Atmospheres*, 125(1):e2019JD031178.

Ardanuy, P. E., Stowe, L. L., Gruber, A., and Weiss, M. (1991). Shortwave, longwave, and net cloud-radiative forcing as determined from nimbus 7 observations. *Journal of Geophysical Research: Atmospheres*, 96(D10):18537–18549.

Arrhenius, S. (1896). Xxxi. on the influence of carbonic acid in the air upon the temperature of the ground. *The London, Edinburgh, and Dublin Philosophical Magazine and Journal of Science*, 41(251):237–276.

Baba, K., Shibata, R., and Sibuya, M. (2004). Partial correlation and conditional correlation as measures of conditional independence. *Australian & New Zealand Journal of Statistics*, 46(4):657–664.

Bellon, G. and Stevens, B. (2012). Using the sensitivity of large-eddy simulations to evaluate atmospheric boundary layer models. *Journal of the Atmospheric Sciences*, 69(5):1582–1601.

Bellouin, N., Quaas, J., Gryspeerdt, E., Kinne, S., Stier, P., Watson-Parris, D., Boucher, O., Carslaw, K. S., Christensen, M., Daniau, A.-L., et al. (2020). Bounding global aerosol radiative forcing of climate change. *Reviews of Geophysics*, 58(1):e2019RG000660.

Blossey, P. N., Bretherton, C. S., Zhang, M., Cheng, A., Endo, S., Heus, T., Liu, Y., Lock, A. P., de Roode, S. R., and Xu, K.-M. (2013). Marine low cloud sensitivity to an idealized climate change: The cgils les intercomparison. *Journal of Advances in Modeling Earth Systems*, 5(2):234–258.

Böing, S. J., Jonker, H. J., Siebesma, A. P., and Grabowski, W. W. (2012). Influence of the subcloud layer on the development of a deep convective ensemble. *Journal of the Atmospheric Sciences*, 69(9):2682–2698.

Bony, S. and Dufresne, J.-L. (2005). Marine boundary layer clouds at the heart of tropical cloud feedback uncertainties in climate models. *Geophysical Research Letters*, 32(20).

Bony, S., Dufresne, J.-L., Le Treut, H., Morcrette, J.-J., and Senior, C. (2004). On dynamic and thermodynamic components of cloud changes. *Climate Dynamics*, 22(2):71–86.

Bony, S., Lothon, M., Delanoë, J., Coutris, P., Etienne, J.-C., Aemisegger, F., Albright, A. L., André, T., Bellec, H., Baron, A., Bourdinot, J.-F., Brilouet, P.-E., Bourdon, A., Canonici, J.-C., Caudoux, C., Chazette, P., Cluzeau, M., Cornet, C., Desbios, J.-P., Duchanoy, D., Flamant, C., Fildier, B., Gourbeyre, C., Guiraud, L., Jiang, T., Lainard, C., Le Gac, C., Lendroit, C., Lernould, J., Perrin, T., Pouvesle, F., Richard, P., Rochetin, N., Salaün, K., Schwarzenboeck, A., Seurat, G., Stevens, B., Totems, J., Touzé-Peiffer, L., Vergez, G., Vial, J., Villiger, L., and Vogel, R. (2022). Eurec^{4}a observations from the safire atr42 aircraft. *Earth System Science Data*, 14(4):2021–2064.

Bony, S., Schulz, H., Vial, J., and Stevens, B. (2020a). Sugar, gravel, fish, and flowers: Dependence of mesoscale patterns of trade-wind clouds on environmental conditions. *Geophysical research letters*, 47(7):e2019GL085988.

Bony, S., Semie, A., Kramer, R. J., Soden, B., Tompkins, A. M., and Emanuel, K. A. (2020b). Observed modulation of the tropical radiation budget by deep convective organization and lower-tropospheric stability. *AGU Advances*, 1(3):e2019AV000155. e2019AV000155 10.1029/2019AV000155.

Bony, S., Stevens, B., Ament, F., Bigorre, S., Chazette, P., Crewell, S., Delanoë, J., Emanuel, K., Farrell, D., Flamant, C., et al. (2017). Eurec 4 a: A field campaign to elucidate the couplings between clouds, convection and circulation. *Surveys in Geophysics*, 38:1529–1568.

Bony, S., Stevens, B., Frierson, D. M., Jakob, C., Kageyama, M., Pincus, R., Shepherd, T. G., Sherwood, S. C., Siebesma, A. P., Sobel, A. H., et al. (2015). Clouds, circulation and climate sensitivity. *Nature Geoscience*, 8(4):261–268.

Bretherton, C. and Blossey, P. (2017). Understanding mesoscale aggregation of shallow cumulus convection using large-eddy simulation. *Journal of Advances in Modeling Earth Systems*, 9(8):2798–2821.

Bretherton, C. S., Blossey, P. N., and Jones, C. R. (2013). Mechanisms of marine low cloud sensitivity to idealized climate perturbations: A single-les exploration extending the cgils cases. *Journal of Advances in Modeling Earth Systems*, 5(2):316–337.

Cesana, G. V. and Del Genio, A. D. (2021). Observational constraint on cloud feedbacks suggests moderate climate sensitivity. *Nature Climate Change*, 11(3):213–218.

Cess, R. D., Potter, G. L., Blanchet, J., Boer, G., Ghan, S., Kiehl, J., Le Treut, H., Li, Z.-X., Liang, X.-Z., Mitchell, J., et al. (1989). Interpretation of cloud-climate feedback as produced by 14 atmospheric general circulation models. *Science*, 245(4917):513–516.

Chen, Y.-S., Zhang, J., Hoffmann, F., Yamaguchi, T., Glassmeier, F., Zhou, X., and Feingold, G. (2024). Diurnal evolution of non-precipitating marine stratocumuli in an les ensemble. *EGUsphere*, 2024:1–42.

Cho, H.-M., Zhang, Z., Meyer, K., Lebsock, M., Platnick, S., Ackerman, A. S., Di Girolamo, L., C.-Labonnote, L., Cornet, C., Riedi, J., et al. (2015). Frequency and causes of failed modis cloud property retrievals for liquid phase clouds over global oceans. *Journal of Geophysical Research: Atmospheres*, 120(9):4132–4154.

Coakley, J. A., Friedman, M. A., and Tahnk, W. R. (2005). Retrieval of cloud properties for partly cloudy imager pixels. *Journal of Atmospheric and Oceanic Technology*, 22(1):3–17.

Colin, M., Sherwood, S., Geoffroy, O., Bony, S., and Fuchs, D. (2019). Identifying the sources of convective memory in cloud-resolving simulations. *Journal of the Atmospheric Sciences*, 76(3):947 – 962.

Colón-Robles, M., Rauber, R. M., and Jensen, J. B. (2006). Influence of low-level wind speed on droplet spectra near cloud base in trade wind cumulus. *Geophysical Research Letters*, 33(20).

Dagan, G., Koren, I., Kostinski, A., and Altaratz, O. (2018). Organization and oscillations in simulated shallow convective clouds. *Journal of Advances in Modeling Earth Systems*, 10(9):2287–2299.

Dauhut, T., Couvreux, F., Bouniol, D., Beucher, F., Volkmer, L., Pörtge, V., Schäfer, M., Ayet, A., Brilouet, P.-E., Jacob, M., et al. (2023). Flower trade-wind clouds are shallow mesoscale convective systems. *Quarterly Journal of the Royal Meteorological Society*, 149(750):325–347.

Denby, L. (2020). Discovering the importance of mesoscale cloud organization through unsupervised classification. *Geophysical Research Letters*, 47(1):e2019GL085190.

Denby, L. (2023). Charting the realms of mesoscale cloud organisation using unsupervised learning. *arXiv preprint arXiv:2309.08567.*

Drager, A. J. and van den Heever, S. C. (2017). Characterizing convective cold pools. *Journal of Advances in Modeling Earth Systems*, 9(2):1091–1115.

Eytan, E., Koren, I., Altaratz, O., Kostinski, A. B., and Ronen, A. (2020). Longwave radiative effect of the cloud twilight zone. *Nature Geoscience*, 13(10):669–673.

Eytan, E., Koren, I., Altaratz, O., Pinsky, M., and Khain, A. (2021). Revisiting adiabatic fraction estimations in cumulus clouds: high-resolution simulations with a passive tracer. *Atmospheric Chemistry and Physics*, 21(21):16203–16217.

Feingold, G., Balsells, J., Glassmeier, F., Yamaguchi, T., Kazil, J., and McComiskey, A. (2017). Analysis of albedo versus cloud fraction relationships in liquid water clouds using heuristic models and large eddy simulation. *Journal of Geophysical Research: Atmospheres*, 122(13):7086–7102.

Feingold, G., McComiskey, A., Yamaguchi, T., Johnson, J. S., Carslaw, K. S., and Schmidt, K. S. (2016). New approaches to quantifying aerosol influence on the cloud radiative effect. *Proceedings of the National Academy of Sciences*, 113(21):5812–5819.

Fiévet, R., Meyer, B., and Haerter, J. O. (2023). On the sensitivity of convective cold pools to mesh resolution. *Journal of Advances in Modeling Earth Systems*, 15(8):e2022MS003382.

Fildier, B., Muller, C., Pincus, R., and Fueglistaler, S. (2023). How moisture shapes low-level radiative cooling in subsidence regimes. *AGU Advances*, 4(3):e2023AV000880.

Foote, E. (1856). Circumstances affecting the heat of the sun's rays. *The American Journal of Science and Arts*, 22(66):382–383.

George, G. (2021). *Observations of meso-scale circulation and its relationship with cloudiness in the Tropics.* PhD thesis, Universität Hamburg Hamburg.

George, G., Stevens, B., Bony, S., Vogel, R., and Naumann, A. K. (2023). Widespread shallow mesoscale circulations observed in the trades. *Nature Geoscience*, 16(7):584–589.

Gerber, H. E., FRICK, G. M., JENSEN, J. B., and HUDSON, J. G. (2008). Entrainment, mixing, and microphysics in trade-wind cumulus. *Journal of the Meteorological Society of Japan. Ser. II*, 86A:87–106.

Glassmeier, F. and Feingold, G. (2017). Network approach to patterns in stratocumulus clouds. *Proceedings of the National Academy of Sciences*, 114(40):10578–10583.

Glassmeier, F., Hoffmann, F., Johnson, J. S., Yamaguchi, T., Carslaw, K. S., and Feingold, G. (2019). An emulator approach to stratocumulus susceptibility. *Atmospheric Chemistry and Physics*, 19(15):10191–10203.

Glassmeier, F., Hoffmann, F., Johnson, J. S., Yamaguchi, T., Carslaw, K. S., and Feingold, G. (2021). Aerosol-cloud-climate cooling overestimated by ship-track data. *Science*, 371(6528):485–489.

Goren, T., Feingold, G., Gryspeerdt, E., Kazil, J., Kretzschmar, J., Jia, H., and Quaas, J. (2022). Projecting stratocumulus transitions on the albedo—cloud fraction relationship reveals linearity of albedo to droplet concentrations. *Geophysical Research Letters*, 49(20):e2022GL101169.

Gryspeerdt, E., Glassmeier, F., Feingold, G., Hoffmann, F., and Murray-Watson, R. J. (2022). Observing short-timescale cloud development to constrain aerosol–cloud interactions. *Atmospheric Chemistry and Physics*, 22(17):11727–11738.

Hadley, G. (1735). Concerning the cause of the general trade-winds. *Philosophical Transactions of the Royal Society of London*, 39:58–62.

Haerter, J. O., Böing, S. J., Henneberg, O., and Nissen, S. B. (2019). Circling in on convective organization. *Geophysical Research Letters*, 46(12):7024–7034.

Haerter, J. O. and Schlemmer, L. (2018). Intensified cold pool dynamics under stronger surface heating. *Geophysical Research Letters*, 45(12):6299–6310.

Han, Q., Rossow, W. B., and Lacis, A. A. (1994). Near-global survey of effective droplet radii in liquid water clouds using isccp data. *Journal of Climate*, 7(4):465–497.

Harris, C. R., Millman, K. J., van der Walt, S. J., Gommers, R., Virtanen, P., Cournapeau, D., Wieser, E., Taylor, J., Berg, S., Smith, N. J., Kern, R., Picus, M., Hoyer, S., van Kerkwijk, M. H., Brett, M., Haldane, A., del Río, J. F., Wiebe, M., Peterson, P., Gérard-Marchant, P., Sheppard, K., Reddy, T., Weckesser, W., Abbasi, H., Gohlke, C., and Oliphant, T. E. (2020). Array programming with NumPy. *Nature*, 585(7825):357–362.

Held, I. M. and Hou, A. Y. (1980). Nonlinear axially symmetric circulations in a nearly inviscid atmosphere. *Journal of the Atmospheric Sciences*, 37(3):515–533.

Helfer, K. C. and Nuijens, L. (2021). The morphology of simulated trade-wind convection and cold pools under wind shear. *Journal of Geophysical Research: Atmospheres*, 126(20):e2021JD035148.

Hersbach, H., Bell, B., Berrisford, P., Hirahara, S., Horányi, A., Muñoz-Sabater, J., Nicolas, J., Peubey, C., Radu, R., Schepers, D., et al. (2020). The ERA5 global reanalysis. *Quarterly Journal of the Royal Meteorological Society*, 146(730):1999–2049.

Heus, T., van Heerwaarden, C. C., Jonker, H. J., Pier Siebesma, A., Axelsen, S., Van Den Dries, K., Geoffroy, O., Moene, A., Pino, D., De Roode, S., et al. (2010). Formulation of the dutch atmospheric large-eddy simulation (dales) and overview of its applications. *Geoscientific Model Development*, 3(2):415–444.

Hoffmann, F., Glassmeier, F., Yamaguchi, T., and Feingold, G. (2020). Liquid water path steady states in stratocumulus: Insights from process-level emulation and mixed-layer theory. *Journal of the Atmospheric Sciences*, 77(6):2203 – 2215.

Hoffmann, F., Glassmeier, F., Yamaguchi, T., and Feingold, G. (2023). On the roles of precipitation and entrainment in stratocumulus transitions between mesoscale states. *Journal of the Atmospheric Sciences*, 80(12):2791–2803.

Hoyer, S. and Joseph, H. (2017). xarray: N-D labeled Arrays and Datasets in Python. *Journal of Open Research Software*, 5(1).

Hudson, J. G. and Noble, S. (2014). Low-altitude summer/winter microphysics, dynamics, and ccn spectra of northeastern caribbean small cumuli, and comparisons with stratus. *Journal of Geophysical Research: Atmospheres*, 119(9):5445–5463.

Hunter, J. D. (2007). Matplotlib: A 2D graphics environment. *Computing in Science & Engineering*, 9(3):90–95.

IPCC AR6, C. . (2023). *The Earth's Energy Budget, Climate Feedbacks and Climate Sensitivity*, page 923–1054. Cambridge University Press.

Janssens, M. (2023a). *Mesoscale Cloud Patterns in the Trade-Wind Boundary Layer*. PhD thesis, Wageningen University.

Janssens, M. (2023b). Supporting data for Ch. 7 of "Mesoscale Cloud Patterns in the Trade-Wind Boundary Layer". *Zenodo*.

Janssens, M., De Arellano, J. V.-G., Van Heerwaarden, C. C., De Roode, S. R., Siebesma, A. P., and Glassmeier, F. (2023). Nonprecipitating shallow cumulus convection is intrinsically unstable to length scale growth. *Journal of the Atmospheric Sciences*, 80(3):849–870.

Janssens, M., George, G., Schulz, H., Couvreux, F., and Bouniol, D. (2024). Shallow convective heating in weak temperature gradient balance explains mesoscale vertical motions in the trades. *Journal of Geophysical Research: Atmospheres*, 129(18):e2024JD041417.

Janssens, M., Jansson, F., Alinaghi, P., Glassmeier, F., and Siebesma, A. P. (2025). Symmetry in mesoscale circulations explains weak impact of trade cumulus self-organization on the radiation budget in large-eddy simulations. *Geophysical Research Letters*, 52(3):e2024GL112288.

Janssens, M., Vilà-Guerau de Arellano, J., Scheffer, M., Antonissen, C., Siebesma, A. P., and Glassmeier, F. (2021). Cloud patterns in the trades have four interpretable dimensions. *Geophysical Research Letters*, 48(5):e2020GL091001.

Jansson, F., Janssens, M., Grönqvist, J. H., Siebesma, A. P., Glassmeier, F., Attema, J., Azizi, V., Satoh, M., Sato, Y., Schulz, H., and Kölling, T. (2023). Cloud botany: Shallow cumulus clouds in an ensemble of idealized large-domain large-eddy simulations of the trades. *Journal of Advances in Modeling Earth Systems*, 15(11):e2023MS003796. e2023MS003796 2023MS003796.

Jeevanjee, N. and Romps, D. M. (2013). Convective self-aggregation, cold pools, and domain size. *Geophysical Research Letters*, 40(5):994–998.

Johnson, R. H., Rickenbach, T. M., Rutledge, S. A., Ciesielski, P. E., and Schubert, W. H. (1999). Trimodal characteristics of tropical convection. *Journal of climate*, 12(8):2397–2418.

Kazil, J., Vogel, R., Alinaghi, P., Bariteau, L., Bayley, C., Blossey, P., Boeing, S., Chandrakar, K. K., Denby, L. C., Falk, N. M., et al. (2025). Cold pool analysis from the cold pool model intercomparison project (cp-mip). In *105th AMS Annual Meeting*. AMS.

Klein, S. A., Hall, A., Norris, J. R., and Pincus, R. (2018). Low-cloud feedbacks from cloud-controlling factors: A review. *Shallow clouds, water vapor, circulation, and climate sensitivity*, pages 135–157.

Lacis, A. A. and Hansen, J. (1974). A parameterization for the absorption of solar radiation in the earth's atmosphere. *Journal of Atmospheric Sciences*, 31(1):118–133.

Lamaakel, O., Venters, R., Teixeira, J., and Matheou, G. (2023). Computational domain size effects on large-eddy simulations of precipitating shallow cumulus convection. *Atmosphere*, 14(7):1186.

Langhans, W. and Romps, D. M. (2015). The origin of water vapor rings in tropical oceanic cold pools. *Geophysical Research Letters*, 42(18):7825–7834.

Li, Z., Zuidema, P., and Zhu, P. (2014). Simulated convective invigoration processes at trade wind cumulus cold pool boundaries. *Journal of the Atmospheric Sciences*, 71(8):2823–2841.

Li, Z., Zuidema, P., Zhu, P., and Morrison, H. (2015). The sensitivity of simulated shallow cumulus convection and cold pools to microphysics. *Journal of the Atmospheric Sciences*, 72(9):3340–3355.

Liqui Lung, F., Jakob, C., Siebesma, A. P., and Jansson, F. (2024). Open boundary conditions for atmospheric large-eddy simulations and their implementation in dales4.4. *Geoscientific Model Development*, 17(9):4053–4076.

Lochbihler, K., Lenderink, G., and Siebesma, A. P. (2021a). Cold pool dynamics shape the response of extreme rainfall events to climate change. *Journal of Advances in Modeling Earth Systems*, 13(2):e2020MS002306. e2020MS002306 2020MS002306.

Lochbihler, K., Lenderink, G., and Siebesma, A. P. (2021b). Cold pool dynamics shape the response of extreme rainfall events to climate change. *Journal of Advances in Modeling Earth Systems*, 13(2):e2020MS002306.

Luebke, A. E., Ehrlich, A., Schäfer, M., Wolf, K., and Wendisch, M. (2022). An assessment of macrophysical and microphysical cloud properties driving radiative forcing of shallow trade-wind clouds. *Atmospheric Chemistry and Physics*, 22(4):2727–2744.

Mapes, B. E. (2024). Evolutionary theory of convective organization. *arXiv preprint arXiv:2404.03480*.

Mathez, E. and Smerdon, J. (2018). *Climate change: the science of global warming and our energy future*. Columbia University Press.

McCoy, I. L., McCoy, D. T., Wood, R., Zuidema, P., and Bender, F. A.-M. (2022). The role of mesoscale cloud morphology in the shortwave cloud feedback. *Geophysical Research Letters*, page e2022GL101042.

Medeiros, B. and Nuijens, L. (2016). Clouds at Barbados are representative of clouds across the trade wind regions in observations and climate models. *Proceedings of the National Academy of Sciences*, 113(22):E3062–E3070.

Meier, R. (2024). Evolution of mesoscale organization in trade cumulus clouds. Master's thesis, TU Delft.

Moncrieff, M. W. and Liu, C. (1999). Convection initiation by density currents: Role of convergence, shear, and dynamical organization. *Monthly Weather Review*, 127(10):2455–2464.

Muller, C. and Bony, S. (2015). What favors convective aggregation and why? *Geophysical Research Letters*, 42(13):5626–5634.

Myers, T. A., Scott, R. C., Zelinka, M. D., Klein, S. A., Norris, J. R., and Caldwell, P. M. (2021). Observational constraints on low cloud feedback reduce uncertainty of climate sensitivity. *Nature Climate Change*, 11(6):501–507.

Möller, F. (1963). On the influence of changes in the co2 concentration in air on the radiation balance of the earth's surface and on the climate. *Journal of Geophysical Research (1896-1977)*, 68(13):3877–3886.

Narenpitak, P., Kazil, J., Yamaguchi, T., Quinn, P., and Feingold, G. (2021). From sugar to flowers: A transition of shallow cumulus organization during atomic. *Journal of Advances in Modeling Earth Systems*, 13(10):e2021MS002619.

Nissen, S. B. and Haerter, J. O. (2021). Circling in on convective self-aggregation. *Journal of Geophysical Research: Atmospheres*, 126(20):e2021JD035331.

Nuijens, L. and Siebesma, A. P. (2019). Boundary layer clouds and convection over subtropical oceans in our current and in a warmer climate. *Current Climate Change Reports*, 5:80–94.

Nuijens, L. and Stevens, B. (2012). The influence of wind speed on shallow marine cumulus convection. *Journal of the Atmospheric Sciences*, 69(1):168–184.

Nuijens, L., Stevens, B., and Siebesma, A. P. (2009). The environment of precipitating shallow cumulus convection. *Journal of the Atmospheric Sciences*, 66(7):1962–1979.

O, K.-T., Wood, R., and Bretherton, C. S. (2018a). Ultraclean layers and optically thin clouds in the stratocumulus-to-cumulus transition. Part II: Depletion of cloud droplets and cloud condensation nuclei through collision–coalescence. *Journal of the Atmospheric Sciences*, 75(5):1653–1673.

O, K.-T., Wood, R., Tseng, H., et al. (2018b). Deeper, precipitating PBLs associated with optically thin veil clouds in the Sc-Cu transition. *Geophysical Research Letters*, 45(10):5177–5184.

Painemal, D. and Zuidema, P. (2011). Assessment of MODIS cloud effective radius and optical thickness retrievals over the southeast pacific with VOCALS-REX in situ measurements. *Journal of Geophysical Research: Atmospheres*, 116(D24).

Paltridge, G. W. (1980). Cloud-radiation feedback to climate. *Quarterly Journal of the Royal Meteorological Society*, 106(450):895–899.

Pietronero, L. (2008). Complexity ideas from condensed matter and statistical physics. *Europhysics news*, 39(6):26–29.

Quinn, P. K., Thompson, E. J., Coffman, D. J., Baidar, S., Bariteau, L., Bates, T. S., Bigorre, S., Brewer, A., de Boer, G., de Szoeke, S. P., Drushka, K., Foltz, G. R., Intrieri, J., Iyer, S., Fairall, C. W., Gaston, C. J., Jansen, F., Johnson, J. E., Krüger, O. O., Marchbanks, R. D., Moran, K. P., Noone, D., Pezoa, S., Pincus, R., Plueddemann, A. J., Pöhlker, M. L., Pöschl, U., Quinones Melendez, E., Royer, H. M., Szczodrak, M., Thomson, J., Upchurch, L. M., Zhang, C., Zhang, D., and Zuidema, P. (2021). Measurements from the rv *Ronald H. Brown* and related platforms as part of the atlantic tradewind ocean-atmosphere mesoscale interaction campaign (atomic). *Earth System Science Data*, 13(4):1759–1790.

Radtke, J., Naumann, A. K., Hagen, M., and Ament, F. (2022). The relationship between precipitation and its spatial pattern in the trades observed during eurec4a. *Quarterly Journal of the Royal Meteorological Society.*

Radtke, J., Vogel, R., Ament, F., and Naumann, A. K. (2023). Spatial organisation affects the pathway to precipitation in simulated trade-wind convection. *Geophysical Research Letters*, 50:e2023GL103579.

Ramanathan, V., Cess, R., Harrison, E., Minnis, P., Barkstrom, B., Ahmad, E., and Hartmann, D. (1989). Cloud-radiative forcing and climate: Results from the earth radiation budget experiment. *Science*, 243(4887):57–63.

Rochetin, N., Hohenegger, C., Touzé-Peiffer, L., and Villefranque, N. (2021). A physically based definition of convectively generated density currents: Detection and characterization in convection-permitting simulations. *Journal of Advances in Modeling Earth Systems*, 13(7):e2020MS002402.

Rotunno, R., Klemp, J. B., and Weisman, M. L. (1988). A theory for strong, long-lived squall lines. *Journal of Atmospheric Sciences*, 45(3):463–485.

Ruppert, J. H. and Johnson, R. H. (2016). On the cumulus diurnal cycle over the tropical warm pool. *Journal of Advances in Modeling Earth Systems*, 8(2):669–690.

Saffin, L., Lock, A., Tomassini, L., Blyth, A., Böing, S., Denby, L., and Marsham, J. (2023). Kilometer-scale simulations of trade-wind cumulus capture processes of mesoscale organization. *Journal of Advances in Modeling Earth Systems*, 15(3):e2022MS003295.

Savic-Jovcic, V. and Stevens, B. (2008). The structure and mesoscale organization of precipitating stratocumulus. *Journal of the Atmospheric Sciences*, 65(5):1587 – 1605.

Schlemmer, L. and Hohenegger, C. (2014). The formation of wider and deeper clouds as a result of cold-pool dynamics. *Journal of the Atmospheric Sciences*, 71(8):2842–2858.

Schlemmer, L. and Hohenegger, C. (2016). Modifications of the atmospheric moisture field as a result of cold-pool dynamics. *Quarterly Journal of the Royal Meteorological Society*, 142(694):30–42.

Schmeissner, T., Shaw, R., Ditas, J., Stratmann, F., Wendisch, M., and Siebert, H. (2015). Turbulent mixing in shallow trade wind cumuli: Dependence on cloud life cycle. *Journal of the Atmospheric Sciences*, 72(4):1447–1465.

Schneider, T., Teixeira, J., Bretherton, C. S., Brient, F., Pressel, K. G., Schär, C., and Siebesma, A. P. (2017). Climate goals and computing the future of clouds. *Nature Climate Change*, 7(1):3–5.

Schulz, H., Eastman, R., and Stevens, B. (2021). Characterization and evolution of organized shallow convection in the downstream north atlantic trades. *Journal of Geophysical Research: Atmospheres*, 126(17):e2021JD034575.

Schulz, H. and Stevens, B. (2018). Observing the tropical atmosphere in moisture space. *Journal of the Atmospheric Sciences*, 75(10):3313–3330.

Schulz, H. and Stevens, B. (2023). Evaluating large-domain, hecto-meter, large-eddy simulations of trade-wind clouds using eurec4a data. *Journal of Advances in Modeling Earth Systems*, 15(10):e2023MS003648.

Scott, R. C., Myers, T. A., Norris, J. R., Zelinka, M. D., Klein, S. A., Sun, M., and Doelling, D. R. (2020). Observed sensitivity of low-cloud radiative effects to meteorological perturbations over the global oceans. *Journal of Climate*, 33(18):7717–7734.

Seabold, S. and Perktold, J. (2010). statsmodels: Econometric and statistical modeling with python. In *9th Python in Science Conference*.

Seethala, C. and Horváth, Á. (2010). Global assessment of AMSR-E and MODIS cloud liquid water path retrievals in warm oceanic clouds. *Journal of Geophysical Research: Atmospheres*, 115(D13).

Seifert, A. (2008). On the parameterization of evaporation of raindrops as simulated by a one-dimensional rainshaft model. *Journal of the Atmospheric Sciences*, 65(11):3608 – 3619.

Seifert, A. and Beheng, K. D. (2001). A double-moment parameterization for simulating autoconversion, accretion and selfcollection. *Atmospheric research*, 59:265–281.

Seifert, A. and Heus, T. (2013). Large-eddy simulation of organized precipitating trade wind cumulus clouds. *Atmospheric Chemistry and Physics*, 13(11):5631–5645.

Seifert, A., Heus, T., Pincus, R., and Stevens, B. (2015). Large-eddy simulation of the transient and near-equilibrium behavior of precipitating shallow convection. *Journal of Advances in Modeling Earth Systems*, 7(4):1918–1937.

Sherwood, S. C., Webb, M. J., Annan, J. D., Armour, K. C., Forster, P. M., Hargreaves, J. C., Hegerl, G., Klein, S. A., Marvel, K. D., Rohling, E. J., et al. (2020). An assessment of Earth's climate sensitivity using multiple lines of evidence. *Reviews of Geophysics*, 58(4):e2019RG000678.

Siebesma, A. P., Bony, S., Jakob, C., and Stevens, B. (2020). *Clouds and climate: Climate science's greatest challenge*. Cambridge University Press.

Singer, C. E., Lopez-Gomez, I., Zhang, X., and Schneider, T. (2021). Top-of-atmosphere albedo bias from neglecting three-dimensional cloud radiative effects. *Journal of the Atmospheric Sciences*, 78(12):4053–4069.

Snodgrass, E. R., Girolamo, L. D., and Rauber, R. M. (2009). Precipitation characteristics of trade wind clouds during rico derived from radar, satellite, and aircraft measurements. *Journal of Applied Meteorology and Climatology*, 48(3):464 – 483.

Stensrud, D. J., Coniglio, M. C., Davies-Jones, R. P., and Evans, J. S. (2005). Comments on "'a theory for strong long-lived squall lines' revisited". *Journal of the Atmospheric Sciences*, 62(8):2989–2996.

Stephens, G. L., Li, J., Wild, M., Clayson, C. A., Loeb, N., Kato, S., L'ecuyer, T., Stackhouse Jr, P. W., Lebsock, M., and Andrews, T. (2012). An update on earth's energy balance in light of the latest global observations. *Nature Geoscience*, 5(10):691–696.

Stevens, B., Bony, S., Brogniez, H., Hentgen, L., Hohenegger, C., Kiemle, C., L'Ecuyer, T. S., Naumann, A. K., Schulz, H., Siebesma, P. A., et al. (2020). Sugar, gravel, fish and flowers: Mesoscale cloud patterns in the trade winds. *Quarterly Journal of the Royal Meteorological Society*, 146(726):141–152.

Stevens, B., Bony, S., Farrell, D., Ament, F., Blyth, A., Fairall, C., Karstensen, J., Quinn, P. K., Speich, S., Acquistapace, C., et al. (2021). Eurec 4 a. *Earth System Science Data Discussions*, 2021:1–78.

Stevens, B. and Brenguier, J. (2009). Cloud controlling factors: Low clouds. In Heintzenberg, J. and Charlson, R., editors, *Clouds in the Perturbed Climate System*. MIT Press.

Stevens, B. and Feingold, G. (2009). Untangling aerosol effects on clouds and precipitation in a buffered system. *Nature*, 461(7264):607–613.

Tobin, I., Bony, S., and Roca, R. (2012). Observational evidence for relationships between the degree of aggregation of deep convection, water vapor, surface fluxes, and radiation. *Journal of Climate*, 25(20):6885–6904.

Tompkins, A. M. (2001). Organization of tropical convection in low vertical wind shears: The role of cold pools. *Journal of the atmospheric sciences*, 58(13):1650–1672.

Tompkins, A. M. and Semie, A. G. (2017). Organization of tropical convection in low vertical wind shears: Role of updraft entrainment. *Journal of Advances in Modeling Earth Systems*, 9(2):1046–1068.

Torri, G. and Kuang, Z. (2019). On cold pool collisions in tropical boundary layers. *Geophysical Research Letters*, 46(1):399–407.

Torri, G., Kuang, Z., and Tian, Y. (2015). Mechanisms for convection triggering by cold pools. *Geophysical Research Letters*, 42(6):1943–1950.

Touzé-Peiffer, L., Vogel, R., and Rochetin, N. (2022). Cold pools observed during eurec 4 a: Detection and characterization from atmospheric soundings. *Journal of Applied Meteorology and Climatology*, 61(5):593–610.

Twomey, S. (1974). Pollution and the planetary albedo. *Atmospheric Environment (1967)*, 8(12):1251–1256.

Twomey, S. (1977). The influence of pollution on the shortwave albedo of clouds. *Journal of Atmospheric Sciences*, 34(7):1149 – 1152.

Vial, J., Albright, A. L., Vogel, R., Musat, I., and Bony, S. (2023). Cloud transition across the daily cycle illuminates model responses of trade cumuli to warming. *Proceedings of the National Academy of Sciences*, 120(8):e2209805120.

Vial, J., Vogel, R., and Schulz, H. (2021). On the daily cycle of mesoscale cloud organization in the winter trades. *Quarterly Journal of the Royal Meteorological Society*, 147(738):2850–2873.

Virtanen, P., Gommers, R., Oliphant, T. E., Haberland, M., Reddy, T., Cournapeau, D., Burovski, E., Peterson, P., Weckesser, W., Bright, J., van der Walt, S. J., Brett, M., Wilson, J., Millman, K. J., Mayorov, N., Nelson, A. R. J., Jones, E., Kern, R., Larson, E., Carey, C. J., Polat, İ., Feng, Y., Moore, E. W., VanderPlas, J., Laxalde, D., Perktold, J., Cimrman, R., Henriksen, I., Quintero, E. A., Harris, C. R., Archibald, A. M., Ribeiro, A. H., Pedregosa, F., van Mulbregt, P., and SciPy 1.0 Contributors (2020). SciPy 1.0: Fundamental Algorithms for Scientific Computing in Python. *Nature Methods*, 17:261–272.

Vogel, R., Albright, A. L., Vial, J., George, G., Stevens, B., and Bony, S. (2022). Strong cloud–circulation coupling explains weak trade cumulus feedback. *Nature*, 612(7941):696–700.

Vogel, R., Konow, H., Schulz, H., and Zuidema, P. (2021). A climatology of trade-wind cumulus cold pools and their link to mesoscale cloud organization. *Atmospheric Chemistry and Physics*, 21(21):16609–16630.

Vogel, R., Nuijens, L., and Stevens, B. (2016). The role of precipitation and spatial organization in the response of trade-wind clouds to warming. *Journal of Advances in Modeling Earth Systems*, 8(2):843–862.

Waskom, M. L. (2021). seaborn: statistical data visualization. *Journal of Open Source Software*, 6(60):3021.

Weger, R., Lee, J., Zhu, T., and Welch, R. (1992). Clustering, randomness and regularity in cloud fields: 1. Theoretical considerations. *Journal of Geophysical Research: Atmospheres*, 97(D18):20519–20536.

Weisman, M. L. and Rotunno, R. (2004). “a theory for strong long-lived squall lines” revisited. *Journal of the Atmospheric Sciences*, 61(4):361–382.

Wes McKinney (2010). Data Structures for Statistical Computing in Python. In Stéfan van der Walt and Jarrod Millman, editors, *Proceedings of the 9th Python in Science Conference*, pages 56 – 61.

Wood, R. (2006). Relationships between optical depth, liquid water path, droplet concentration, and effective radius in adiabatic layer cloud. *University of Washington*, 3.

Wood, R., O, K.-T., Bretherton, C. S., Mohrmann, J., Albrecht, B. A., Zuidema, P., Ghate, V., Schwartz, C., Eloranta, E., Glienke, S., et al. (2018). Ultraclean layers and optically thin clouds in the stratocumulus-to-cumulus transition. Part I: Observations. *Journal of the Atmospheric Sciences*, 75(5):1631–1652.

Xie, Y. and Liu, Y. (2013). A new approach for simultaneously retrieving cloud albedo and cloud fraction from surface-based shortwave radiation measurements. *Environmental Research Letters*, 8(4):044023.

Xue, H., Feingold, G., and Stevens, B. (2008a). Aerosol effects on clouds, precipitation, and the organization of shallow cumulus convection. *Journal of the Atmospheric Sciences*, 65(2):392–406.

Xue, H., Feingold, G., and Stevens, B. (2008b). Aerosol effects on clouds, precipitation, and the organization of shallow cumulus convection. *Journal of the Atmospheric Sciences*, 65(2):392 – 406.

Yamaguchi, T., Feingold, G., and Kazil, J. (2019). Aerosol-cloud interactions in trade wind cumulus clouds and the role of vertical wind shear. *Journal of Geophysical Research: Atmospheres*, 124(22):12244–12261.

Zhang, M., Bretherton, C. S., Blossey, P. N., Austin, P. H., Bacmeister, J. T., Bony, S., Brient, F., Cheedela, S. K., Cheng, A., Del Genio, A. D., et al. (2013). Cgils: Results from the first phase of an international project to understand the physical mechanisms of low cloud feedbacks in single column models. *Journal of Advances in Modeling Earth Systems*, 5(4):826–842.

Zhang, Y., Stevens, B., and Ghil, M. (2005). On the diurnal cycle and susceptibility to aerosol concentration in a stratocumulus-topped mixed layer. *Quarterly Journal of the Royal Meteorological Society: A journal of the atmospheric sciences, applied meteorology and physical oceanography*, 131(608):1567–1583.

Zhang, Z. and Platnick, S. (2011). An assessment of differences between cloud effective particle radius retrievals for marine water clouds from three MODIS spectral bands. *Journal of Geophysical Research: Atmospheres*, 116(D20).

Zuidema, P., Li, Z., Hill, R. J., Bariteau, L., Rilling, B., Fairall, C., Brewer, W. A., Albrecht, B., and Hare, J. (2012). On trade wind cumulus cold pools. *Journal of the Atmospheric Sciences*, 69(1):258–280.

Zuidema, P., Torri, G., Muller, C., and Chandra, A. (2017). A survey of precipitation-induced atmospheric cold pools over oceans and their interactions with the larger-scale environment. *Surveys in Geophysics*, 38:1283–1305.

Zuidema, P., Xue, H., and Feingold, G. (2008). Shortwave radiative impacts from aerosol effects on marine shallow cumuli. *Journal of the atmospheric sciences*, 65(6):1979–1990.

CURRICULUM VITÆ

Pouriya ALINAGHI

I am fascinated by the structured patterns in nature and the elegant mathematics and physics that underlie them. I especially enjoy visualizing their beauty from raw data, turning 0s and 1s into insight. I find it deeply rewarding to simplify scientific concepts for the public. Outside research, I find joy in music, poetry, tennis, and most importantly gathering with my family and friends.

2021-2025	**Ph.D. Candidate in Atmospheric Science** Delft University of Technology, Delft, The Netherlands Thesis: Mesoscale Organization of Precipitating Trade-Cumulus Fields Teaching: Assistant of the minor course on The Science of Climate Change
2019-2021	**M.Sc. in Applied Earth Sciences (Cum Laude)** Delft University of Technology, Delft, The Netherlands Thesis: Shallow Cumulus Clouds as Complex Networks Additional Thesis: Estimation of Turbulence Intensity from Cup Anemometer-Based Mean Wind Speed Data via Fractal Interpolation
2017-2019	**Mathematics Teacher** Mofid High School, Tehran, Iran
2013-2017	**B.Sc. in Civil and Environmental Engineering** University of Tehran, Tehran, Iran

List of Publications

🗎 **Alinaghi, P.**, Janssens, M., Choudhury, G., Goren, T., Siebesma, A. P., & Glassmeier, F. (2024). Shallow cumulus cloud fields are optically thicker when they are more clustered. Quarterly Journal of the Royal Meteorological Society, 150(763), 3566–3577. https://doi.org/10.1002/qj.4783.

🗎 **Alinaghi, P.**, Siebesma, A. P., Jansson, F., Janssens, M., & Glassmeier, F. (2025). External Drivers and Mesoscale Self-Organization of Shallow Cold Pools in the Trade-Wind Regime. Journal of Advances in Modeling Earth Systems, 17(1), e2024MS004540. https://doi.org/10.1029/2024MS004540.

Janssens, M., Jansson, F., **Alinaghi, P.**, Glassmeier, F., & Siebesma, A. P. (2025). Symmetry in mesoscale circulations explains weak impact of trade cumulus self-organization on the radiation budget in large-eddy simulations. Geophysical Research Letters, 52(3), e2024GL112288.

🗎 **Alinaghi, P.**, Jansson, F., Blázquez, D. A., and Glassmeier, F.: Cold pools mediate mesoscale adjustments of trade-cumulus fields to changes in cloud droplet number concentration, Atmos. Chem. Phys., 25, 6121–6139, https://doi.org/10.5194/acp-25-6121-2025, 2025.

🗎 **Alinaghi, P.**, Janssens, M., & Jansson, F. (2025). Warming from cold pools: A pathway for mesoscale organization to alter Earth's radiation budget. arXiv preprint arXiv:2506.01750.

🗎 Included in this thesis.

Conference Contributions

May 2022	**2nd Workshop on Cloud Organization, Utrecht, The Netherlands** *Local (co-)organizer* Outreach: The role of clouds in the climate system Poster Presentation: Dependence of cloud radiative effect on cloud organization
October 2022	**BBOS Autumn Symposium, Oranjewoud, The Netherlands** Oral Presentation: Are *Flowers* clouds brighter than *Sugar* clouds?
May 2023	**Aerosol, Cloud, Precipitation, and Climate Workshop, Houston, Texas, USA** Oral Presentation: Microphysics-organization-radiation interactions in shallow cumulus clouds in the trades
June 2023	**Art Event with J. F. Thomas and E. Volkova at Jan van Eyck Academie Open Studios, Maastricht, The Netherlands.** Invited Talk: Demystifying cloud patterns in the climate system
July 2023	**Joint CFMIP-GASS Conference, Paris, France** Poster Presentation: Trade-cumulus fields are brighter when they are more clustered
July 2023	**International Space Science Institute (ISSI), Bern, Switzerland** Invited as an early-career researcher to the ISSI proposal team with the aim of constraining trade-cumulus feedback by process understanding
September 2023	**3rd Workshop on Cloud Organization, Trieste, Italy** Poster Presentation: Dependence of shallow cumulus cold pools on external and internal variability

September 2023	**Studium Generale, TU Delft Library, Delft, The Netherlands** Invited Talk and Panelist: Uncertainty in climate change
April 2024	**European Geophysical Union 2024, Vienna, Austria** Oral Presentation: Cold pools in the trades; external drivers and self-organization impact
July 2024	**4th Workshop on Cloud Organization, Trieste, Italy** Oral Presentation: Cold pools mediate mesoscale adjustment of trade-cumulus fields to cloud-droplet number perturbations
January 2025	**SRON, Leiden, The Netherlands** Invited Talk: Dependence of mesoscale organization on the micro-scales in the trade-wind regime
March 2025	**TU Delft Climate Action Annual Event, Green Village, Delft, The Netherlands** 🏆 Won the best paper award for the climate science division Invited Pitch: Tropical clouds hold both beauty and the key to climate change
May 2025	**International Space Science Institute (ISSI), Bern, Switzerland** Invited as an early-career researcher to the ISSI proposal team with the aim of constraining trade-cumulus feedback by process understanding During this second meeting, I shared the results of **Chapter 5** and contributed to the mesoscale review and dataset papers.

ACKNOWLEDGMENTS

Like many others, you are probably one of those who come directly to the last pages of a thesis to read the acknowledgments section. Hello to you!

I could write many lines about the fact that a PhD is a roller coaster ride, but if you slightly smooth the curve over time, you realize that you are growing. One important thing I learned during my PhD is that it is better not to focus too much on your current state, but rather on the first or even the second derivative of your state with respect to time! Only then can you truly see how much you have grown and how much potential you still have to continue growing. It is only with this perspective that you can appreciate the hard, low, or disappointing moments when nothing seems to work.

So, first and foremost, I would like to deeply thank everyone who has constantly reminded me of this perspective. Thank you! You have been one of the most important reasons why this booklet could come into existence over the past four years. And maybe equally important: one big anti-acknowledgment to those who tried their best to shift my focus back to the current state!

After this general part, I would like to specifically thank the people whose roles have been crucial during my PhD journey. First, my sincere thanks to Sukanta, who played a key role in drawing Pier's attention to my additional thesis on fractal interpolation of turbulence time series. This eventually led Pier to encourage me to apply for this PhD position — even though I had not yet begun my MSc thesis project at the time.

Next, a special thank you goes to Franziska, for giving me the opportunity to work on your Branco-Weiss Fellowship project exploring the network perspective on cloud organization. I feel very fortunate to have had you as my supervisor. You have played a pivotal role in helping me develop my storytelling and science communication skills — both in writing and presenting. I have also learned a great deal about networks and the dynamical systems approach to mesoscale cloud organization, thanks to your insightful and original perspective that both complements and challenges traditional views in atmospheric science.

A heartfelt thank you goes to you, Pier. Although you were officially the promoter of my PhD, you did me a great favor by becoming actively involved and taking on a real supervisory role especially for chapter 2. Your approach complemented Franziska's ideas so well — I feel incredibly lucky to have had such a complementary combination of perspectives in my PhD advisors. You have not only been an impressive and generous source of knowledge, but your openness and enthusiasm to discuss clouds and cold pools have often been a source of light during darker days of my PhD journey. I will never forget your and Gabie's kindness when you invited me to your home while I was recovering from mental and physical illness during the winter of 2022. I also truly enjoyed our tennis match on a spring evening in Utrecht in 2023 — even though you completely smashed me!

The next thank you is for you, Martin! You have not only been a fellow PhD student and later a professor who co-authored several of my works — you have also been an incredibly smart, wise, warm, and approachable friend who has consistently supported and encouraged me. What amazes me is that every impression I've had of you has been entirely positive, without a single exception. After every meeting or message from you, I always felt uplifted — as if I was working on something meaningful and exciting. Your presence in all the papers and projects we worked on brought sharpness and strength. Anyone would be lucky to have you involved in any kind of project. Also, thanks for carefully reading and revising the Dutch summary of this thesis.

The next thank you goes to you, Fredrik! Without your invaluable help — especially in running large-eddy simulations on some of the fastest supercomputers in the world — this thesis could not have been completed within four years. You are undoubtedly one of the key reasons this PhD thesis exists today. A crucial strength of this work lies in its data component, and that too comes largely thanks to you. I'm also deeply grateful for how promptly — and sometimes even immediately — you responded to all my DALES-related questions. Many, many thanks again!

Thank you, Steef! First, for kindly accepting to serve as the external member of the committee for all my PhD progress meetings and for providing insightful, out-of-the-box feedback. Second, many thanks for generously sharing the DALES code lines for homogenizing the rain-evaporation tendency, which accelerated the progress of **Chapter 5**.

My next thank you goes to Ben — thank you for always being so welcoming and for explaining concepts in dynamical systems theory so clearly. I've also really appreciated your kindness and friendship. Thank you, Marleen and Shafi, for taking the time to read my thesis introduction and for your great help with the Dutch summary. And thank you, Zach for reading through the introduction as a native English speaker. Robert, I truly enjoyed working with you on your interesting MSc project and later on your satellite study — it was a pleasure being involved. Valentina, thank you as well — I've really enjoyed our coffee breaks during the final months of my PhD. Many thanks to all my GRS colleagues, especially Alessandro, Dai, Mariska, Kevin, Owen, Wiestke, Sophie, Weilun, Tina, Yosra, Felix, Fritjhof, Caspar, Marloes, Koen, Edoardo, and any other name that I have not mentioned.

I also want to express my sincere gratitude to some of my MSc teachers at GRS. Thank you, Stephan, Louise, Bas, and Herman. Your doors were always open whenever I had questions — whether about the atmosphere or about navigating my PhD. Your support over the past six years in Delft has meant a great deal to me. A special thank you also goes to our secretaries, Debbie, Natascha, and Cindy, for their consistently warm and strong support throughout.

I would like to take a moment to especially thank Geet and Hauke for inviting me to join the ISSI proposal team. Our first meeting in Bern in August 2023 was one of the key moments where I truly began to see the direction of my PhD work — it helped me find clarity and a sense of where I stood. Beyond the science, just hearing “Bern” or “ISSI” brings back amazing memories of spending time with brilliant, kind people — Raphaela, Leif, Emilie, Irene, Isabel, Ryan, Nina, Xuanyu, and Piyush — as well as swimming (with of course, Dolphins) in the Aare, enjoying fondue, and taking in the views at Rosengarten and beautiful Bern.

I also want to thank my friends in the Netherlands for the wonderful and refreshing times we've shared — Amir, Hamid, Mahdi, Mahtab, Anastazia, and Morteza. Even though we are far from Iran, you've brought a sense of home to me here. I truly felt I was never far away. My heartfelt thanks also go to my friends in Iran and beyond the Netherlands, whose warm support has never been limited by distance: Mojtaba, Soheil, Amin, Mahdi, Hassan, and Mohammad — thank you!

And, last but not least — Maman, Baba, and Parsa — without you, there would be no Pouriya. Without your support, I wouldn't have endured a single moment of being away from you. Without your support, there would have been no MSc at TU Delft — and no PhD to follow. This is where words truly fall short of expressing how deeply grateful I am, from the bottom of my heart.

There's also one person who has been by my side through almost every single moment of this PhD. Remember that rollercoaster I mentioned? Yasamin has been right there next to me the whole way. Thank you for being with me, for bearing with me through the lows, and for being a constant, shiny source of strength, energy, and love — love you so much!

As this text hopefully conveys, I feel immensely grateful to have been surrounded by such warm and supportive people. I'm also deeply thankful that I had the opportunity to work on a project I truly love — one that allowed me to learn, grow, and enjoy the process. Looking ahead, I hope the insights I've gained can shine some light on the not-so-bright days of our planet. I hope to continue contributing meaningfully and to keep walking this beautiful path I've been on so far.

Thank you for reading this far — if you did, that means a lot.

Pouriya Alinaghi
Delft, May 2025

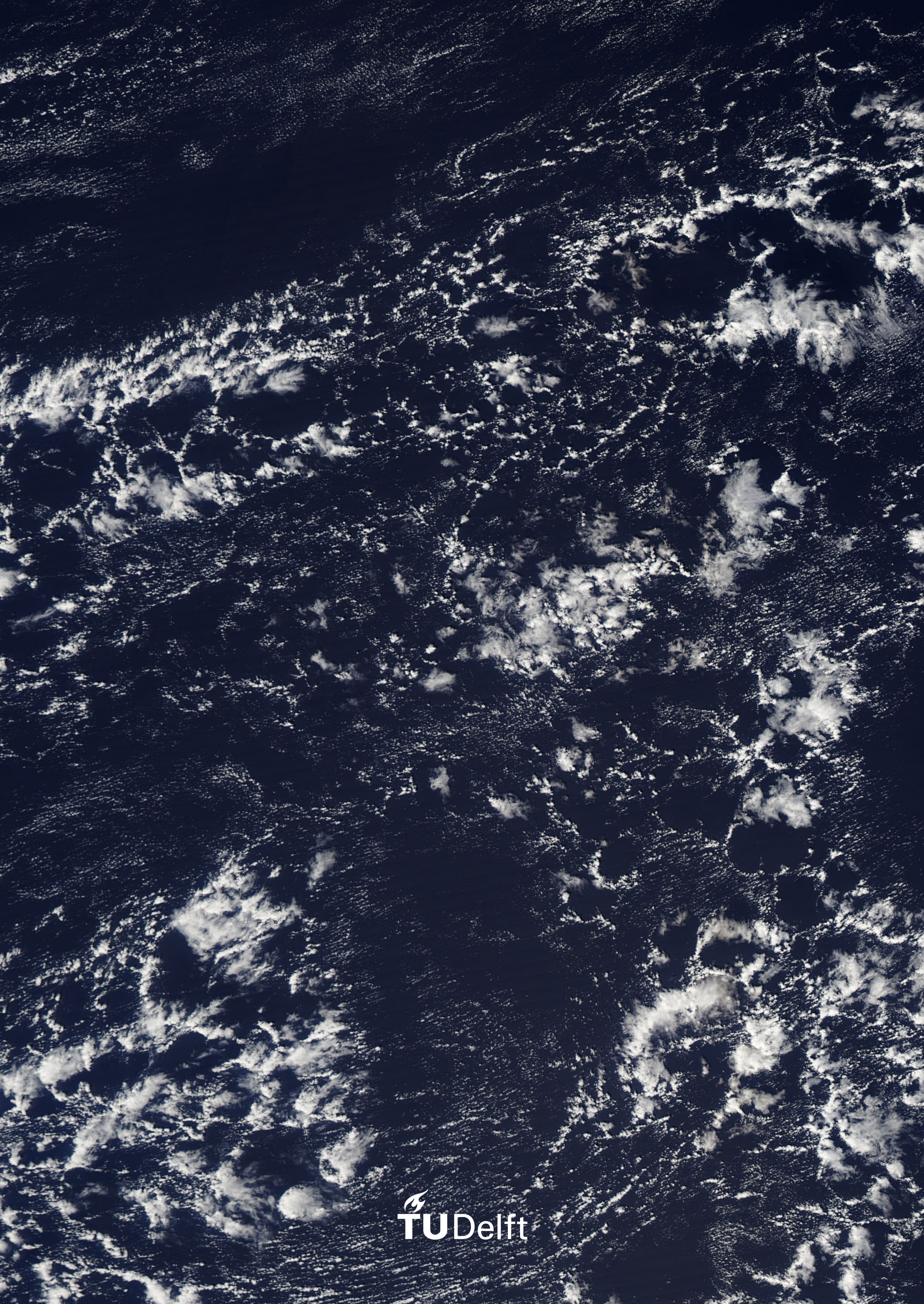
TUDelft